DOCTOR OF SCIENCES

Taphonomy of fossil integumentary structures and bones from Ornithodira
Chemical composition and modes of preservation

Cincotta, Aude

Award date:
2017

Awarding institution:
University of Namur

University of Namur
Department of Geology
Institute of Life, Earth and Environment

Taphonomy of fossil integumentary structures and bones from Ornithodira:

Chemical composition and modes of preservation

Thesis submitted for the fulfilment of the requirements for the degree of Doctor in Sciences

Members of the Jury:
Prof. J. Yans (UNamur) (supervisor), P.Godefroit (RBINS) (supervisor), V. Debaille (ULB), G. Garcia (Univ. Poitiers), V. Hallet (UNamur), M. McNamara (UCC), G. Terwagne (UNamur)

Aude Cincotta – December 2017

museum
Royal Belgian Institute of Natural Sciences

fnrs
FREEDOM TO RESEARCH

Cover graphic design: © Presses universitaires de Namur

Cover picture: reconstructions of: *Tupandactylus imperator*; *Anchiornis huxleyi*, by M. A. DiGiorgio; *Serikornis sungei*, by E. Willoughby; *Kulindadromeus zabaikalicus*, by J. Dos Remedios, photo: T. Hubin.

Rempart de la Vierge, 13
B - 5000 Namur (Belgium)

Printed in Belgium
ISBN: 978-2-87037-999-8
Legal deposit: 12/2017/1881/45

CONTENTS

ACKNOWLEDGMENTS

Acknowledging people remains difficult because one should not forget anybody we met during your PhD, which is not easy when our mind is too busy trying to finish the manuscript. That is why, I would filike first to make a general thank you to everyone I met and work with during my PhD thesis. I particularly thank all the people I met during the various conferences I went to. I had so interesting and great moments with you.

This PhD thesis would not have been possible without the grant support provided by the "Fonds National pour la Recherche Scientifique",
Thanks to C. Pisani, the director of the Royal Belgian Institute of Natural Sciences, for allowing me to spend four fantastic years collaborating with the Museum.
I have learnt that doing a PhD thesis may look like studying the sociology of a specific part of the population, here the researchers…Before beginning my doctoral thesis I could not imagine how dealing with people could, sometimes, be more important than dealing with the thesis itself. I am glad to have overcome both professional and personal issues during these four years. This made me grow up. But I could not have done it without the support of wonderful people:

First, I would like to gratefully thank my PhD supervisors, Johan and Pascal, for their implication and the great help they provided throughout these last four years (and even more since my Master thesis). Working at the reunion of geology and palaeontology was a most enriching experience.
There are field works I cannot forget, I went to destination I could never imagine to go. The PhD was also a personal adventure that made me a more determined person to do my best to protect and respect the biodiversity. When travelling around the world I have seen breathtaking scenaries, undisturbed wildlife, and I really want it to stay intact.

During the various conferences and scientific stays, I met loads of extremely smart, interesting and kind people. I really want to thank them for their warm welcome and availability: Valentina, Eugenia, Maria, Sofia, Svetlana, Johan, Pierre, and Johann.

My colleagues have a very special place in my heart, lunchbreaks playing cards constitute cheerful memories, as well as enjoying a drink on a terrasse on sunny days. I would like to thank my fellow players and friends from the Royal Belgian Institute of Natural Sciences: Jonica, Mona, Sidonie, Marie, Paolo(a) (the worthy inventor of the "rikiki"), Kretch, Cyrille, Olivier, Léonard, Bernard, Zozo (the inventor of the "rakaka", a slightly modified version of the "rikiki"), Floréal, Stijn (you will probably recognise the non-random order of your names), Thierry, Etienne, Koen, Adriano,

Nathan, Aldo, Wim, and all the others from the Directorate "Earth and History of Life". I had so interesting and inspiring discussions about Science but also societal phenomena, with all of you. It was so nice to work in such a friendly atmosphere.

A very special thanks to Ulysse, my PhD fellow, with whom I visited China for the first time and learnt (hum…) to use chopsticks. It was so great to share these four years working on feathered stuffs with you.
Thomas, Christian, Jean-François, Julien, Stéphane, Thierry L., Thierry H., thank you all for your helpful advices, assistance in lab works and various analyses, great pictures/SEM images, noon joggings, beers, coffees, books, and kindness!

Another warm thank you goes to my colleagues from the Departments of Geology and Geography at the University of Namur: Flore, Lorraine, Louise, Sabine, Sam, Colette, Delphine, Elisabeth, Sofia, Véro, Françoise, Vincent, Corentin, Augustin, Amaël, Alan, Gaëtan, Ludo, Sébastien, and all the others. A special mention goes to Michèle, thank you for your comfort in all circumstances!

I would also like to warmly thank people I met during the various analytical procedures I used during these last four years, I learnt a lot from you: Vinciane (ULB), Corry (UNamur), Guy and Julien (UNamur), Céline and Laurent (UNamur), Martine and Robert (UHasselt), Pierre (Synchrotron SOLEIL), and Thanh Thuy, Sylvie, Christelle, and their staff (UPMC). A sincere thank you to Géraldine and Xavier (Univ. Poitiers) for their always warm welcome.

Faire de la course à pied m'à vraiment aider à gérer mon stress, ma fatigue parfois, et m'a permis de passer de chouettes moments loin des préoccupations liées à la thèse. Le mental joue énormément en course à pied et il peut aussi aider à affronter la vie quotidienne. Je voudrais vraiment remercier mes compagnes et compagnons de jogging qui sont toujours hyper enthousiastes et motivés à l'idée de souffrir ☺ avec moi : Stéphane (le coach !), Silva, Michèle, Evelyne, Sylvie, Stéphanie, Bernadette, Ariane, Véronique, et les autres.

Je voudrais vraiment remercier mes amis, Céline, Pauline, Anne-Elizabeth, Patrizia, Eric, car malgré le fait qu'on ne se soit pas vu très souvent ces derniers temps, vous êtes toujours là…

Ce n'était pas non plus toujours évident d'expliquer en quoi consiste ma vie de doctorante, ma recherche, ce que je fais tous les jours (non, je ne vais pas en cours, et non je ne suis pas archéologue…grrr ☺).

Et enfin, "last but not least", ma famille…qui a tenu une place très importante durant ces quatre années de thèse. Valérie, merci de m'avoir aidée à gérer mon stress ;-), mes grand-mères, mon frère Cyril, Angelo (Grazie !). Et mes parents, merci de

m’avoir suivie dans mes projets et encouragée à faire ce que j’aime, malgré les difficultés que cela peut parfois représenter. Merci de m’avoir nourrie, au propre comme au figuré, et encouragée pour que après 28 années (déjà !) je sois devenue la personne que je suis actuellement.

LIST OF FIGURES

State of the art

Methodology

Chapter 1

Chapter 2

Chapter 3

Chapter 4

Chapter 5

Chapter 6

Chapter 7

Conclusions and perspectives

TABLES

Introduction

In palaeontology and geology, research for ancient traces of life is fascinating. Fossils are, in regard to the whole geological time spanned from the first evolved organisms to modern ones, relatively rare and provide a load of information on their biology. Palaeontologists dig up fossils, describe specimens and try to understand their behaviour, their interaction with their contemporaneous biota, whereas geologists study outcropping rocks, collect and analyse them in the laboratory with the aim to date and understand the depositional environment of the fossils. These two disciplines are closely interlocked, they represent two matched fields of research. This thesis discusses the question of soft tissue preservation using diverse analytical techniques from different scientific areas. Chemistry as well as biology and physics are well-developed research areas that are used by palaeontologists for the study of a panel of materials. Techniques that were dedicated to the study of inorganic or non-fossil organic material are now routinely used for taphonomic purposes in palaeontology.

The goal here is not to provide extensive interpretations of the different analyses we made in each discipline, but to try to choose the best analytical methods, i.e. those that are the most adapted to the fragile and heterogeneous fossil soft tissues. Results obtained from various methods also need to be easily compared together to bring valuable data. Generally, when dealing with scientifically "important" fossils, scientists try to avoid their destruction, as much as possible. Non-destructive methods are therefore performed as a first step in the analysis process. However, in some cases, the most accurate analyses still require to destroy the sample, at least to acquire information on its chemical composition. Relatively new methods, in the field of palaeontology, are nowadays judged as suitable for analysing a small portion of a sample, limiting its destruction to a surface of several millimetres to even nanometres, only. Those analyses are called "non-destructive" because the destruction is so limited – in some cases not even visible to the naked eye – that the sample appears unaltered. This thesis focuses on two, interconnected, topics: (1) the characterisation of the degree of preservation of various fossil soft tissues and, (2) the reconstruction of the deposition environment of two localities that have yielded bones and/or soft tissues.

The thesis is organised in three sections: each section contains one or several chapters that are written as papers in peer-review journals. The considered chapters contain a rather varied content, in any case, linked to the preservation of fossils and, especially of soft parts. These data have been published in international journals, are submitted for publication, or are in preparation.
The two first headings deal with the state-of-the-art and methodologies applied on fossil and modern soft tissues. The first one is dedicated to the **state-of-the-art** research in the field of the taphonomy of fossil soft tissues. Certain, useful, notions

regarding the soft tissue composition are reviewed in an attempt to introduce and better understand the next chapters. The second, **the Methodology,** is a review of the various analytical methods that were used during this PhD thesis. This chapter has an interest in giving an overview of all the given possibilities to study ancient fragile samples.

The **first section** concerns the chemical and descriptive taphonomy (i.e., the modes of preservation) of fossil feathers from the paravian dinosaurs *Anchiornis huxleyi* and *Serikornis sungei*, and the primitive neornithischian dinosaur *Kulindadromeus zabaikalicus*.

Chapter one deals with pigment organelles (melanin) and molecules in the plumage of dinosaurs. The ultrastructure of the feathers of *Anchiornis* is analysed by scanning and transmission electron microscopy (SEM and TEM). Remains of pigment organelles, melanosomes, are observed in several samples located on the skull and the tail of this Late Jurassic specimen. The elongate and narrow shape of these microbodies is characteristic of eumelanosomes, which give a brown or black colouration to the soft tissues. Geochemical analyses by time-of-flight secondary-ion-mass-spectrometry (ToF-SIMS) detect traces of negative ions characteristic of melanin and comparison with a variety of melanins and other organic substances reveal that the traces of fossil melanin more likely resemble eumelanin of animal origin. This work therefore provides new evidence of the possible preservation of pigments in fossil feathers.

In **chapter two**, *Anchiornis* plumage is analysed under a different perspective, for a completely different goal, and with other techniques. The type of preservation of the fossil feathers, and therefore the organic matter constitutive of these soft tissues is studied in detail. The chemical composition of fossil feathers and their embedding sediment is investigated by ion beam analyses (particle-induced X-ray emission - PIXE - and elastic backscattering spectrometry - EBS), nuclear magnetic resonance (^{13}C CP-MAS NMR) and pyrolysis in the presence of TMAH (TMAH Py-GC-MS). Feathers from a modern bird buzzard (*Buteo buteo*) are analysed for comparative purposes. The ultrastructure and mineralogy of the feathers and sediment are studied with scanning electron microscopy (SEM) and energy dispersive spectrometry (EDS). The fossil melanosomes are preserved within a fine clayey matrix. IBA indicates that concentration gradients of carbon are present in the fossil feathers and the matrix. C is greatly enriched in the near surface layers from the fossil feathers, which is not the case in the embedding matrix. Traces of sulphur are also detected in the fossil feathers. According to ^{13}C NMR and Py-GC-MS analyses, the composition of the fossil feathers is dominated by long aliphatic chains, but it slightly different from the matrix, indicating an in-situ polymerisation of original compounds. This work shows that despite the excellent morphological preservation of the fossil, its constitutive organic matter has undergone severe diagenetic transformation.

Chapter three describes the anatomy of a four-winged paravian dinosaur and discusses the morphology of its feathers. The skeletal anatomy of *Serikornis sungei* indicates that, despite its four feathered limbs, this small theropod dinosaur was not able to fly. The symmetry and lack of barbules in *Serikornis* feathers show that they were not aerodynamically adapted for flight, and rather suggest it was a ground-dweller.

Chapter four is a short article dealing with the trace element composition of integumentary structures. The body of the primitive neornithischian *Kulindadromeus zabaikalicus* from Siberia was covered both by epidermal scales and elongate epidermal structures interpreted as primitive feathers. The composition of these elongated proto-feathers is investigated here by Synchrotron X-ray fluorescence (μ-XRF) and X-ray absorption near-edge spectroscopy (μ-XANES). The purpose of this work is somewhat different from the others because the analyses being performed here are to test the method on our material, providing potential interesting results that we think worthwhile presenting. These analyses reveal that copper is enriched in the elongate epidermal structures from *Kulindadromeus* and that their Cu-coordination chemistry is similar to organic Cu in modern bird feathers and in natural eumelanin. This would indicate that the feathers of *Kulindadromeus* were pigmented by eumelanin, suggesting that a wide range of primitive feathers could already contain pigments.

Section II discusses the age, taphonomy and depositional setting of bones and soft tissues excavated from the Kulinda locality, where the primitive neornithischian dinosaur *Kulindadromeus zabaikalicus* was discovered.

Chapter five concerns the dating of Kulinda locality, and therefore of *Kulindadromeus zabaikalicus*. U-Pb radiochronological dating of zircons and monazites collected from volcaniclastic deposits and their granitic source gave a maximum Aalenian (Middle Jurassic) age. Subsequent palynological investigations refine the age of deposition to the Bathonian (i.e., between 168.3 ± 1.3 Ma and 166.1 ± 1.2 Ma). These dating are important given the phylogenetic position of *Kulindadromeus* amongst Dinosauria. The dating also indicated that the first proto-feather like epidermal appendages may have appeared earlier, in a common ancestor that lived during the Triassic.

Chapter six discusses the modes of preservation of soft tissues – epidermal scales and feathers - found closely connected to the articulated bones of *Kulindadromeus zabaikalicus*. The source and origin of the volcaniclastic deposits from Kulinda locality are examined, in an attempt to better understand the various degree of soft tissue preservation. The proto-feather like structures are observed in connection with the bones in a bone bed reflecting a very short to absent transport of the dinosaur carcasses, prior to their cover by clay-rich sediments. By opposition, two other bone beds show scattered bones with very few or no traces of soft tissues, indicating a high degree of disarticulation and transport of the carcasses prior to deposition. The

volcaniclastic deposits from Kulinda are derived from nearby acidic plutonic and volcanic sources produced in a complex geodynamic setting, related to the closure of the Mongol-Okhotsk Ocean throughout the Jurassic in Siberia.

Section III deals with the environmental reconstruction and bone taphonomy of a Late Cretaceous dinosaur locality from south-eastern France (Velaux-La Bastide Neuve) located in the Aix-en-Provence Basin.

In **chapter seven**, new sedimentological investigations are associated to the taphonomy of the vertebrate assemblages. The Velaux locality is characterised by riverine and lacustrine deposits that have yielded a diverse assemblage of vertebrate remains, including a new Azdharchid pterosaur taxon, a titanosaurid sauropod, theropod teeth, ornithischian (ankylosaurid and rhabdodontid) dinosaurs, crocodilians, chelonians, and fishes (including hybodont sharks). Plants, decapods and microfossils - represented by charophytes, ostracods, and molluscs - complete the assemblage. The sedimentary environment of Velaux represents a transition from a river sedimentation, with channel, overbank (levee) and floodplain facies, to a lake sedimentation with lacustrine limestones. The vertebrate remains have been exclusively deposited in channel, overbank and floodplain facies. Although reworked elements from Aptian marine limestones have been found in the lower part of the section, no indication of any contemporaneous marine influence has been observed in the Velaux deposits. This is confirmed by the continental aspect of the sedimentation in the Aix-en-Provence Basin at that period.

This PhD thesis makes reference to the following papers:

- "Molecular composition and ultrastructure of Jurassic paravian feathers"

Johan Lindgren, Peter Sjövall, Ryan M. Carney, Aude Cincotta, Per Uvdal, Steven W. Hutcheson, Ola Gustafsson, Ulysse Lefèvre, François Escuillié, Jimmy Heimdal, Anders Engdahl, Johan A. Gren, Benjamin P. Kear, Kazumasa Wakamatsu, Johan Yans & Pascal Godefroit

Published in Scientic Reports, *2015*

- "Chemical taphonomy of morphologically well-preserved dinosaur feathers: a multi-technique approach"

Aude Cincotta, Thanh Thuy Nguyen Tu, Julien L. Colaux, Guy Terwagne, Sylvie Derenne, Pascal Godefroit, Christelle Anquetil, and Johan Yans

To be submitted

- "A new Jurassic theropod from China documents a transitional step in the macrostructure of feathers"

Ulysse Lefèvre, Andrea Cau, Aude Cincotta, Dongyu Hu, Anusuya Chinsamy, François Escuillié, and Pascal Godefroit

Published in The Science of Nature, *2017*

- "Synchrotron micro X-ray fluorescence (μXRF) and absorption spectroscopy (μXANES) suggests the presence of eumelanin pigment in the proto-feathers of *Kulindadromeus zabaikalicus* (Middle Jurassic of Siberia)"

Aude Cincotta, Pascal Godefroit, Johan Yans, and Pierre Guériau
To be integrated to further work

- "A Middle Jurassic age for the neornithischian *Kulindadromeus zabaikalicus*, the oldest dinosaur with 'feather-like' structures from Siberia"

Aude Cincotta, Katerina B. Pestchevitskaya, Sofia M. Sinitsa, Valentina S. Markevich, Vinciane Debaille, Svetlana A. Reshetova, Irina M. Mashchuk, Andrei O. Frolov, Axel Gerdes, Johan Yans, and Pascal Godefroit
To be submitted

- "Exceptional preservation of soft tissues in the neornithischian dinosaur *Kulindadromeus zabaikalicus* and the reconstruction of the depositional environments"

Aude Cincotta, Johan Yans, Katerina B. Pestchevitskaya, Irina M. Mashchuk, Andrei O. Frolov, Vinciane Debaille, Sofia M. Sinitsa, Svetlana A. Reshetova, Yuri Bolotsky, and Pascal Godefroit
In preparation

- "Integrated palaeoenvironmental reconstruction and taphonomy of a unique Upper Cretaceous vertebrate-bearing locality (Velaux, south-eastern France)"

Aude Cincotta, Johan Yans, Pascal Godefroit, Géraldine Garcia, Jean Dejax, Mouloud Benammi, Sauveur Amico, and Xavier Valentin
Published in PLoS ONE, *2015*

State of the art

1. Introduction

Characterisation of ancient biomolecules in fossil soft tissues is crucial to understand the mechanisms that allowed their morphological, and in some cases chemical, preservation. Since the last few years an increasing number of studies have been performed on a wide range of fossil soft tissues with the aim to explain and characterise the early diagenesis processes they have undergone. This chapter will define the scientific terminology and review the notion of exceptional preservation in specific fossiliferous localities and will focus on the composition of certain soft tissues – feathers and scales – in an attempt to introduce the next chapters.

2. Ornithodira

The fossils analysed in this thesis are all part of a group named "Ornithodira", which groups both the dinosaurs and pterosaurs (Fig.1). In the literature, Ornithodira are defined as a clade including Pterosauria, Dinosauromorpha, their most recent common ancestor, and all their descendants (Benton, 2004). This clade is supported by the following apomorphies (derived traits, i.e., traits that are unique to a group): the deltopectoral crest on the humerus subrectangular; the astragalar caudal groove absent; and the calcaneal tuber rudimentary or absent (Benton, 2004).

Dinosauria includes three clades characterised by specific variations in their skeletal anatomy, but that are commonly differentiated by the geometry of the pelvic bones, (1) the Sauropodomorpha and (2) the ancestors of birds, the Theropoda, are both characterised by a pubis oriented forwards ("reptile-like" pelvis), and (3) the Ornithischia, with a pubis oriented backwards ("bird-like" pelvis). All non-avian dinosaurs disappeared at the end of the Cretaceous period.

Pterosauria includes two distinct groups, (1) the Rhamphorhynchoidea, which had a long tail and are known from the Upper Triassic to the Upper Jurassic, and (2) the Pterodactyloidea, which had a short tail, appeared in the Upper Jurassic and became extinct at the end of the Cretaceous, like the non-avian dinosaurs (Wellnhofer, 1991).

3. Fossil *Lagerstätten*

Exceptional preservation of fossils like those preserving soft parts are observed in specific localities named *Lagerstätten*. Originally, Fossil *Lagerstätten* were defined by Seilacher et al. (1985) as "rock bodies unusually rich in palaeontological information, either in a quantitative or qualitative sense".

This concept includes both localities that are rich in well-preserved fossils and those that are characterised by their particularly rich concentration of fossils. The two different types of *Lagerstätten* are called: (1) the *Konservat-Lagerstätten*, those that are characterised by a good preservation of the fossils, reflected by the presence of soft parts or well-articulated skeletons, and (2) the *Konzentrat-Lagerstätten*, those that contain a great amount of fossils concentrated at the same locality and, thence, not specifically related to a certain type of preservation. The *Konservat-Lagerstätten* constitute important, and rare, fossiliferous localities for the study of the preservation of ancient integumentary structures. These sites are the ones that will be examined in this thesis. Some of the most remarkable *Konservat-Lagerstätten* include the late Neoproterozoic Ediacara biota (Australia, 575-542 Ma), which record the first elaborate forms of life; the Early Cambrian Chengjiang biota (China, 520 Ma), which shows soft tissue replication by pyrite and clay minerals (Gabbott et al., 2004); the Middle Cambrian Burgess Shale biota (Canada, 405-410 Ma), which displays authigenic replacement of soft tissues by clays (Orr et al., 1998) but also the first hard, mineralised, parts of marine metazoans; the Late Jurassic Solnhofen Limestones in Bavaria (Germany), well known for having yielded eleven specimens of the early bird *Archaeopteryx*. One of them – the Thermopolis specimen – exhibits a preserved plumage that retains faint traces of (probably diagenetic) metal in its structure (Bergmann et al., 2010). Other localities show excellent details of soft tissues, such as the Late Jurassic Yanliao Biota in Liaoning Province (China) with exquisitely

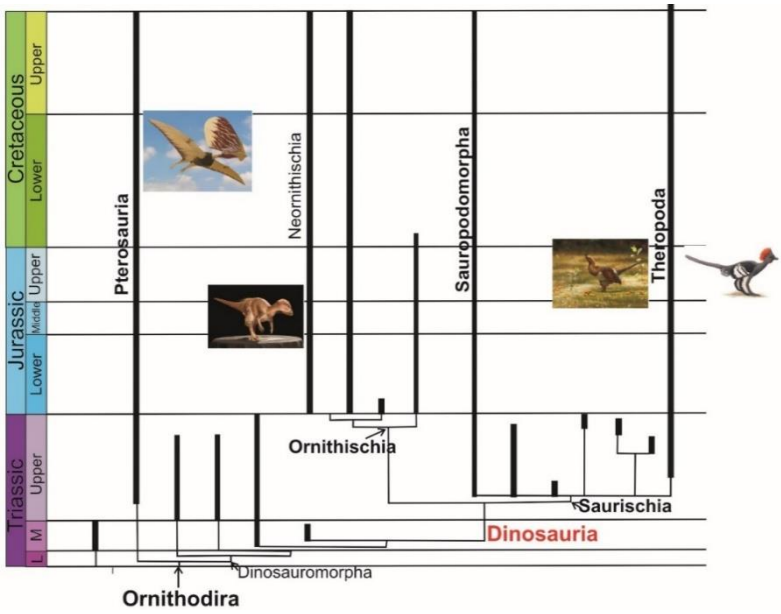

Figure 1. Simplified phylogenetic tree of Ornithodira. Pterosauria (pterosaurs) and Dinosauria (dinosaurs) are two sister-groups. Dinosauria includes Saurischia ("reptile-like" pelvis) and Ornithischia ("bird-like" pelvis). The fossils studied in this dissertation are all included in the Ornithodira.

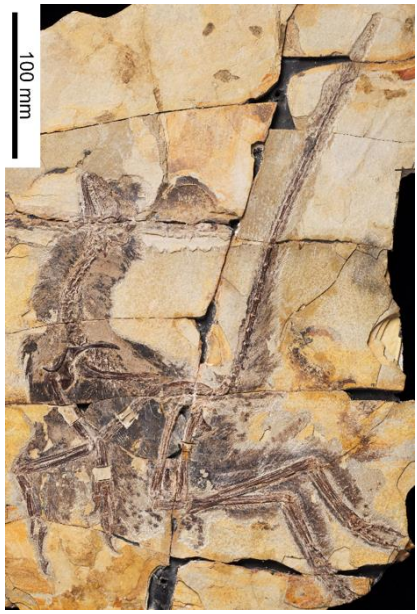

Figure 2. *Serikornis sungei*, a four-winged paravian dinosaur from the Late Jurassic *Konservat-Lagerstätte* of Jianchang (Liaoning, China) (from Lefèvre et al., 2017).

preserved specimens – e.g., the paravians *Anchiornis huxleyi* (Xu et al., 2009a), *Eosinopteryx brevipenna* (Godefroit et al., 2013b), *Aurornis xui* (Godefroit et al., 2013a) and *Serikornis sungei* (Fig.2 ; Lefèvre et al., 2017), the pterosaur *Jeholopterus* (Kellner et al., 2010), as well as finely preserved insects and arachnids; the highly diversified Early Cretaceous Jehol Biota that preserved a huge amount of fossils with soft parts – e.g., the dromaeosaur *Microraptor gui* (Xu et al., 2003), the enormous basal tyrannosauroid *Yutyrannus huali* that shows feather-like structures (Xu et al., 2012), the birds *Sapeornis chaoyangensis* (Zhou & Zhang, 2002a), *Jeholornis prima* (Zhou & Zhang, 2002b), and *Confuciusornis sanctus* (Hou et al., 1995), the mammal *Eomaia scansoria* (Ji et al., 2002), abundant fishes, turtles, amphibians, but also the earliest angiosperm plant *Archaefructus* (Sun et al., 1998); or the younger Eocene Messel locality in Germany that yielded well-preserved soft parts of mammals, birds, amphibians, fishes, among others.

4. Taphonomy of soft tissues

All these remarkable localities, with their fossilised soft tissues, provide highly valuable data and lead to a better comprehension of the biology of extinct animals. In particular, the discovery of feathered theropod dinosaurs have filled a “gap” in the evolution history of feathers. The analysis of the structure and composition of modern bird feathers and its comparison with fossils brings new data on the plumage

colouration in dinosaurs and early birds (Barden et al., 2011; Clarke et al., 2010; Li et al., 2010; Lindgren et al., 2015; Vinther et al., 2009; Vinther et al., 2008; Vinther et al., 2016; Zhang et al., 2010).

The presence of feathers in dinosaurs that were not able to fly suggested they had other functions, such as display or thermal regulation. Dinosaurs were at first thought to be ectothermic reptiles (Desmond, 1979), but these recent findings radically changed the understandings on dinosaur – especially theropod – physiology and confirmed that, at least some of the dinosaurs were endothermic. The type of body covering recovered from fossilised animals may, therefore, indicate whether it was homeotherm (warm-blooded) or poikilotherm (cold-blooded). Indications on the integumentary coverage can, in addition, bring further information on the way they adapted to their environment (whether they were flying, non-flying, arboreal, cursorial, aquatic, etc.), or on their sexual behaviour (sexual dimorphism). Thence, these exceptionally preserved soft tissue fossils are a boon for palaeontologists.

Study of fossil soft tissues has increased greatly over the past ten years. The research for original molecular compounds in, in some cases hundreds of million year old fossils benefitted from recent developments in a series of analytical techniques. Some of those techniques, now commonly used, were initially devoted to other scientific fields, generally in applied research topics. For instance, organic geochemistry techniques were widely applied in source rock potential assessment and soil organic matter characterisation (e.g., Witte et al., 1988; Horsfield, 1989; Larter & Horsfield, 1993; Guggenberger et al., 1995; Kögel-Knabner, 1997; Kelemen et al., 2007). By now, it is employed in subjects as diverse as comparing compositions between two types of soya sauces (Kamal et al., 2016); prospecting the quality of olive oil (Sacchi et al., 1997); characterising the origin of amber (e.g., Galletti & Mazzeo, 1993; Sodhi et al., 2013); or analysing hair belonging to Egyptian mummies (Bertrand et al., 2003).

The application of cutting-edge techniques for the molecular characterisation of fossil soft tissues helped interpreting taphonomic patterns. For example, pyrolysis gas-chromatography mass-spectrometry has been repeatedly used to understand how diagenetic processes modify the molecular composition of fossils (e.g., Baas et al., 1995; Stankiewicz et al., 1998; Gupta et al., 2008; Gupta et al., 2007b; Manning et al., 2009b; Barden et al., 2015). Similar methods are used in decay experiments on modern animals, with the aim to help at assessing the chemical changes undergone by their extinct ancestors (e.g., Gupta et al., 2009).

5. Keratins

5.1. Composition

Epidermal appendages - hair, feathers, nails, epidermal scales (also named scutes), horns, beaks, claws, hoofs - are non-vascularised (“dead”) tissues composed of insoluble proteins, keratins, present under two different molecular conformations, the alpha-keratin and the beta-keratin. Keratin is composed of filaments that have

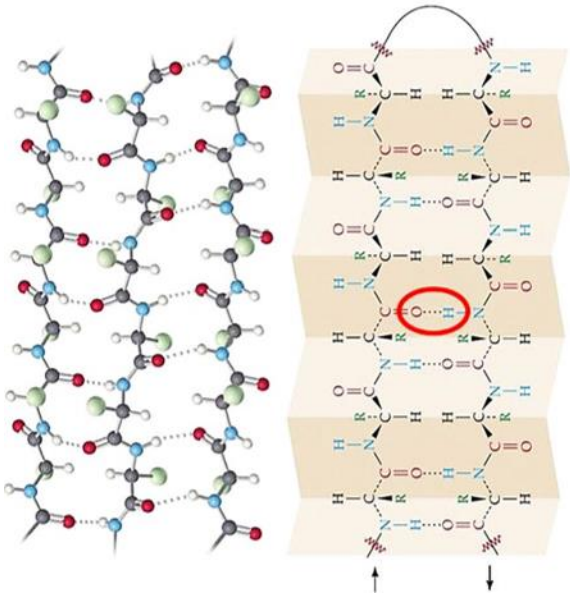

Figure 3. Molecular structure of alpha-keratin (from Wang et al., 2016). The abundant hydrogen bonds provide great stability to the molecule. The three-dimensional structure of the alpha-keratin typically corresponds to a helix.

nanometre sized diameters (~7 nm in α-keratin and ~3-4 nm in β-keratin; Squire & Vibert, 1987; Fraser et al., 1971) and are embedded in an amorphous matrix, the gamma keratin (Lucas & Stettenheim, 1972a). What distinguishes these two types of keratins is their molecular secondary structure: α-keratin units are composed of two polypeptide chains helically-coiled (Fig. 3), where cross-linking by cystine - amino acid containing disulphide bonds - and hydrogen bonds are responsible for the high stability of the molecule; the secondary structure of β-keratin filament is formed by two antiparallel pleated sheets assembled by hydrogen bonds, each pleated sheet being composed of four polypeptide chains laterally linked together by intermolecular hydrogen bonds (Fig. 4) (Woodin, 1954; Fraser et al., 1971; De Leeuw & Largeau, 1993). The α-keratin helices can be converted into β-keratin sheets by stretching (Pauling & Corey, 1951; Kreplak et al., 2004). The keratins provide mechanical support for integumentary structures and therefore have a significant role in protecting the animal body against external "attacks" from the environment. In mammals, alpha-keratin only is observed in the integumentary appendages (except in pangolins, which have both alpha- and beta-keratins in their epidermal coverage), whereas both α- and β-keratins are present in bird and reptile epidermal structures. The function of the α-keratin is to provide a waterproof layer and mechanical resistance to the integumentary appendages, although the β-keratin is typically contained in hard tissues and also plays a role in strengthening the skin hardness (Gregg & Rogers, 1986; Fraser & Parry, 1996). Keratins contain abundant disulphide and hydrogen

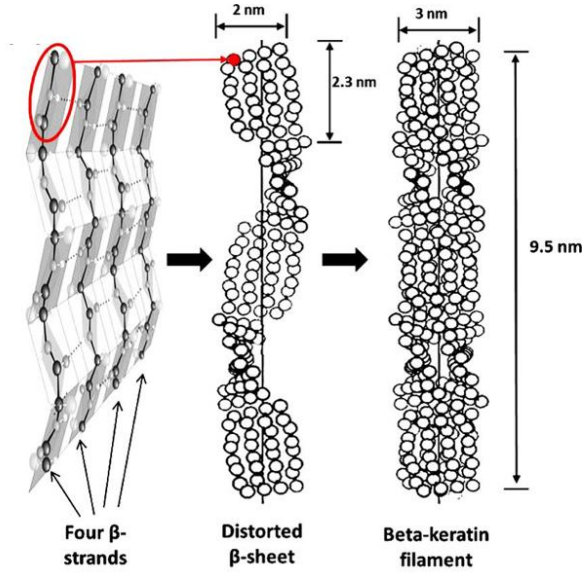

Figure 4. Molecular structure of beta-keratin (from Wang et al., 2016). The molecule is formed by four polypeptide chains linked together by strong hydrogen bonds. The 3D structure of the beta-keratin corresponds to a pleated sheet.

bonds. This particular molecular composition makes keratinous products insoluble and greatly resistant to degradation.

Keratins from feathers comprise the following eighteen amino acids, in variable quantities: serine, glycine, proline, alanine, leucine, valine, cysteine, glutamic acid, aspartic acid, threonine, arginine, isoleucine, phenylalanine, tyrosine, methionine, lysine, histidine, and tryptophan

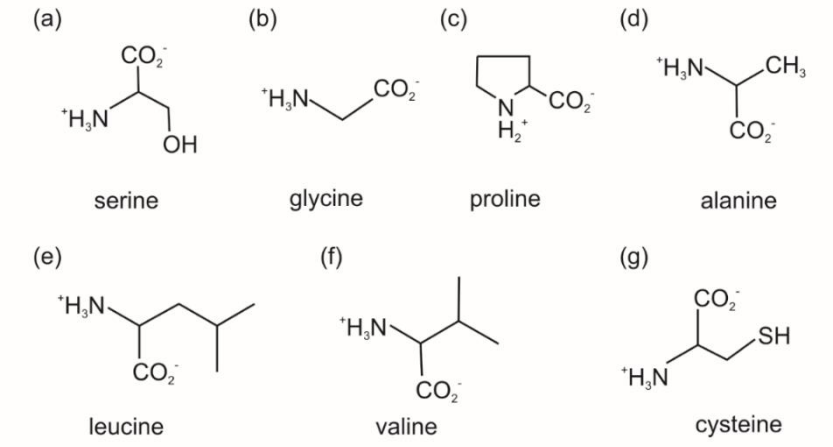

Figure 5. Molecular structure of the main amino acid compounds from feather keratin.

The molecular composition of the main amino acids from chicken feather keratin is shown in Figure 5.

5.2. Keratins in integumentary structures

In this chapter, I will focus on the main keratin-containing epidermal appendages preserved as fossils and studied in this thesis: feathers and epidermal scales. Feathers are preserved around the skeleton of several small theropod dinosaurs, including *Anchiornis huxleyi* (YFGP-T 5199) and *Serikornis sungei* (PMOL-AB00200) from the Upper Jurassic Tiaojishan Formation in northern China, and both proto-feathers and epidermal scales were found associated with remains of the primitive neornithischian dinosaur *Kulindadromeus zabaikalicus* from Transbaikal region (Russia) (Godefroit et al., 2014). In addition, soft tissues from a pterosaur cranial crest were studied but the origin of these structures is not well understood. The fossil of the tapejarid pterosaur, probably a new species, shows two types of soft tissues: body coverage "feather-like" appendages and a soft tissue crest, likely of epidermal origin. These epidermal structures allow a better understanding of their function in ancient archosaurs. All these epidermal appendages show some degree of similarity in their structures, and they all represent important fossils relative to the evolution history of integumentary body coverage in Ornithodira.

5.2.1. Feathers

Types of feathers

Feathers are integumentary appendages that forms the body coverage of modern birds. The typical feather morphology consists of a proximal shaft and a vane. The shaft constitutes the lower part of the feather and comprises a translucent calamus at its proximal end and an opaque rachis, the central part of a feather, which extends distally towards the tip of the feather. The remaining part of the feather, the vane, consists in

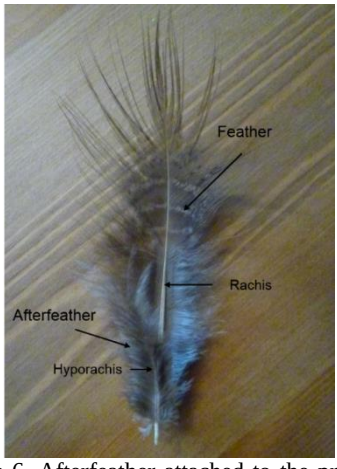

Figure 6. Afterfeather attached to the proximal part of a contour feather. The afterfeather has its own rachis (called hyporachis) and barbs.

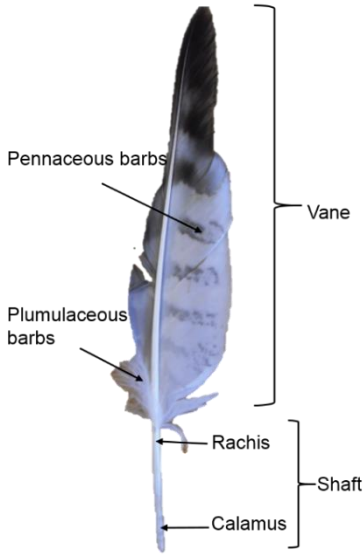

Figure 7. Structure of a flight feather (remige) sampled on a buzzard bird (*Buteo buteo*; collection number: A4011A01).

the assemblage of barbs and barbules that extend laterally from the rachis. There are five different types of feathers on the bird's body: (1) contour feathers, (2) flight feathers (remiges and rectrices), (3) down feathers, (4) filoplumes, and (5) bristles:

(1) In contour feathers (Fig. 6), the calamus is short and almost spherical. The vane contains barbs and barbules that extend symmetrically from the rachis. They are characterised by a fluffy texture proximally and a flat texture distally (Lucas & Stettenheim, 1972b). Afterfeathers are common in contour feathers. They are attached to the proximal part of the feather and comprise their own rachis – the hyporachis - and barbs. Afterfeathers form smaller, auxiliary feathers typical of contour feathers.

(2) Flight feathers are asymmetric, mainly composed of pennaceous feathers (Fig. 7). The asymmetric structure of the vane in remiges and rectrices – wing and tail feathers, respectively – is essential to develop aerodynamism and then for flight. In flight feathers, the calamus is ellipsoidal and longer than in contour feathers (Lucas & Stettenheim, 1972b). The rachis is composed of internal septa, generally containing fith, which make feathers rigid but flexible enough for flight (Rutschke, 1966). Flight feathers also bear afterfeathers. Scanning electron microscopy images of the section of a flight feather (Fig. 8a) clearly show the porosity of the rachis, with its numerous hollow cavities, also containing pigment organelles (Fig. 8b).

(3) Down feathers are entirely plumulaceous feathers and do not usually possess rachis, although, when present, it is very short (Lucas & Stettenheim, 1972b). Barbules in down feathers are loose because, unlike flight and contour feathers,

they do not show hooklets on their distal end. Down feathers mainly have an insulating function.

(4) Filoplumes are distributed on the whole body of modern birds and are commonly located under the other feather types (contour, flight, down). They are elongated and thin feathers characterised by a relatively short calamus, and a long, narrow rachis that distally bears a tuft of barbs and barbules (Lucas & Stettenheim, 1972b). Their function, although not fully understood, might be to detect minute variations in atmospheric currents and therefore serve as sensitive organs to readily readjust the movement of feathers (Lucas & Stettenheim, 1972b).

(5) Bristles are characterised by a sharp, elongate rachis and by the presence of barbs on the proximal part of the feather, only. The distal end of the rachis of bristles is, therefore, relatively smooth. Bristles are mostly located on the heads of modern birds and fulfill various functions, according to their exact location. Bristles located around the nostrils prevent the passage of external substances (dust, etc.) into the nostrils. Similarly, bristles growing adjacent to the beak might help at catching insects in certain bird species. Those specialised feathers most probably have a sensory function (Lucas & Stettenheim, 1972b).

Composition

The major amino acid constituents of the feather β-keratin are serine, glycine, proline, alanine, and leucine (Wang et al., 2016). In modern birds, feathers are not only flight

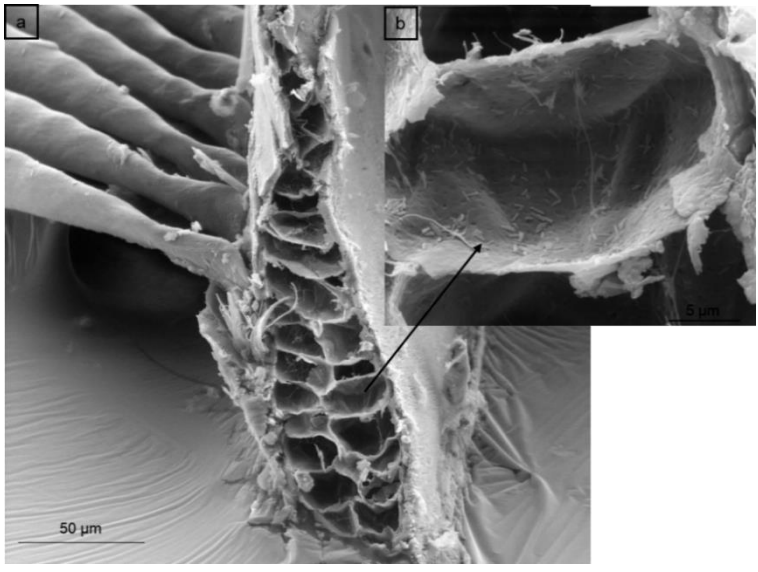

Figure 8. Scanning electron microscope (SEM) images of the distal portion of a buzzard flight feather. (a) Section of the rachis showing internal hollow cavities and adjacent barbs, (b) close-up of a single cavity lined by elongate microbodies, probably corresponding to melanosomes.

structures but serve for a variety of functions, such as thermal insulation (down feathers), sexual display (e.g., the colorful "eye patterns" in peacock feathers), protection against external environmental agents like water and solar radiation, or camouflage (e.g., the plumage of the nightjar, *Caprimulgus europaeus*, which mimics branch or ground patterns).

The production of keratin in feathers begins early relative to their formation process and might, in some cases, even finishes before the complete formation of the feathers (Lucas & Stettenheim, 1972a). A feather is composed of about 91% of proteins (not only keratins), 2% of lipids (cholestenol and free fatty acids), and the rest is essentially water. The quantity of each amino acid remains constant in similar parts of a feather - the rachis, barbs, or barbules - but the relative proportion of these amino acids shows some variation in feathers from different bird species. Feathers constitute important sources of proteins. For that reason, feathers have been extensively studied in the field of the bioindustry – especially biopolymers – to find the best way to extract proteins and to exploit their high nutritional content and high availability (Bertsch & Coello, 2005). In such cases, poultry feathers represent easily available nutritive and sustainable resources (Barone et al., 2005).

5.2.2. Epidermal scales

Amino acid content in the keratin contained in epidermal scales appears to be similar to that observed in feather keratin, except in their relative proportions. For instance, keratin contained in turtle scales comprises high quantities of glycine, cysteine, proline, serine and is characterised by relatively higher proportion of the aromatic amino acid tyrosine than in feathers (e.g., Toni et al., 2007). The molecular structure of scale β-keratin is also rather similar to those of feather β-keratin.

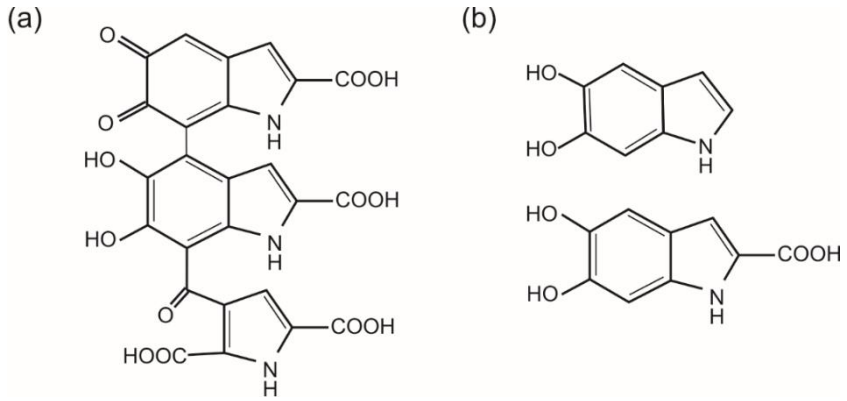

Figure 9. Molecular composition of the black-brown pigment eumelanin (After Wondrak et al., 2006). (a) Eumelanin molecule formed by the polymerization of (b) 5,6-dihydroxyindole and 5,6-dihydroxyindole-2-carboxylic acid.

6. Melanin and colouration

Melanin is an insoluble, biopolymeric pigment formed by the enzymatic oxidation of the amino acid tyrosine in the melanocytes (Lucas & Stettenheim, 1972a). Once synthesised, melanin granules are stored in cell organelles, the melanosomes. The simplified mechanism for melanin production implies copper-bearing hydroxylase that forms the dihydroxyphenylalanine (DOPA) from the tyrosine (Kruh, 1989). The DOPA is subsequently oxidised and forms indole quinone cycles. The polymerisation of these indole quinones eventually leads to the formation of melanin. Two main types of melanins exist (although there are in reality four different types) the eumelanin and the phaeomelanin, contained in the eumelanosomes and phaeomelanosomes, respectively. The eumelanin (Fig. 9a) is a black and dark brown pigment characterised by a high molecular weight and that consists of polymers of 5,6-dihydroxyindole and 5,6-dihydroxyindole-2-carboxylic acid (Fig. 9b). The phaeomelanin (Fig. 10) is a red, yellow, brownish pigment of low molecular weight composed of sulphur-containing derivatives of benzothiazine. Additionnally, there exists a third type of melanin, called the allomelanin, which will not be discussed here due to its presence in plants, only. Melanins are present in a broad range of tissues and organs, such as eyes, skin, hair, feathers, ink sacs of cephalopods, and in fungi and bacteria (e.g., Solano, 2014). The function of melanin can be rather diverse, for example: (1) it absorbs the entire visible light spectrum and ultraviolet radiation, protecting the tissues against sun damages, (2) it induces pigmentation and therefore has a role in the camouflage and sexual display, (3) it has a strong affinity for metallic ions and is a chelator for cations such

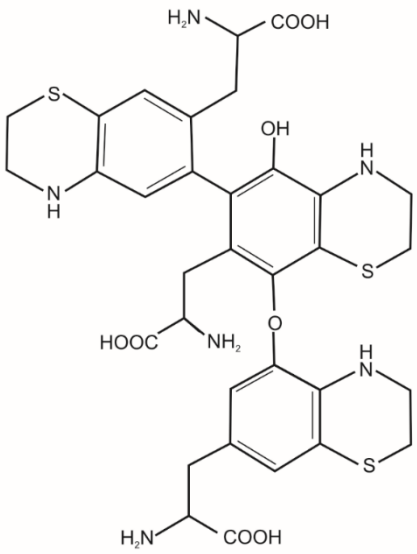

Figure 10. Molecular structure of the red-yellow pigment phaeomelanin (after Wondrak et al., 2006). The molecule is characterized by the presence of sulfur in the aromatic rings.

as Fe^{3+}, Ca^{2+}, Zn^{2+} and Mg^{2+} , and especially for Pb^{2+} and Cu^{2+} (Larsson & Tjälve, 1978; Szpoganicz et al., 2002; Hong et al., 2004), (4) it strengthens the tissue structure, and (5) it allows the regulation of the body temperature because of the absorption of visible and infrared light (Cesarini, 1996). It should be noted that although the eumelanin has a photoprotector function, the phaeomelanin is, on the contrary, a photosensibilizator (Chedekel et al., 1978).

7. Melanosomes versus bacteria: issue for their distinction in fossils

The presence of morphologically preserved melanosomes together with preserved chemical derivatives of melanin has been observed in the integumentary appendages of several fossils (Li et al., 2010; Barden et al., 2011; Barden et al., 2014; Lindgren et al., 2012; Lindgren et al., 2014; Lindgren et al., 2015; McNamara et al., 2016). These findings were used in the attempt to reconstruct (with some prudence) the colouration of extant organisms. There is controversy about the substantial presence of preserved melanosomes in fossil integumentary appendages, and some authors suggest that the structures, observed and identified as pigment organelles, could rather represent fossilised bacteria (Pinheiro et al., 2012; Moyer et al., 2014). Bacteria and melanosomes are indeed similar in size and shape. The determination of a melanic origin for the microbodies observed in various fossil tissues therefore requires a combination of extensive chemical (e.g., gas chromatography-mass spectrometry, Fourier transformed infrared spectroscopy, or time-of-flight secondary ion mass spectrometry) and structural analyses (scanning and transmission electron microcopy). Data on the morphology and the chemical composition are both needed to to make the right assumption. Bacteria exist under a broad range of shapes (e.g., helical, rod, round, or even amorphous). Rod-shaped bacteria, such as the modern

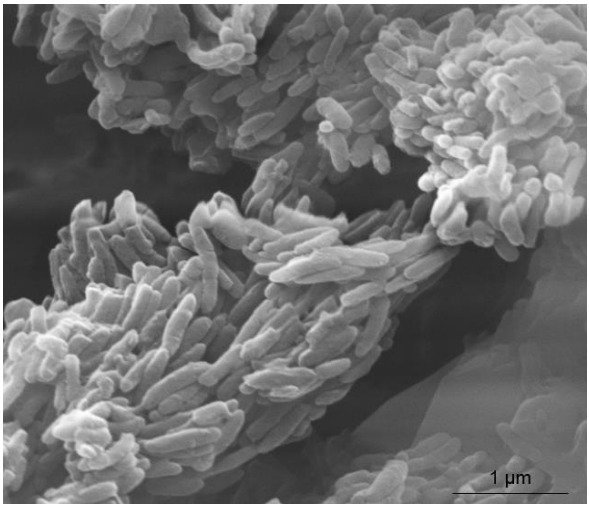

Figure 11. Elongate microbodies attributed to eumelanosomes, in integumentary structures of a Lower Cretaceous pterosaur from the Crato Formation (Brazil).

bacteria *Bacillus subtilis*, are morphologically comparable to the elongate melanosomes, the eumelanosomes. Melanosomes have sizes ranging between 0.3 and 3.0 μm in modern bird feathers (Lubnow, 1963). Eumelanosomes (Fig. 11) are generally longer and have more regular shapes - typically rod or ellipsoidal - than phaeomelanosomes, which are rounded. It should be mentioned that not only melanins are responsible for coloration in epidermal tissues (and in particular feathers): carotenoids and porphyrins are other pigments providing orange, yellow and red colorations. They nevertheless seem to have lower resistance to degradation than melanins and are not retained in ancient soft tissues.

Diagenetic processes - occurring as soon as the soft tissues are deposited – may have an influence on the morphology of melanosomes. Decay experiments on feathers have been carried out in laboratories in order to reproduce, as far as possible, diagenetic processes and to identify possible morphological changes in melanosomes under diverse temperature and pressure conditions (McNamara et al., 2013; Colleary et al., 2015). These experiments showed that the morphology of melanosomes may somehow be altered by diagenetic processes, which mainly lead to their shrinkage (due to dehydration) and/or merging (Colleary et al., 2015). These morphological changes therefore have an implication when reconstructing the colour of fossil soft tissues. Comparisons between modern bacteria in decaying feathers and feather melanosomes showed that melanosomes are always observed within the feather structure, not on its surface (Moyer et al., 2014). Fossil melanosomes should therefore be present as internal layers only and, more importantly, they should not be present in the embedding sediment. Moreover, melanosomes are embedded in an amorphous keratin matrix that, when preserved, should undoubtedly indicate the melanosome origin for the microbodies. On the contrary, a bacterial origin for the fossil microbodies should be verified by checking whether they form a continuous layer on the surface of the fossil. In addition, in feathers, melanosomes show some alignment along the main axis of the rachis, barbs or barbules, which is not the case for bacteria (Knight et al., 2011). Vinther et al. (2009) observed that melanosomes were aligned along the long axis of fibres from Eocene fossil feathers, whereas this type of organisation does not appear in bacteria. Finally, it cannot be excluded that bacteria and melanosomes may occur together in fossils.

A critical point to mention is that rod-shaped “bacteria” only have been observed in fossil soft tissues. This contrasts greatly with the large variety of dimensions displayed in modern bacteria. Whether these rod-shaped structures are indeed bacteria, one must explain why the other bacterial morphologies are not observed as well. Were the depositional environments only suitable for one type of bacteria? This is probably not the case, since depositional environments for soft tissues were as diverse as lacustrine (e.g., Briggs et al., 1997; Barden et al., 2011; Wogelius et al., 2011; Lindgren et al., 2015), lagoon (e.g., Barthel et al., 1990; Schwark et al., 2009; Pinheiro et al., 2012) marine (e.g., Briggs et al., 1991; Wilby et al., 1996; Gabbott et al., 2004; Butterfield et al., 2007), or even fluvial settings (e.g., Manning et al., 2009b;

Knight et al., 2011; Zelenitsky et al., 2012). However, the extracellular polymeric substance (EPS) found in bacteria cell walls operates as a nucleation site for mineral replacement (Westall et al., 1995). It means that bacteria can easily be mineralised, and then fossilised. Additionally, melanin is also synthesised by bacteria, which makes the interpretation of the results difficult. For example, anaerobic bacteria use melanin as electron acceptor and reduce Fe^{3+} into Fe^{2+} (Plonka & Grabacka, 2006). The melanins from melanosomes and bacteria are, nonetheless, chemically different, allowing their discrimination by using sensitive analytical techniques (e.g., Lindgren et al., 2015). A complete distinction between these two microbodies is therefore possible by combining investigations of the ultrastructure and molecular composition of the microbodies found in fossil soft tissues.

In this PhD thesis, my aim is to provide supplementary knowledge on the degree of preservation of fossil soft tissues by using conventional analytical methods that, even though, have previously been performed on soft tissues, were not used on theropod feathers yet. Additionnally, this work refers to other, less familiar, techniques that appears to be highly interesting, convenient and useful in the study of fossil soft tissues. The fossil material used here is of high scientific value and is studied in detail for the first time. The taphonomy of bone beds is also particularly important for the reconstruction of ancient habitats, and will be applied to new fossil-bearing localities, including one locality showing well-preserved soft tissues.

Methodology

Various analytical techniques were employed as tools in organic geochemistry applied to palaeontology. The complete analytical procedure applied to the fossils is reviewed in detail in the diverse chapters of the thesis. The aim, here, is somehow different, and consists in providing an overall explanation of each of the analytical methods that are used in this PhD thesis. Diverse Archosauria integumentary structures such as epidermal scales, feathers, feather-like appendages, and their embedding sediment, are studied using an array of techniques frequently used for the analysis of fossil soft tissues (Fourier transformed infrared spectroscopy, Pyrolysis gas chromatography-mass spectrometry, scanning electron microscopy, and energy dispersive X-ray spectroscopy). Other, less conventional or less easily accessible, techniques (ion beam analysis or techniques using synchrotron radiations) are applied here on palaeontological material, even though they are generally applied to inorganic surfaces or archaeological materials. For that purpose, fossil samples of dinosaur feathers and 'feather-like' structures, bird feathers, pterosaur soft tissue crest and integumentary appendages, as well as modern equivalents to those structures - bird feathers - were first sampled (usually by using a sterile scalpel blade) in order to be further analysed.

By using a wide variety of complementary geochemical techniques, one of the objectives of this work is to characterise the chemical composition of ancient tissues, and, therefore, to determine their preservation state. It is clear that methods used together bring much more valuable information than each method taken individually, particularly in the case of heterogeneous material as it is the case with fossils. The primary factor I paid attention to concerning the choice of well-suitable analytical techniques for the study of fossil soft tissues, was the use of non-destructive methods, as far as possible. The great majority of the methods used in my PhD thesis meet that criteria. In addition, most of the techniques used here do not require long sample preparations prior to analysis, but usage of solvents to remove extant organic contaminants, as much as possible. It should be noted that some methods did not generate positive results in this work. They nonetheless represent top technologies frequently used for the chemical characterisation of fossil soft tissues that I think essential to mention. In particular, ToF-SIMS analysis was made on theropod feathers, independently from that discussed in the Chapter 1. The experiment worked although the results were clearly different from those shown in Chapter 1. This is why, I preferred to focus on the use of innovative (i.e., IBA) techniques.

The following geochemical techniques have been used – with varying degrees of success – for the purpose of characterising the preservation level of fossil

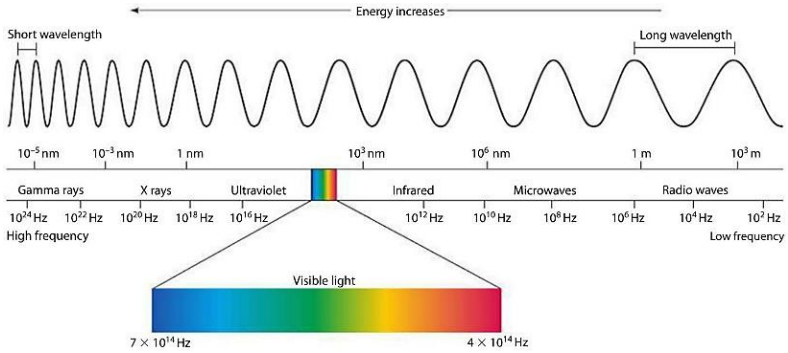

Figure 12. The electromagnetic spectrum divided in seven regions, showing characteristic wavelengths and energies of all the electromagnetic radiations.

integumentary structures: (1) Scanning Electron Microscopy (SEM) associated to Backscattered Electron analysis (BSE), (2) X-ray Diffraction (XRD), (3) laboratory X-ray fluorescence (XRF) and Energy Dispersive X-ray spectroscopy (EDS), (4) Particle-Induced X-ray Emission (PIXE) and Elastic Backscattering spectroscopy (EBS), (5) Time of Flight – Secondary Ions Mass Spectroscopy (ToF-SIMS), (6) Fourier Transform Infrared spectrometry (FTIR), (7) ^{13}C Solid-State Cross Polarisation /Magic Angle Spinning Nuclear Magnetic Resonance (CP/MAS ^{13}C NMR), and (8) Pyrolysis Gas-Chromatography Mass-Spectrometry in the presence of TMAH (TMAH Py-GC-MS).

Spectroscopy

Before detailing each method one after another, it is necessary to introduce the notion of spectroscopy. Indeed, all the techniques used in this work are based on the principle of electromagnetic radiations or - in other words - oscillating electric and magnetic fields that induce each other (Hecht, 1999). The spectroscopy concerns methods that examine the interaction between electromagnetic radiation and matter. The electromagnetic spectrum (Fig. 12) focuses on all the electromagnetic radiations that exist on Earth and comprises: (1) radio waves, (2) microwaves, (3) infrared, (4) visible light – the region of the electromagnetic spectrum that humans are able to see -, (5) ultraviolet, (6) X-rays, and (7) γ-rays. The radiated energy increases from the radio waves to the γ-rays. An important property of the electromagnetic radiation is to share both wave and particle behaviors. They are therefore characterised both by their wavelengths (λ) and frequencies (ν), as it is described in the following equation:

$c = \lambda\nu$, with c = velocity

A particle is also characterised by its energy (E), defined as: $E = h\nu = \frac{hc}{\lambda}$, with h= Planck's constant (6.63 x 10^{-34} J.s).

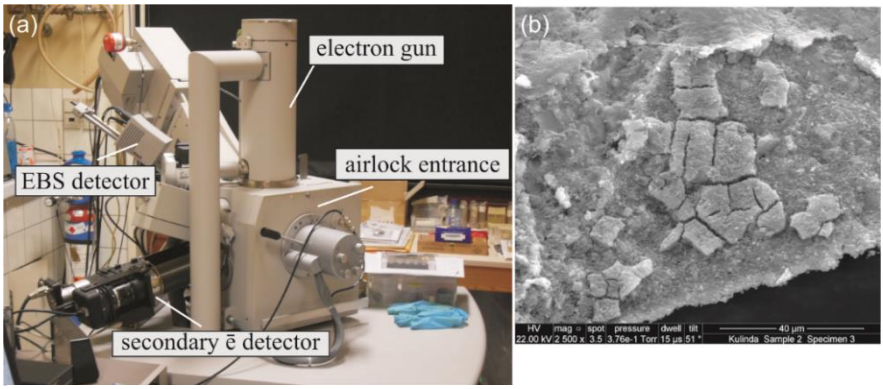

Figure 13. (a) Scanning electron microscope from the RBINS, (b) secondary electron image of epidermal scales from the neornithischian *Kulindadromeus zabaikalicus*. The image of the sample displays a dessicated surface, probably resulting from the alteration of the original organic material.

Each method used for the study of fossil samples operates on a characteristic range of wavelengths: radio waves are the longest and range between a few centimeters to thousands of kilometers; microwaves range from a few centimeters to 0.1 cm; IR range from 0.1 cm to 700 nm; visible light ranges from about 700 nm to 400 nm; UV light ranges between 400 and 10 nm; X-rays range between 10 and 0.1 nm; and Gamma rays have the shortest wavelengths, down to 10^{-3} nm. The diverse analyses performed here required methods that focus on four regions of the electromagnetic spectrum. They are, by decreasing wavelength (and increasing energies): infrared light, visible light, UV, and X-rays.

4.1. Scanning Electron Microscopy (SEM) and Backscattered Electron analysis (BSE)

The Scanning Electron Microscopy (SEM) is a standard technique used in a broad range of disciplines for the observation of very small materials and structures. Inside the microscope, electrons are generally produced by the heating of a tungsten filament at high temperature in the electron gun. Electrons are further bind in a beam and focused by lenses in which a magnetic field is applied. The sample surface is scanned point by point by the electron beam, which results in emission of a series of particles, such as backscattered electron, X-rays, or secondary electrons. In SEM, emitted secondary electrons are detected to form a topographic (two-dimensional) image of the sample. Figure 13 shows the apparatus of an environmental SEM (Fig. 13a) and a typical topographic image of fossil soft tissues obtained using the secondary electron mode (Fig.13b). By contrast, the backscattered electron mode is used to determine the elemental composition of polished samples. Heavy elements backscatter electrons much more than light elements, resulting in brighter images for mineral phases that contain heavier elements (Fig. 14). Prior to analyses, vacuum is made in the

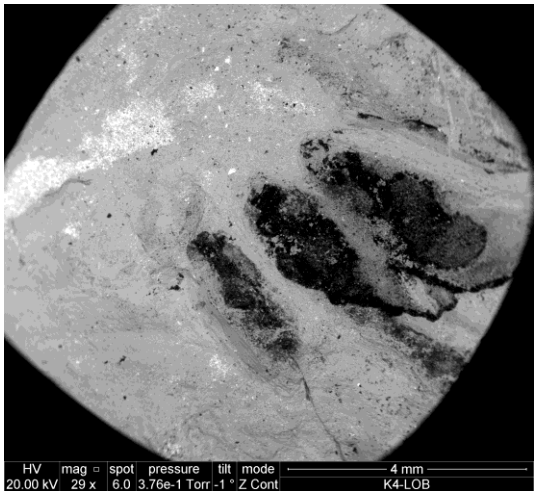

Figure 14. Backscattered electron (BSE) image of integumentary appendages from the neornithischian dinosaur *Kulindadromeus zabaikalicus*. Black areas are characterised by a lighter elemental composition (carbon) than bright spots (iron oxides).

microscope chamber to avoid filament oxidation, but also to keep the sample clean, and to avoid electron deflection from the set beam trajectory.

SEM was used, here, to characterise the ultrastructure (microscopic structure) and mineralogy of fossil soft tissues, with the aim to determine their preservation state. Samples were collected using sterilized tweezers and mounted on carbon tapes. Most samples were sputter coated with gold to avoid surface charging and then to effectively observe tiny structures such as crystals or organelles.

In this thesis, the samples were studied under low vacuum with an environmental QUANTA 200 (FEI) scanning electron microscope (RBINS), at voltage ranging between 20-30 kV and working distances between 8-15 mm. Subsequent EDS analyses (single point and mapping) were performed with the same apparatus. For

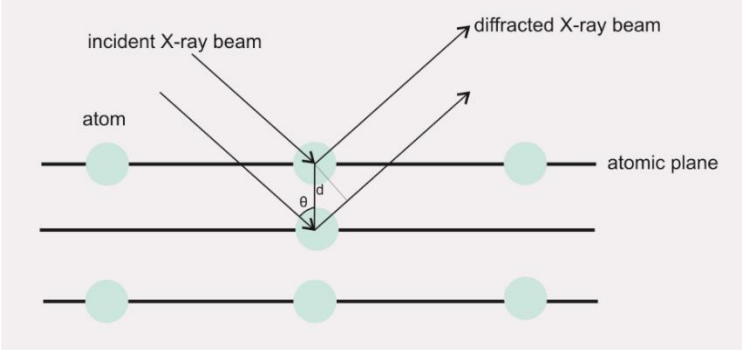

Figure 15. Principles of the diffraction of incident X-ray beams on the atomic planes of a mineral (after Klein et al., 2007); d: distance between two successive atomic planes; θ: diffraction angle.

observation of tiny mineralogical structures, samples were mounted on double-sided carbon tapes and were sputter-coated with gold (Baltec SCD 050). Some analyses have also been performed on a field-emission JEOL 7500F (UNamur), at 15 kV and working distances of 8 mm.

4.2. X-ray Diffraction (XRD)

X-ray diffraction was used in this thesis to determine the mineralogical composition of samples. The principle of this analytical technique is based on the diffraction of incident X-rays on the atomic planes of a crystal. The incident X-rays are produced by bombarding a metal source, here copper, with electrons, which originate from the heating of a tungsten filament (the cathode). Electrons are then accelerated towards the sample to analyse (the anode) by applying a difference in potential. Minerals are three dimensional structures presenting a certain degree of ordering. When X-rays interact with the crystallographic planes (that are arranged in a specific way), it generates their diffraction (Fig. 15). X-rays are electromagnetic radiation and therefore, by definition, share particle and wave properties. Diffraction only occurs when the waves produced by the interaction of incident X-rays and atoms are "in phase" (Klein et al., 2007).

The geometry of the atomic – crystallographic - planes is characteristic of a given mineral phase, which is determined by calculating the distance (d) between successive atomic planes by means of the Bragg's law:

$\mathbf{n\lambda = 2\,d\,\sin\theta}$, with λ: the wavelength of the element that produces the incident X-rays; θ: the diffraction angle measured by the diffractometer.

Samples are ground to obtain a fine powder, which is then mounted on a glass slide. In powders, crystals are randomly oriented, enhancing the probability for obtaining θ angles that satisfy to the Bragg's law. All possible X-ray diffractions are therefore produced and detected by an X-ray detector in the diffractometer (Fig. 16). We used a PANanalytical Empyrean diffractometer (IRSNB) with Cu K_α radiation. A tube voltage of 45 kV and a tube current of 40 mA were used. The goniometer scanned from 3° to 69° 2θ for the bulk rock. The semi-quantitative interpretation of data was made using Visual Crystal 6 software. Additional analyses have been performed on both bulk rock and clay mineral with a Philips diffractometer using Cu K_α radiations (UNamur). A tube voltage of 40 kV and a tube current of 30 mA were used. The goniometer scanned from 3° to 70° 2θ for the bulk rock and from 3° to 30 ° 2θ for clay minerals. The clay minerals (< 2 µm fraction) have been isolated by successive centrifugations after decarbonatation of the crushed rock with HCl 1N. The preparation was mounted on glass slides. Three distinct analyses have been performed in order to identify the diverse clay phases: (1) natural (air-dried), (2) ethylene-glycol solvation and (3) heating at 490 °C during two hours. Identification of clay minerals was made according to the position of the (001) series of basal reflections on the X-ray diagrams.

4.3. X-ray Fluorescence (XRF) and Energy Dispersive X-ray Spectroscopy (EDS)

X-ray fluorescence and X-ray Spectroscopy (EDS) are based on the same principle, but use different excitation sources. In the first case, X-rays are the excitation source, whereas, in the second case, electrons make the source. These two techniques consist on the detection of secondary or primary X-rays, respectively, which are characteristic of an element. These techniques are therefore used to analyse the elemental composition of samples. When the X-rays or electrons interact with the internal electron from an atom, they cause the ejection of an electron out of the electron orbitals. As a result, an electron from an outter layer migrates towards the gap left by the ejected core electron and emits energy. This electron transition and the related energy emission are responsible for the production of X-rays, which are characteristic of an element. The detected X-rays therefore provide an information about the elemental composition of a sample. XRF and EDS are generally performed on polished sections to avoid relief effects. When using standard XRF or EDS apparatus, the required polishing of fossil samples may cause damage or information loss. For example, fossil feathers are very thin and polishing could peel off the interest layer. The heterogeneity of fossils is particularly difficult to cope with but, these methods provide extremely precise elemental composition of minute sized structures (at very small scales the fossil is homogeneous) by using synchrotron radiation. In the last case, due to the huge amount of various particles present in air, the incident beam is slowed and high energies are then required for the beam to arrive at the sample surface with no major energy loss. Synchrotron X-ray fluorescence is a technique available in

Figure 16. X-ray diffractometer of the Geological Survey (RBINS, Brussels) used for XRD analyses of powdered rocks.

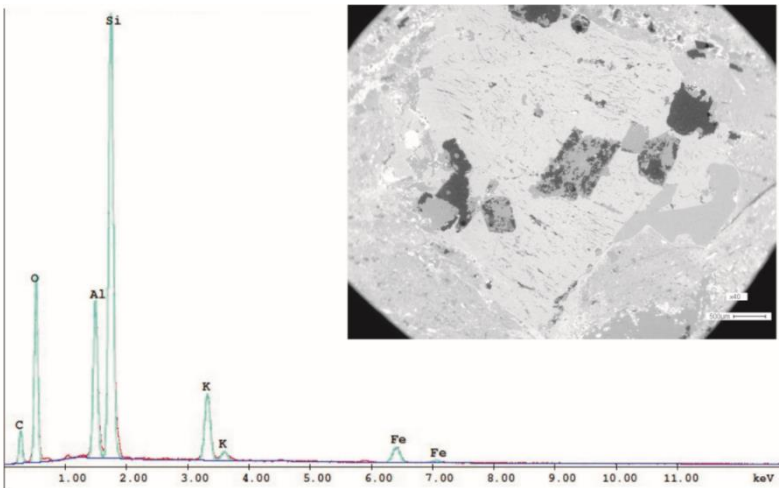

Figure 17. Energy dispersive x-ray spectroscopy spectrum of a polished rock section. It is used here to determine the elemental composition of the mineral phase and identify the variation in composition of a single mineral. The mineral mainly contains silicon, aluminium, and potassium.

synchrotron facilities (circular particle accelerators) for determining and mapping the elemental composition of ancient – archaeological or fossil – material in air. This is highly valuable when working on fossils because it does not either require extensive preparation procedures. Another advantage of using synchrotron radiation, is that the acquisition rate for spectra is very rapid with a better sensitivity to trace elements. Figure 17 displays a spectrum obtained from the EDS analysis of rock thin sections. The XRF analyses were made at the Synchrotron SOLEIL (Gif-sur-Yvette, France) on ornithischian primitive feathers. The results are shown in Chapter 4. EDS has been performed at the RBINS (Brussels) with an environmental QUANTA 200 (FEI) scanning electron microscope (RBINS), at voltage between 20-23 kV.

4.4. Ion Beam Analysis (IBA): Particle-Induced X-ray Emission (PIXE) and Elastic Backscattering Spectrometry (EBS)

PIXE and EBS are two complementary techniques that were used together for high energy ion beam analysis (IBA). EBS provides data on major element content as well as depth profiling of these elements, whereas PIXE provides data on heavy elements contained in a light matrix. The advantage of using IBA is that techniques – that give partial information when taken separately - can be used together to bring additional data. IBA includes a series of spectrometric techniques, such as PIXE and EBS but also RBS, ERD, NRA, and PIGE (Jeynes et al., 2012).

High energies are needed to obtain accurate particle analyses and they are reached by using particle accelerators. Two broad types of particle accelerators are found: (1)

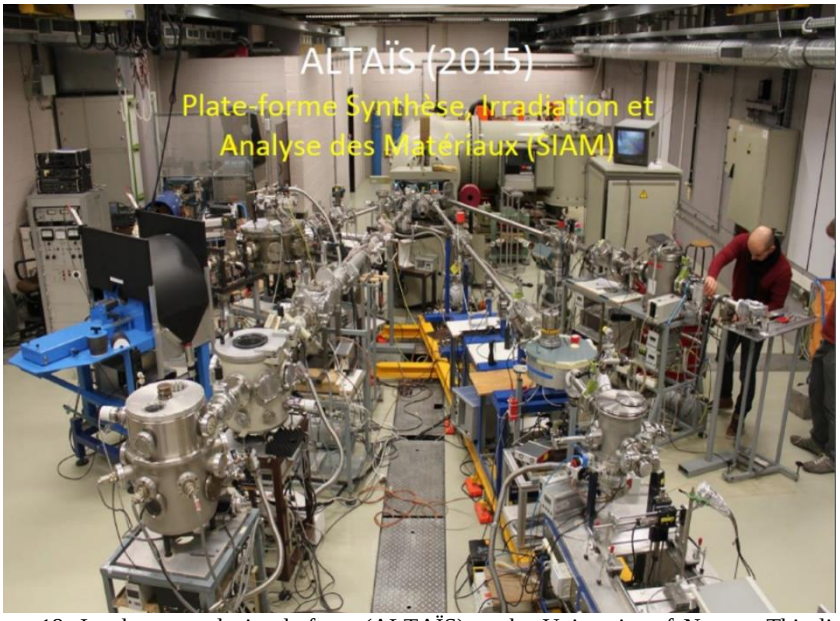

Figure 18. Ion beam analysis platform (ALTAÏS) at the University of Namur. This linear particle accelerator develops several beam lines, generally used on multi-layered material. It was applied here to characterise the chemical composition of fossils.

circular accelerators, such as the Large Hadron Collider (LHC) at CERN ("Conseil Européen pour la Recherche Nucléaire") in Switzerland, where particles can be accelerated to extremely high energies in the order of teraelectronvolts (TeV), mainly for astrophysics purposes; the Stanford Synchrotron Radiation Lightsource (SSRL) that provides beam lines where electrons are accelerated to several gigaelectonvolts (GeV), or the SOLEIL synchrotron in France; (2) linear accelerator, such as that from the University of Namur, ALTAÏS. It is a small linear accelerator where particles can reach energy of several megaelectronvolts (MeV) (Fig. 18). In a linear accelerator, particles are accelerated by passing once through electric fields, whereas in a circular accelerator, particles accumulate more energy as they are accelerated each time they turn around. In the ALTAÏS accelerator, source particle were protons, accelerated to high energy in the range of 3 MeV.

PIXE and EBS

The principle of Particle-Induced X-ray Emission is rather simple: high-energy particles (e.g., protons, He, α-particles) are sent towards the surface of a given sample and interact with atoms located at and just beneath the surface (Fig.19). The energy of the incident particle is transferred to an electron (Terwagne, 2015). Atoms from the sample are then ionised, which results in the ejection of electron from atomic inner shells. The subsequent rearrangement of electrons from the outer shells eventually conducts to the emission of characteristic X-rays (Fig.20).

Elastic Backscattering Spectroscopy (EBS) in the high energy – typically, MeV - range is anther IBA technique extensively used in physics for thin film analysis. The method allows the determination of light elements as a function of depth underneath the surface – also called depth profiling - of the studied material. Here, interaction of the incident proton beam with atoms from the sample surface induces elastic scattering of the incident particles. Element characterisation is possible by measuring the activity – elastic diffusion - of the charged particles after their interaction with the targeted atoms (Leavitt et al., 2010). The method is tested, here, on fossil – partly mineralised – material in an attempt to obtain accurate, in depth, elemental compositions for the samples. For analyses of fossil samples, the used cross sections were non-Rutherford, and the method consists then of an Elastic (non-Rutherford) Backscattering Spectrometry.

The combination of PIXE and EBS permits to simultaneously detect light and heavy elements from a targeted surface. The combined PIXE/EBS analysis required the use of three detectors, one for detection of X-rays and two for detection of backscattered particles. The first detector - a germanium detector, also called Ultra LEGe - was mounted at 135 ° relative to the beam direction. The two EBS detectors were mounted at 170° and 165°, respectively. Diverse types of absorbers in association (or not) with a funny collimator were tested. Our analysis detected sulfur in very low abundance: its signal was "hidden" by the strong signal from silicon that dominates the sediment composition. A 6 µm Al-absorber filter was therefore used to attenuate the dominant

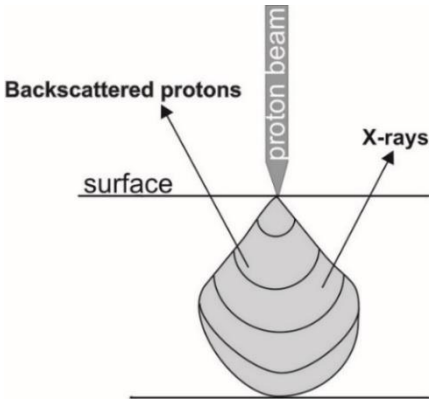

Figure 19. Interaction between a high energy proton beam and matter. PIXE and EBS are based on the emission of X-rays and elastic backscattering of protons, respectively, from a targeted atom.

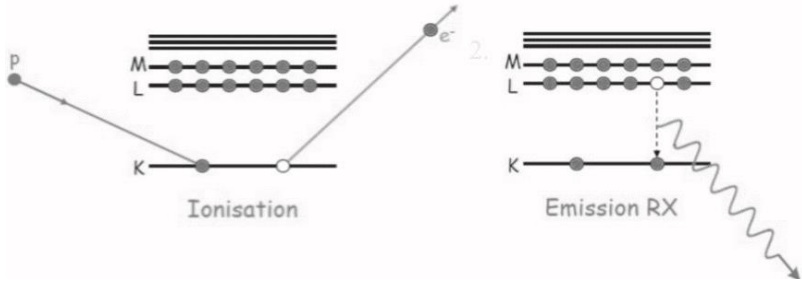

Figure 20. Illustration of the mechanisms of ionisation and X-ray emission, induced by the energetic transition of an electron filling a void left by the ejection of an inner electron. This mechanism is involved in PIXE, but also other X-ray spectroscopy techniques such as XRF or EDX.

Si peak, and allow a better sensitivity to S. Results on fossil soft tissue and sediment analyses by IBA are shown in Chapter 2.

4.5. Time of Flight – Secondary Ions Mass-Spectrometry (ToF-SIMS)

In Time of Flight spectrometry, material is ionised by a pulsed electron beam. Ions are then accelerated by a voltage in the range of several kilovolts and are separated following their masses during what is called "flight" time. The arrival time of ions at the detector is compared to the time of voltage pulsed. It is, therefore, the total time of flight of ions in the mass spectrometer that is measured. Ions having different masses will have different flight times. ToF-SIMS analyses on fossil and modern feathers were performed at the SIAM platform (Synthesis, Irradiation & Analysis of Materials) of the University of Namur (Belgium). The aim of the analysis was to test the technique in our laboratories. The analyses showed that the fossil feather spectrum and those from the surrounding sedimentary matrix are similar, and that both samples therefore contain similar compounds (Fig. 21). It was necessary to build data bases with reference material (modern organic materials such as modern feathers, pigments from diverse organisms and tissues, etc.) to strengthen our results. We eventually decided to stop the ToF-SIMS analyses because other results were already obtained on the same samples in another laboratory specialised in the study of organic materials (and fossils). Additionally, some other innovative analytical techniques retained my attention and I decided to focus on these other ones.

4.6. Fourier Transformed Infra-red spectroscopy (FTIR)

Infrared (IR) spectroscopy is a technique used to identify functional groups in organic and inorganic compounds. IR spectroscopy is based on matter behaviour when it is subjected to IR radiations (Alpert et al., 1970). A source of IR radiation, usually a laser, is sent on the surface of a given sample. The infrared radiated energy is absorbs by molecules at the surface, leading to their excitation. In response, chemical bonds

from the molecules start vibrating. The mode of vibration is characteristic of a given functional group (e.g., C-C, C-O, C=O, and O-H) and the chemical composition of the sample can, therefore, be inferred from the induced molecular vibrations.

FTIR is a useful tool to analyse fossil material since it characterise the chemical structure of constitutive compounds with no damage to the samples. It has been used in many molecular studies of organic material, such as pigments (e.g., Centeno & Shamir, 2008; Liu et al., 2005; Muroya et al., 2000), bird feathers (e.g., Carrillo et al., 2012; Dove et al., 2007; Giraldo & Moreno-Piraján, 2013), or keratin (e.g., Bendit, 1966; Wang & Cao, 2012). Those studies provide useful comparison for analysis of equivalent fossil material. By contrast, FTIR has, so far, only been little used for soft tissue analysis of fossil vertebrates (Barden et al., 2014; Edwards et al., 2011; Glass et al., 2012b; Manning et al., 2009b; McNamara et al., 2016).

IR spectra represent the transmittance, or the quantity of incident light passing through a given sample (expressed in percentage) on the wavenumber (expressed in cm^{-1}). Our spectra were recorded in the mid-IR with a MCT detector over a wavenumber range of 650 – 4000 cm^{-1}, with a resolution of 4 cm^{-1} (average number of scans is 32).

Typically, spectra can be divided into two broad spectral regions, the functional group region, above 1500 cm^{-1} and the fingerprint region, between 1500 and 600 cm^{-1}. Most of the valuable peaks are located in the first region. Each peak in the spectrum corresponds to a given vibration of an organic function in the molecule.

Here, Attenuated Total Reflectance (ATR) was used to analyse palaeontological samples. We chose to use the ATR essentially because it is a non-destructive tool that permits direct observation and avoid preparation – especially grinding -, and therefore

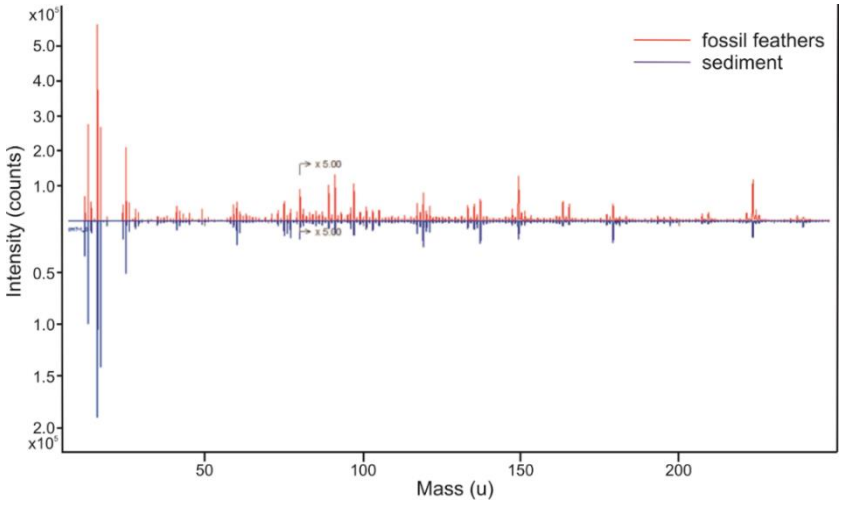

Figure 21. ToF-SIMS spectra of fossil feathers (in red) from the paravian theropod *Anchiornis huxleyi* (YFGP-T5199) and the surrounding sediment (in blue). Both spectra display similar patterns and did not permit to distinguish the fossil from its sedimentary matrix.

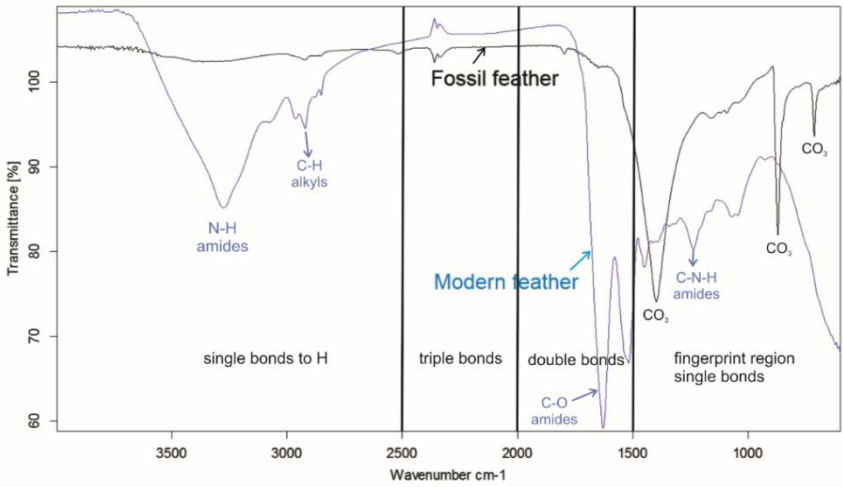

Figure 22. Spectra of Cretaceous (black) and modern (blue) bird feathers studied by ATR-FTIR at the University of Hasselt (TANC). The spectra are divided in four spectral region. The spectrum of the fossil feather is dominated by inorganic peaks attributed to CO_3 deformation and stretching from calcium carbonates. The spectrum of the modern feather rather displayspeaks that are attributed to organic functional groups, such as those from amides.

prevents major damage of valuable samples. The principle of ATR is based on the attenuation effect of light when it is reflected at the interface between a compound with a high refractive index, and a sample with a low refractive index (Kazarian & Chan, 2013). Therefore, the ATR mode uses a crystal of high refractive index - here germanium - that is brought into contact with the surface of the sample. A pressure is then applied and an IR beam is directed with a high angle of incidence into the crystal. The IR beam is reflected and gives rise to a wave called an evanescent wave that is projected into the sample (Glassford et al., 2013). Eventually, the internal reflection is subsequently detected by the detector located in the spectrometer.

Spectra were recorded for the following samples: (1) three modern bird feathers of different colours (red, yellow, and green) collected from a woodpecker (*Picus veridis*); (2) theropod feathers (*Anchiornis huxleyi*); (3) two isolated bird feathers from the Cretaceous of Brazil; (4) a fragment of a pterosaur cranial crest; and (5) integumentary structures from the same pterosaur specimen. Spectra were taken in ATR mode with a Hyperion 2000 microscope coupled to a Vertex 70 spectrometer (Brücker) (UHasselt, Toegepaste en Analytische Chemie). The ATR objective is in germanium. The ATR crystal was cleaned after each scan. The spectrometer was coupled to Bruker microscope. All spectra were obtained after the subtraction of the background spectrum from the sample spectrum. Identification of peaks was made using Opus software. All the spectra obtained from the fossils have similar peak distribution than their embedding sediment, they are dominated by inorganic functions (Fig. 22). The spectra from diverse modern feathers show the same pattern as well. This method was not further developed in this thesis because of the time required for the analysis of data, but will be discussed in a further work.

4.7. ^{13}C Solid-State Cross Polarisation/Magic angle Spinning Nuclear Magnetic Resonance (CP/MAS ^{13}C NMR)

Nuclear magnetic resonance is based on the property of nuclei to orientate when they are subjected to an external magnetic field. NMR is abundantly used in organic geochemistry and was used here to assess the chemical structure of organic materials. The method is generally used in combination with gas chromatography to obtain information about the chemical environment of atoms and then to infer the structure of organic molecules. Atomic nuclei behave like spherical particles that can rotate around an axis, and therefore have an angular momentum, or spin. In atoms, nuclei with an odd mass number (e.g., ^{1}H, ^{13}C, ^{15}N) are characterised by their spin state (I), related to their angular momentum (Fig. 23). Only nuclei having a non-zero spin have the ability to orientate in a magnetic field, and then be used for NMR analysis. Since we deal with organic matter-containing material, nuclear magnetic resonance was performed on the ^{13}C nuclei. A pulse of electromagnetic radiation is sent on a sample at a given frequency. Then, ^{13}C nuclei subjected to the magnetic field interact with the radiation and pass into an excited state. After excitation, they return to their original energy state, which results in the generation of a signal.

After detection, the signal is eventually transformed into a spectrum, which is characteristic of the chemical structure – more precisely, the chemical environment of the carbon nuclei – of organic molecules.

Solid state ^{13}C NMR has been extensively applied for the structural characterisation of various organic materials, such as kerogens (e.g., Burdelnaya et al., 2014; Dennis et al., 1982; Longbottom et al., 2016; Mao et al., 2010; Miknis et al., 1984), soil organic matter (e.g., Guggenberger et al., 1995; Poirier et al., 2000; Eusterhues et al., 2003; Dymov et al., 2015), or river and marine sedimentary organic matter (e.g., Mengchang et al., 2008; Templier et al., 2013; García et al., 1994; Sardessai & Wahidullah, 1998). The method has even been applied to meteoritic compounds (Biron et al., 2015; Gardinier et al., 2000). ^{13}C NMR provides information on the chemical environment of the ^{13}C atoms present in the analysed substance. The spectra are divided in several peak regions characteristic of organic functions.

The study of modern proteinaceous compounds such as keratin or melanin from feathers, hair, horns, wool by ^{13}C NMR provides a broad knowledge of their chemical structure. For instance, ^{13}C NMR permitted to study the structural conformation of keratin in bird feathers, hair, and wool (Kricheldorf & Müller, 1984; Zhang et al., 2012); in keratin films obtained from wool in various experimental conditions (Yoshimizu et al., 1991); in natural melanin (Duff et al., 1988; Adhyaru et al., 2003); or in the chitinous cuticle of invertebrates (Schaefer et al., 1987; Baas et al., 1995; Gupta et al., 2009).

The use of that method for analysing fossils, and especially soft tissue fossils, is still low. No occurrence of ^{13}C NMR studies on fossil soft tissues from vertebrates have been recorded so far. The research is, however, rather extensive on fossil plants, such as spores (Hemsley et al., 1996), seed coats (van Bergen et al., 1994), or wood (Jones, 1994), all containing highly resistant biomolecules, such as sporopollenin, one of the most resistant non-mineralized compounds (De Leeuw & Largeau, 1993).
Results on ^{13}C CP-MAS NMR of Jurassic paravian dinosaur feathers are discussed in detail in Chapter 2.

4.8. Pyrolysis Gas-Chromatography Mass-Spectrometry in the presence of TMAH (TMAH Py-GC-MS)

The first step in analysing organic samples by gas chromatography is the pyrolysis. Here, on-line pyrolysis was used, namely it is connected to the rest of the analytical machinery. Pyrolysis consists of breaking big (macro-) biomolecules into smaller fragments, which are then directly sent to the gas chromatographer. The direct coupling of pyrolysis with the gas chromatographer has the advantage to prevent material loss between the two pieces of equipment. Another asset to the use of that technique is that it requires only very little quantities of material (generally, in the range of a few micrograms). In the next step, fragmented organic compounds still present in the sample are separated and identified in the gas chromatographer by measuring their retention times on a capillary column (0.25 mm in diameter). Accordingly, gas chromatography works on the basis of compound affinity for a stationary phase located in the column. A mobile phase, here helium, is the carrier gas for injected compounds. A detector is placed at the end of the column and detects each compound that has a characteristic retention time on the column. In organic samples, the molecules can be polar or non-polar. Because capillary columns are non-polar, polar compounds cannot be efficiently separated. Derivation products such as TMAH

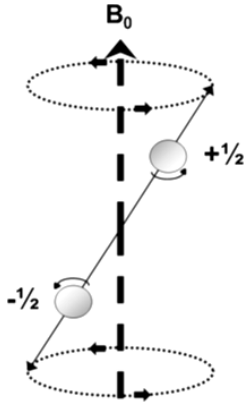

Figure 23. Illustration of the spin momentum of a ^{13}C nucleus that is submitted to an external magnetic field (From Tognarelli et al., 2015).

(tetramethylammonium hydroxide) are, therefore, used in gas-chromatography in order to detect all, polar and non-polar, compounds. TMAH enhances the thermal break-down of macromolecules and methylate pyrolysis products, which in turn enhance their detection and identification in GC-MS. In the last step of the analysis, split compounds are ionised in the mass spectrometer and then separated according to their mass (m/z). Eventually, moieties are identified by interpreting mass spectral data. The molecular structure of the studied organic compounds is then inferred from their fragments. It should be noted that a certain amount of molecular fragments are lost during the experiment and will never be detected.
Results on TMAH Py-GC-MS of Jurassic paravian dinosaur feathers are discussed in Chapter 2.

Section I

The first section of this thesis focuses on the study of the degree of preservation of epidermal structures, especially feathers, of two paravian and one neornithischian dinosaurs. The taphonomy is investigated in following two distinct ways: (1) the description of the fossil soft tissues based on imagery techniques and (2) the application of a series of complementary analytical techniques. Both types of methods provide a better understanding of the fossilisation processes that allowed the morphological preservation of the soft tissues.

Two papers are dedicated to the study of the feathers from the paravian dinosaur *Anchiornis huxleyi* (YFGP-T5199), one paper deals with the macrostructure of the plumage of the paravian *Serikornis sungei*, and one paper is dedicated to the high resolution analysis of the primitive feathers of the neornithischian *Kulindadromeus zabaikalicus* from Siberia.

Chapter 1

Lindgren et al. (2015), published in *Scientific Reports*

Molecular composition and ultrastructure of Jurassic paravian feathers

My implication in this chapter dedicated to the analysis of fossil feathers is related to the study of the feather ultrastructure. My role was to collect a series of samples (S2 to S13 in Fig.1.1) from the plumage of a theropod dinosaur and to observe these samples by scanning electron microscopy (SEM) with the aim to look for melanosomes.

Abstract

Feathers are amongst the most complex epidermal structures known, and they have a well-documented evolutionary trajectory across non-avian dinosaurs and basal birds. Moreover, melanosome-like microbodies preserved in association with fossil plumage have been used to reconstruct original colour, behaviour and physiology. However, these putative ancient melanosomes might alternatively represent micro-organismal residues, a conflicting interpretation compounded by a lack of unambiguous chemical data. We therefore used sensitive molecular imaging, supported by multiple independent analytical tests, to demonstrate that the filamentous epidermal appendages in a new specimen of the Jurassic paravian *Anchiornis* comprise remnant eumelanosomes and fibril-like microstructures, preserved as endogenous eumelanin and authigenic calcium phosphate. These results provide novel insights into the early evolution of feathers at the sub-cellular level, and unequivocally determine that melanosomes can be preserved in fossil feathers.

1. Introduction

The Middle-Late Jurassic fossil assemblage found in the Tiaojishan Formation of Liaoning Province in north-eastern China has yielded unparalleled evidence on the early evolution of birds (Godefroit et al., 2013a; Godefroit et al., 2013b; Hu et al., 2009; Xu et al., 2011). Most importantly, the identification of various feather-like integumental appendages in non-avian and stem avialan theropods has illuminated the diversity and distribution of plumage structures during their adaptive transition towards use in flight (Godefroit et al., 2013a). Epidermal traces in the Tiaojishan Formation are preserved as either faint impressions or phosphatized and carbonized residues (Godefroit et al., 2013a; Li et al., 2010). The latter were long thought to be a product of keratin-degrading bacteria (Davis & Briggs, 1995). However, more recent interpretations have favoured fossilised melanosomes; that is, melanin-bearing cellular organelles responsible in part for the coloration of skin and its structural derivatives (Vinther et al., 2008). This landmark hypothesis has spawned an entirely new field of exploratory inference into dinosaurian colour (Carney et al., 2012; Li et al., 2012a; Li et al., 2010; Vinther et al., 2009; Vinther et al., 2008; Zhang et al., 2010), behaviour (Li et al., 2010) and physiology (Li et al., 2014).

Nevertheless, it has also met with vivid debate (see Edwards et al., 2014 for review). This centres on the observation that microbes colonizing the epidermal tissues during decay are virtually indistinguishable from the melanosome-like microbodies recognized in fossils (Schweitzer, 2011a). Such criticism is aggravated by the lack of unequivocal molecular traces from melanic pigments in ancient feathers and feather-like appendages (McNamara, 2013; Moyer et al., 2014). Indeed, claims of melanosomes found in the plumage of non-avian dinosaurs and stem avialans have fundamentally relied upon external morphology (Carney et al., 2012; Li et al., 2014; Li et al., 2012a; Li et al., 2010; Vinther et al., 2009; Vinther et al., 2008; Zhang et al., 2010), but this is demonstrably inadequate for discriminating pigment organelles from pervasive bacteria (Moyer et al., 2014). Furthermore, chemical data (Barden et al., 2011; Egerton et al., 2015; Manning et al., 2013; Wogelius et al., 2011) have proven inconclusive or lacking in specificity (Vinther, 2015), and alleged melanosomes occurring as imprints (‘mouldic melanosomes’; Zhang et al., 2010) problematically imply that the surrounding substrate was more resistant to degradation than the microbodies themselves (Schweitzer, 2011a). The matrix retaining ‘mouldic melanosomes’ is assumed to be either residual keratin (Zhang et al., 2010) or ‘remineralised melanin’ (Li et al., 2010), yet no attempt has been made to test these hypotheses (Moyer et al., 2014). An alternative origin might therefore be plausible because melanosome-like impressions are occasionally found in clay minerals, together with silica crystals and other sedimentary grains adjacent to preserved integumentary structures (Egerton et al., 2015; Moyer et al., 2014).

Here we address the unresolved problem of accurately identifying microbodies, imprints and fibrous structures associated with fossilised feather remains via high-

resolution imaging and molecular analysis of an exceptionally preserved new specimen (YFGP-T5199, housed in Yizhou Fossil and Geology Park) of the paravian *Anchiornis* (Xu et al., 2009a). Our results show that multiple local taphonomic pathways incorporating both organic and geochemical agents contributed to the retention of fibrils, eumelanin pigment and eumelanosomes in the integumentary filaments of YFGP-T5199.

2. Methodology

Fourteen feather samples (denoted S1–S14) were removed from YFGP-T5199 (Fig.1.1) using either a sterile scalpel or a hand-operated saw. One sample (S1) selected for molecular analysis was triple-washed successively in acetone, 96% ethanol and Milli-Q water to remove potential contaminants from human handling. The sample was then dried under a hood, wrapped loosely in fresh aluminium foil and stored in isolation inside a sealed sterile glass container. 'Fresh' feather material was exposed prior to analysis by removing encasing sediment with a sterile scalpel; the resulting sample chip was subsequently split into part and counterpart pieces. Fresh aluminium foil was used to cover all work areas, and sterile surgical gloves were used during all handling and preparation. Our treatment procedure was identical for all modern reference samples. All experiments were repeated in order to validate the results.

2.1. Scanning Electron Microscopy (SEM) and Field Emission Gun (FEG)-SEM

Initial screening of S1 was performed using a Hitachi S-3400N SEM on the uncoated sample under low vacuum, and the elemental composition was determined via elemental mapping using EDX analysis (1900 sec scanning time at 15 keV, 62.0 μA and a working distance of 10 mm). Following ToF-SIMS analysis, S1 was sputter-coated with a gold/palladium mixture and re-examined using a Zeiss Supra 40VP FEG-SEM (2 keV, working distance 3-5 mm, Everhart-Thornley secondary electron detector). Samples S2–S14 were sputter-coated with gold or gold/palladium and analysed using an environmental QUANTA 200 (FEI) SEM and a Zeiss Supra 40VP FEG-SEM.

2.2. Transmission Electron Microscopy (TEM)

Fossil feather material was removed from S1.1 using a sterile scalpel and placed in pure alcohol. The alcohol was then replaced with acetone, and stepwise substituted with epoxy resin (AGAR 100 Resin kit, R1031) to fully infiltrate the remnant tissues. The epoxy was left to polymerize at 60 °C for 48 h. Infiltrated sub-samples were trimmed with a razor blade and then 1.5 μm thick sections were cut using a glass knife

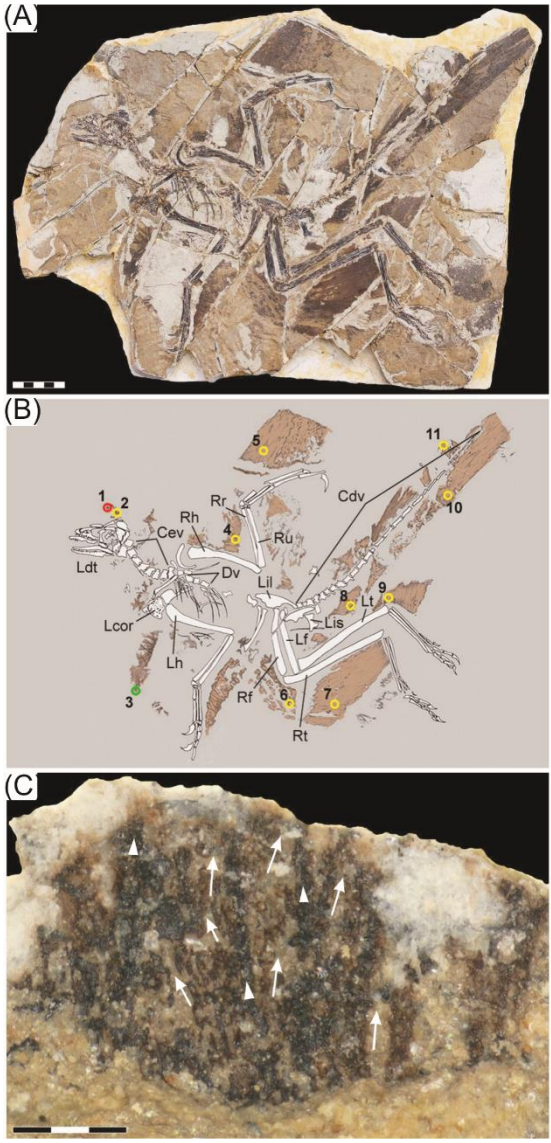

Figure 1.1. *Anchiornis huxleyi* specimen YFGP-T5199. (A) Photographic and (B) diagrammatic representation. Numbered circles denote location of plumage samples used for molecular and/or imaging analyses. Red circle (S1) demarcates the'forecrown' sample used as the basis for our investigation; yellow circles (S2–S14) indicate samples used for supportive SEM imaging. Cdv, caudal vertebrae; Cev, cervical vertebrae; Dv, dorsal vertebrae; Lcor, left coracoid; Ldt, left dentary; Lf, left femur; Lh, left humerus; Lil, left ilium; Lis, left ischium; Lt, left tibia; Rf, right femur; Rh, right humerus; Rr, right radius; Rt, right tibia; Ru, right ulna. Scale bar: 5 cm. Photograph by P. Godefroit and U. Lefèvre. Drawing by U. Lefèvre. (**C**) Detail of S1 after initial preparation showing darker central strands (arrowheads) with diffuse arrays of filaments branching laterally at acute angles (arrows). Note that the analysed area is still covered by sedimentary matrix (see also Supplementary Fig. S1.1). Scale bar: 300 µm. Photograph by J. Lindgren.

mounted on an ultratome (Leica Ultracut UCT). A diamond knife was employed for

the ultra-thin sectioning at 50 nm, after which slices were fixed to pioloform-coated copper grids. These were inserted into a JEOL JEM-1230 transmission electron microscope run at 80 kV. Areas of interest were photographed using a Gatan MultiScan 794 CCD camera.

2.3. Time of Flight - Secondary Ion Mass Spectrometry (ToF-SIMS).

The 'freshly' prepared part and counterpart sub-samples of S1.1 were fixed on a metal block using double-sided tape (Supplementary Fig. S1.1) and then immediately inserted into a ToF-SIMS IV instrument (IONTOF GmbH). ToF-SIMS analyses in the static SIMS mode were performed using 25 keV Bi^{3+} primary ions and low energy electron flooding for charge compensation. High mass resolution data were acquired in the bunched mode ($m/\Delta m \sim 5000$) at a spatial resolution of ~3–4 μm, whereas high image resolution data were obtained without bunching ($m/\Delta m \sim 300$, spatial resolution ~0.2-0.5 μm); in both cases at 256 x 256 pixels. The coordinates for all positions investigated were monitored in order to allow for subsequent FEG-SEM analysis of the same areas.

2.4. IR microspectroscopy.

Fossil tissues and sediments were removed from S1 using a sterile scalpel, suspended in Milli-Q water, and then placed on sterile CaF_2 infrared windows and left to air dry under a hood at room temperature. Likewise, standard samples were dissolved in Milli-Q water and then casted onto CaF_2 infrared windows. Infrared microspectroscopic measurements were recorded at two beamlines: SMIS at the SOLEIL synchrotron radiation facility, France, and D7, MAX-IV laboratory, Sweden. At SOLEIL, the infrared photon source was coupled to a Thermo Fisher Nicolet Nexus 5700 FTIR spectrometre equipped with a Continuum XL microscope. A single point MCT-A detector and a 15×15 μm aperture were used for the measurements. At MAX-IV laboratory, the set up combined a Hyperion 3000 microscope with a Bruker IFS66/v FTIR spectrometre. The image spectra were recorded in off-line mode using a MCT focal plane array detector consisting of 128×128 individual detector elements. Both microscopes operated in transmission mode at 4 cm^{-1} resolution.

3. Results

3.1. Fossil specimen and rationale for sample selection.

An extensively feathered Jurassic paravian referable to *Anchiornis huxleyi* was recovered from the Yaolugou locality in Jianchang County, western Liaoning (see the Supplementary information and the Appendix "A1" for more information). Although initially classified as a non-avian troodontid theropod (Hu et al., 2009), recent studies suggest that *Anchiornis* represents a stem avialan, more primitive than *Archaeopteryx* (Foth et al., 2014; Godefroit et al., 2013a). The fossil is diagenetically flattened but otherwise essentially complete, comprising an articulated skeleton with plumage remnants forming a dark corona around the bones (Fig.1.1A, B). Some integument

residues were lost during preparation (see the Supplementary Methods); however, patches of feathers and feather-like structures extend along the back half of the skull, lateral to the shoulder girdle, above the pelvic girdle, and along the forelimbs, hind limbs and tail (Fig. 1.1A, B). Fourteen samples (S1–S14) ranging in size from about 2 × 2 to 10 × 10 mm were removed from the plumage surfaces (Fig.1.1B). One of these (S1) was selected for detailed morphological and molecular examination. S1 was collected some distance above the skull roof (Fig.1.1B), in the region of the 'forecrown' *sensu* Li et al. (2010) (note that the inferred dorsal crest in *Anchiornis* may be an artefact of preservation; Foth, 2012; Li et al., 2012b). The sample was considered optimal for investigation because: (1) it showed greyish-brownish coloration indicative of organic remains; (2) was uncovered from a 'fresh' sub-surface layer within the sedimentary matrix; (3) produced part and counterpart sub-samples that revealed internal structuring of the filamentous epidermal appendages (Supplementary Fig. S1.1); and (4) similar 'crest' feathers from another *Anchiornis* fossil (see below) have been interpreted as housing phaeomelanosomes (Li et al., 2010); that is, spheroid melanosomes dominated by phaeomelanin pigment (Liu et al., 2005).

3.2. Description of the filamentous epidermal structures and microbodies

The integumentary appendages in S1 superficially resemble feathers of extant birds. They comprise a larger (and darker) central strand (Fig.1.1C—arrowheads) with diffuse filamentous arrays branching off laterally at acute angles (Fig.1.1C—arrows). In their current, somewhat compressed state, the finer filaments range in width from about 20 to 30 μm, whereas the larger strands measure approximately 40 to 50 μm across. Under scanning electron microscopy (SEM) the individual filaments appear as thick, folded sheets of amorphous matter. This morphology is consistent with that of experimentally degraded feathers (McNamara et al., 2013), and suggests distortion via diagenetic compression and/or elevated temperatures. However, some regions seemingly retain original structure, including continuous layers of densely packed fibrils organised into macrofibrils and/or fibril bundles with a predominantly longitudinal orientation (Fig. 1.2). Most fibrils are shown in relief, suggesting that they retain at least some of their original three-dimensional form (Fig.1.2A); however, extensive folding, wrinkling and branching (Fig.1.2D-arrows, E) are congruent with loss of tension during decomposition (Lingham-Soliar et al., 2009; Lingham-Soliar & Murugan, 2013). Uneven fracturing has exposed the fibrous material in oblique tangential (Fig.1.2A) and transverse views (Fig.1.2C, D), revealing that it is part of larger structures (fibres or barbules) with a cylindrical shape (Fig.1.2C). The fibrous elements range in size from about 80 nm (fibrils) to >10 μm (fibres/barbules) in diameter. These dimensions are broadly comparable to those recorded for keratinous components of extant bird feathers (Lingham-Soliar et al., 2009; Lingham-Soliar & Murugan, 2013; Martinez-Hernandez et al., 2005), despite the extent of diagenetic mineralisation (see below).

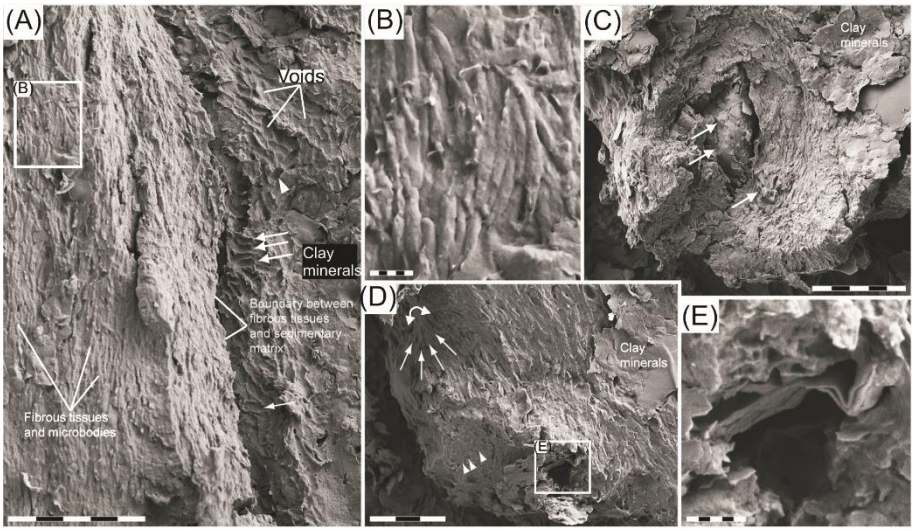

Figure 1.2. Ultrastructure of YFGP-T5199 'forecrown' feathers. (A) FEG-SEM micrograph of fibril-like structures and solid microbodies (left side of image), and densely spaced voids made in the adjacent sedimentary matrix ('Clay minerals': right side of image). Note that the fibrous structures and microbodies are roughly aligned parallel to one another, whereas the imprints are more randomly oriented (those with a longitudinal axis set almost perpendicular to the main direction of the fibrous tissues are marked with arrows). Also note highly variable shape of the voids (one with a sub-circular outline is marked with an arrowhead). Scale bar: 5 μm. (B) Enlargement of (A) showing aligned, rod-shaped microbodies with rounded termini. Scale bar: 500 nm. (C) Oblique transverse view of densely packed fibrils demonstrating their organisation into a larger cylindrical structure, presumably a fibre or barbule. Arrows point at sedimentary infill with randomly oriented elliptical impressions. Scale bar: 5 μm. (D) Cross-section of stacked and somewhat ragged fibril-like microstructures with a solid interior (arrowheads). The arrowhead hemi-circle partially encloses a presumed fibril bundle. Note branching patterns (arrows), possibly indicating loss of tension. Scale bar: 3 μm. (E) Detail of the area marked in (D) showing a wrinkled and partially folded microstructure roughly similar in dimensions to a macrofibril. Scale bar: 500 nm.

Ultrathin sections visualised using transmission electron microscopy (TEM) revealed micrometre-thick, layered structures (Fig.1.3), superficially similar to sectioned keratin fibrils of extant feathers (see Moyer et al., 2014, Fig.1a).

Stacks of elongate microbodies are locally seen tightly adhering to, partially embedded in, or even merged with the fibrous substrate (Fig.1.2A, B). These are crudely aligned in parallel to one another, and their overall orientation follows that of the fibrous tissues (Fig.1.2A, B). Individual elements are rod-shaped with rounded termini, and substantially longer than wide. Most of these rods are straight or gently bent (Fig.1.2B); however, others are strongly flexed (Supplementary Fig. S1.2d, e-arrow). Within the matrix immediately adjacent to the fibrous tissues are densely spaced imprints infesting either a eumelanin/calcium phosphate residue (see discussion below and Supplementary Fig. S1.2c, d, f), clay minerals (Fig.1.2A) or microcrystalline aggregates (Fig.1.2C and Supplementary Fig. S1.2h). Some

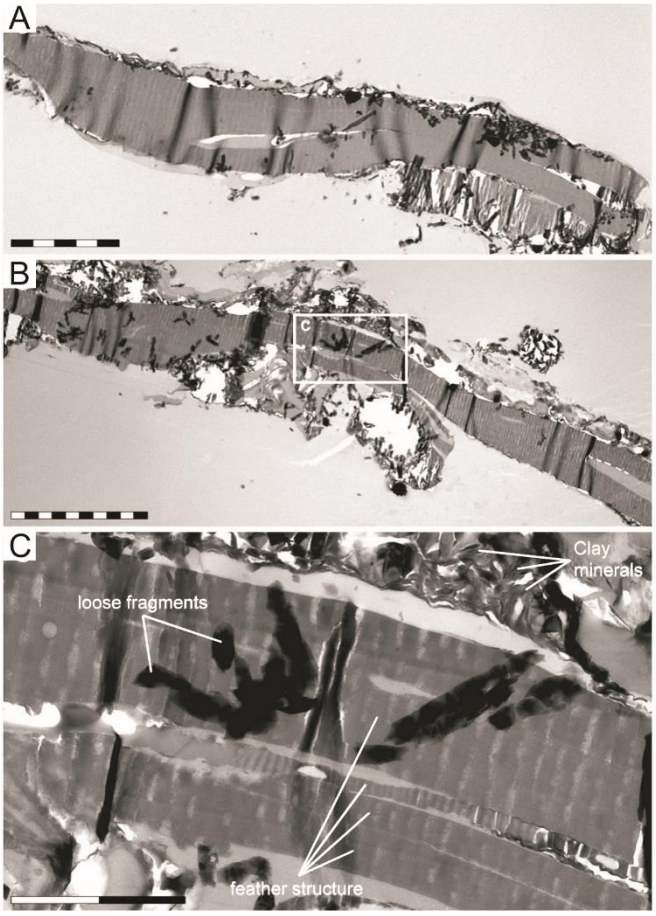

Figure 1.3. TEM micrographs of YFGP-T5199 'forecrown' feathers**.** (A) Layered microstructures that are superficially similar in both size and organisation to keratin fibrils of extant bird feathers. The corrugated internal texturing and partial rupturing are artefacts of the TEM cutting process. This sample chip was also used for SEM-EDX (Fig.1.4) and IR microspectroscopic (Fig.1.8) analysis. Scale bar: 5 μm. (B) A separate section from the same chip a few micrometres deeper in the fossil feather substrate. Scale bar: 10 μm. (C) Enlargement of (B) showing details of the feather residues and adhering clay minerals. Scale bar: 2 μm.

impressions correspond in shape and size to the rod-shaped microbodies (Supplementary Fig. S1.2d, f, g). Additionally, they show similar alignment (Supplementary Fig. S1.2d, f, g), and rod-like elements are even retained in a few imprints (Supplementary Fig. S1.2d, e-arrow). Other impressions are morphologically more diverse, ranging from ovoid to elongate, and they are also more randomly oriented (sometimes with their long axis set almost perpendicular to that of the fibrous tissues; Fig.1.2A-arrows and Supplementary Fig. S1.2h).

Ultimately, while the morphological and organisational similarities of the fibrous structures and microbodies to those of degraded feather keratin and remnant eumelanosomes are striking (Supplementary Fig. S1.3; see also Ichida et al., 2001;

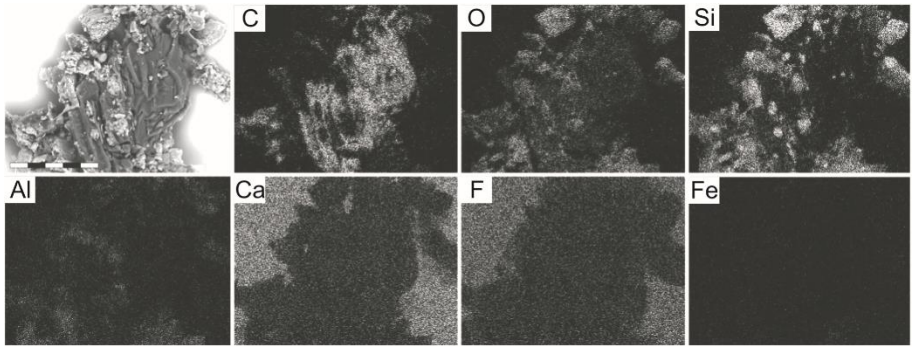

Figure 1.4. Single-element SEM-EDX maps of YFGP-T5199 'forecrown' feathers. White indicates high intensity whereas black indicates low intensity. Note relatively high levels of carbon (**C**) in the fossil feather material, whereas the sediment is dominated by silica (**Si**) and oxygen (**O**), with minor quantities of aluminium (**Al**) and only trace amounts of iron (**Fe**). Intensities from calcium (**Ca**) and fluoride (**F**) derive from the underlying spectrophotometric window (for IR microspectroscopic analysis). Scale bar: 50 μm.

Lingham-Soliar et al., 2009; Lingham-Soliar & Murugan, 2013; Rodziewicz & Laba, 2008), integration of chemical data is necessary to discriminate between endogenous residues and exogenous microorganisms that may occur associated with decaying keratinaceous substrates (see Ichida et al., 2001, fig. 6).

3.3. Elemental and molecular analyses

Energy-dispersive X-ray microanalysis (EDX) identified carbon as the primary component in the integumentary remains, which suggests an organic source (Fig.1.4). In addition, time-of-flight secondary ion mass spectrometric (ToF-SIMS) imaging analysis detected negative ions characteristic of melanic pigments localized specifically to areas with fibrous tissues and embedded microbodies (e.g., see A1-A3; Figs.1.5B,C and 1.6a and Supplementary Figs. S1.2a-e, S1.4a, e, S1.5). Detailed comparisons with modern reference samples further revealed that all 'characteristic' peaks of the eumelanin molecular structure were present in the fossil spectra, with considerable agreement in both mass position and relative signal intensity distribution (Fig. 6a and Supplementary Table S1.1). In contrast, the surrounding sediment yielded mainly silica-related negative ions indicative of silicate-rich minerals (e.g., A4; Fig.1.5B, C and Supplementary Figs S1.2a, S1.4b, e, S1.5). Phosphate-containing ions were also encountered over the entire surface, but at significantly higher intensities in the melanin-dominated areas (Fig.1.5C and Supplementary Fig. S1.4d).

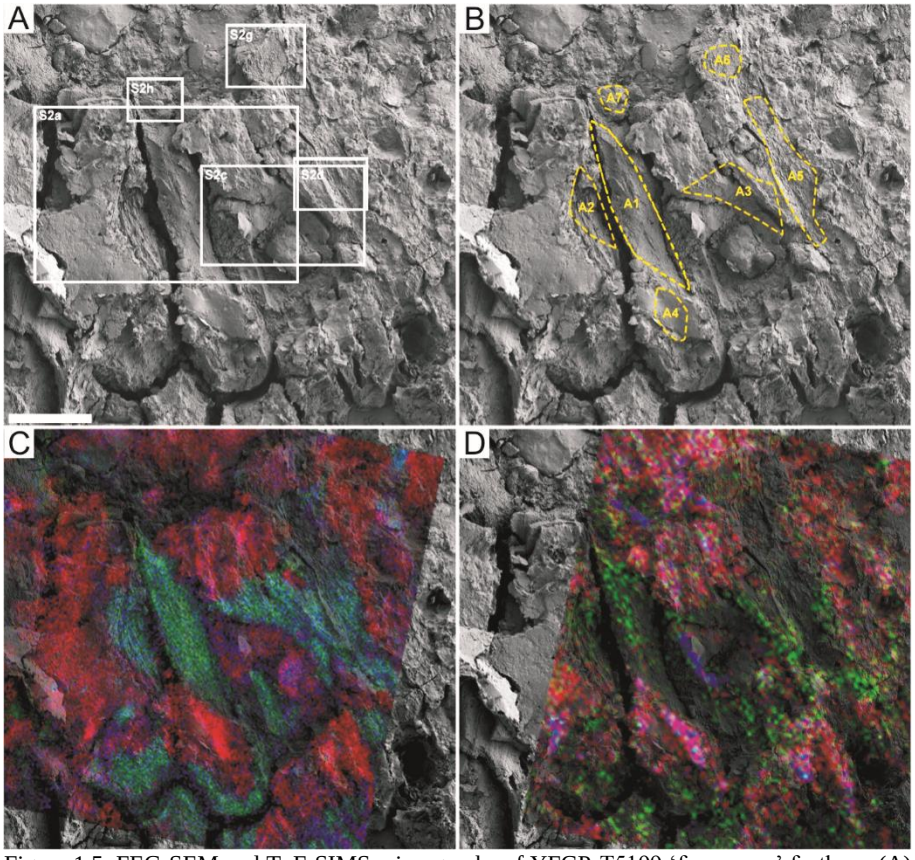

Figure 1.5. FEG-SEM and ToF-SIMS micrographs of YFGP-T5199 'forecrown' feathers**.** (A) FEG-SEM micrograph of feather material and surrounding sediments. Close-up images of the delimited areas are shown in Supplementary Fig. S1.2. Scale bar: 20 μm. (B) Same image as in (A). Stippled yellow lines mark areas (A1–A7) from which the spectra in Figs 1.6 and 1.7 and Supplementary Figs S1.5 and S1.7 were collected. (C) A semi-transparent negative ion image showing the spatial distribution of peaks characteristic of eumelanin (green), phosphate (blue) and silica (red) superimposed onto the FEG-SEM image (see also Supplementary Fig. S1.4). (D) A semi-transparent positive ion image showing the spatial distribution of peaks corresponding to calcium phosphate (green), potassium (blue) and aluminium + silicon (red) superimposed onto the FEG-SEM image (see also Supplementary Fig. S1.6).

Positive ion mode spectra generated directly from the feather residues showed increased intensity of calcium phosphate-related ions, indicating preferential localisation of this mineral to the fibrous tissues and microbodies (e.g., A1-A3; Figs.1.5-B, D and 1.6B and Supplementary Figs S1.6-a, e, S1.7). Mineral-related ions, including aluminium, silicon, magnesium, and potassium, were found in the adjacent matrix (e.g., A4; Fig.1.5B, D and Supplementary Figs. S1.6b‑e, S1.7); these probably denote illite group clay minerals (Meunier, 2005), as intimated by the TEM imaging (Fig. 1.3C).

ToF-SIMS spectra from areas with microbody imprints (e.g., A5‑A7; Fig.1.5 and Supplementary Figs S1.2c, d, f‑h, S1.4‑S1.7) detected varied molecular compositions, ranging from melanin/calcium phosphate-dominated residues (A5) to silicate minerals (A6 and A7), incorporating regionalised intensities of calcium phosphate-related ions (A6). Comparative analyses were undertaken on synthetic and natural variants of eumelanin and phaeomelanin, keratin, two peptidoglycans, five

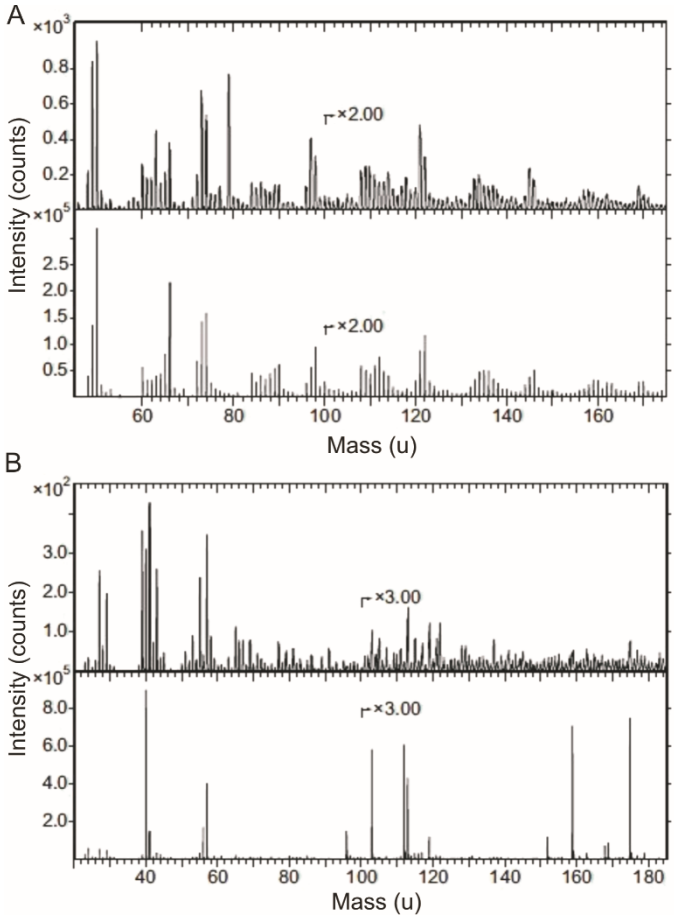

Figure 1.6. ToF-SIMS spectra from area A1 together with eumelanin and hydroxyapatite. (A) Negative ion ToF-SIMS spectra from A1 (top) and synthetic eumelanin (bottom). Note that all major peaks in the synthetic eumelanin spectrum are also present in the fossil spectrum, and that they occur with approximately the same relative signal intensity distribution (see also Supplementary Table S1.1), indicating the presence of significant amounts of eumelanin at the surface of the fibrous tissues. Additional peaks in the fossil spectrum originate from phosphate ($PO_2^-$and PO_3^- at 63 and 79 u, respectively) and silicate related ions (SiO_2^-, SiO_3^- and SiO_3H^- at 60, 76 and 77 u, respectively). (B) Positive ion ToF-SIMS spectra from A1 (top) and hydroxyapatite (bottom). Note characteristic calcium phosphate peaks at 103, 159 and 175 u in the fossil spectrum, corresponding to $CaPO_2^+$, $Ca_2PO_3^+$ and $Ca_2PO_4^+$, respectively (see Supplementary Table S1.2 for peak assignments).

hopanoids, three porphyrins, and three microbial mats (Leefmann et al., 2013; Lindgren et al., 2014; Lindgren et al., 2012). We also examined a chemically derived pyomelanin, as well as pyomelanin from the bacterium *Vibrio cholera* and eumelanin from the bacterium *Saccharophagus degradans* (Fig.1.7). Based on these data, the fossil melanin from YFGP-T5199 displayed closest agreement with animal eumelanin (Fig.1.7). Spectra acquired from the microbial melanins were also compatible in their 'characteristic' eumelanin peaks at 73, 74, 97, 98, 121, 122, 145, and 146 u; importantly though, these were significantly different in their relative abundances. The synthetic pyomelanin spectrum lacked all peaks corresponding to nitrogen-containing ions, including those indicative of eumelanin at 50, 66, 74, 98, 122, and 146 u. Minor contributions from sulfur-containing organics were identified in the spectra from YFGP-T5199, including C_nNS^- ions at 58 (n = 1), 82 (n = 3) and 106 (n = 5) u, and C_nHS^- ions at 57 (n = 2), 81 (n = 4) and 105 (n = 6) u. These peaks were likewise prominent in the synthetic and natural phaeomelanin samples (Fig.1.7), and showed significant co-localisation with 'typical' eumelanin-related peaks (Supplementary Fig. S1.4a, c). However, the sulfur-containing, possible phaeomelanin-related peaks were conspicuously weak in the fossil spectra (Figs.1.6A

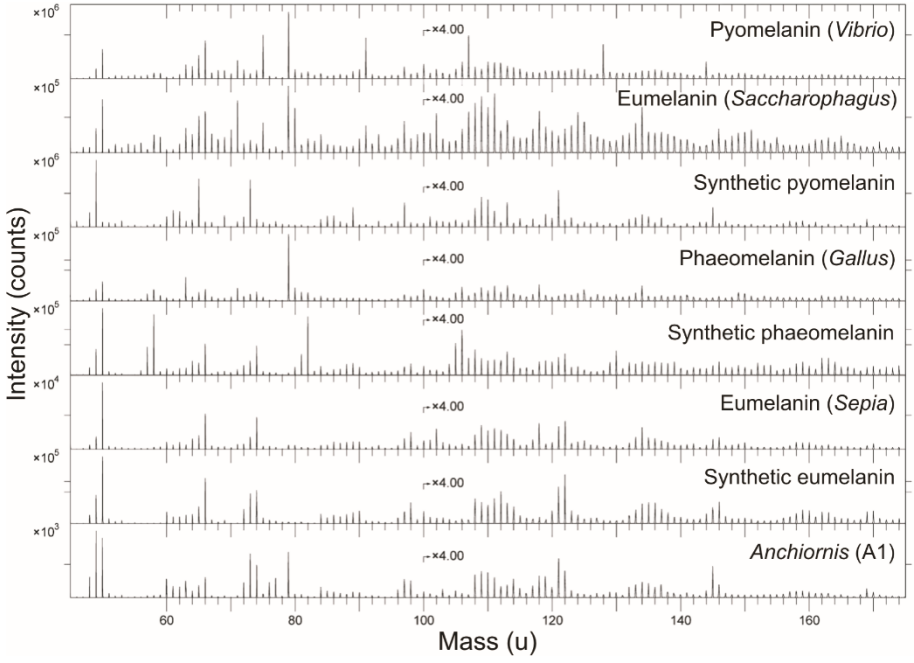

Figure 1.7. ToF-SIMS spectra acquired from melanin reference samples and A1. Negative ion ToF-SIMS spectra from various melanin standards and reference samples together with the spectrum from area A1. All spectra were acquired with the ToF-SIMS instrument optimised for high mass resolution. The prominent peak at 79 u (PO_3^-) in the spectra from pyomelanin (*Vibrio*), eumelanin (*Saccharophagus*) and phaeomelanin (*Gallus*) derives from phosphate-containing contaminants, most likely originating from the melanin extraction and/or purification process.

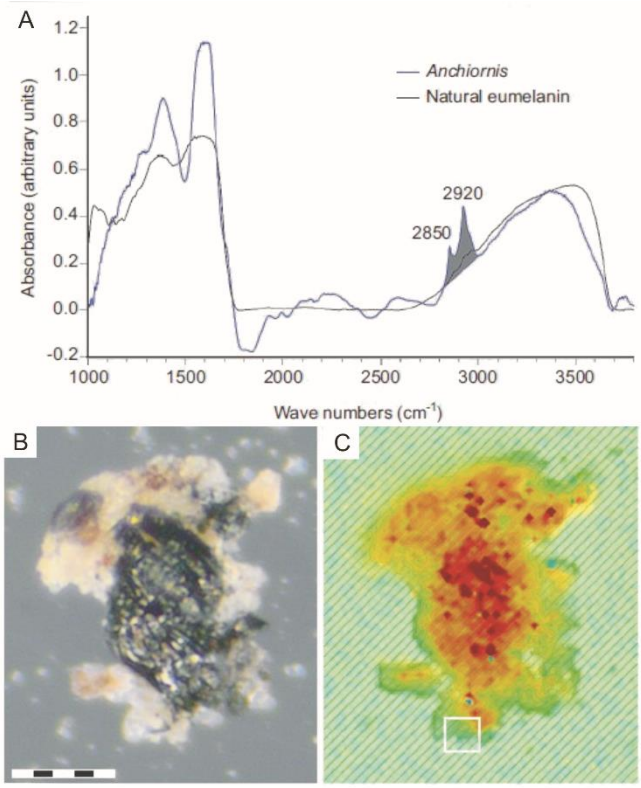

Figure 1.8. IR absorbance data from YFGP-T5199 'forecrown' feathers. (A) Single point IR spectrum recorded from the lower part of the sample chip illustrated in (B, C). Broad-band absorbance occurs in the 900–1800 and 2500–3700 cm^{-1} regions, consistent with natural eumelanin. The YFGP-T5199 spectrum was recorded using transmission mode and a 15×15 μm aperture to reduce sediment contributions. The C-H stretch region used for the absorbance imaging in (C) is shaded in grey. (B) Optical and (C) IR absorbance image (superimposed onto an optical image), the latter recorded by a focal plane array detector (see the Supplementary Methods). The IR image is based on the absorbance of the C-H stretches in the 2820–3000 cm^{-1} region from 2,760 individual spectra (the absorbance increases from yellow to red). The C-H stretches are associated with eumelanin-like spectra, which in conjunction with the lack of other organics on the sample chip (as evidenced by ToF-SIMS), suggest derivation primarily from eumelanin residues. Note that the spatial distribution of the C-H stretch absorbance intimately follows the blackish feather material (see consistency with the carbon distribution recorded by SEM-EDX; Fig. 1.4). Scale bar: 50 μm.

and 1.7), thus preventing confident determination of phaeomelanin or diagenetic incorporation of sulfur into the eumelanin molecular structure (as has been previously suggested for other fossil eumelanins; Lindgren et al., 2014; Lindgren et al., 2012).

No bacterial peptidoglycans or hopanoids were detected, and proteinaceous components consistent with keratins were also absent. Lastly, there were no signs of consolidates and/or preservatives that might potentially compromise the chemical integrity of the sample. These results were corroborated by IR microspectroscopic

measurements, which produced localised absorbance consistent with natural eumelanin, albeit with minor contributions from the surrounding sedimentary matrix (Fig. 1.8).

4. Discussion

The microscopic organisation of the epidermal remains in YFGP-T5199 closely resembles decayed keratin fibrils and eumelanosomes found in extant bird feathers, especially after selective biodegradation of the amorphous polymer matrix (Ichida et al., 2001; Lingham-Soliar et al., 2009; Lingham-Soliar & Murugan, 2013; Rodziewicz & Laba, 2008). The exceptional morphological fidelity of these filamentous appendages also reveals a fibrillar hierarchy reminiscent of the rachis and barb cortex (Lingham-Soliar et al., 2009), which may have imparted a flexural stiffness to the 'forecrown' feathers in YFGP-T5199. The mechanical architecture of paravian feathers can thus be shown to extend beyond gross macroanatomy (Xu et al., 2009b; Xu et al., 2001), to a sub-cellular level of biological organisation.

Multiple independent lines of evidence advocate a eumelanosome origin for the rod-shaped microbodies in the epidermal tissues: (1) the presence of animal eumelanin; (2) the size, shape, distribution, and parallel alignment, which unlike bacterial cells do not form serial chains indicative of microbe fission (see Moyer et al., 2014, figs 1e and 2a, S1c2 and Ichida et al., 2001, fig. 6); and (3) the embedment within fibril-like structures (similar to feather keratin). Yet despite this striking morphological resemblance, we failed to detect any proteinaceous components indicative of keratins. Instead, the fibrous tissues consisted of eumelanin and calcium phosphate, the latter possibly derived from mineral replacement. Indeed, post-burial melanin leakage might have provided a mechanism for either epidermal tissue stabilisation or replication in YFGP-T5199 that was further facilitated by the rapid growth of authigenic minerals (Briggs, 2003; Briggs & Wilby, 1996; Gabbott et al., 2001). Early mineralisation is a common way of preserving labile soft tissues (Briggs, 2003; Briggs & Wilby, 1996; Gabbott et al., 2001), and often involves calcium phosphate in fossilised melanic and/or keratinous structures, including ink sacs (Glass et al., 2013; Kear et al., 1995), feathers (Bergmann et al., 2010; Li et al., 2010) and claw sheath material (Schweitzer et al., 1999).

The association of biomolecules with a mineral substrate is thought to increase the preservation potential of organic compounds, either via adsorptive inhibition of autolysis in decay-inducing enzymes, or by fixation of mineral ions into stabile organometallic complexes that impede molecular breakdown (Schweitzer et al., 1999; Yu et al., 2009). Polymer-calcium phosphate (Briggs, 2003; Briggs & Wilby, 1996; Schweitzer et al., 1999) and/or polymer-clay (Edwards et al., 2011; Gabbott et al., 2001; Pan et al., 2014; Yu et al., 2009) interactions could thus be responsible for the retention of eumelanin molecules in YFGP-T5199. Regardless, eumelanin itself is resistant to decay (Hollingworth & Barker, 1991) because of its extremely dense and

insoluble polymer composition that is both antimicrobial and chemically robust (McGraw & Hill, 2006; Sulaimon & Kitchell, 2003), even in comparison with keratin (Zhang et al., 2010). Furthermore, mature melanosomes are essentially solid aggregations of melanin, which is polymerised onto an insoluble amyloid fibril scaffolding (Delevoye et al., 2011; Watt et al., 2010), thus imparting an architectural stability that likely allows these specialised organelles to persist in the fossil record.

Some imprints observed in the matrix bordering the fibrous microstructures (e.g., A5) are reasonably interpreted as external moulds of pigment organelles based on their dimensional, distributional and chemical compatibility with the rod-like microbodies interpreted here as remnant eumelanosomes (Fig. 1.5 and Supplementary Fig. S1.2d-f), and might have been derived via sample preparation or disruption - e.g., impression from microbodies located on the counterpart (a scenario experimentally shown to produce melanosome imprints in the keratin matrix of modern feathers; Vinther et al., 2009). A melanosome origin is also plausibly inferred for other mouldic structures in YFGP-T5199, including those exposed in A6 (note the continuous alignment of the impressions in A5 and A6; Fig. 1.5B). However, the molecular composition in this region broadly corresponds to that of the host rock (albeit with an increased amount of calcium phosphate), indicating mould formation primarily by aluminosilicate clays. It is therefore possible that local, rapid nucleation and precipitation of clay minerals proceeded in synchrony with the decomposition of the keratinous feather material, thereby encapsulating more stable organic structures (such as the eumelanosomes) within clay nanofabrics. At a later stage, the entombed organelles also decayed, leaving hollow void spaces that for unknown reasons remained empty (assuming that these melanosome 'pseudomorphs' are not negatives from positive reliefs on the counterpart slab).

The affinity of other imprints is more enigmatic, including those in A7 (Supplementary Fig. S1.2h). Not only are these voids morphologically more diverse, but they are also highly disorganised in comparison to the solid eumelanosomes (Fig.1.2A and Supplementary Fig. S1.2h). Spatially, these impressions are also seemingly restricted to aluminosilicate clays and microcrystalline clay aggregates along the bedding plane (Fig.1.2A and Supplementary Fig. S1.2h). We were unable to locate any three-dimensional microstructures matching the imprints, implying that maker(s) of these moulds were less resistant to decay than the eumelanosomes.

In modern feathers, melanosomes can be organised into discrete layers where individual organelles are either consistently aligned or more erratically oriented with only local uniformity in directions (Shawkey et al., 2015; Vinther et al., 2009). Thus, the fossil imprints may comprise moulds of melanosomes that exhibit more variability in shape, and originated from the outer cortex (which can exhibit less melanosome alignment, Vinther et al., 2009). These organelles may also be more prone to degradation because of greater exposure. Alternatively, preservation biases and diagenesis could potentially modify the appearance of fossil structures (Orange et al., 2013; Pan et al., 2014), although this would require the pigment organelles to be

transformed not only in size (as has been previously demonstrated; McNamara et al., 2013), but also in shape and orientation during the fossilisation process (assuming that they were originally aligned in approximate parallel with the bedding plane).

On the other hand, colonies of keratin-degrading microorganisms often comprise a consortium of taxa, resulting in a mixture of shapes and sizes (Ichida et al., 2001). They are also inherently associated with decaying feathers, and can form clustering patterns where neighbouring cells are oriented in common directions (see Ichida et al., 2001, Fig. 6). Furthermore, because some decay is necessary to initiate mineralisation (Briggs, 2003), and because calcium phosphate precipitation can be microbially induced (Briggs & Wilby, 1996; Hirschler et al., 1990), a micro-organismal mediator could be rationally invoked in the partial replacement of the feather material. This, coupled with morphological evidence of fossilised microbes (Westall, 1999), has implications for the interpretation of the more enigmatic imprints observed in the matrix bordering the fibrous microstructures in YFGP-T5199 (Fig. 1.2A and Supplementary Fig. S1.2h). Given the extensive fossil record of microorganisms (Pacton et al., 2006; Westall, 1999), and that some of these voids were not associated with an animal eumelanin molecular signature (e.g., A7), a microbial origin for these particular imprints cannot be excluded. Accordingly, we argue caution against interpreting all fossilised microbodies and impressions as melanosomes, and reconstructing plumage colours based on morphology alone.

An interesting aspect of the fossilised melanosomes in YFGP-T5199 is their exclusively elongate shape (Fig. 1.B and Supplementary Fig. S1.2e). This deviates markedly from the relatively stocky microbodies reported from the 'fore crown' feathers of another referred specimen of *A. huxleyi* (BMNHC PH828, housed in Beijing Museum of Natural History) (Li et al., 2010). With a few possible exceptions (Fig. 1.2A-arrowhead), we also detected no phaeomelanosome-like structures (see Li et al., 2010). Several explanations might account for these discrepancies, including ontogeny, intraspecific variability and sexual dimorphism, as well as taphonomy, and/or sampling (that is, different regions within a multi-coloured crest). We also have to entertain the possibility that: (1) YFGP-T5199 and BMNHC PH828 represent different taxa; (2) integumentary melanosomes intermingle with melanosomes from other parts of the body in one of the two specimens; and (3) the microbodies and impressions reported by Li et al., 2010 and us are different structures altogether.

Indeed, BMNHC PH828 is considerably smaller (~60% by ulna and tibiotarsus length) than YFGP-T5199, and hence it may represent an earlier ontogenetic stage of *A. huxleyi*. Furthermore, YFGP-T5199 possesses a uniquely short dorsodistal process of the ischium (see the Supplementary information and Appendix "A1"), which suggests the possibility of intraspecific and/or sexual differences that may also be reflected in the expressed colour pattern. However, the referral of BMNHC PH828 to *A. huxleyi* is problematic, and we cannot exclude that this specimen represents a closely related but different paravian taxon (see the Supplementary information).

Additionally, while it has been shown that increased temperature and pressure can reduce the size of melanosomes (McNamara et al., 2013), such alterations may not also include shape (but also see Carney et al., 2012). Taphonomy, therefore, presumably cannot account for the different microstructures seen in YFGP-T5199 and BMNHC PH828. Even though melanosomes can potentially disperse during decay (McNamara et al., 2014), the microbodies in S1.1 are located deeply within a fibrous matrix interpreted as fossilised keratin. We thus conclude that the melanosomes most feasibly derive from the 'fore crown' feathers of YFGP-T5199 as opposed to other dermal tissues and/or internal organs (but whether this is also true for BMNHC PH828 has yet to be determined).

Although a re-investigation of the affinity and preservation of BMNHC PH828 is beyond the scope of this study, we note that the 'phaeomelanosome' imprints reported by Li et al., 2010 (see Li et al., 2010, Fig. S5) are preserved in sedimentary grains rather than recognizable feather traces, similar to our more enigmatic impressions. Thus, these imprints may also represent either remobilized melanosomes or non-melanosome microstructures.

5. Conclusion

Our integrated structural and direct chemical approach provides compelling evidence that eumelanosomes and endogenous eumelanin pigment are preserved in the feather remains of YFGP-T5199. This result adds to a growing chronicle of molecular eumelanin detection in fossils (Glass et al., 2013; Glass et al., 2012a; Lindgren et al., 2014; Lindgren et al., 2012; Tanaka et al., 2014), and demonstrates the aptitude of rigorous experimental techniques for identifying ancient biomolecules and their use in characterising 'palaeo-colours'.

Supplementary information for "Molecular composition and ultrastructure of Jurassic paravian feathers

Supplementary Tables

Supplementary Table S1.1. Mass positions, ion assignments and relative signal intensities of selected eumelanin peaks. Observed mass positions, ion assignments and relative signal intensities of peaks related to the eumelanin molecular structure in negative ion ToF-SIMS spectra from area A1 and A2, together with synthetic and natural (*Sepia*) eumelanin. The spectra were acquired with the instrument optimised for high mass resolution. The relative signal intensities were obtained by normalising the measured intensities over the added intensities of all included peaks.

Ion	Theoretical mass	Observed mass			Relative signal intensity		
		Anchiornis	*Sepia* eumelanin	Synthetic eumelanin	*Anchiornis*	*Sepia* eumelanin	Synthetic eumelanin
C_4	48.000	48.000	48.000	47.998	0.039	0.019	0.027
C_4H	49.008	49.009	49.009	49.009	0.125	0.058	0.070
C_3N	50.003	50.005	50.006	50.006	0.125	0.167	0.140
C_4HO	65.003	65.007	65.011	65.007	0.026	0.037	0.034
C_3NO	65.998	66.000	66.001	66.001	0.042	0.092	0.085
C_6	72.000	71.999	72.001	71.997	0.028	0.018	0.025
C_6H	73.008	73.008	73.009	73.007	0.086	0.047	0.054
C_5N	74.003	74.004	74.005	74.004	0.064	0.082	0.077
C_7	84.000	83.998	83.999	83.997	0.020	0.019	0.017
C_7H	85.008	85.006	85.008	85.004	0.017	0.013	0.011
C_6N	86.003	86.009	86.006	86.005	0.019	0.020	0.018
C_6HN	87.011	87.013	87.011	87.011	0.013	0.018	0.016
C_6H_2N	88.019	88.013	88.011	88.012	0.012	0.019	0.019
$C_2H_3NO_3$	89.011	89.006	89.011	89.008	0.015	0.021	0.024
C_5NO	89.998	89.998	90.000	90.000	0.015	0.025	0.028
C_8	96.000	95.996	95.998	95.995	0.018	0.014	0.018
C_8H	97.008	97.006	97.008	97.005	0.055	0.039	0.040
C_7N	98.003	98.003	98.003	98.002	0.035	0.045	0.044
C_9	108.000	107.994	107.992	107.995	0.014	0.014	0.018
C_9H	109.008	109.003	109.002	109.003	0.016	0.020	0.011
C_8N	110.003	110.008	110.005	110.004	0.014	0.015	0.014
C_8HN	111.011	111.011	111.010	111.009	0.011	0.016	0.014
C_8H_2N	112.019	112.013	112.010	112.011	0.009	0.016	0.016
$C_4H_3NO_3$	113.011	113.011	113.012	113.011	0.009	0.014	0.013
C_7NO	113.998	114.002	113.998	113.996	0.013	0.013	0.012
C_{10}	120.000	119.994	119.991	119.995	0.009	0.007	0.008
$C_{10}H$	121.008	121.004	121.005	121.003	0.031	0.017	0.022
C_9N	122.003	122.002	122.000	121.999	0.019	0.022	0.025
C_{11}	132.000	131.991	131.991	131.993	0.007	0.006	0.007
$C_{11}H$	133.008	133.002	133.000	133.001	0.012	0.010	0.009
$C_{10}N$	134.003	134.005	134.000	134.002	0.012	0.018	0.012
$C_{10}HN$	135.011	135.008	135.004	135.007	0.009	0.011	0.011
$C_{10}H_2N$	136.019	136.011	136.006	136.009	0.009	0.011	0.011
$C_9H_3NO_3$	137.011	137.013	137.009	137.012	0.014	0.010	0.009
C_9NO	137.998	138.020	138.009	138.018	0.007	0.007	0.008
C_{12}	144.000	143.989	143.992	143.991	0.005	0.004	0.006
$C_{12}H$	145.008	145.002	145.003	145.000	0.017	0.009	0.013
$C_{11}N$	146.003	146.000	146.000	146.000	0.010	0.011	0.012

Supplementary Table S1.2. Mass positions and ion assignments of non-melanic peaks in A1 and A2. Observed mass positions and ion assignments of selected peaks that are not related to the eumelanin structure in positive and negative ion ToF-SIMS spectra from area A1 and A2.

Positive ions	**Observed mass (A1+A2)**	**Theoretical mass**	**Origin**
Ca^+	39.962	39.963	Ca_xPO_y
$CaPO_2^+$	102.922	102.926	Ca_xPO_y
$Ca_2PO_3^+$	158.878	158.883	Ca_xPO_y
$Ca_2PO_4^+$	174.867	174.878	Ca_xPO_y
Negative ions			
C_2HS^-	59.982	56.980	S-containing organic
CNS^-	57.976	57.975	S-containing organic
C_4HS^-	80.980	80.980	S-containing organic
C_3NS^-	81.973	81.975	S-containing organic
C_6HS^-	104.974	104.980	S-containing organic
C_5NS^-	105.971	105.975	S-containing organic
PO_2^-	62.964	62.963	Phosphate
PO_3^-	78.960	78.958	Phosphate
SiO_2^-	59.966	59.966	Silicate
SiO_3^-	75.960	75.961	Silicate
SiO_3H^-	76.968	76.969	Silicate
$SiAlO_4^-$	118.936	118.938	Silicate

Supplementary Table S1.3. Selected length measurements of YFGP-T5199 (mm).

Skull	59.5
Cervical series	56.5
Dorsal series	97.5
Caudal series	236.5
Scapula	31.0
Humerus	70.0
Deltopectoral crest	18.0
Ulna	59.5
Manus	95.0
Metacarpal I	14.0
Metacarpal II	38*
Metacarpal III	31*
Manus phalanx I-1	27.0
Manus phalanx I-2	16.5
Manus phalanx II-1	25.0
Ilium	35.5
Preacetabular	16.0
Postacetabular	16.0
Pubis	49.5
Ischium	16.0
Femur	69.5
Tibiotarsus	106.0
Metatarsus	61.0
Metatarsal I	12.0
Pes	90.0
Anterior caudal vertebra	6.5
Posterior caudal vertebra	16.0

*Estimated value

Supplementary Table S1.4. Relative length proportions of selected skeletal elements in some Jurassic avialans. Measurements are taken from the literature (Hu et al., 2009; Wellnhofer, 2009; Xu et al., 2009a).

	YFGP-T5199	*Anchiornis* IVPP V14378	*Anchiornis* LPM-B00169	BMNHC PH828	*Aurornis* YFGP-T5198	*Eosinopteryx* YFGP-T5197	*Archaeopteryx* HMN 1880/1881	*Xiaotingia* STM 27-2
Skull/femur	0.87	-	0.96	-	0.86	0.89	0.99	0.72
Scapula/femur	0.44	0.62	0.68	-	0.55	0.49	1.07	0.65
Scapula/humerus	0.46	0.65	0.66	0.58	0.63	0.63	0.89	0.77
Humerus/femur	1.00	0.96	1.04	-	0.88	0.79	1.21	0.85
Radius/humerus	0.85	-	0.81	-	0.83	0.81	1.03	0.75
Ulna/humerus	0.90	0.89	0.80	0.88	0.98	1.11	0.89	0.92
Manus/femur	1.37	1.38	1.55	-	1.09	1.17	1.48	2.55*
Tibiotarsus/femur	1.56	1.57	1.61	-	1.37	1.43	1.30	-
Tibiotarsus/humerus	1.56	1.63	1.54	1.64	1.56	1.83	1.13	-
Pes/femur	1.53	1.56	1.56	-	1.11	1.34	1.18	-
Metacarpal I/ metacarpal II	0.35	-	0.37	0.39	0.35	0.40	0.25	0.42

*Estimated ratio

Supplementary Figures

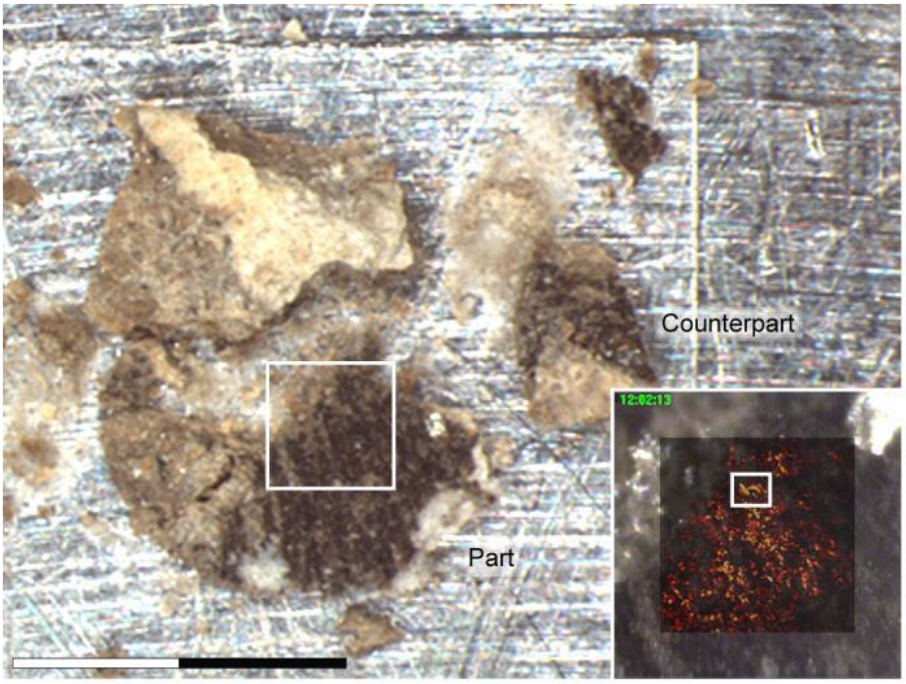

Supplementary Figure S1.1. YFGP-T5199 feather sample S1. S1 prior to molecular analysis. Note that the sample has been split into part and counterpart sub-samples. Inset shows a semi-transparent ToF-SIMS total ion image superimposed onto the demarcated area. The highlighted area in the ion image corresponds to the region analysed in Fig. 1.5 and Supplementary Figs S1.4 and S1.6. Scale bar: 2 mm.

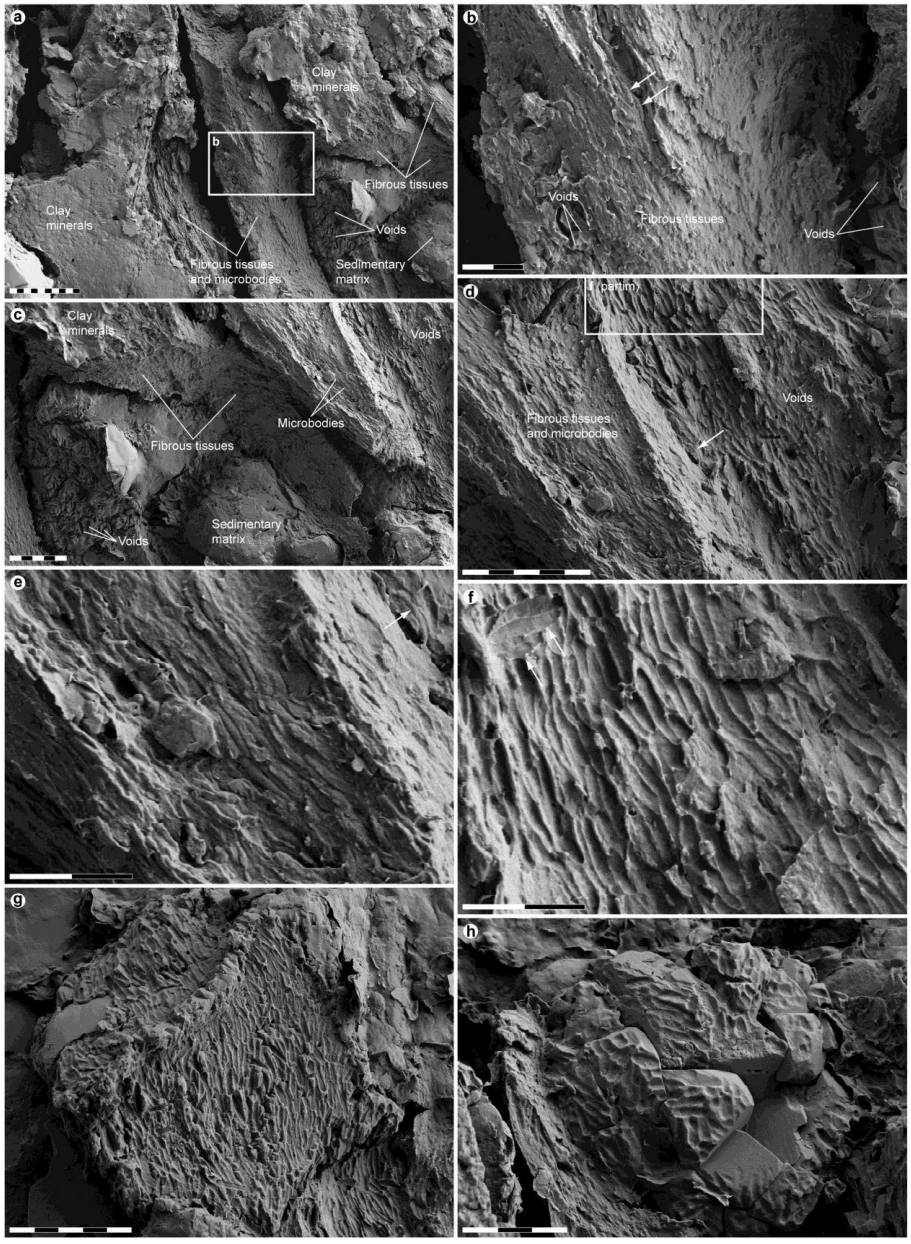

Supplementary Figure S1.2. FEG-SEM micrographs of area A1–A7. Close-up images of feather material and surrounding sediments in sample S1 (see also Fig. 1.5). (a) Overview of A1 and A2. Scale bar: 10 µm. (b) Enlargement of (a) illustrating degraded, fibril-like tissues, imprints ('Voids') and a few microbodies (arrows). Scale bar: 2 µm. (c) Overview of A3 and A5 (partim). Note transversely and longitudinally fractured fibrous tissues, intruding sedimentary matrix with scattered voids, and densely spaced microbodies. Scale bar: 5 µm. (d) Detail of A3 and A5 showing

elongate microbodies embedded within fibril-like elements and densely spaced imprints oriented along the three-dimensional structures. Arrow indicates a microbody located in the same plane as the impressions. Scale bar: 5 µm. (e) Close-up image depicting eumelanosome-like microbodies within fibrous tissues. Arrow marks a partially encased microbody (see also d). Scale bar: 2 µm. (f) Enlargement of (d) demonstrating consistent orientation of imprints, albeit with some exceptions (arrows). Scale bar: 2 µm. (g) Overview of A6 showing regular orientation of impressions. Scale bar: 5 µm. (h) Overview of A7 displaying randomly arranged imprints. Scale bar: 3 µm.

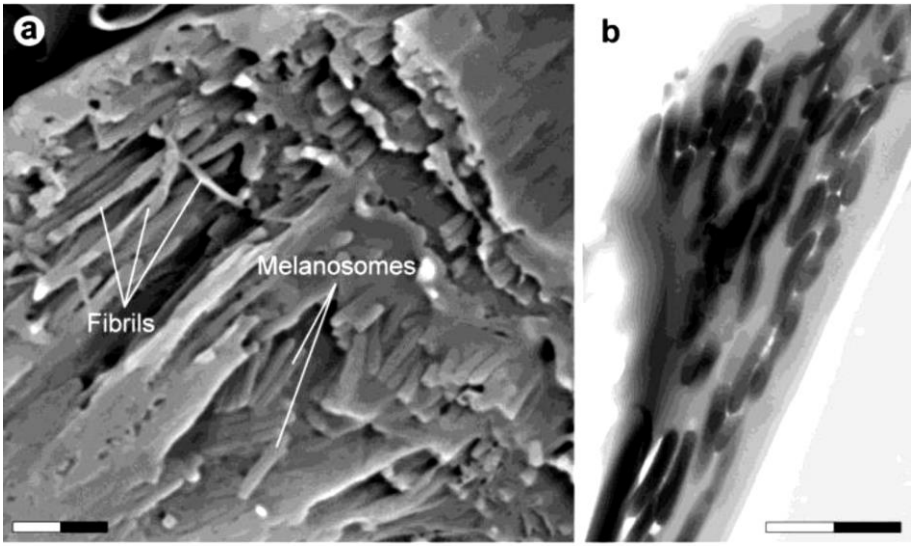

Supplementary Figure S1.3. SEM and TEM micrographs of extant *Corvus* sp. feathers. (a) Oblique transverse section of barbule. Note elongate melanosomes embedded within keratin fibrils. Scale bar: 2 µm. (b) TEM micrograph showing elongate melanosomes within a longitudinally sectioned barbule. Scale bar: 2 µm.

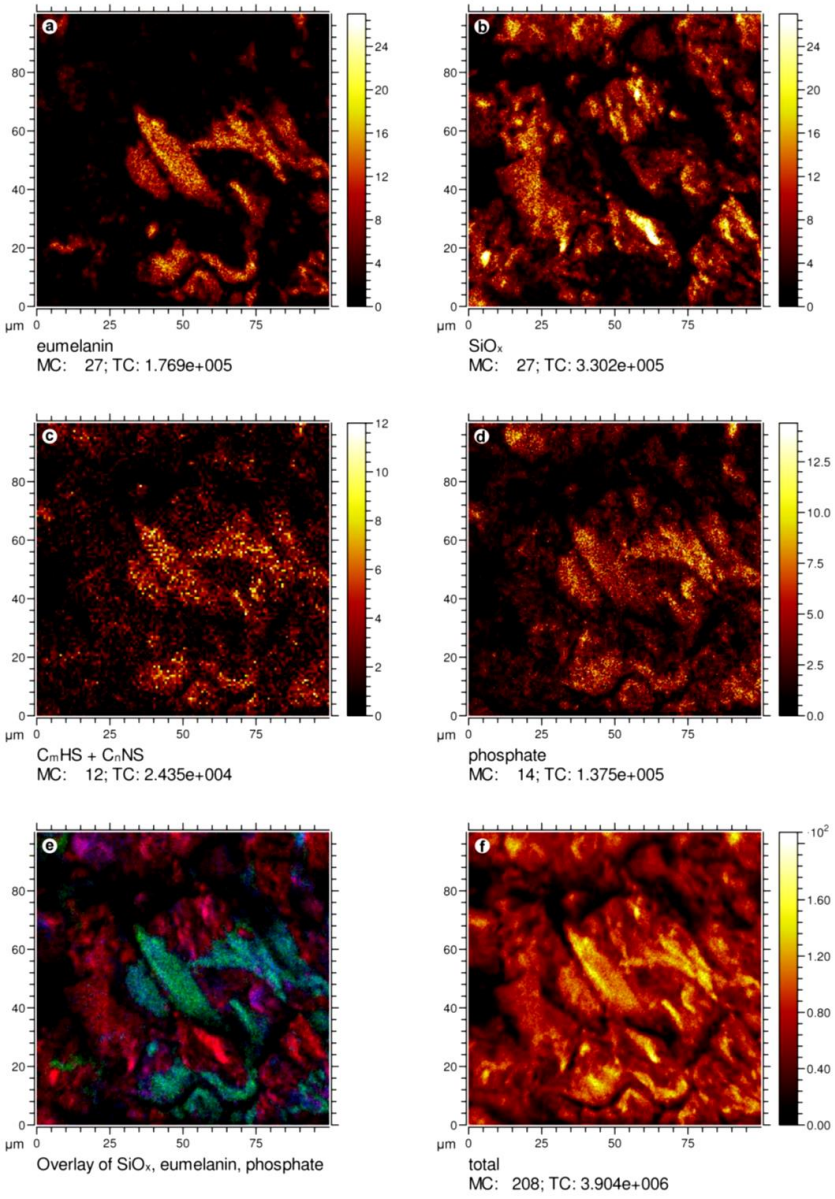

Supplementary Figure S1.4. Negative ion ToF-SIMS images of sample S1. Negative ion ToF-SIMS images of sample S1 showing the added signal intensity of peaks characteristic of (a) eumelanin (50 + 66 + 73 + 74 + 97 + 98 u), (b) silica (60 + 76 + 77 + 119 u), (c) sulphur-containing organics (57 + 58 + 81 + 82 + 105 + 106 u), and (d) phosphate (63 + 79 u), as well as (e) an overlay image of eumelanin (green), silica (red) and phosphate (blue) (same illustration as in Fig. 1.5C) and (f) the total ion image. Ion assignments are indicated under each image.

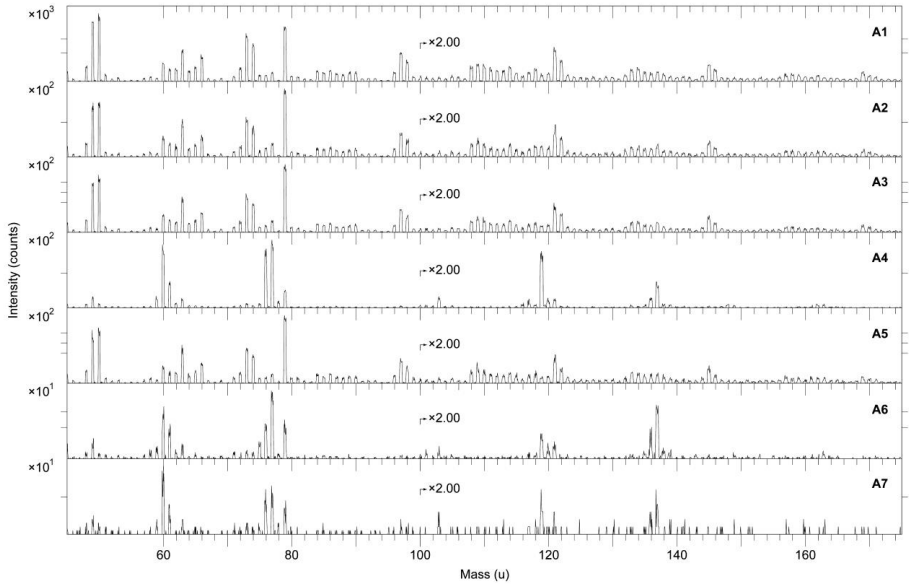

Supplementary Figure S1.5. Negative ion ToF-SIMS spectra representing A1–A7. Negative ion ToF-SIMS spectra obtained from area A1–A7 (Fig. 1.5B). Note striking resemblance between the spectra acquired from A1–A3 and A5, and the reference spectra from natural and synthetic eumelanin (Fig. 1.7). Peaks at 63 and 79 u correspond to phosphate ions. Also note that the spectra from A4, A6 and A7 are dominated by peaks representing silica ions. All spectra were acquired with the ToF-SIMS instrument optimised for high image resolution.

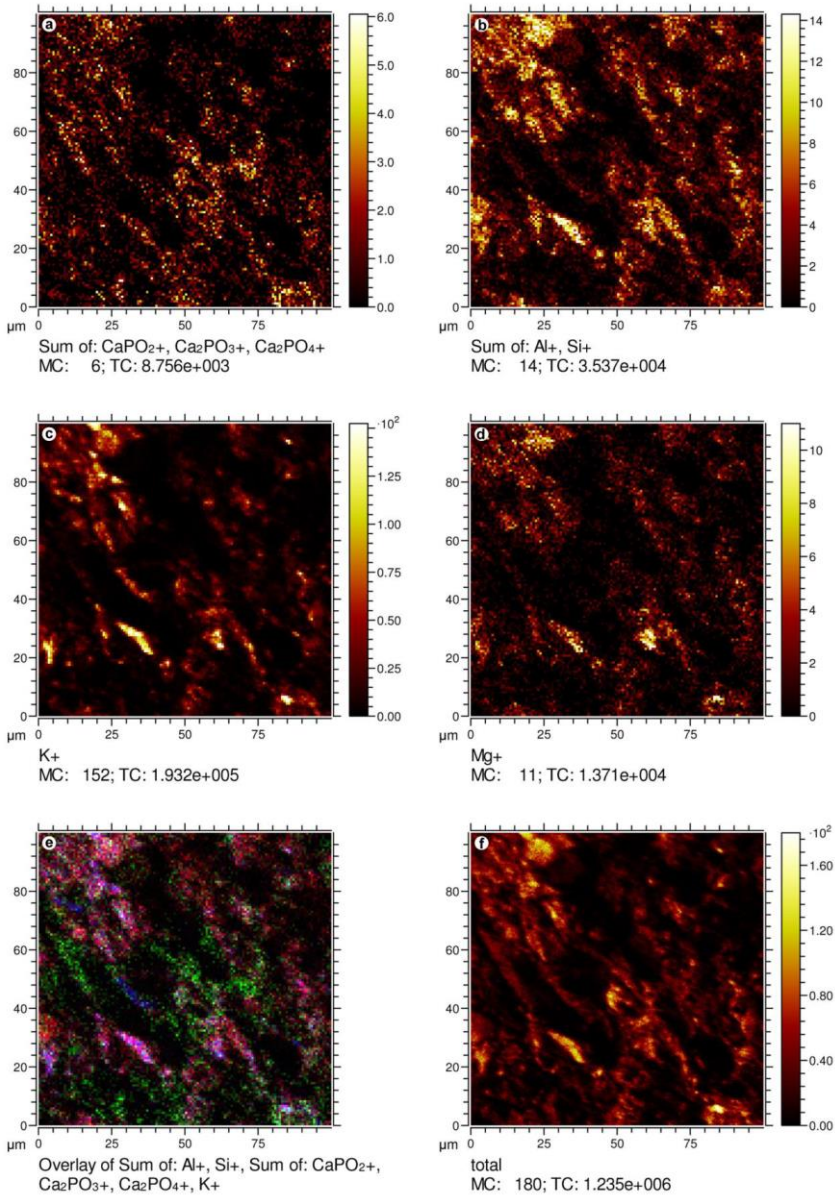

Supplementary Figure S1.6. Positive ion ToF-SIMS images of sample S1. Positive ion ToF-SIMS images of sample S1 showing the signal intensity of peaks characteristic of (a) calcium phosphate (103 + 159 + 175 u), (b) aluminum + silicon (27 + 28 u), (**c**) potassium (39 u), and (d) magnesium (24 u), as well as (e) an overlay image of calcium phosphate (green), aluminum + silicon (red) and potassium (blue) (same illustration as in Fig. 1.5D) and (f) the total ion image. Ion assignments are indicated under each image.

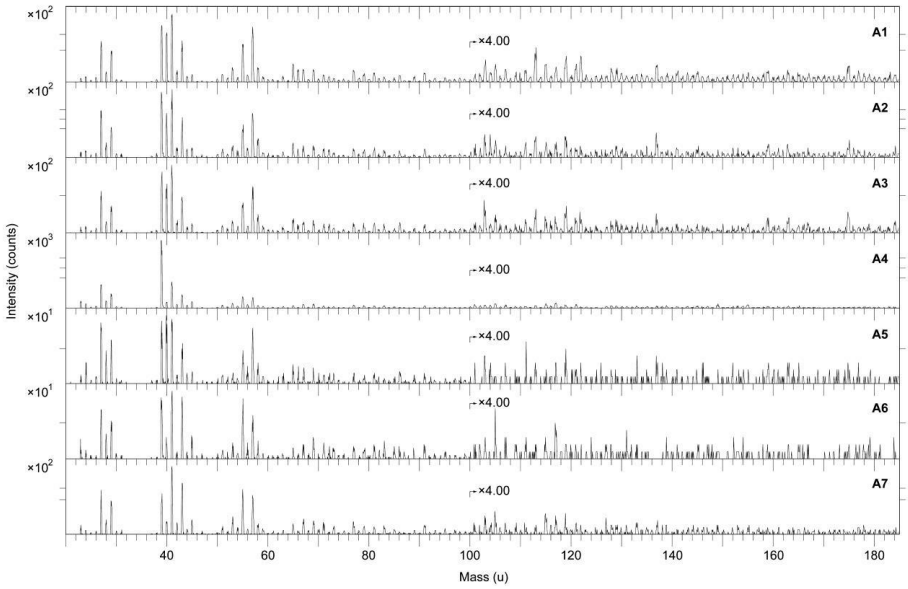

Supplementary Figure S1.7. Positive ion ToF-SIMS spectra representing A1–A7. Positive ion ToF-SIMS spectra obtained from area A1–A7 (Fig. 1.5-B). Note relatively strong signal intensity from ions representing calcium (40 u) and calcium phosphate (103, 159 and 175 u) in A1–A3. All spectra were acquired with the ToF-SIMS instrument optimised for high image resolution.

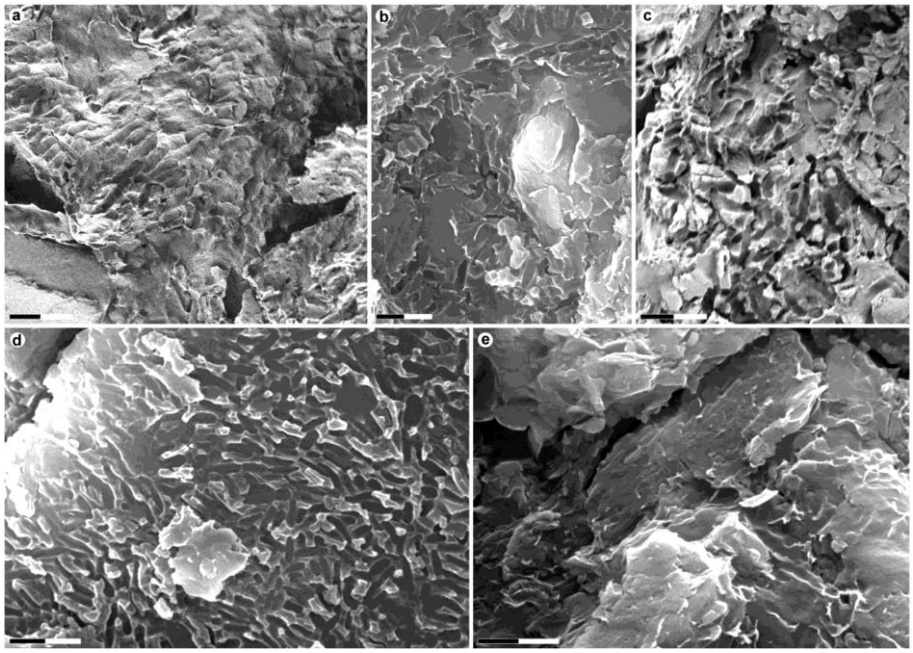

Supplementary Figure S1.8. Microbodies and imprints associated with the plumage in YTGP-T5199. FEG-SEM and SEM micrographs of (a) sample S5, (b) S11, (c) S12, (d) S13, and (e) S14. Scale bars: 2 μm.

Chapter 2

This chapter is based on: Cincotta et al., *to be submitted*

Chemical taphonomy of morphologically well-preserved dinosaur feathers: a multi-technique approach

Abstract

A panel of geochemical techniques is used here to investigate the ultrastructure and molecular composition of fossil feathers preserved in association with the skeleton of a small Jurassic paravian dinosaur *Anchiornis huxleyi*. Parallel analysis of extant buzzard feathers was undertaken in order to test whether the soft tissues morphologically preserved in the fossil also exhibit a high degree of chemical preservation. Scanning electron microscopy (SEM) and energy dispersive spectroscopy (EDS) were used to characterise the mineralogy of the surrounding sediment and revealed the preservation of melanosome-like microbodies in the fossil. Carbon gradients along a depth profile and co-occurrence of carbon and sulfur was shown in the fossil by elastic backscattering (EBS) and particle-induced X-ray emission (PIXE). The molecular composition of modern and fossil soft tissues was assessed from solid-state ^{13}C nuclear magnetic resonance (^{13}C CP-MAS NMR) and pyrolysis gas-chromatography mass-spectrometry in the presence of TMAH (TMAH-Py-GC-MS). The proteinaceous material that comprises the modern feathers is not present in the fossil feathers. The latter and the embedding sediment exhibit and are dominated by a highly aliphatic character. However, there are substantial differences between these samples, revealing that the organic matter of the fossil feathers is, at least partially, derived from original feather constituents. The preservation of the fossil feathers, primarily expressed by the preservation of their morphology, seems to be associated with

The studied samples consist of fossil feather fragments dissected from the posterior end of the tail (see Fig. 2.1, the dark area in the white box, top right) of YFGP- T5199, as well as fragments of the host sediment (Fig. 2.1, the light area in the white box, top right). To test for possible contamination of the chemistry of the fossil feathers by the sediment, the sediment samples were analysed using the same methodology as for the fossil feathers. Two types of sediment the *in situ* polymerisation of endogenous lipids.

1. Introduction

Preservation of soft-bodied animals –with non-mineralised tissues - in the whole geological record is relatively rare. Soft parts of organisms are usually lost during the diverse degradation processes occurring during fossilization. Their constitutive labile organic compounds are usually too fragile to be preserved, compared to the "hard" – biomineralised – parts, which are generally better preserved. However, some important fossil-bearing sites yield not only exquisitely preserved skeletons but also remains of soft tissues, such as skin, scales, hair or feathers (e.g., Allison & Briggs, 1993; Pan et al., 2013; Zhu et al., 2005b). Feathers, the epidermal appendages that form the external covering of modern birds, have been discovered preserved in close association with fossils of theropod dinosaurs in *Konservat-Lagerstätten* - localities that are characterized by the unusual quality of the fossils - from the Upper Jurassic and Lower Cretaceous of China (Chu et al., 2016; Godefroit et al., 2013a; Hu et al., 2009; Xu et al., 2012; Xu et al., 1999; Xu et al., 2009a) and Germany (Rauhut et al., 2012). During the last twenty years, Liaoning Province, in north-eastern China, has yielded well-preserved vertebrate fossils with soft parts (e.g., Benton et al., 2008; Kellner et al., 2010; Li et al., 2012a). The most striking discoveries were exquisitely well-preserved feathered theropod dinosaurs, evidencing their relationship with

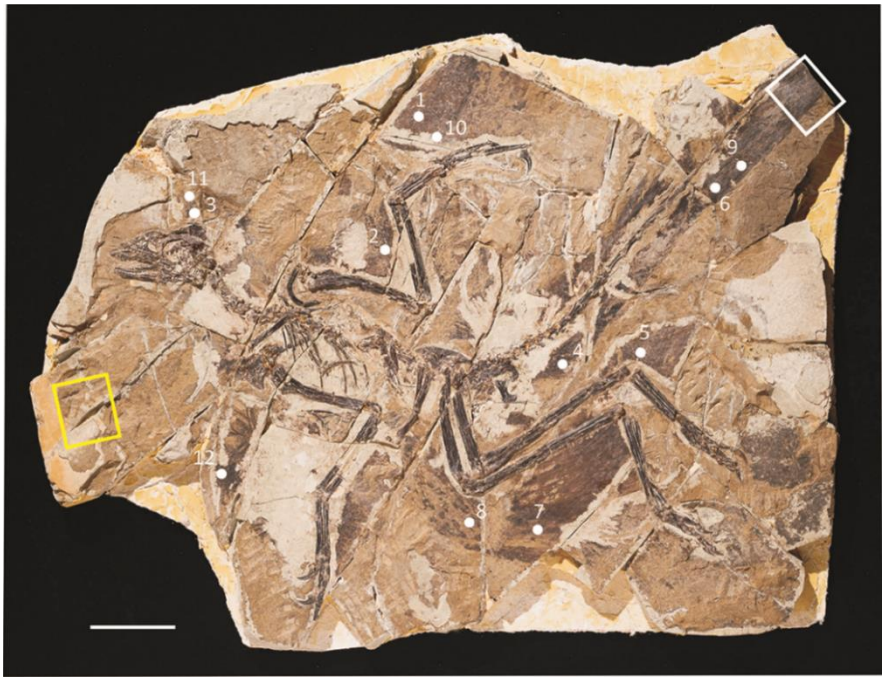

Figure 2.1. *Anchiornis huxleyi* (YFGP-T5199). Photograph of the Jurassic feathered theropod with location of sampled areas. The white box indicates locations of fossil feather and embedding sediment sampling, while the yellow box indicates location of "remote" sediment sampling, for NMR, Py-GC-MS, and IBA analyses. White dots are samples used for SEM imaging and EDS. Scale bar = 5 cm. Photograph by Thierry Hubin (IRSNB).

modern birds. Since the discovery of the Early Cretaceous *Sinosauropteryx prima* in 1996 (Ji & Ji, 1996), many other feathered specimens have been found (Hu et al., 2009; Li et al., 2012a; Xu et al., 2012; Xu et al., 2015). In the same way, the discovery of one of the most primitive birds, *Archaeopteryx lithographica*, associated with well-preserved feathers, constitutes a gigantic step in the comprehension of bird – and feather – evolution (Christiansen & Bonde, 2004). Interestingly, elongated filaments interpreted as primitive feathers were observed in ornithischian – non-theropod – dinosaurs (Mayr et al., 2002; Zheng et al., 2009a). Recently, both "feather-like" structures and scales were discovered together with remains of the Middle-Upper Jurassic neornithischian *Kulindadromeus zabaikalicus* collected in volcaniclastic deposits from Siberia (Godefroit et al., 2014). The fossil feathers show a large range of preservation degrees (e.g., Schweitzer, 2011b; Xing et al., 2016). The study of these diversely preserved structures is crucial for a better understanding of the taphonomic processes leading to their preservation. In most cases, feathers and other types of preserved soft-tissues were deposited in calm, low-energy environments (e.g., Kellner & de Almeida Campos, 2002). They are found in a broad range of environmental settings: shallow-marine (e.g., Martill & Heimhofer, 2007; Barthel, 1964; Heimhofer & Martill, 2007), lacustrine (e.g., Harms, 2002; Sullivan et al., 2014; Zhou & Wang, 2010), or terrestrial (Manning et al., 2013). Different modes of preservation occur for the soft-tissues: carbonaceous films (e.g., Li et al., 2010; Lindgren et al., 2015), phosphate (Allison & Briggs, 1993; Briggs et al., 1993), pyrite (Briggs et al., 1991; Farrell et al., 2013a; Leng & Yang, 2003), clay minerals (Gabbott et al., 2001; Martin et al., 2004), aluminosilicates (Butterfield et al., 2007), or a combination of these minerals (Wilby et al., 1996).

Feathers are epidermal appendages composed mainly of keratin (Lucas & Stettenheim, 1972a), which is present as two secondary structures, alpha-helixes and beta-sheets, corresponding to alpha- and beta-keratin, respectively (e.g., Fraser & MacRae, 2012). Alpha-keratin plays a hydrophobic role in avoiding water loss, whereas beta-keratin increases the skin hardness (Fraser & Parry, 1996; Gregg & Rogers, 1986). According to (Lucas & Stettenheim, 1972b), the amino acid content of keratin in modern bird feathers seems homogenous in identical parts of the feather (e.g., in rachis of feathers belonging to the same species), but varies from one bird species to another. Nonetheless, feather keratin always comprises high amounts of serine, glycine, proline, and, in lower quantities, valine, leucine, alanine and cysteine (Arai et al., 1983, 1986; Gregg & Rogers, 1986; Murphy et al., 1990; O'Donnell & Inglis, 1974; Saravanan & Dhurai, 2012; Staroń et al., 2011).

The aim of this study is to determine the chemical composition and structure of the fossil feathers of the theropod dinosaur, *Anchiornis huxleyi* (YFGP-T5199), collected from Upper Jurassic deposits of the Tiaojishan Formation (Liaoning Province, China). Previous study of the same specimen focused on the identification of pigment remains, and demonstrated preservation of melanosomes in the feathers (Lindgren et al., 2015). Here, we report new and complementary geochemical

information about the preservation of the fossil feathers using a range of analytical tools. The surrounding sediment and modern feathers were analysed in parallel to ascribe pristine constituents.

Scanning electron microscopy (SEM) and energy dispersive X-ray spectroscopy (EDS) were used to identify preserved pigment organelles and the embedding matrix. X-ray diffraction (XRD) was used to analyse the mineralogical composition of the samples in an attempt to understand the role of sediment mineralogy in the preservation of soft tissues. Ion beam analysis (IBA), including Particle-Induced X-ray Emission (PIXE) and Elastic Backscattering Spectrometry (EBS) were used here for the first time on fossil soft tissues to get further insights into the elemental composition of the samples. This approach was recognised as a promising archaeometric tool (Jeynes and Colaux 2016) and it was recently successfully applied to human bone analyses (Beck 2014). Organic geochemistry techniques, namely ^{13}C-Nuclear Magnetic Resonance (NMR) and Pyrolysis Gas Chromatography-Mass Spectrometry in the presence of TMAH (TMAH-Py-GC-MS) were used to characterise the functional groups and other biomolecular components present.

2. Sample description and preparation

The studied specimen, *Anchiornis huxleyi* (YFGP- T5199) (Fig. 2.1), is a basal Avialae (for a complete description of the specimen see the Supplementary Information in Lindgren et al., 2015: pp. 18-23) that was collected from the Tiaojishan Formation in the Yaolugou locality (Liaoning Province, China), and belongs to the Yizhou Fossil and Geology Park in Liaoning. The Tiaojishan Formation consists of hundreds of meters of alternating sedimentary and volcanic beds (Liu et al., 2012a; Yang et al., 2006; Yuan et al., 2005). Absolute dating on a laterally equivalent formation – the Lanqi Formation – indicates an age ranging between 165.0 ± 1.2 Ma and 153.0 ± 2.0 Ma (Chang et al., 2009; Zhang et al., 2008), which spans the Callovian-Kimmeridgian (Middle-Late Jurassic) interval (Gradstein et al., 2012). YFGP- T5199 is embedded in thinly laminated carbonate sediments, corresponding to alternation of very thin marl and thicker clay laminae. These sediments were deposited in a lake affected by episodic volcanic eruptions (Nan et al., 2012). Recent U-Pb radiochronological analyses on zircons from the Jianchang locality indicate that the Yanliao Biota, that includes *Anchiornis* as well as pterosaurs and eutherian mammals, is Oxfordian in age (Chu et al., 2016). The plumage of the specimen studied herein is preserved as dark brown residues around the skeleton, especially around the tail and the forelimbs, and on the skull.

The studied samples consist of fossil feather fragments dissected from the posterior end of the tail (see Fig. 2.1, the dark area in the white box, top right) of YFGP-T5199, as well as fragments of the host sediment (Fig. 2.1, the light area in the white box, top right). Two types of sediment samples were studied: (1) surrounding sediment directly associated to the feathers from the tail (see the light area in the white

box on Fig. 2.1) and (2) sediment located > 100 mm from the fossil on the same slab (see yellow box on Fig. 2.1). Two modern brown wing feathers of *Buteo buteo* (buzzard, Aves: Accipitriformes; RBINS collection number: A4011A01) were analysed for comparative purposes. Different parts of the feathers, rachis and barbs, were analysed with IBA. The modern feathers come from a specimen that died naturally and was sorted at -18 C° at the Royal Belgian Institute of Natural Sciences prior to analysis.

Two types of samples were collected on the fossil specimen: millimetre-sized samples for SEM and EDS, in addition to centimetre samples for the other analytical approaches. We took 12 millimetre-sized samples (Fig. 2.1) from different regions of the body of YFGP-T5199 with a sterile scalpel. The samples were mounted on double-sided carbon tape and sputter-coated with gold (Baltec SCD 050). Centimetre-sized fragments of approximately 5 mm² and 2 mm thick, from fossil feathers (white box in Fig. 2.1) and sediment (yellow box in Fig. 2.1) were dissected with sterile scalpel. Samples were cleaned with distilled water without any additional preparation prior to analysis. Several points were analysed with IBA on one centimetre fragment containing both fossil feathers and their host sediment, and one fragment of sediment (Supplementary Fig. S2.1). Other centimetre-sized samples from the same region were collected for NMR and Py-GC-MS (white and yellow boxes on Fig. 2.1). These samples were crushed and lipids were extracted in order to (1) eliminate potential contaminants related to sample manipulation and (2) concentrate macromolecular organic matter which mainly corresponds to proteins in modern feathers. Samples were ground to a fine homogeneous powder in an agate mortar. Lipid extraction involved three successive ultrasonications (ten minutes) in 15 ml of dichloromethane/methanol (2:1, v/v), at room temperature and centrifugation at 3500 rpm (ten minutes). The supernatant was removed and the pellet was dried under nitrogen and stored in the dark at 5 °C prior to analysis.

3. Methodology

3.1. Scanning Electron Microscopy (SEM) and Energy-dispersive X-ray spectroscopy (EDS)

Samples were imaged under low vacuum with an environmental QUANTA 200 (FEI) scanning electron microscope at an acceleration voltage of 20–30 kV and a working distance of 8–15 mm. Subsequent EDS analyses (single point and mapping) were performed using either an environmental QUANTA 200 (30 kV, working distance of 10 mm) or a field-emission JEOL 7500F (15 kV, working distance of 8 mm).

3.2. X-ray diffraction (XRD)

XRD analyses were carried out on both bulk rock and clay minerals with a Philips diffractometer using Cu K_α radiation. A tube voltage of 40 kV and a tube current of 30 mA were used. The goniometer scanned from 3° to 70° 2θ for the bulk rock and from 3° to 30 ° 2θ for clay minerals. The clay minerals (< 2 µm fraction) were isolated by successive centrifuging after decarbonation of the crushed rock with 1N HCl. The preparation was mounted on glass slides and treated in the following ways: (1) natural (air-dried), (2) ethylene-glycol solvation and (3) heated at 490 °C for two hours. Clay minerals were identified according to the position of the (001) series of basal reflections on the X-ray diagrams.

3.3. Ion Beam Analysis (IBA): Particle-Induced X-ray Emission (PIXE) and Elastic Backscattering Spectrometry (EBS)

EBS and PIXE measurements were performed using a 3 MeV proton (^{1}H) beam from the Tandetron linear accelerator ALTAÏS (University of Namur). PIXE is sensitive to Na to U elements whereas EBS signals are enhanced for light elements (e.g., C, N and O) due to strong non-Rutherford cross-sections. The beam spot size was reduced to ca. 0.5 mm in diameter to minimise topographic effects. Backscattered particles were detected using two detectors mounted at scattering angles of 170° and 165°, whereas the emitted X-rays were collected with an Ultra-LEGe (Ultra Low Energy Germanium) detector mounted at 135°. Angles are given relative to the incident beam direction. A selective filter (6 µm of Al) was mounted in front of the Ultra-LEGe detector to lower the strong silicon signal and therefore enhance the rather weak S signal observed in the fossil feather. Two locations were analysed in the fossil feather, the host sediment was analysed at three different locations (at 1.7, 3.2, and 4.8 mm away from the fossil) and the remote sediment, in one location. Two locations were analysed in the modern brown feather: one in the barb and one in the rachis. All analyses used the same experimental settings.

A certified reference material (BCR-126A lead glass from NIST) was analysed to (1) calibrate the detectors (both EBS and PIXE) and (2) estimate the accuracy of the PIXE measurements. The EBS spectra were analysed with DataFurnace software (Jeynes et al., 2003) together with the cross-sections generated by SigmaCalc (Gurbich, 2016), while the PIXE spectra were manipulated with GUPIX software (Campbell et al., 2010). The mean elemental composition of the matrix to be used in GUPIX was determined by integrating the depth profiles of the main components observed by EBS (i.e., C, O & Si) on a given interval (0–100 000 TFU). For each analysis point, the mean concentration of the major elements was derived from the EBS spectra and used as the matrix composition used by GUPIX to fit the PIXE spectra. Using DataFurnace, the experimental spectrum can be inverted to recover the elemental depth profiles (examples are shown for carbon in Supplementary Fig. S2.3).

Integration of these elemental depth profiles allows derivation of the concentration of each element at a given depth. The integral of C, O and Si depth profiles (integration limits set to 0–25 000 TFU, or 0–3 µm considering a density of 2.65 g/cm³) yield the C, O and Si equivalent thicknesses given in TFU (for thin film unit, or 10^{15} atoms/cm^2).

3.4. ^{13}C Nuclear Magnetic Resonance (CP-MAS ^{13}C NMR) and Curie point Pyrolysis-Gas Chromatography-Mass Spectrometry (Py-GC-MS)

Solid state ^{13}C NMR is a spectroscopic method that reveals the chemical environment of carbon atoms in organic compounds. ^{13}C NMR spectra of lipid-extracted samples were obtained at 125 MHz (Bruker Avance 500 spectrometer) using a 4 mm zirconium rotor, with a cross-polarisation (CP) sequence and magic angle spinning (MAS) at 14 kHz. CP-MAS ^{13}C NMR spectra were acquired with contact time of 1 ms and recycle time of 1s (fossil and sediment) or 3s (modern feather). Each spectrum was the result of 6 000 (modern samples) to 400 000 (sediment) scans.

Py-GC-MS gives insight into the molecular composition of organic macromolecular materials through their thermal degradation into molecular fragments that can be separated by gas chromatography (GC) and further identified by mass spectrometry (MS). Tetramethylammonium hydroxide (TMAH) was used to enhance the thermal breakdown of macromolecules and induce *in situ* methylation of pyrolysis products, which, in turn, enhance their detection and identification in GC-MS. The samples were mixed with an excess of TMAH (25 wt % in methanol) in a 1:1 (wt/wt) ratio before loading in ferromagnetic tubes with Curie temperature of 650 °C. Between 2 mg (modern samples) and 16 mg (sediment) were used. Curie point pyrolysis was carried out with a Pilodist Curie flash pyrolyser. Samples were heated at their Curie temperature for 10 s under a He flow of 1 ml min^{-1}. The instrument was coupled directly to a GC-MS system. The pyrolysis products were separated using a Trace Thermo gas chromatograph equipped with a Rxi5SilMS column (30 m × 0.25 mm i. d., 0.5 µm film thickness). Helium was used as carrier gas at constant pressure of 15 psi. The injector temperature was 280°C in spitless mode. The oven temperature was maintained at 50°C for 10 minutes and was progressively increased to 310°C at 2°C min^{-1}. Coupled to the gas chromatograph was a DSQ Thermo mass spectrometer, with a heated interface (310°C), electron energy at 70 eV and ion source at 220°C, scanning from m/z 35 to 800 at 2 scans s^{-1}. Compounds were assigned on the basis of their mass spectra, comparison with the NIST library mass spectra, published mass spectra (e.g., Gallois et al., 2007; Templier et al., 2013) and GC retention times.

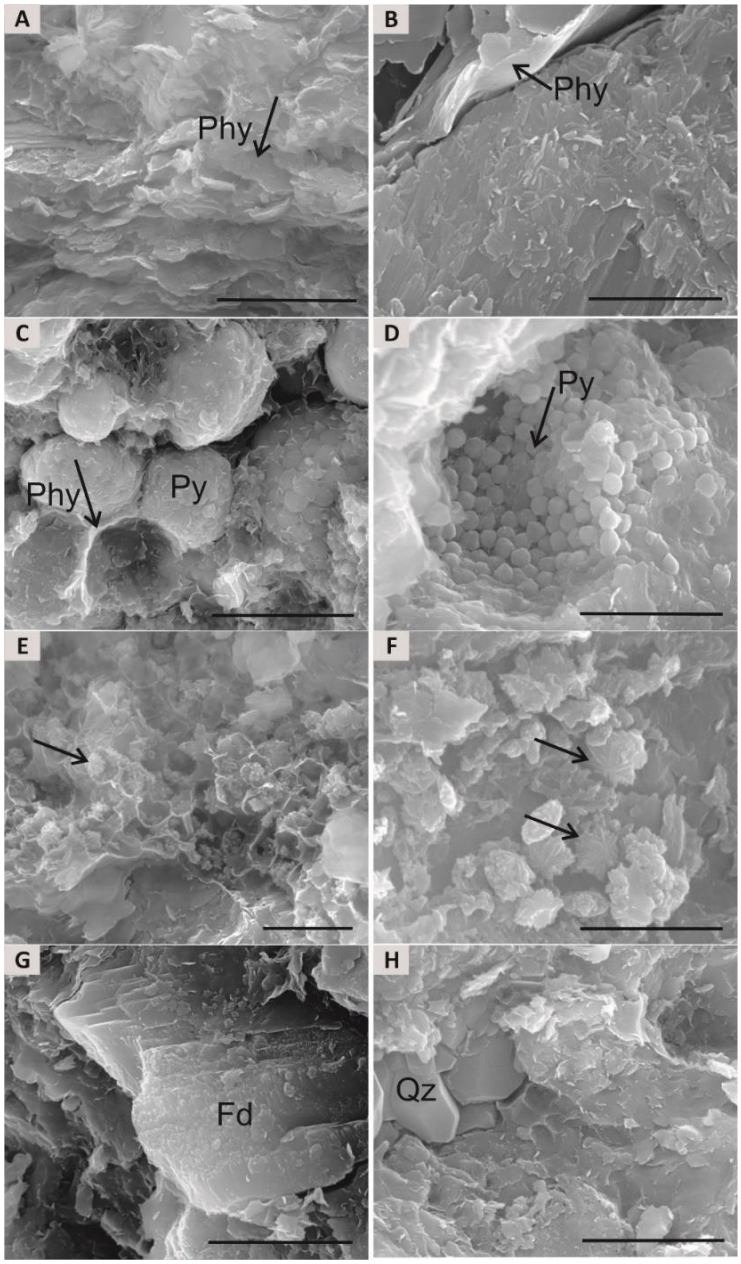

Figure 2.2. Scanning electron microscopy (SEM) images of minerals observed in the plumage of *Anchiornis huxleyi*. (A), (B) thin platelets of phyllosilicates observed in sample 7 (see Fig. 2.1 for location); scale bar = 5 µm (A) and 3 µm (B), (C) Pyrite framboids (sample 1); scale bar = 10 µm, (D) Pyrite crystallites (sample 1); scale bar = 5 µm, (E) Clayed pores containing small star-shaped iron-oxide crystals (sample 8); scale bar = 2 µm, (F) Star-shaped iron oxides (sample 1); scale bar = 2 µm, (G) Feldspar crystal surrounded by clay sheets (sample 5); scale bar = 5 µm, (H) Quartz crystals embedded in a clayed matrix (sample 9); scale bar = 5 µm.

4. Results and discussion

4.1. Micromorphology, elemental and mineralogical composition

SEM of the fossil feathers reveals they are embedded in a sedimentary matrix containing mainly quartz, carbonates, and phyllosilicates. The latter are organised in thin platelets oriented parallel to each other (Fig. 2.2A, B). A feather sample from the right wing of *Anchiornis* (sample 1 on Fig. 2.1) showed abundant rounded crystals that are present only beneath the feather surface. They occur mainly as framboids (Fig. 2.2C), but also as individual microcrystallites (Fig. 2.2D) and, in some cases, are associated with voids. Framboids are spheroidal or ovoid, 6-9 µm in diameter, and contain dozens of < 1 µm euhedral crystals. In contrast, individual cubic crystals are much smaller (about 500 nm^3) and contain micro-crystallites. EDS analyses indicate that the sediment is composed mostly of Fe and Si, with less O, Al, C, Ca (and less Mn, K, Mg), probably indicating a dominant mineralogy of silica (quartz), calcite, and various phyllosilicates. XRD analyses confirmed the presence of these minerals in the sediment (Fig. 2.3A). In addition, the XRD spectrum of the < 2 µm phase shows that expandable material, such as illite and interstratified illite/smectite, is present in the sediment (Fig. 2.3B). Due to the characteristic framboidal shape and the elemental composition of the crystal clusters observed beneath the fossil feather surface, they are attributed to diagenetic iron oxides or hydroxides. Indeed, although the framboidal habit is common for iron sulfides, the lack of sulfur here shows they are rather iron oxide pseudomorphs probably resulting from the *in situ* weathering of pyrite framboids (Blanco et al., 2013; Kaye et al., 2008; Nordstrom, 1982; Wang et al., 2012). These structures are associated with thin clay overgrowths, indicating that the iron oxides (or the preceding pyrites) precipitated first (Figs. 2.2C, E). Tiny star-shaped minerals, probably iron oxides, were observed and detected by X-ray spectroscopy (Fig. 2.2F), although the relatively large ion beam diameter does not allow the determination of their accurate elemental composition. Calcium carbonates, feldspars (Fig. 2.2G) and quartz (Fig. 2.2H) are also present in the sedimentary matrix.

Elongate microbodies, 650 to 950 µm, and their associated moulds were observed in three samples (6, 9, and 12, on Fig. 2.1) collected from the anterior and posterior parts of the tail (see Fig. 2.4, A-D). Microbody imprints are abundant, tightly packed together and randomly oriented (Figs. 2.4A, B). The microbodies and their imprints likely represent traces of melanosomes, similar microbodies have previously been observed in feathers from the crest of *Anchiornis* (Lindgren et al., 2015). Here, isolated elongated structures were also observed (Fig. 2.4C). These fossil organelles are preserved within the thin clay-rich sediment. Elemental mapping and EDS analyses of a region containing both 3D melanosomes and moulds revealed that carbon is enriched in the 3D melanosomes relative to the embedding sediment (Fig. 2.5A, B).

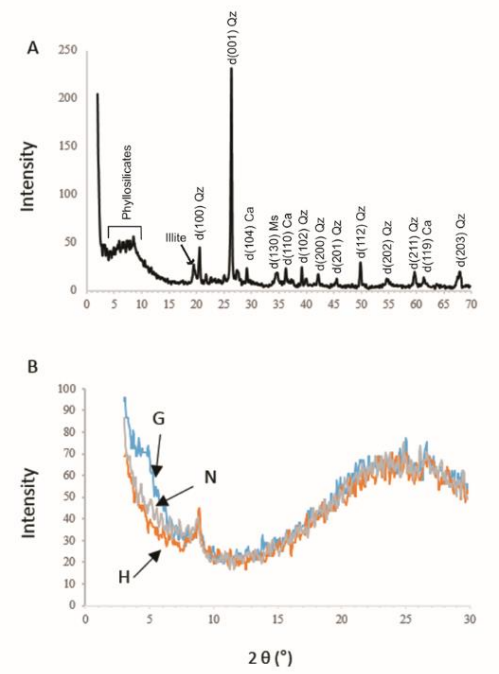

Figure 2.3. X-ray powder diffraction patterns of the embedding sediment. Spectrum of (A) the bulk rock; qz, quartz; ca, calcite, (B) the fraction < 2 µm, with spectra of natural (N), glycolated (G), and heated (H) sample.

4.2. Depth profiling, light and heavy element composition

The great virtue of EBS is to be capable of yielding elemental depth profiles non-destructively from the outermost microns of the sample with good sensitivity and depth resolution (Jeynes & Colaux, 2016). A typical EBS spectrum obtained from the fossil feather is shown in Supplementary Figure S2.2 together with its best fit. Inversion of the experimental spectrum recovers the elemental depth profiles (examples are shown for carbon in Supplementary Fig. S2.3). Integration of these elemental depth profiles allows derivation of the concentration of each element at a given depth. Figure 2.6A clearly shows that the carbon enrichment in the near surface region decreases at increasing distances from the fossil feather, reaching a minimum in the "remote" sediment sample. Concentrations of oxygen and silicon (although less obvious) follow an opposite trend. This result strongly suggests that the fossil feather is preserved as a carbonaceous layer located at the uppermost part of the sample (i.e., 0–3 µm depth given a density of 2.65 g/cm³) and suggests that fossil organic matter could have impregnated the sediment only in a nearby area. It should be noted that the

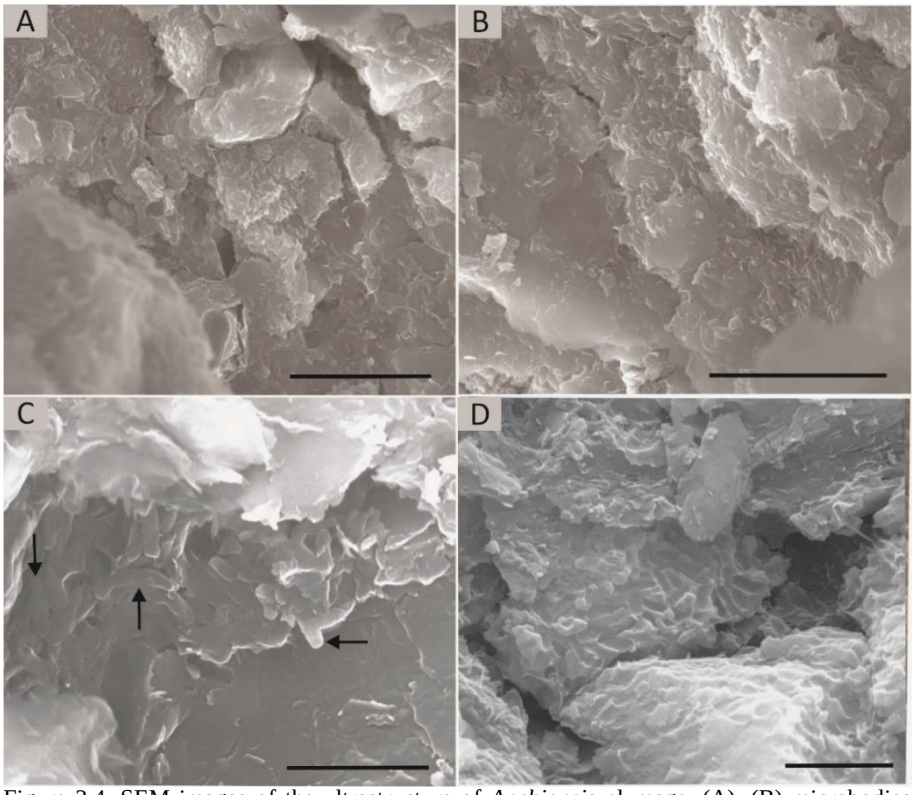

Figure 2.4. SEM images of the ultrastructure of *Anchiornis* plumage. (A), (B) microbodies imprints observed in sample 6 (see Fig. 2.1 for location), (C) Elongated microbodies (arrows), and (D) imprints observed in samples 9 (C) and 12 (D). Scale bars: (A) and (B) 10 µm, (C) 2 µm, (D) 2.5 µm.

nitrogen concent is not discussed here, because its very low content rendered its determination uncertain. The ca. 5 at.% of N required to satisfactorily fit the experimental EBS spectrum were not attained in the fossil feathers, whereas there was no indication of N at all in the "remote" sediment sample.In contrast, EBS analysis of modern buzzard feathers shows homogeneous concentrations of elements with depth (data not shown). Carbon content in the buzzard feathers is about 60 at.%, while nitrogen and oxygen are both around 20 at.% for the rachis and ca. 25 and 15 at.%, respectively, for the barbs. Typical PIXE spectra acquired from the fossil feather, host sediment and "remote" sediment are shown in Figure 2.6B. The samples differ in the amount of several elements present. Of particular interest is the sulfur content. An interrelation between sulfur and carbon is also highlighted (Table 2.1). Concentrations of sulfur measured in the fossil feathers ($1.8 \pm 0.2 \times 10^3$ wt. ppm) and, to a lesser extent, in the host sediment ($1.0 \pm 0.1 \times 10^3$ wt. ppm), together with its minor presence in the "remote" sediment ($0.98 \pm 0.04 \times 10^3$ wt. ppm) suggest that S is associated with the soft tissues. The results obtained are given in Table 2.1 and the details on the global uncertainty calculations can be found in Supplementary Table 2.1.

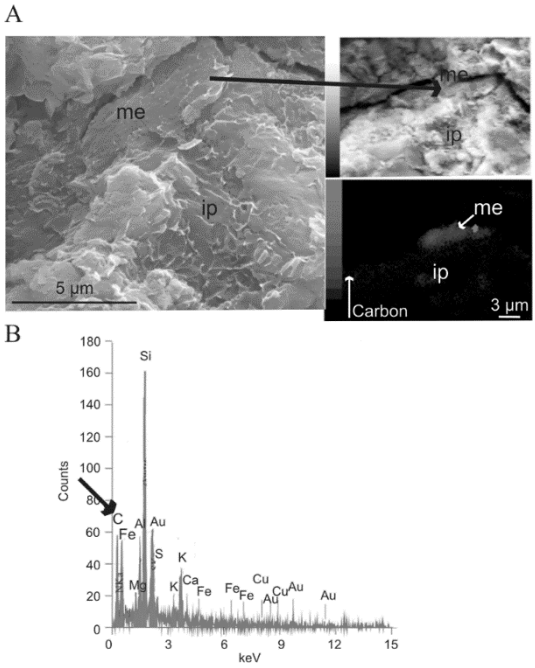

Figure 2.5. Elemental composition of the melanosomes and the embedding sediment. (A) SEM image of a zone including both elongated melanosomes (me) and imprints (ip). The top left map displays the zone where the mapping was performed. The map on the bottom left shows the abundance of carbon in the same area. (B) EDS spectrum at the point located in the area containing the elongated melanosomes.

Substantial quantities of sulfur have are present in the modern feathers (40.1 ± 4.0 x 10^3 wt. ppm, Table 2.1) and may originate from sulfur-containing biomolecules, such as amino acids or the pigment phaeomelanin (Bortolotti, 2010; Cesarini, 1996; Harrap & Woods, 1964; Murphy et al., 1990; Riley, 1997; Saravanan & Dhurai, 2012). A phaeomelanin origin for the sulfur in the fossil feathers is not discussed here, since the detection of phaeomelanin requires other analytical techniques (e.g., Colleary et al., 2015; Lindgren et al., 2015). Only elongate rod-shaped melanosomes (eumelanosomes) were identified here (Lindgren et al., 2015; and references herein). Alternatively, the presence of sulfur in the fossil feathers, can be attributed to its abiogenic incorporation from the depositional environment (Sinninghe-Damsté & De Leeuw, 1990; Sinninghe-Damsté et al., 1989; Sinninghe-Damsté et al., 1988; McNamara et al., 2016). Organic matter has the ability to form complexes with inorganic elements, which can be traced in fossil soft tissues (e.g., Gueriau & Bertrand, 2015; Manning et al., 2013; Wogelius et al., 2011).Various ways of incorporating metals and other trace elements in sedimentary organic matter during

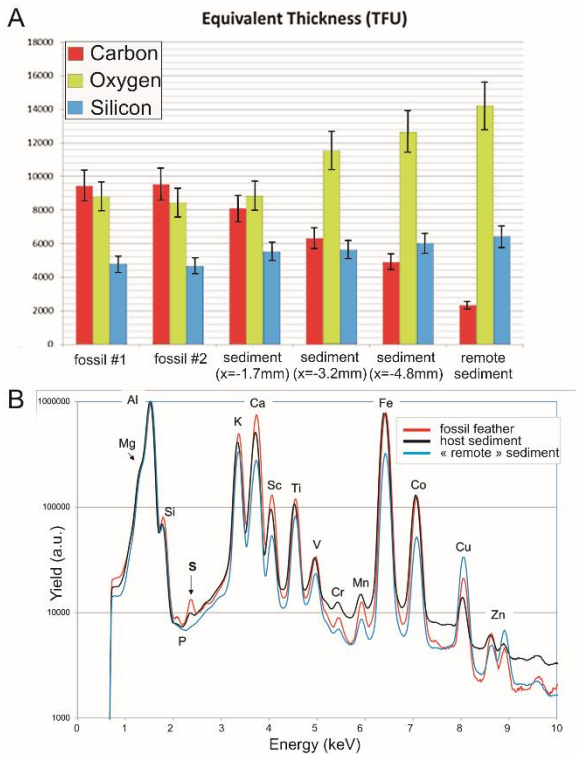

Figure 2.6. Results of Elastic Backscattering Spectrometry (EBS) and Particle-Induced X-ray Emission (PIXE) analyses on the fossil feathers, the host sediment and the "remote" sediment. (A) Total content of C, O and Si obtained by EBS by integrating the C, O and Si depth profiles over the 0 – 25 000 TFU interval. (B) PIXE spectra obtained for one point of analysis in the fossil feather (red), the embedding sediment (black), and the remote sediment (blue). The spectra are normalised to the Al signal (which is mainly coming from the selective filter) to allow for a direct comparison.

early diagenesis exist and include complexation with dissolved organic ligands, adsorption, and chemical precipitation (Davis, 1984).

4.3. Functional groups in the organic matter

The ^{13}C CP-MAS NMR spectrum of buzzard feathers (Fig. 2.7A) shows well-resolved peaks between 10 and 65 ppm corresponding to aliphatic carbon and a narrow peak at 173 ppm, due to carboxylic carbon. Two additional, less intense, signals can be seen at 129 ppm and 158 ppm. On the whole, this spectrum appears quite similar to that of several keratinous materials, such as feather keratin (Barone et al., 2005; Kricheldorf & Müller, 1984), wool keratin (Yoshimizu & Ando, 1990) or gecko setae keratin (Jain et al., 2015). It also shares some similarities with various types of melanins (Adhyaru et al., 2003; Duff et al., 1988).

Table 2.1. PIXE-derived concentrations data for S and C in fossil and modern feathers, and sediments. See Supplementary Table S2.1 for details on the global uncertainty calculations.

	[S] (wt. ppm)	[C] (wt.ppm)
Fossil Feather #1	1739	80,385
Fossil Feather #2	1946	82,171
+1.6 mm	1162	72,012
+3.2 mm	801	49,213
+4.8 mm	893	41,835
Remote sediment	98	20,331
Rachis	37,142	547,174
Barbs	43,070	314,962

Indeed, the carboxylic peak should mainly correspond to the signal of amides (O=C-N) groups involved in the peptidic bonds. Carbon atoms bearing both COOH and NH_2 groups (termed C_α) in the amino acids (except glycine) resonate between 50 and 60 ppm. They account for the peaks at 52.9 and 60.2 ppm in the broad aliphatic signal, whereas that at 42.6 ppm is assigned to the C_α of glycine. The other peaks are mainly associated with the amino acid side chains, with that at 30.8 ppm being assigned to C_β along with C in long alkyl chains, and those at 19.8 and 25.7 ppm to C_γ and C_δ. The 129 ppm peak is typical for aromatic carbons, including those from phenylalanine and tyrosine (Jain et al., 2015; Yoshimizu & Ando, 1990). Finally, the peak at 158 ppm can be ascribed to the O-alkyl C of tyrosine and/or the C of the guanidino group (N-C=N) of arginine (Jain et al., 2015; Yoshimizu & Ando, 1990). This spectrum is in agreement with previous reports indicating that keratin is a major constituent of feathers (Lucas & Stettenheim, 1972c). In comparison to the spectrum of modern feathers, the ^{13}C NMR spectra of the fossil feathers and their surrounding sediment show much simpler patterns (Fig. 2.7B, C). The spectra are similar to each other and both are dominated by a broad peak in the aliphatic region, maximizing at 30 ppm and thus indicative of long alkyl chains. Two additional broad signals contribute to the spectra. The first one occurs as a broad shoulder between 68 and 80 ppm, in the O-alkyl C and N-alkyl C range, and the second one is a broad peak at 129 ppm, in the aromatic carbon region. When compared to the spectrum of the modern feather, the aliphatic signal is poorly resolved; the aromatic peak is broad and no resonance could be detected in the carboxylic region. These features indicate that the proteinaceous contribution identified in the buzzard feather is no longer present in the fossil sample.

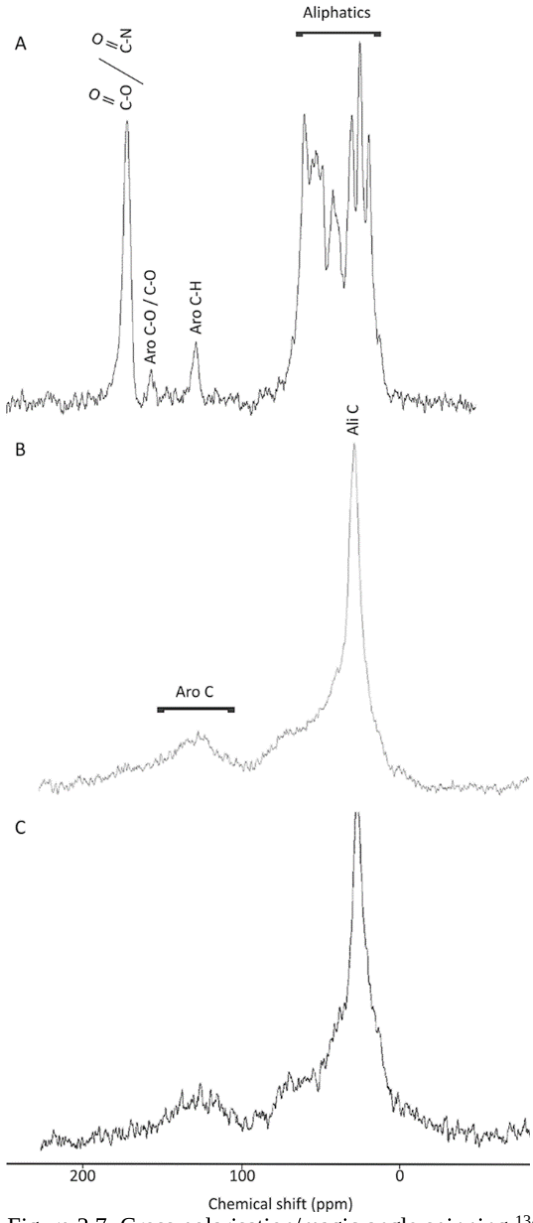

Figure 2.7. Cross polarisation/magic angle spinning ^{13}C nuclear magnetic resonance (CP-MAS ^{13}C-NMR) spectra of (A) the modern bird feather, (B) the fossil feathers, and (C) the host sediment. Major functional groups are indicated on each peak.

However, a more precise comparison can be achieved at the molecular level thanks to pyrolysis in the presence of TMAH coupled with GC-MS.

4.3. Molecular building blocks of organic matter

Pyrochromatograms (TMAH Py-GC-MS) were obtained for the three following samples: the modern and fossil feathers, and the embedding sediment. The pyrochromatogram of the modern feather is dominated by cyclic molecules containing nitrogen, along with toluene **1**, methylbutanenitriles **2, 3** and cyclohexanedione derivatives **11** (Fig. 2.8A). The major pyrolysis products are listed in Table 2.2 and their molecular structures can be seen in the Appendices "A2". Products **6**, **8**, **10** from direct methylation of alanine, valine and proline confirm the proteinaceous origin for the feathers. This is further supported by the occurrence in substantial amounts of alkylnitriles **2**, **3** resulting from decarboxylation of isoleucine and leucine, and of methoxybenzenes **7**, **9** released through homolysis of the side chain of tyrosine. Toluene **1**, pyrrole **4** and ethylbenzene **5** are rather ubiquitous compounds in sedimentary organic matter. However, they can also be released upon pyrolysis of phenylalanine and serine (Gallois et al., 2007). Mass spectral fragmentation patterns (base peak at m/z 82) suggest an origin from the side chain of histidine for compound **16**. Similarly, compound **17** probably corresponds to a valine derivative as its mass spectrum is characterized by the loss of 42 amu (i.e., valine side chain). Dimethylcyclohexanedione **11** was reported as pyrolysis product of glycine (Moldoveanu, 2009). Glycine is also present as its diketopiperazine **15** resulting from combined dehydration and cyclisation (Simmonds et al., 1972). The same mechanism involving two different amino acids (isoleucine-glycine) leads to another diketopiperazine **18** (Hendricker & Voorhees, 1996). The formation of more complex diketopiperazines was proposed by Templier et al. (2013) from tripeptide units. Similar mechanism can be invoked for the formation of compound **19** from valine, as well as compounds **20** and **21** from serine and leucine (Table 2.2, and Supplementary Fig. S2.4). Imidazolidinedione **12** probably results from the internal cyclisation of tripeptide comprising an alanine unit as reported by Templier et al. (2013) (Supplementary Fig. S2.4). The formation of imidazolidinone **13** can be related to the decomposition of bicyclic amidine derived from valine (Basiuk & Navarro-González, 1997) as suggested by Templier et al. (2013) (Supplementary Fig. S2.4). Another decomposition pathway of bicyclic amidine is probably responsible for the formation of imidazolidinone **14** from valine and possibly glycine (Templier et al., 2013).

TMAH py-GC-MS analysis of modern feathers thus highlights the presence of glycine, serine, leucine, alanine, valine and proline moieties in buzzard feather keratin, in agreement with previous studies on feather keratin (Fig. 2.8A; Arai et al., 1983, 1986; Murphy et al., 1990; O'Donnell & Inglis, 1974; Saravanan & Dhurai, 2012; Staroń et al., 2011). Additionally, pyrolysis products derived from isoleucine, phenylalanine and tyrosine occurred in substantial amounts although they are often considered as minor constituents of feather keratin. However, homolysis of the side chain of phenylalanine and tyrosine favors high yields in TMAH pyrolysis (Gallois et al., 2007). Despite its acknowledged high abundance in feather keratin, cysteine is

absent in the pyrochromatogram of buzzard feather, probably because it mainly releases H_2S upon pyrolysis (Moldoveanu, 2009) not detected in the presently used analytical conditions.

By comparison, pyrochromatograms of the fossil feathers and their embedding sediment are simpler. They are dominated by *n*-alkane/*n*-alkene doublets (Fig. 2.8B,C), resulting from the homolytic cleavage of long alkyl chains. In the fossil feathers, these doublets comprise from 8 to 30 carbon atoms, and exhibit a smooth distribution except intense C_{18} doublet. An additional series of fatty acid methyl esters with alkyl chain ranging from C_8 to C_{30} and maximising at C_{16} is also identified (Table 2.2). It results from the release upon pyrolysis of a series of fatty acids that is methylated thanks to TMAH. In addition to these series, a methoxybenzene substituted by two methyl groups or an ethyl group **22** is detected in minor amounts at the beginning of the pyrochromatogram. Its origin can be attributed either to polysaccharides such as cellulose or to lignin, depending on its substitution pattern (Choi et al., 2013; Seitz & Ram, 2000). A trimethylbenzene and a methylated derivative of methoxyaniline **23** also contribute to this part of the pyrochromatogram. However, the most prominent pyrolysis products **24** corresponds to the C_{18} alcohol methylated through TMAH pyrolysis.

The pyrochromatogram of the embedding sediment shares several similarities with that of the fossil feathers. It is dominated by series of alkane/alkene doublets and fatty acid methyl esters. Although the distribution of the fatty acid methyl esters is similar in both samples, that of the doublets differs. Indeed, although their range (C_8 – C_{30}) is similar, the maximum of the series appears at C_{15} in the sediment instead of a marked predominance of C_{18} in the fossil (Table 2.2). Moreover, when comparing the minor compounds eluting at the beginning of the pyrochromatogram, compounds **22** and **23** are common in both samples, whereas a higher number of homologues of alkylbenzenes occurs in the sediment. However, the most striking difference is the much weaker abundance of octadecanol **24** in the sediment spectrum. Taken together, these differences clearly show that even though some imprint from the sediment may have contributed to the fossil feather pyrolysate, at least some features are typical for the fossil feathers. They notably include the C_{18} doublet and octadecanol **24**.

The predominance of the alkane/alkene doublets in the pyrolysate is in agreement with the strong aliphatic signal observed in NMR (Fig. 2.7). A similar highly aliphatic character has been reported in preserved soft tissues from other fossil organisms, such as in cuticles from Carboniferous arthropods (Baas et al., 1995; Stankiewicz et al., 1998), skin from a Cretaceous mummified hadrosaur (Manning et al., 2009b), and Cretaceous fish scales (Gupta et al., 2008). C_1 to C_3 alkylbenzenes were also identified in pyrolysates of Oligocene weevil and tadpole, and associated matrix (Barden et al., 2015; Gupta et al., 2007a).

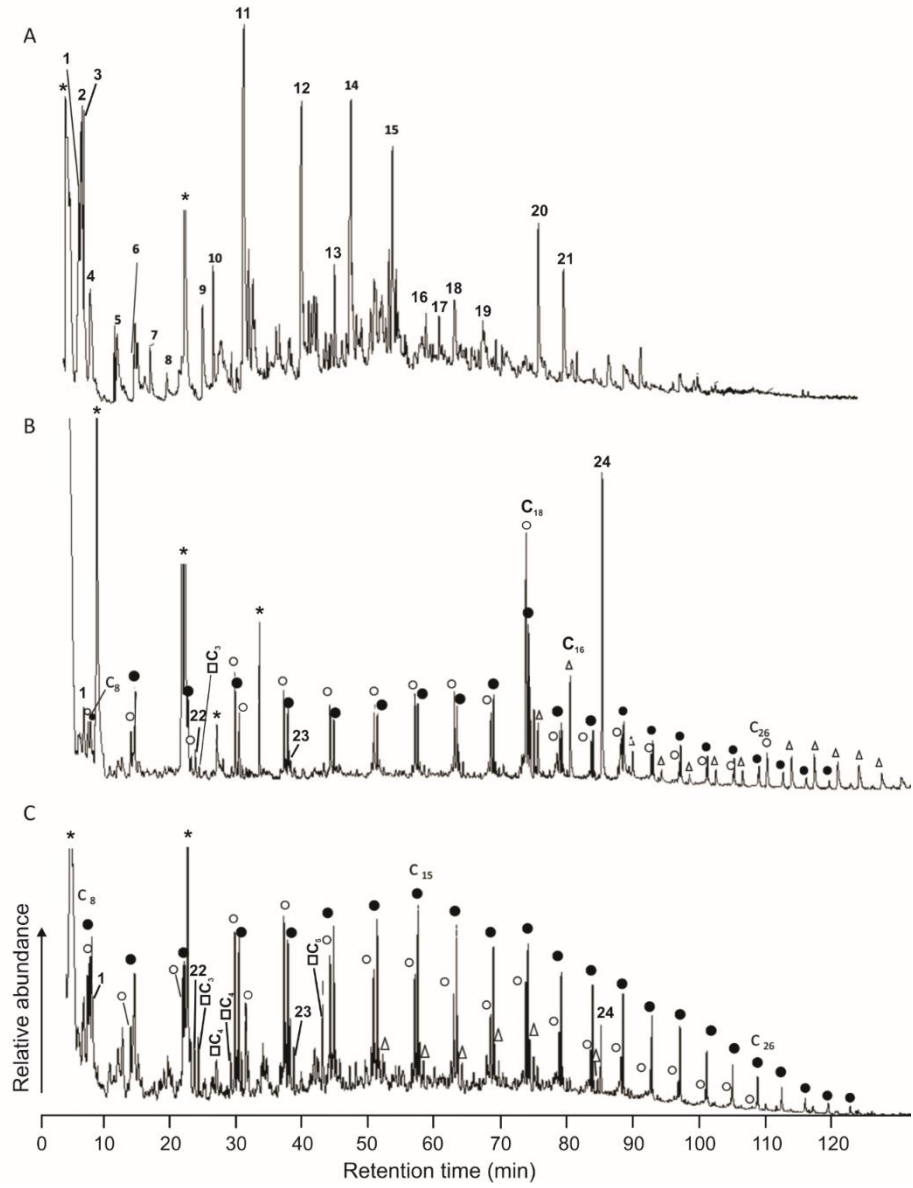

Figure 2.8. Chromatograms of the products formed during the pyrolysis of (A) modern buzzard feathers, (B) fossil feathers, and (C) remote sediment. Peak identifications are given in Table 2.2. C_n: carbon chain, with n indicating the length of the chain; ●, *n*-alkanes; ○, *n*-alkenes; Δ, fatty acid methyl esters; □, alkyl benzenes, *, TMAH and column phase derivatives.

The aliphatic series dominating the pyrolysate of the fossil feathers likely reflect either selective preservation of macromolecular aliphatic matter preexisting in the extant organism (Tegelaar et al., 1989) or *in situ* polymerisation of aliphatic lipids

(Gupta et al., 2007a; Stankiewicz et al., 2000). No aliphatic series could be detected in the pyrolysate of modern feathers, likely precluding the first hypothesis. In contrast, several aliphatic series were identified in the lipid extract of the modern feathers (*n*-alkanes, *n*-acids, *n*-alcohols; data not shown); they thus constitute potential precursors for the aforementioned aliphatic moieties of the fossil organic matter. The absence of signal typical for proteinaceous material in both NMR spectra and pyrochromatogram of the fossil feathers is noteworthy. In agreement with the commonly accepted lability of proteins, this feature likely indicates their extensive degradation upon diagenesis. It must be noted that similar diagenetic degradation of proteinaceous moieties were previously put forward for Paleozoic annelid fossils (Dutta et al., 2010).

Although PIXE analyses showed that carbon and sulfur are closely associated in the fossil feathers, no organosulfur compounds could be detected in the pyrolysate. This may be due to diagenetic conditions that prevented sulfuration of organic matter via intra-molecular incorporation of sulfur. The occurrence of iron oxides or hydroxides as framboid crystals (SEM and EDX characterisation) suggests sulfur may have been preferentially used for the formation of iron sulfides (such as pyrite) during early diagenesis (Sinninghe-Damsté & De Leeuw, 1990). During later diagenesis, pyrite framboids were probably *in situ* weathered into the iron oxides and hydroxides observed beneath the carbonaceous surface of feathers, thus releasing sulfur that may have further associated with organic compounds. Such associations may have favoured/enhanced organic matter preservation and are consistent with the interrelation between sulfur and carbon highlighted by PIXE analyses.

Table 2.2. Main products released from pyrolysis of modern feathers, fossil feathers and embedding sediment in the presence of TMAH.

Peak	RT (min)	Major characteristic ions[a] (m/z)	Mole-cular ion	Compound	Possible origin[b]	Modern feather	Fossil feather[c]	Host sediment[c]
1	6.7	91; 92; 39; 65	92	Toluene	(Phe)	X	X	X
2	6.9	55, 54, 42	83	Butanenitrile, 2-methyl	Ileu	X		
3	7,1	43, 41, 39, 68	83	Butanenitrile, 3-methyl	Leu	X		
4	8.0	67; 41; 39; 40	67	Pyrrole	(Ser)	X		
5	12.1	91; 55; 106; 65	106	Benzene, ethyl	(Phe)	X		
6	14.8	72; 42; 56; 131	131	N,N- Dimethylalanine methylester	Ala	X		
7	17.0	108; 78; 65; 39	108	Benzene, methoxy-	Tyr	X		
8	19.5	86; 102; 42; 55	145	N-Methylvaline methyl ester	Val	X		
9	25.0	122; 77; 107; 91	122	Benzene, 1-methoxy-4-methyl	Tyr	X		
10	26.5	84; 42; 100; 58	143	N-Methylproline methyl ester	Pro	X		
11	31.2	56; 140; 42; 112	140	Cyclohexane-1,4-dione, dimethyl	Gly	X		
12	39.7	42; 127; 142; 56	142	Imidazolidinedione, trimethyl	Ala?	X		
13	44.8	56; 126; 139; 41	182	Imidazolinone, isobutyl, isopropyl	Val	X		
14	47.2	128; 42; 71; 113	170	Imidazolidinone, trimethyl, isopropyl	Val-(Gly)	X		
15	53.6	128; 42; 57; 71	128	Piperazine-2,5-dione, methyl	Gly	X		
16	58.6	82; 167; 182; 110	182	?	His?	X		
17	60.5	152; 41; 55; 137	194	?	Val?	X		

18	62.9	142; 113; 42; 71	198	Piperazine-2,5-dione, 1-methyl, 3-(1-methylpropyl)	Ileu-Gly	X		
19	67.1	142; 113; 42; 98	?	Piperazine-2,5-dione, N-(1-oxo-2-amino-3-methyl-butyl) derivative	Val	X		
20	75.5	139; 70; 42; 168	210	Piperazine-2,5-dione, N-methyl, 3-methylidene, 6-(3-methylbutyl)	Ser-Leu	X		
21	79.2	168; 139; 70; 42	210	Isomer of compound 20	Ser-Leu	X		
22	23.7	136, 121, 122, 91	136	Methoxybenzene, ethyl or dimethyl	Lignin or cellulose		X	X
23	38.1	136, 122, 137	137	Aniline, methoxy, methyl	?		X	X
24	86.3	45; 57; 97; 224	284	Octadecane, 1-methoxy	?		X	X
●		43; 57; 71; 85		*n*-alkanes	Aliphatic chains		C_8-C_{30} (C_{18}, C_{11})	C_8-C_{29} (C_{15})
○		55; 43; 69; 83		*n*-alk-1-enes	Aliphatic chains		C_8-C_{26} (C_{11}, C_{18})	C_8-C_{29} (C_{11}, C_{18})
Δ		87; 74; 43; 55		Fatty acid, methyl esters	Aliphatic chains		C_8-C_{30} (C_{16})	C_8-C_{30} (C_{16})
□		91, 105		Alkyl benzenes	?		C_3	C_3-C_5 (C_5)

[a] MS fragments are in order of decreasing abundance, with base peak underlined.

[b] Compounds in brackets indicate possible origin that is not univocal; Ala, alanine; Gly, glycine; His, histidine; Phe, phenylalanine; Pro, proline; Ser, serine; Tyr, tyrosine; Val, valine; ? Tentative origin

[c] C_{range} (C_{max}, C_{submax})

RT = retention time

5. Conclusions

The methods used in this study provide new and complementary information about how the plumage of *Anchiornis huxleyi* (YFGP-T5199) is preserved. SEM and EDS reveal that fossil feathers are preserved in a fine-grained material constituted of K-rich phyllosilicates, illite and interstratified illite/smectite. EBS and PIXE analyses show that both light (C, N, O) and heavy (S, Na, Ca, etc.) elements are present in the fossil samples, even at very low concentrations. Carbon is the dominant element in the fossil feathers; they are also enriched in sulfur with respect to their host sediment. EBS mapping of the interior of samples revealed a number of distinct layers that decrease in carbon concentration with depth. As a result, the feathers are preserved in the uppermost part of the sample as a thin carbon-rich layer. High resolution imaging of the feather microstructure revealed the presence of elongated (650-950 nm) carbonaceous microbodies; they likely correspond to melanosomes. Molecular characterisation (^{13}C NMR and Py-GC-MS) of the organic matter in the host sediment, fossil feathers and modern feathers shows that the fossil does not displays the complex amino-acid signature typical for keratin, the main constituent of modern feathers. Although the organic matter of the fossil feathers and their embedding sediment are both dominated by aliphatic moieties, they exhibit substantial differences (distribution pattern of series, occurrence of components specific to the feathers) suggesting that the organic matter of the fossil feathers is derived, at least partially, from original constituents of the feathers.

Altogether, these results show that the fossil feathers can be unequivocally described as compression fossils, as described in Schweitzer, (2011: p. 192). The finely grained (clay-rich) embedding sediment contributed to the morphological preservation of *Anchiornis* soft tissues. As stressed by Schweitzer, (2011: p. 192), the fine grain size of the sediments probably prevents degradation of soft-tissues by microbes, and subsequent loss of degraded organic matter in the environment before and during diagenesis. However, the lack of protein-derived moieties in the fossil organic matter shows that the latter had been significantly altered during diagenesis. The excellent morphological preservation of the fossil soft tissue is not associated here with a high preservation level of organic matter. Hence, the fossil feather had likely undergone a complex diagenetic history including several steps affecting differentially their morphology and chemistry. *In situ* polymerisation of lipids was likely the main process responsible for organic matter preservation in the fossil feather. Additionally, sulfur incorporation probably played a role in several steps of the fossil preservation. This integrative multidisciplinary study thus appears as a powerful approach to decipher morphological, mineralogical, structural and chemical features of fossil soft tissues and their fossilisation processes.

Supplementary information for "Chemical taphonomy of morphologically well-preserved dinosaur feathers: a multi-technique approach"

	[S] (wt. ppm)	Global Uncertainty (wt. ppm)	Counting Statistics (%)	Fit Error (%)	Uncertainty from BCR-126A analysis (%)	Uncertainty on cross-sections (%)	Global Uncertainty (%)
Fossil Feather #1	1739	221	4.4	6.8	9.8	5	13.7
Fossil Feather #2	1946	196	1.2	1.9	9.8	5	11.2
+1.6 mm	1162	143	4.3	6.1	9.8	5	13.3
+3.2 mm	801	82	1.8	2.5	9.8	5	11.4
+4.8 mm	893	107	4	5.7	9.8	5	13.0
Remote sediment	98	35	19.2	25.6	9.8	5	33.8
Rachis	37,142	3652	0.2	0.4	9.8	5	11.0
Barbs	43,070	4236	0.2	0.5	9.8	5	11.0

Supplementary Table S2.1. Details of the global uncertainty calculations for sulphur concentration in the fossil feathers (duplicate analysis), embedding sediment (three successive analysis spots at 1.6, 3.2, and 4.8 mm away from the fossil feathers), remote sediment, and modern bird feathers (barbs and rachis)

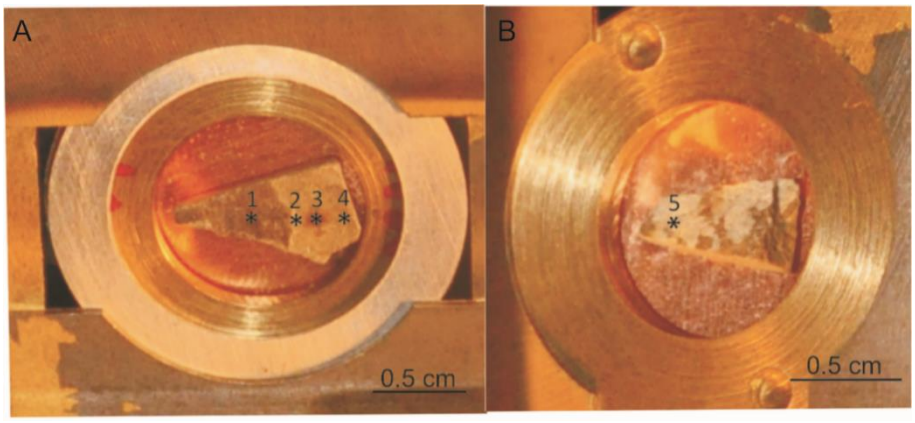

.**Supplementary Figure S2.1**. Samples mounted on a copper tape for IBA analyses. (A) fossil feather (dark brown area, on the left) and embedding sediment (light area, on the right); the four analysis points are shown by the black asterisks. (B) remote sediment. Correspondence with Figure 2.5 in the text is as follows: 1, fossil #1 and fossil #2; 2, sediment (x = -1.7 mm); 3, sediment (x = -3.2 mm); 4, sediment (x = -4.8 mm); 5, remote sediment

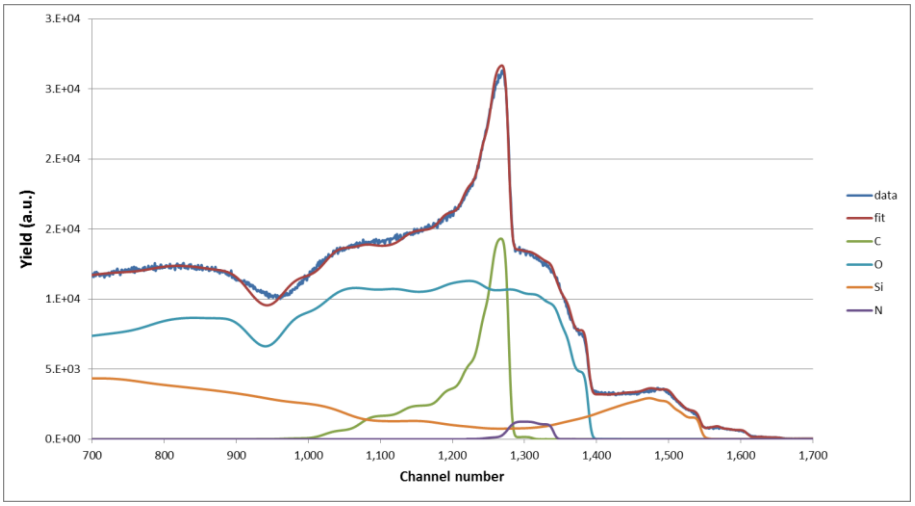

Supplementary Figure S2.2. Experimental (dark blue) and fitted (red) EBS curves acquired from the fossil feather during about 4 hours. The channel number is directly proportional to the energy of the backscattered protons. Knowing the stopping power of the sample (i.e. energy loss per quantity of material passed through by a particle), the abscissa can readily be converted into depth scale, going from the surface (high channel numbers) to the bulk (lower channel numbers).
Partial spectra for C (green), O (light blue), Si (orange) and N (purple) are also represented to highlight the large carbon gradient with the highest concentration near

the surface rapidly decreasing into depth. Note that the nitrogen signal is rather weak but the experimental curve could not be properly fitted without its contribution. Using DataFurnace, one can invert the experimental spectrum to recover the elemental depth profile.

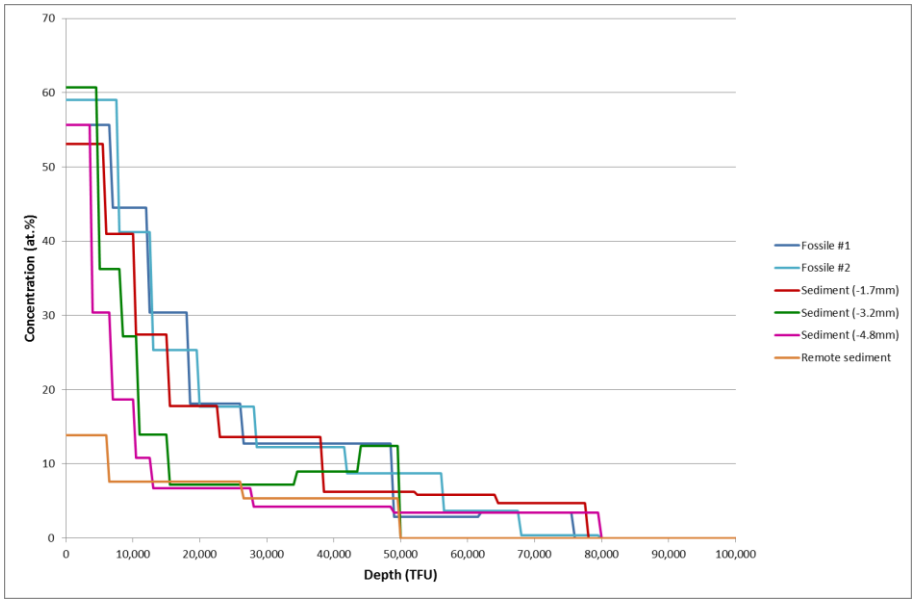

Supplementary Figure S2.3. Carbon depth profiles obtained by fitting the experimental EBS spectra acquired from different locations on the fossil (see Fig. S2.1) with DataFurnace. The abscissa is given in Thin Film Unit (TFU or 10^{15}atoms/cm²). TFUs are density-independent thickness units, equivalent to mass/area, which can be converted to nanometric depth providing that the density of the analyzed material is known. Fossil #2 is a straight repeat of Fossil #1, demonstrating the reliability of the EBS technique for deriving the C elemental depth profiles. One can observe that the carbon enrichment in the near surface region is decreasing when stepping away from the fossil feather. Carbon content is significantly lower in the remote sediment.

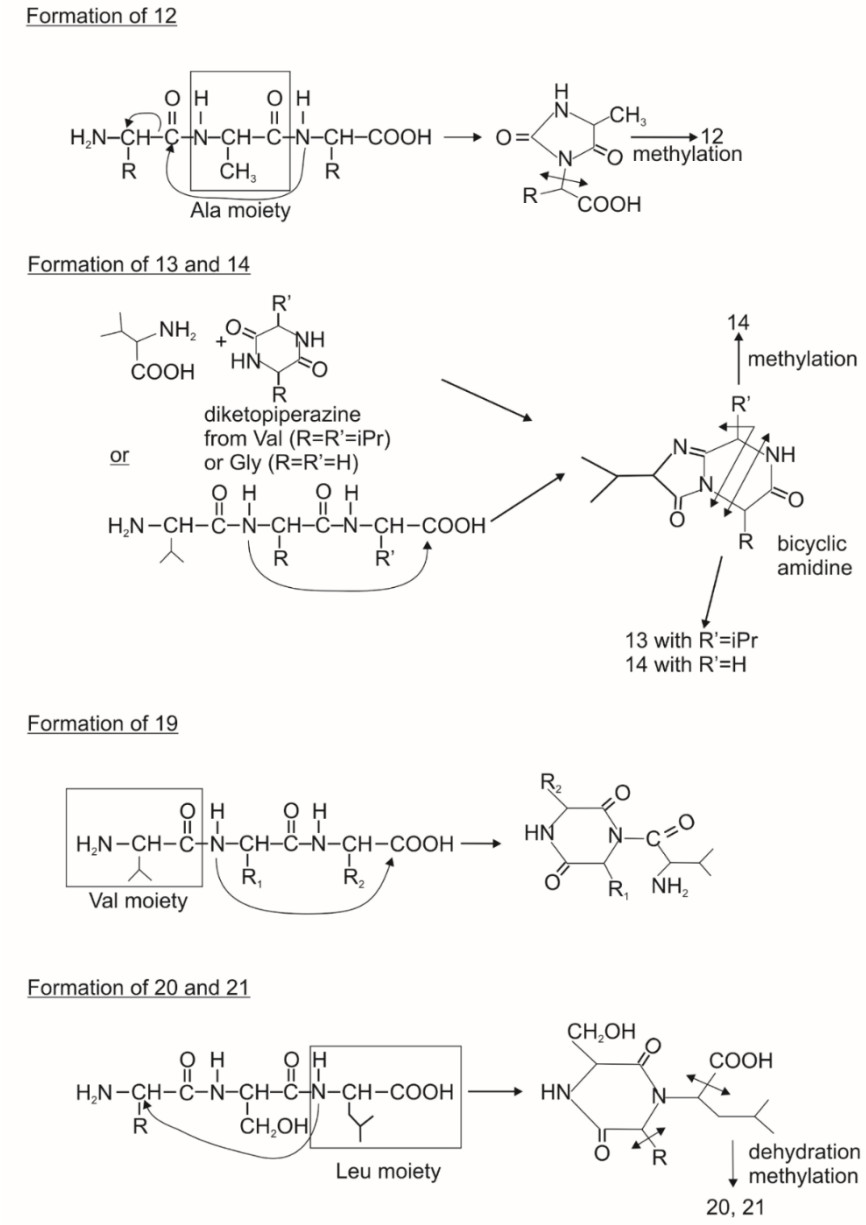

Supplementary Figure S2.4. Formation mechanisms of diverse compounds obtained by pyrolysis of modern bird feathers in the presence of TMAH.

Chapter 3

Modified after Lefèvre et al. (2017), *published in The Science of Nature*

A new Jurassic theropod from China documents a transitional step in the macrostructure of feathers

As a co-author of this publication, I have participated in the analysis of the ultrastructure of feathers from this new taxon of theropod dinosaur by SEM. I additionally analysed the mineralogical composition of the feathers and host sediment (SEM/EDS).

Abstract

Genuine fossils with exquisitely-preserved plumage from the Late Jurassic and Early Cretaceous of north-eastern China have recently revealed that bird-like theropod dinosaurs had long pennaceous feathers along their hindlimbs and may have used their four wings to glide or fly. Thus, it has been postulated that early bird flight might initially have involved four wings (Han et al., 2014; Hu et al., 2009; Xu et al., 2003). Here, we describe *Serikornis sungei* gen. et sp. nov., a new feathered theropod from the Tiaojishan Formation (Late Jurassic) of Liaoning Province, China. Its skeletal morphology suggests a ground-dwelling ecology with no flying adaptations. Our phylogenetic analysis places *Serikornis*, together with other Late Jurassic paravians from China, as a basal paravians, outside the Eumaniraptora clade. The tail of *Serikornis* is covered proximally by filaments and distally by slender rectrices. Thin symmetrical remiges lacking barbules are attached along its forelimbs and elongate hindlimb feathers extend up to its toes, suggesting that hindlimb remiges evolved in ground-dwelling maniraptorans before being co-opted to an arboreal lifestyle or flight.

1. Introduction

The Late Jurassic-Early Cretaceous formations of north-eastern China are well known for the extraordinary abundance and diversity, and the exceptional preservation of feathered dinosaurs that shed light on the origin and early diversification of birds (Han et al., 2014). Several small non-avian paravians (e.g., *Microraptor*, *Pedopenna*, *Anchiornis*, *Changyuraptor*, *Xiaotingia*, *Jianianhualong*) are characterised by long pennaceous feathers attached to both their tibia and metatarsus, suggesting that early bird flight might initially have involved four wings (Han et al., 2014; Hu et al., 2009; Xu et al., 2017; Xu & Zhang, 2005; Xu et al., 2003). However, because deinonychosaurian theropods and earliest birds show a similar distribution of long pennaceous feathers along their forelimbs, hindlimbs and tail, and because different hypotheses of paravian phylogenies have recently been proposed (Godefroit et al., 2013a; Godefroit et al., 2013b; Hu et al., 2009; Xu et al., 2011), the origin and early evolution of feather-based flight within Paraves remains controversial. Moreover, the morphology and internal structure of the feathers in the earliest paravians is poorly documented, so their real aerodynamical capacities remain conjectural. For example, the presence or absence of interlocked barbules, commonly considered as a criterion for determining whether a feather can produce useful aerodynamic lift (Zhang et al., 2006), remains unclear in the Late Jurassic basal paravians from China described so far.

Here we report a new paravian theropod, *Serikornis sungei* gen. et sp. nov., from the Late Jurassic Tiaojishan Formation of Linglongta (Jianchang County, Liaoning Province, China), based on a complete articulated skeleton, PMOL-AB00200, with associated integumentary structures. The plumage of this new specimen brings new information on the structure and function of the feathers in basal paravians and consequently on the early evolution of flight.

2. Material and Methods

This published work and the nomenclatural acts it contains have been registered in ZooBank, the proposed online registration system for the International Code of Zoological Nomenclature. The ZooBank life science identifiers can be resolved and the associated information viewed by appending the life science identifiers to the prefix http://zoobank.org/. The life science identifiers for this publication are urn:lsid:zoobank.org:pub:65432F68-4DF9-4CC2-BE86-F366B858893A.

3. Results

3.1. Systematic paleontology

Theropoda Marsh, 1881;
Maniraptora Gauthier, 1986;
Paraves Sereno, 1997;

Avialae Gauthier, 1986;

Serikornis sungei gen. et sp. nov.

The ethymology of the genera *Serikos*, comes from the ancient Greek and means ‘silk’. It refers to the body of the specimen, almost entirely covered with plumulaceous-like feathers; *Ornis*, is the ancient Greek word for ‘bird’; the species is named in honor of Sun Ge, for his contribution to our knowledge of Jurassic and Cretaceous ecosystems in Asia.

PMOL-AB00200 is a single complete articulated skeleton with associated integumentary structures preserved on a slab (Fig. 3.1A, B). PMOL-AB00200 was collected in the Tiaojishan Formation (Oxfordian, Upper Jurassic; Chu et al., 2016) from Daxishan village, Linglongta (Jianchang County, Liaoning Province, China).

3.2. Diagnosis

Serikornis is characterised by the following combination of characters (autapomorphies are marked with an asterisk): four anterior maxillary teeth twice as long as the others regarding the crown height*; coracoid tuber well-developed and laterally projected from the lateral margin of the coracoid and forming a subglenoid shelf along the caudoventral margin of the bone; the distal end of the lateral process of the coracoid is thicker than the proximal part and forms a ventral rounded bump;

Figure 3.1. Photograph and drawing of the basal bird *Serikornis sungei* sp. nov. from the Late Jurassic of north-eastern China. (A) PMOL-AB00200 photograph, (B) Line drawing. Abbreviations: cev, cervical vertebrae; co, coracoids; cv, caudal vertebrae, fu, furcula; il, ilium; is, ischium; lf, left femur; lfi, left fibula; lh, left humerus; lma, left manus; lpes, left pes; lr, left radius; ls, left scapula; lt, left tibia: lu, left ulna; pu, pubis; ra, radiale; rf, right femur; rh, right humerus; rma, right manus; rpes, right pes; rr, right radius; rt, right tibia; ru, right ulna; sk, skull.

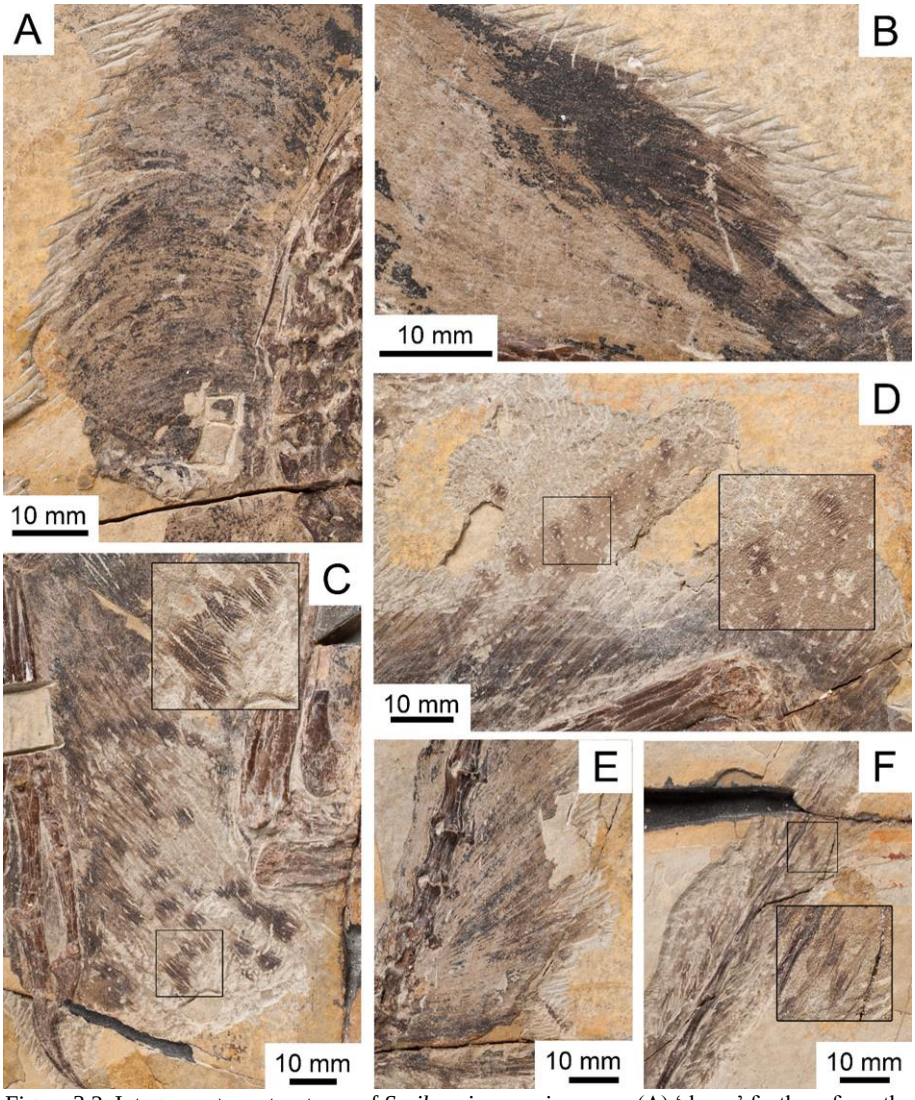

Figure 3.2. Integumentary structures of *Serikornis sungei* sp. nov. (A) 'down' feathers from the neck region, (B) 'contour' feathers from the back region, (C) symmetric feathers of the left wing where the remiges and the contour feathers cannot be distinguished, (D) tibial feathers on the posterior face of the right femur, (E) metatarsal feathers recovered after a second preparation, (F) distal part of the tail covered by numerous 'down' feathers.

ventrodistal process of ischium narrow, hook-like, strongly deflected caudodorsally and set at the distal end of the ischium*; smooth ventral side of coracoid devoid of small pits. The complete description of the specimen is available in the Appendix "A3".

3.3. Plumage description

Feather impressions are present around the entire skeleton, extending onto the pedal phalanges (except the unguals), as also described in *Anchiornis* (Hu et al., 2009) and *Xiaotingia* (Xu et al., 2011) (Fig. 3.2). It is not possible to observe whether the long and thin filaments that cover the top of the skull remain isolated or are bundled proximally. Feathers similar to those previously identified in the dromaeosaurid theropod *Sinornithosaurus* (Ji et al., 2001) cover the neck of *Serikornis* and consists of bundles of filaments that are joined together proximally and remain nearly parallel as they extend distally (down-like feathers) (Fig. 3.2A). The back of *Serikornis* is entirely covered by contour-like feathers with well-defined rachis and transversely-inserted barbs (Fig. 3.2B). As in *Anchiornis*, the forelimb wings appear to be formed by multiple layers of relatively short, slender, symmetrical and poorly differentiated feathers inserted on a large propatagium; unlike in *Archaeopteryx*, *Microraptor*, *Confuciusornis* and modern birds, remiges and coverts cannot be distinguished (Fig. 3.2C) (Brown et al., 1994; Chiappe et al., 1999; Li et al., 2012a; Longrich et al., 2012). The number of pennaceous feathers attached to the forelimb cannot be accurately estimated. As in *Anchiornis* (Hu et al., 2009) and *Eosinopteryx* (Godefroit et al., 2013b), the longest forelimb feathers are attached near the distal end of the forearm and the proximal end of the manus, and are about 150% the humeral length. The large number of undifferentiated forelimb feathers are arranged in several rows in *Serikornis*, suggesting the presence of a large propatagium, a fleshy structure made of skin filling the angle between the humerus and the forearm (Baumel, 1993; Brown et al., 1994; Feduccia & Czerkas, 2015), in life. In modern birds, the propatagium is mainly responsible for the aerodynamical profile of the wing (Brown et al., 1994; Lucas & Stettenheim, 1972c), but this structure is also necessary for the insertion of numerous covert feathers responsible for the cambered dorsal surface of the wing (Brown et al., 1994). The development of a large propatagium in basal paravians is therefore supported by the presence of numerous layers of feathers along the forearm in *Serikornis*, but also in *Anchiornis* (Longrich et al., 2012; Wang et al., 2017)

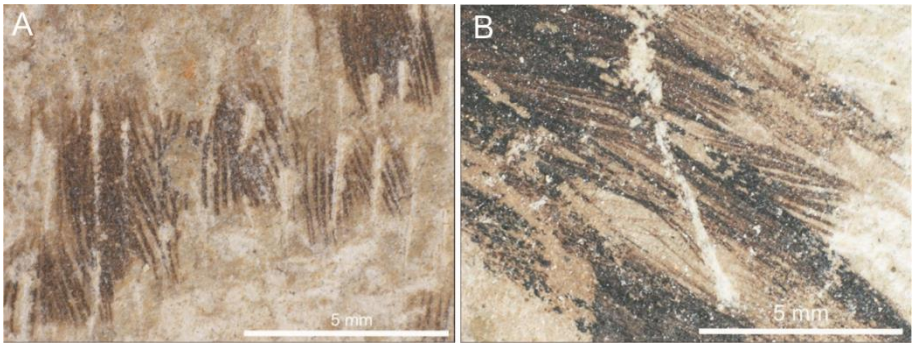

Figure 3.3. Optical microscopy close-ups on the (A) remiges and back contour feathers (B) of *Serikornis*. Pictures show the total absence of barbules and the constant width of each barb.

although this character could be inherited from a common ancestor with oviraptorosaurs as this character is also present in *Caudipteryx* (Feduccia & Czerkas, 2015). In *Serikornis*, the vanes of the remiges obviously lack barbules, as observed in both optical and electronical microscopy (Figs 3.3A,B and S3.7) and this is confirmed by the absence of basal expansions along the barbs that mark the insertion of barbules in modern feathers (Lucas & Stettenheim, 1972c); however, those basal expansions have not been observed either in early bird specimens assumed to have barbules (see the supplementary informations). Of course, it cannot be excluded that this apparent absence of barbules is a taphonomic bias. However, thin integumentary structures, with a mean width of 43 ± 2 µm, similar to the range of modern barbule widths (e.g., 23 µm in the shelduck up to 80 µm in the single comb chicken; [D'Alba et al., 2014; Lucas & Stettenheim, 1972c]), are preserved in the neck region indicating that the absence of barbules does not reflect preservation conditions. If barbules were really missing, the pennaceous feathers of *Serikornis* did not form an efficient aerial surface for supporting the air pressure during a wing propelled flight (Lucas & Stettenheim, 1972c). Ji et al. (1998) argued that the presence of a well-formed vane in fossilised feathers, as observed in *Serikornis*, is an indirect evidence for the presence of barbules. However, the distal part of the covert feathers of the cassowary (*Casuarius casuarius*) do not form a loose tangle of barbs although they are devoid of barbules (Fig. S3.8). Moreover the proximodistal distances between the proximal barbs in this bird are sometimes insufficient to allow interlocking barbs. It is therefore conceivable that complete interlocked vanes evolved later in paravian evolution, when the main role for feather changed from a social/thermoregulatory display to a flight function.

Densely packed integumentary filaments that are joined together proximally are present along the posterior part of the hindlimbs - from the femur up to the penultimate pedal phalanges -, contrasting with *Eosinopteryx* in which the lower leg is devoid of any integumentary structures (Godefroit et al., 2013b), although it cannot be excluded that this character reflects taphonomical conditions. Besides the down-like feathers, meticulous preparation of PMOL-AB00200 reveals the presence of tibial and of short metatarsal remiges (Figs 3.2D and S3.11), as in *Anchiornis*, *Archaeopteryx* and *Sapeornis* (Foth et al., 2014; Xu & Zhang, 2005; Xu et al., 2003; Zheng et al., 2013b). *Serikornis* can be viewed as a tetrapterygian paravian (= four-wing biplan made of elongated feathers) although its forewing is composed of undifferentiated contour, and its flight feathers and the hindwing includes both pennaceous and plumulaceous-like feathers (both wings may lack barbules). As in *Anchiornis*, the presence of both plumulaceous-like feathers and pennaceous feathers on the hindwing of PMOL-AB00200 represents a transitional stage between the fully plumulaceous leg of basal coelurosaurians (e.g. *Sinocalliopteryx* and *Yutyrannus*) and a fully pennaceous hindlimb recovered in more derived Avialae (e.g. *Archaeopteryx* and *Sapeornis*) (Godefroit et al., 2013a; Hu et al., 2009; Zheng et al., 2013b).

The tail of *Serikornis* is proximally covered by numerous down-like feathers (Fig. 3.2E), while short pennaceous symmetric feathers with a slender rachis are inserted

along the distal end of the tail (Fig. 3.2F). The distal tail feathers of *Serikornis* cannot be considered as true rectrices (that is, large-sized asymmetrical feathers of the tail) but more closely resemble tectrices (upper tail coverts) in Avialae (O'Connor et al., 2013). As in the hindlimb, the tail feathers of *Serikornis* therefore represent a transitional condition between the fully plumulaceous tail filaments of more basal coelurosaurs and the longer rectrices inserted all along the tail of *Anchiornis* (see YFGP-T5199 specimen in Lindgren et al., 2015) and basal Pennaraptorans (Foth et al., 2014; Hu et al., 2009).

4. Discussion

Our results are consistent with the presence of four wings as the primitive condition for Eumaniraptora (more information in the Appendice "A3") and inherited by basal birds or, in other words, that the flapping flight of modern birds was preceded by a four-winged gliding stage (Godefroit et al., 2013a; Godefroit et al., 2013b; Longrich et al., 2012; Xu et al., 2011; Xu & Zhang, 2005; Xu et al., 2003; Zheng et al., 2013b). Fully developed hindlimb wings, implying the presence of elongated remiges along both the tibia and the metatarsus, are present in *Microraptor* (Xu et al., 2003), *Pedopenna* (Xu & Zhang, 2005), *Anchiornis* (Xu & Zhang, 2005), *Changyuraptor* (Han et al., 2014), and *Sapeornis* (Zheng et al., 2013b). Although the hindlimbs of *Serikornis* are covered both by bundles of filaments joined proximally and by fully developed pennaceous feathers, this pattern remains consistent with the tetrapterygian condition of basal birds. *Eosinopteryx* seems to be devoid of hindlimb wings: pennaceous feathers are only present along the posterior part of the thigh and crus but this absence can be the result of a taphonomic bias. This apparent reduction of the hindlimb plumage may be regarded as a secondary loss in *Eosinopteryx* (Godefroit et al., 2013b) or as an ontogenetically-controlled feature.

The symmetrical vanes on the hindwing feathers of *Serikornis*, *Anchiornis* and *Pedopenna* (Xu & Zhang, 2005) seem to be less efficient from an aerodynamic perspective than those of more derived paravians; so these taxa may have used their hindwing feathers for other functions, such as visual display or mate recognition. The high plasticity in the development of metatarsal plumage in paravians can still be observed in modern birds, with the recurrent development of feathered feet in birds of prey (e.g. *Aquila chryseatos*, *Asio flammeus*, *Bubo scandiacus*) or in chicken breeds such as Silkies (Barrows, 1981; Bartels, 2003). Although their small size suggests that these animals were probably not top predators, they would have needed fast movements to escape predation. In this way, the development of hindwing feathers remains disadvantageous and should be regarded as a sign of sexual selection (Chiappe et al., 1999; O'Connor & Chang, 2015).

Although elongated rectrices are present along the distal half of the tail in Oviraptorosauria (Ji et al., 1998; Xu et al., 2010) and *Microraptor* (Li et al., 2012a), they seem to be absent in *Serikornis*, *Aurornis*, and *Eosinopteryx*, which may suggests that the tail of those basal paravians had no aerodynamic function in increasing the

total lift of the animal while gliding as in *Archaeopteryx* (Longrich et al., 2012), nor any display function as well. The long bony tail was completely covered by elongated pennaceous rectrices in both *Anchiornis* (Hu et al., 2009) and *Archaeopteryx* (Foth et al., 2014), whereas *Jeholornis* had both proximal and a distal tail fans (O'Connor et al., 2013). The tail plumage is highly variable in pygostylian birds: a pair of elongate rectrices in *Confuciusornis* male specimens (Chinsamy et al., 2013) and in some Enantiornithes (Wang et al., 2014), a graded fan of pennaceous feathers in *Sapeornis*, a forked tail of pennaceous feathers in *Schizooura*, and a fan-shaped tail of pennaceous feathers in *Hongshanornis* and in most modern birds (Lucas & Stettenheim, 1972c; Wang et al., 2014). Rectrices are secondarily absent in *Confuciusornis* females (Chinsamy et al., 2013) and some enantiornithine female birds (Foth et al., 2014; Zheng et al., 2013a).

Although they extensively covered both arms and hands, the forelimb feathers of the Late Jurassic basal paravians *Anchiornis*, *Eosinopteryx*, and *Serikornis* remained unspecialised and undifferentiated into elongated remiges and shortened coverts, unlike in *Archaeopteryx*, *Microraptor* and modern birds (Foth et al., 2014; Longrich et al., 2012): all were rather short, slender, symmetrical and, at least in *Serikornis* and *Eosinopteryx*, devoid of barbules, contrasting with the more elongated and asymmetrical wing feathers with well-developed barbules in *Archaeopteryx* (Carney et al., 2012; Foth et al., 2014) and modern birds (Lucas & Stettenheim, 1972c). Based on these results, the forelimb feathers in Late Jurassic basalmost paravians were obviously not adapted for active flight (although glide flight cannot be excluded) and were therefore more likely related to other biological phenomena, including visual display and sexual selection (Foth et al., 2014; Ji et al., 1998; Li et al., 2010; O'Connor et al., 2013; Prum & Brush, 2002; Xu & Guo, 2009).

The supposed limited flight capabilities of *Aurornis*, *Eosinopteryx* and *Serikornis*, as evidenced by the study of their preserved plumage, is also reflected in their osteology. Their forelimbs are proportionally shorter and more gracile than in *Anchiornis* and *Archaeopteryx* (Supplementary Tables S3.1-S3.2), resulting in a reduced wing surface. All these specimens also have a relatively straight ulna and radius (thus limiting the pronation and supination movements necessary for producing a wing beat), lack a bony sternum for attachment of powerful pectoral muscles, and have proximodistally decreasing pedal phalanges, together with small pedal unguals that are poorly recurved (Pike & Maitland, 2004). Moreover, the relatively high ratio of tibiotarsus length to femur length can be regarded as a good evidence of cursoriality (Boles, 1997). All these characters suggest that basal paravians were primarily ground-dwelling animals with good cursorial abilities (Foth et al., 2014; Hu et al., 2009). However the manual digits of *Serikornis* are long and slender with strongly curved unguals I and III. This supposes that they could have been effective for climbing trees as in *Archaeopteryx* (Feduccia, 1993; Manning et al., 2009a; Wellnhofer, 2009). In this way, the hindlimbs can be regarded as less specialised than the forelimbs for grasping.

The recent discovery of a patagium in scansoriopterygids (a lineage found among basalmost paravians in our phylogenetic analysis, and lacking evidence of remiges) (Xu et al., 2015) suggests that the earliest adaptation to an arboreal/gliding lifestyle among paravians did not involve exaptation of the plumage as an aerodynamic surface. This is particularly true as the insertion of several rows of forelimb feathers requires a large propatagium. The absence of true flying adaptation in the "tetrapterygian" *Serikornis* and the gliding membrane of scansoriopterygids both challenge an aerodynamic function as earliest driver of plumage elaboration in basalmost Paraves.

Birds and, by extension, some other archosaurs are characterised by a pneumatic postcranial skeleton with invasion of bones by the pulmonary air-sac system (Benson et al., 2012; O'connor & Claessens, 2005). This system allows a flow-through ventilation and exceptionally-efficient gas exchanges (Duncker, 1971), and has two evident additional functions: weight reduction in large-bodied or flying taxa and density reduction by energetic savings during foraging and locomotion (Benson et al., 2012; Bramwell & Whitfield, 1974; Britt, 1993; Cope, 1877; Currey & Alexander, 1985). The latter function is widely accepted as the main reason for skeletal pneumatisation because body-size has no significant influence on the proportion of pneumatised skeletal compartments (O'Connor, 2004).

Pneumatic foramina (that is, the opening that allows an air sac to enter bone) are proportionally much larger than the primitive nutriment foramina in non-pneumatic vertebrae (including apneumatic bird vertebrae) (Britt et al., 1998). Pneumatic foramina are present in most tetanuran theropods (Benson et al., 2012; Britt et al., 1998), dromaeosaurs (Makovicky et al., 2005; Ostrom, 1969), oviraptorosaurs (Osmólska et al., 2004), birds (Apostolaki et al., 2015; Baumel, 1993; O'Connor, 2004), sauropods (Cope, 1877; Marsh, 1877; Upchurch et al., 2004; Wedel, 2007), and pterosaurs (Bonde & Christiansen, 2003; Butler et al., 2009; Claessens et al., 2009; Eaton, 1910; Seeley, 1870). The character distribution of pneumaticity shows that although axial pneumaticity may lighten the skeleton, its evolution cannot be considered to be an adaptation for flight (Britt et al., 1998). The pneumaticity of cervical and anterior dorsal vertebrae occurred early in theropod evolution (Benson et al., 2012) and the presence of pneumatic foramina in vertebrae of non-avialan and avialan theropods indicates that some components of the avian air-sac lung system was already, to some degree, in place (Britt et al., 1998).

Britt (1993) proposed several osteological correlates of vertebral pneumaticity, based on osteological study of extant ratites (*Struthio camelus* and *Dromaius novaehollandiae*) (e.g. large external foramina, external fossae with a crenulate surface texture, thin outer bone walls) (Benson et al., 2012). However, O'Connor (2006) noted that several of these features are present in crocodilians, which lack postcranial pneumaticity. Thus, the presence of internal chambers (called camerate or camellate based on the number and size of internal chambers) opening externally via large (and thus not simply vascular) foramina are the only unambiguous evidences of

skeletal pneumaticity (Britt et al., 1998; O'Connor, 2006; Wedel, 2007). The presence of a high pneumaticity of the anteriormost cervical vertebrae and the limited flight capacities of *Serikornis* suggest that high pneumatisation in small maniraptorans reflects the demands of an increasingly high-performance metabolic regime rather than a prerequisite for flight (Benson et al., 2012; Britt et al., 1998; Cubo & Casinos, 2000; Currey & Alexander, 1985; Fajardo et al., 2007; O'Connor, 2004). Further analyses are required to explore the pneumaticity of the whole specimen. The laminography technique is promising as it allows to investigate the proportion of pneumaticity without external traces of foramina or pneumaticity.

Supplementary information for "A new Jurassic theropod from China documents a transitional step in the macrostructure of feathers"

Supplementary Tables

Table S3.1: Deltopectoral length to humeral length ratio among Jurassic paravians

Species	DCL	HL	DCL/HL
Serikornis (PMOL-AB00200)	16	60.7	3.79
Anchiornis (YFGP-T5199)	18	70	3.88
Aurornis (YFGP-T5198)	12	58	4.83
Eosinopteryx (YFGP-T5197)	12.5	37.9	3.03
Archaeopteryx (HMN 1880/1881)	21	65	3.09

DCL = deltopectoral crest length; HL = humeral length

Table S3.2: Selected measurements of *Serikornis sungei*

Anatomical region	Length (in mm)
Anterior cervical vertebra	8.1
Posterior cervical vertebra	9.9
Anterior dorsal vertebra	6.7
Posterior dorsal vertebra	6.6
Anterior caudal vertebra	7.7
Middle caudal vertebra	13.0
Posterior caudal vertebra	10.8
Humerus	60.7
Ulna	50.8
Radius	50.5
Metacarpal I	12.0
Metacarpal II	32.0
Metacarpal III	30.0
Manual phalanx I-1	27.5
Manual phalanx II-1	20.0
Manual phalanx II-2	23.5
Manual phalanx III-1	7.5
Manual phalanx III-2	6.5
Manual phalanx III-3	16.0
Manual ungual I	17.0
Manual ungual II	19.0
Manual ungual III	12.7
Scapula	37.8
Ilium	33.0
Pubis	63.0
Ischium	16.0*
Femur	67.4
Tibiotarsus	95.2
Metatarsal I	8.5
Metatarsal II	48.5
Metatarsal III	48.5
Metatarsal IV	53.0
Metatarsal V	15.5
Pedal phalanx I-1	9.0
Pedal phalanx II-1	9.0
Pedal phalanx II-2	11.0
Pedal phalanx III-1	12.0
Pedal phalanx III-2	10.0
Pedal phalanx III-3	10.0
Pedal phalanx IV-1	9.0
Pedal phalanx IV-2	8.0
Pedal phalanx IV-3	6.0
Pedal phalanx IV-4	7.0
Pedal ungual I	3.0
Pedal ungual II	13.0
Pedal ungual III	5.5
Pedal ungual IV	8.0

Measurements are in mm ; * refers to estimated value

Table S3.3: Selected relative proportions of elements across published *Anchiornis* specimens and *Serikornis*

	Anchiornis YFGP-T5199 **(Lindgren et al., 2015)**	*Anchiornis* IVPP V14378 **(Xu et al., 2009)**	*Anchiornis* LPM-B00169 **(Hu et al., 2009)**	*Anchiornis* BMNHC PH828 **(Li et al., 2010)**	*Serikornis* PMOL-AB00200
Scapula length/femur length	0.44	0.62	0.68	-	0.56
Scapula length/humerus length	0.46	0.65	0.66	0.58	0.62
Radius length/humerus length	0.85	-	0.81	-	0.83
Ulna length/humerus length	0.90	0.89	0.80	0.88	0.84
Tibiotarsus length/femur length	1.56	1.57	1.61	-	1.41
Humerus length/femur length	1.01	0.96*	1.04	-	0.90
Metacarpal I/metacarpal II	0.35	-	0.37	0.39	0.38

Measurements are in mm ; * refers to estimated value

Table S3.4: Relative proportions of selected elements in basal Jurassic avialans

	Anchiornis IVPP-V14378	*Aurornis* YFGP-T5198	*Eosinopteryx* YFGP-T5197	*Archaeopteryx* HMN/1880/1881	*Xiaotingia* STM 27-2	*Mei* IVPP-V12733	*Serikornis* PMOL-AB00200
Scapula length/humerus length	0.65	0.63	0.63	0.89	0.77	1.07	0.62
Scapula length/femur length	0.62	0.55	0.49	1.07	0.65	0.56	0.56
Humerus length/femur length	0.96	0.88	0.79	1.21	0.85	0.52	0.90
Radius length/humerus length	-	0.83	0.81	1.03	0.75	0.93	0.83
Ulna length/humerus length	0.89	0.98	0.98	0.89	0.92	-	0.84
Tibiotarsus length/femur length	1.57	1.37	1.43	1.30	-	1.31	1.41
Pes length/femur length	1.56	1.11	1.34	1.18	-	1.30	1.28
Metacarpal I length/metacarpal II length	-	0.35	0.36	0.25	0.42	-	0.38

Table S3.5: EDX elemental distribution on sample 2 (see Fig. S3.14)

Element	Energy (keV)	Mass (%)	Error (%)	Atom (%)
C	0.277	40.06	0.08	52.50
O	0.525	35.27	0.15	34.71
Al	1.486	3.97	0.06	2.32
Si	1.739	13.82	0.06	7.75
K	3.312	1.69	0.09	0.68
Ca	3.69	1.36	0.11	0.54
Fe	6.398	2.68	0.31	0.76

Supplementary Figures

Supplementary Figure S3.1. X-ray radiography of PMOL-AB00200. The posterior part of the skull is missing. There is a mismatch in the manual phalanges together with a lack of some parts due to the overlapping of this anatomical region between two slabs. In consequence, the total length of the left and right manus remains unknown.

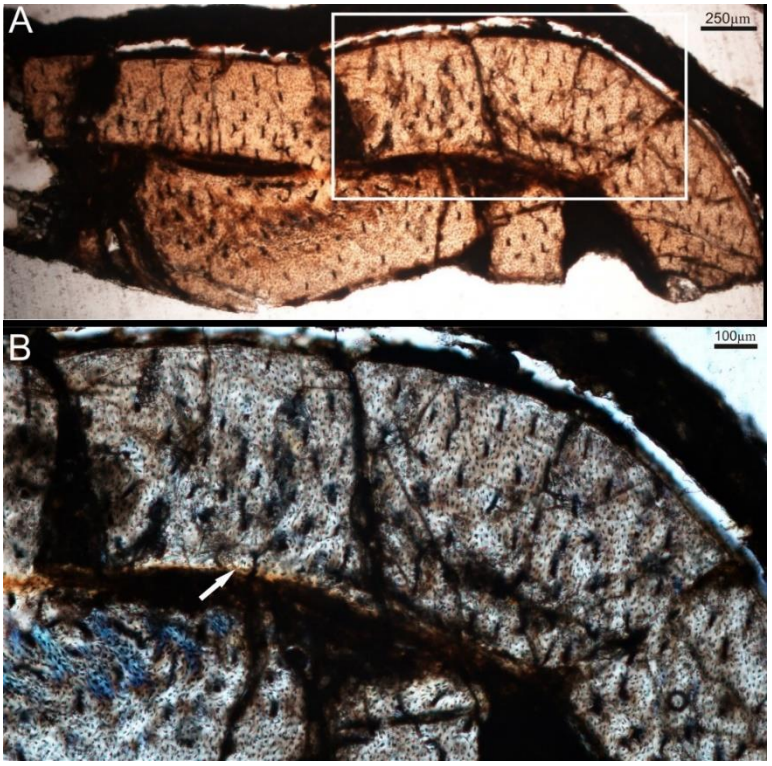

Supplementary Figure S3.2. Histological section of the femur of *Serikornis sungei*. (A), low magnification showing the entire cortex of the bone. (B), higher magnification of the framed area. The arrow indicates the narrow inner circumferential layer (ICL). Notice the uneven peripheral margin of the bone wall, and the lack of an outer circumferential layer (OCL).

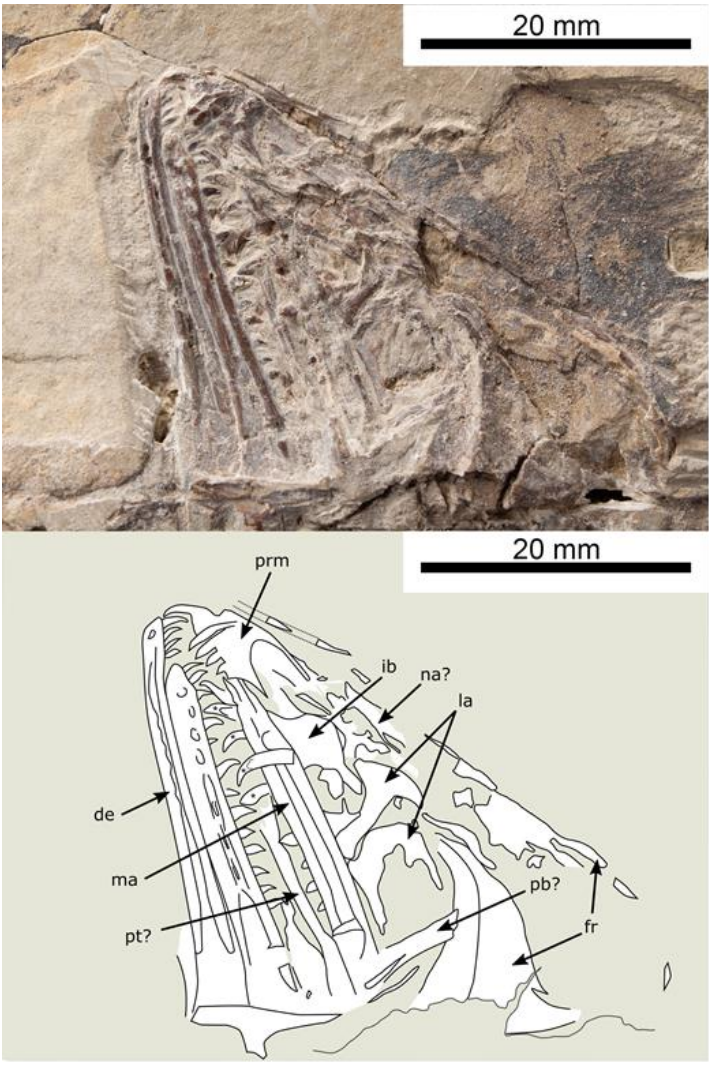

Supplementary Figure S3.3. Photograph and line drawings of *Serikornis sungei*. Abbreviations. de, dentaries; fr, frontals; ib, interfenestrial bar; la, lachrymal; ma, maxillary; na, nasal; pb, postorbital bar; prm, premaxilla, pt, pterygoid.

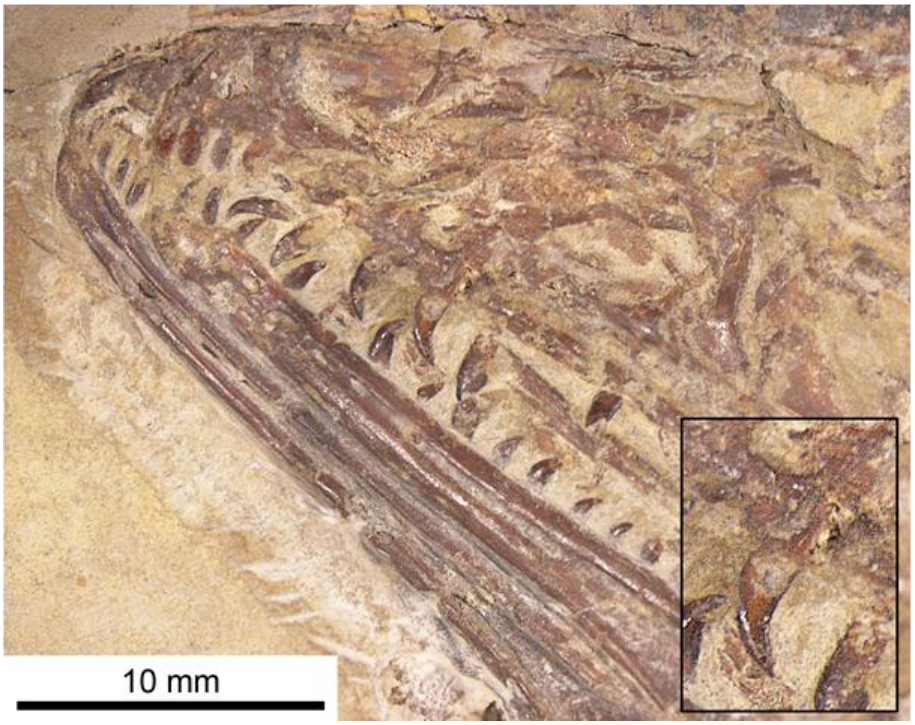

Supplementary Figure S3.4. Close-up of the rostral part of the skull *Serikornis sungei*. Arrow points toward the root of the third maxillary tooth which is inserted in the ventral margin of the maxillary.

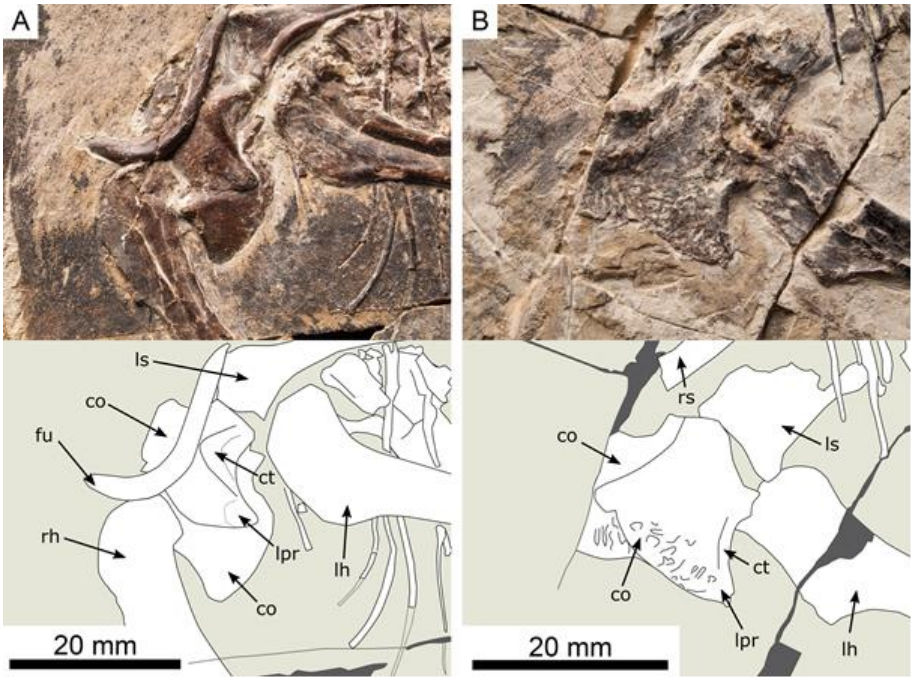

Supplementary Figure S3.5. Comparison of the scapular girdle in *Serikornis sungei* (A) and *Anchiornis huxelyi* (YFGP-T5199) (B). Note the presence of numerous pits on the anterior surface of the coracoid of *Anchiornis* that are completely absent in *Serikornis*. Abbreviations. bt, biceps tubercle; co, coracoids; ct, coracoid tuber; fu, furcula; lh, left humerus; ls, left scapula; rs, right scapula.

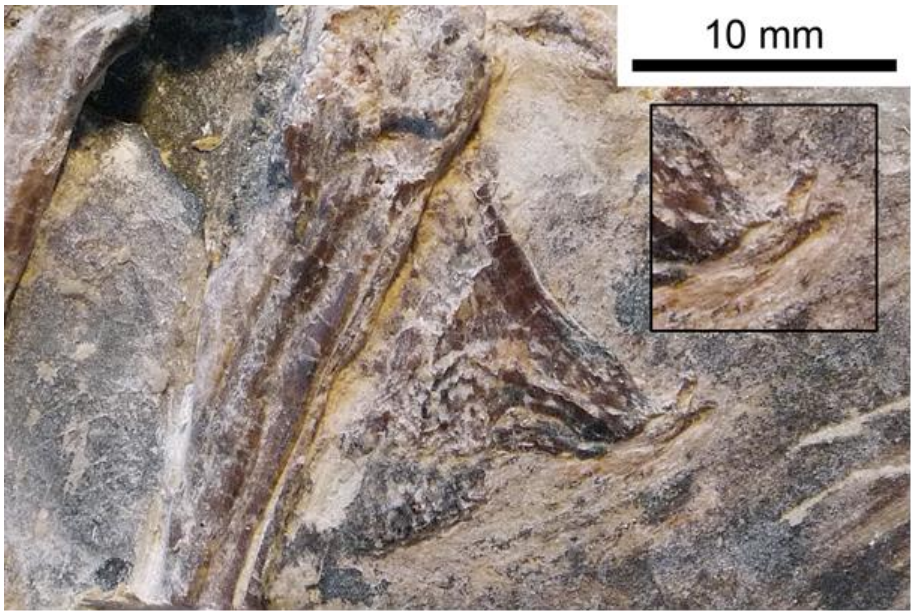

Supplementary Figure S3.6. Close-up of ischia of *Serikornis sungei*. The box focuses on the caudodorsally deflected hook-like ventrodistal process.

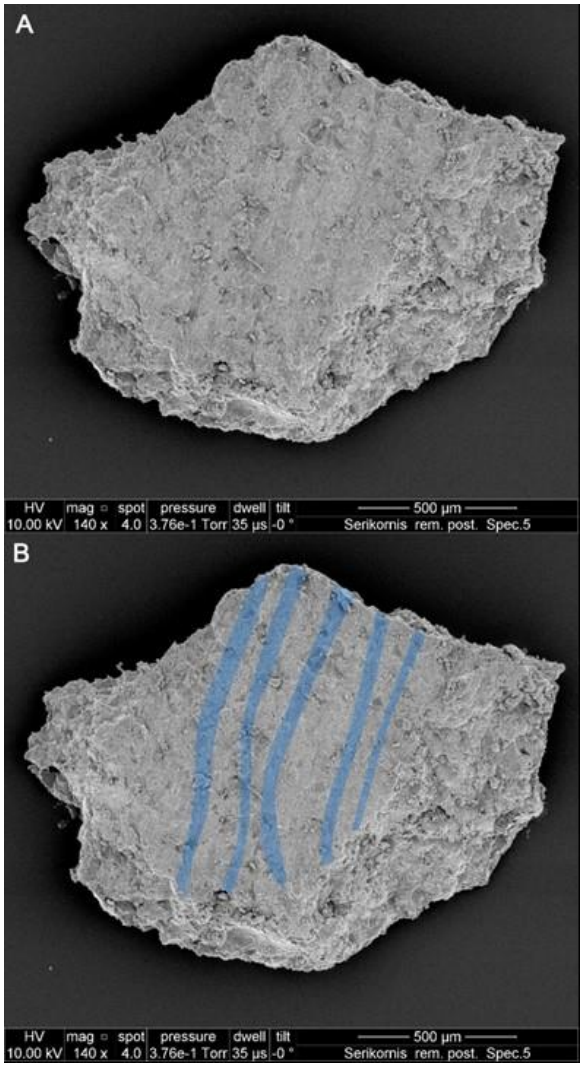

Supplementary Figure S3.7. Image of feather barbs collected on the posterior remige at the level of the tight under SEM microscope. The homogeneity of the surface just permits to distinguish feint impressions of the barbs. This sample has been analysed under EDX instrument and shows that the darker regions (in blue on b) are richer in carbon than the surrounding sediment (Fig. S3.18). This result supports the fact that the imprints represent fossil barbs. There are no imprints of barbules connecting barbs together. No other details can be observed under scanning electron microscopy. (a) original micrograph of feather barbs. (b) the outlines of the barbs are underlined in blue.

Supplementary Figure S3.8. Contour feather of *Casuarius casuarius*. (a) overview of the complete feather retaining the afterfeather, (b) close-up of the distal tip of the feather. The most distal barbs are devoid of barbules but do not form a loose tangle.

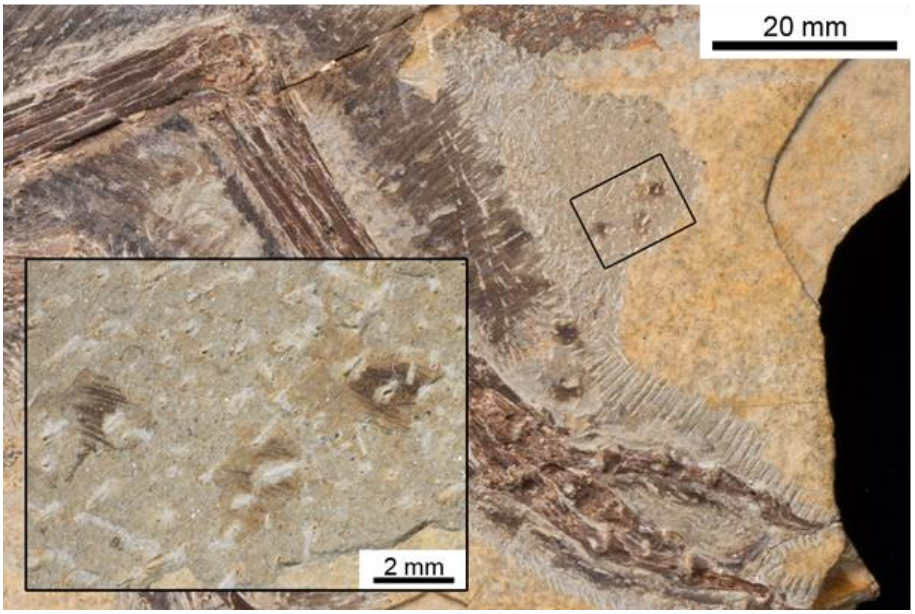

Supplementary Figure S3.9. Close-up on metatarsal feathers of *Serikornis sungei*. Only few parts of pennaceous feathers have been uncovered. Box magnifies the feathered region.

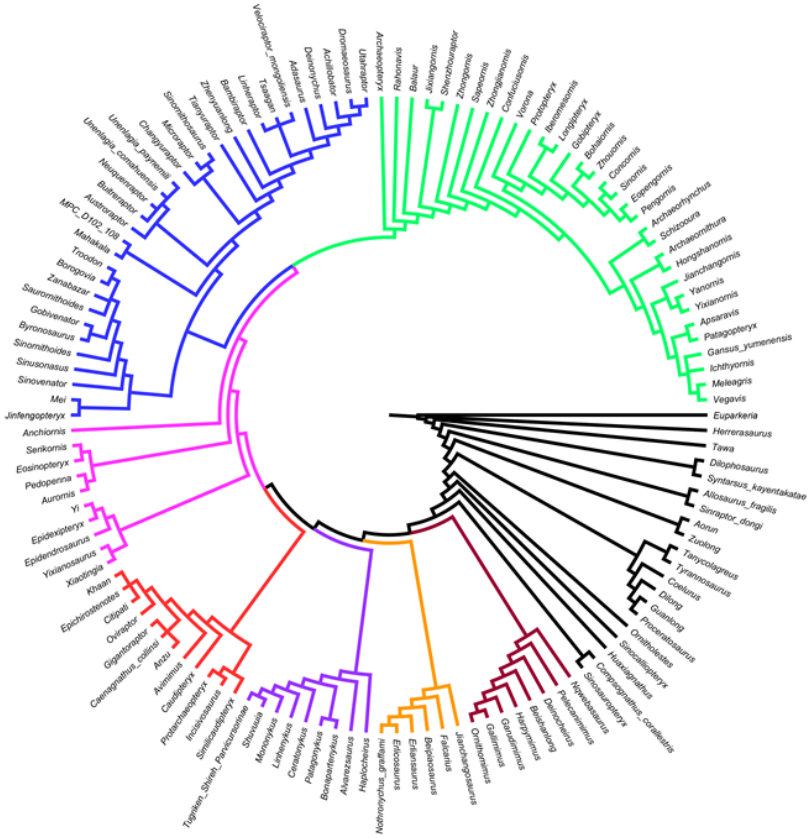

Supplementary Figure S3.10. Consensus tree recovered after phylogenetic analysis. Tree length = 5743. Consistency index (CI) = 0.2614. Homoplasy index (HI) = 0.7386. CI excluding uninformative characters = 0.2332. HI excluding uninformative characters = 0.7668. Retention index (RI) = 0.5732. Rescaled consistency index (RC) = 0.1498.

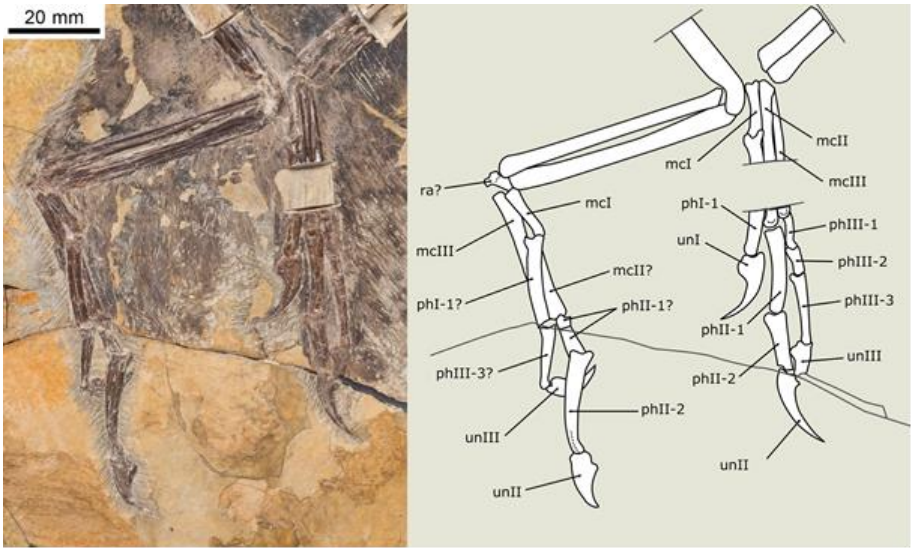

Supplementary Figure S3.11. Close-up on manus of *Serikornis sungei*. Mc, metacarpal; ph, phalanx; ra, radial; un, ungual.

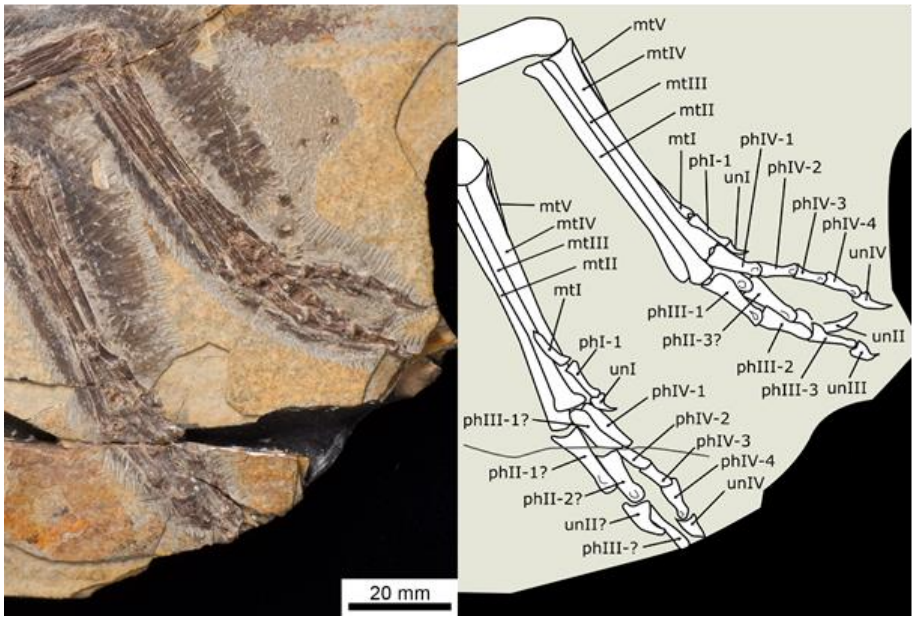

Supplementary Figure S3.12. Close-up on the pes region of *Serikornis sungei*. Mt, metatarsal; ph, phalanx; un, ungual.

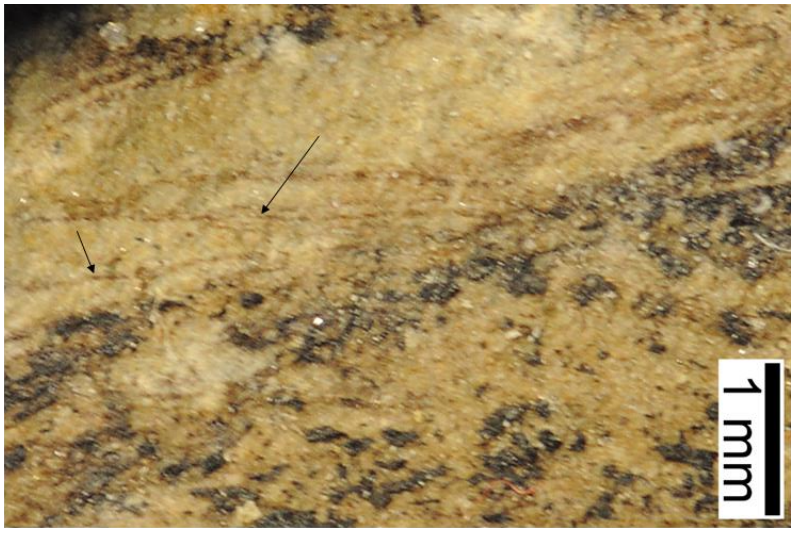

Supplementary Figure S3.13. Slender integumentary structures found on the neck region of PMOL-AB00200. Arrows point to well-defined structures with a mean width of 43 ± 2 µm.

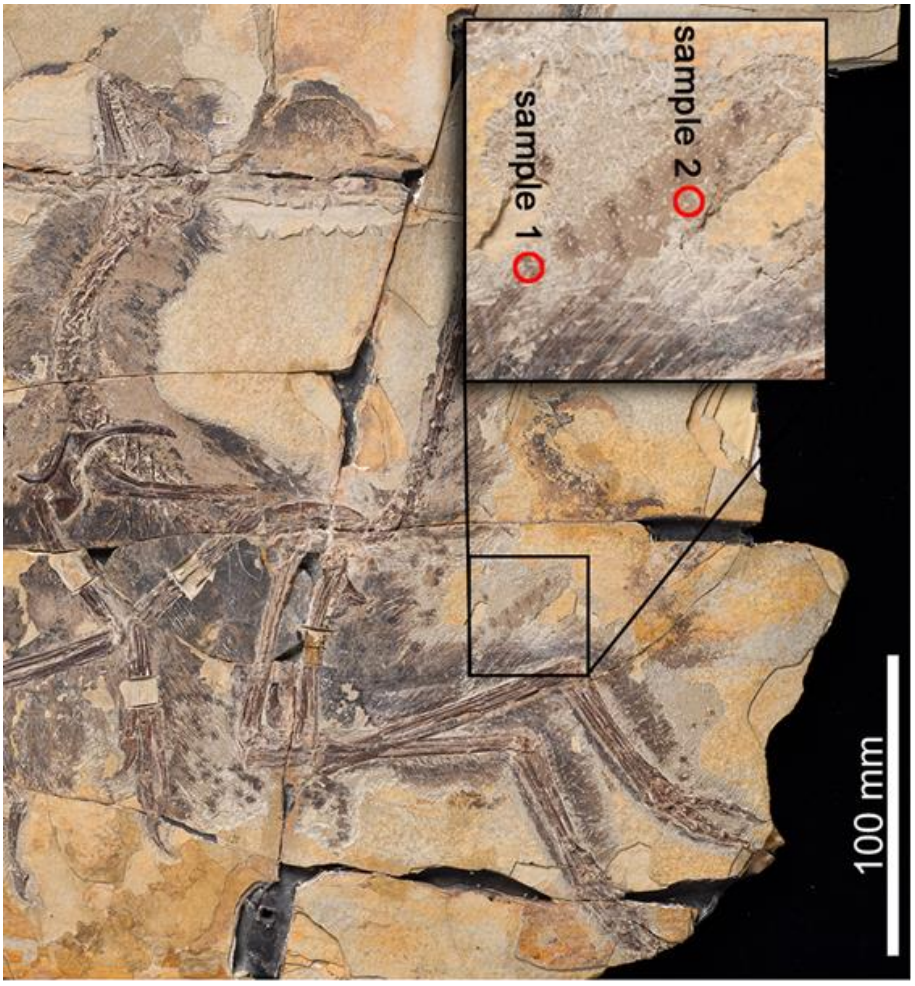

Supplementary Figure S3.14. Samples used for scanning electron microscopy (SEM) and energy dispersive X-ray analysis (EDS). Two samples have been collected on the left humerus.

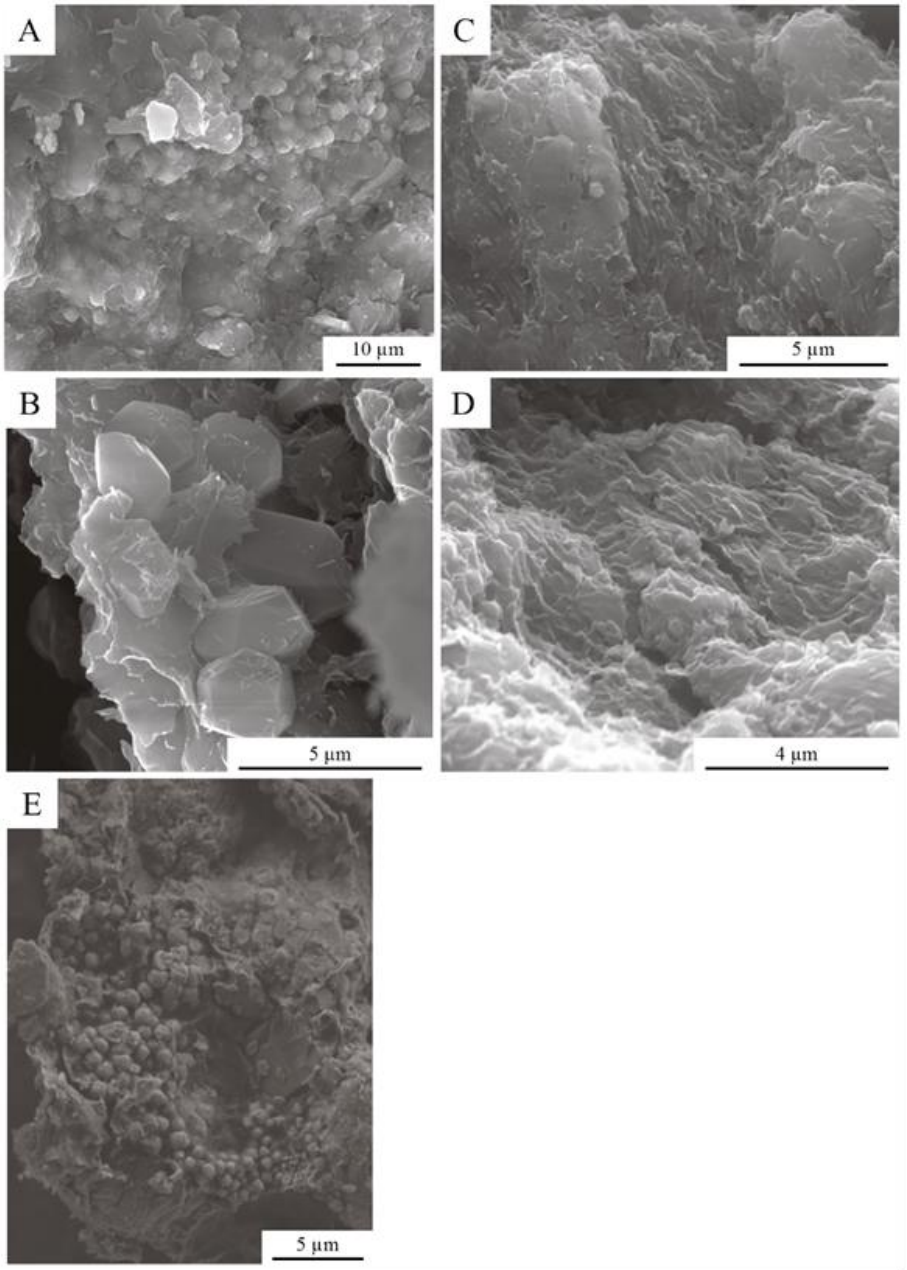

Supplementary Figure S3.15. SEM images of the feathers of *Serikornis sungei*. (A) and (B), Phyllosilicates, pyrite framboids and carbonate crystals. (C) and (D), elongate imprints of microbodies. (E) cubic iron oxides.

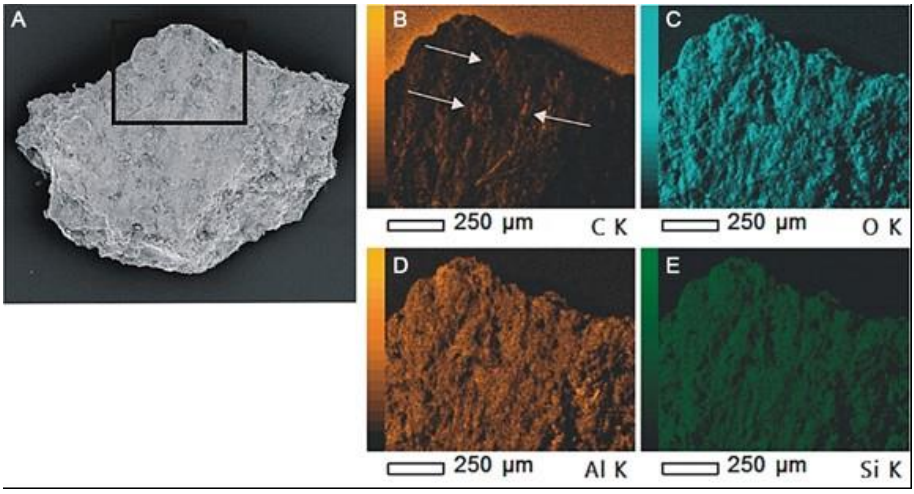

Supplementary Figure S3.16. EDS Mapping of the main elements analysed in the feathers of *Serikornis*. (A) location of the analysed area; mapping of (B) carbon, (C) oxygen, (D) aluminum, (E) silicon. Arrows point on the carbonaceous filaments.

Supplementary Figure S3.17. Life reconstruction of *Serikornis sungei* by Emily Willoughby

Supplementary Text

Material and Methods

Pictures were taken using a Lumix GX1 (Panasonic). Close-up pictures were taken with a Stemi 2000-C (Zeiss) binocular magnifier coupled with an Axiocam MRc (Zeiss). A caliper was used to obtain osteological measurements. Additional measurements (e.g., angles) were calculated using ImageJ program.

Origin and age of PMOL-AB00200

The specimen of *Serikornis sungei* was acquired by the Yizhou Fossil & Geology Park (YFGP) and the localisation of the counterslab remains unknown.

The Tiaojishan Formation is widely exposed in the region of the Daxishan village where the *Anchiornis huxleyi* holotype (LPM-B00169) (Hu et al., 2009) was discovered. The origin of the specimen is based on information provided by the collector and sediment texture comparison with other fossils from the same region. Further studies are required on micro-sedimentary structures and on pollen assemblages to certify the age of *Serikornis sungei*, as it is also the case for the *Anchiornis huxleyi*, *Xiaotingia zhengi* and *Aurornis xui* specimens.

The Tiaojishan Formation crops out in the West Liaoning Province and is 130-190 meters thick (Chang et al., 2009). This Formation is composed of alternated volcanic and sedimentary rocks, including basalts, andesites, rhyolites, tuffs, tuffaceous sandstones and conglomerates (Chang et al., 2009). The abundance of exquisitely preserved fossils is made possible as a result of the interbedded tuffs originating from volcanic events (Chang et al., 2009). SHRIMP U-Th-Pb analysis of samples from the Tiaojishan Formations give ages that vary between 165 ± 1.2 Ma and 153 ± 2.0 Ma (Yang & Li, 2008). Zhang et al. (2008) obtained that the upper boundary of the Tiaojishan Formation dates between 156 and 153 Ma whereas Chang et al. (2009) recovered ages of 160.7 ± 0.4 Ma and 158.7 ± 0.6 Ma from $^{40}Ar/^{39}Ar$ analysis on an equivalent Formation in North Hebei Province. All of these results indicate that the Tiaojishan Formation spans the Callovian (Middle Jurassic) and the Kimmeridgian (Late Jurassic) (Gradstein et al., 2012). New U-Pb radiochronological data indicate that the Daxishan section spans an age interval ranging between 160.889 ± 0.069 Ma and 160.254 ±0.045 Ma, corresponding to the Oxfordian (Late Jurassic; Gradstein et al., 2012) (Chu et al., 2016).

Ontogenic stage

This specimen is a sub-adult individual based on the following features: bone extremities are rough in appearance, neural arches of caudal vertebrae are completely fused to their corresponding centra (supported by X-ray analysis, Fig. S3.1), sacral vertebrae are completely fused together despite the ventral part is missing and histological sections show the absence of an outer circumferential layer (OCL), an

uneven periosteal surface which indicates that periosteal growth was still occurring at the time of death (Fig. S3.2).

Complete anatomical description of *Serikornis sungei*

The holotype of *Serikornis* is about 49 cm in length. The skull lies on two slabs and most of bones are mainly shattered. Maxillary process of the premaxilla is short and does not exclude the maxilla from the ventral margin of the external naris, as in *Archaeopteryx* and *Anchiornis* (Godefroit et al., 2013b; Lindgren et al., 2015) but in contrast with the condition seen in *Aurornis* and *Eosinopteryx* (Godefroit et al., 2013a; Godefroit et al., 2013b). As in *Eosinopteryx*, the rostral plate and the maxillary process of the premaxilla are particularly short and robust (Godefroit et al., 2013b). Premaxillary and dentary teeth in the symphyseal region are more closely packed than are the teeth in the posterior part of the dentary, a feature characteristic of troodontids (Xu et al., 2011; Zhou & Li, 2009). Maxillary teeth are triangular in labial view and unserrated as in *Aurornis, Anchiornis, Eosinopteryx, Mei, Byronosaurus* and *Archaeopteryx* (Godefroit et al., 2013a; Godefroit et al., 2013b; Zhou & Zhang, 2003). The first fourth maxillary teeth are longer (twice the height) than the next ones (about twice the height), an anisodont condition unique among basal Avialae. The gap between the 4th and 5th maxillary teeth cannot be viewed as a diagnostic character as a tooth root is still in place on the bone (Fig. S3.4). As in *Aurornis*, the anterior half of the dentary is more slender than the posterior part, a condition that differs from that of *Anchiornis*. This bone has subparallel dorsal and ventral margins (Godefroit et al., 2013b). The dentary bears a posteriorly widening groove on the labial surface, as in *Aurornis, Anchiornis, Xiaotingia, Eosinopteryx, Archaeopteryx* and troodontids (Godefroit et al., 2013a; Godefroit et al., 2013b; Hu et al., 2009; Xu et al., 2011). The lacrimal is straight in lateral view. As in *Xiaotingia, Archaeopteryx* and troodontids, the descending process of the lacrimal is inset relative to the anterior and posterior processes. The best preserved frontal is wide and sub-triangular in dorsal view, a condition shared with troodontids and Avialae (e.g. *Jeholornis, Archaeopteryx, Confuciusornis*) (Xu & Zhang, 2005). There is no thickening of the orbital rim as in *Aurornis, Eosinopteryx, Xiaotingia, Anchiornis, Mei* and *Archaeopteryx* (Godefroit et al., 2013a; Godefroit et al., 2013b; Hu et al., 2009; Lefèvre et al., 2014; Xu et al., 2011; Zhou & Zhang, 2003).

At least eight cervical vertebrae are present in *Serikornis* but the total number of vertebrae remains unknown due to taphonomic bias. The cervical ribs of PMOL-AB00200 are as long as their corresponding centra, a character shared with *Eosinopteryx* but contrasting with the shorter cervical ribs seen in *Troodon formosus* and the much longer ones of *Archaeopteryx* and *Aurornis* (Godefroit et al., 2013a; Godefroit et al., 2013b). The middle and posterior dorsals are proportionally elongate as in *Anchiornis, Mei,* and *Eosinopteryx* (Godefroit et al., 2013b). As in *Archaeopteryx, Anchiornis,* and basal deinonychosaurs, the dorsal centra are devoid of distinct pneumatic foramina or bearing shallow depressions on their lateral surfaces

(Godefroit et al., 2013b). The tail of PMOL-AB00200 is composed of 27 caudal vertebra and is 3.9 times the lenght of the femur as in the Eichstätt specimen of *Archaeopteryx* (Godefroit et al., 2013b). The transition point is placed at the level of the 5^{th}-6^{th} caudal vertebrae. Anteriormost caudals are proportionally short as in *Eosinopteryx* and *Aurornis* (Godefroit et al., 2013a; Godefroit et al., 2013b). The neural spine is developed on only the anteriormost three-four caudal vertebrae as in *Aurornis* and *Eosinopteryx* (Godefroit et al., 2013a; Godefroit et al., 2013b). Chevrons resemble those of *Archaeopteryx* showing vertically oriented rectangular plates in the anteriormost centra, followed by lower and more elongated posterior processes from the sixth to the twelfth caudal. As in *Anchiornis, Eosinopteryx,* and *Archaeopteryx*, the middle and posterior caudal vertebrae each bears a distinct groove on the lateral surface near the junction between the centrum and the neural arch (Godefroit et al., 2013b; Zhou & Zhang, 2003).

The scapula is long, thin, and ribbon-shaped. Its distal end is thin and sharp, a condition closer to modern birds than basal avialans (Forster et al., 1998; Xu et al., 1999; Zhou & Li, 2009). The scapula is significantly shorter (0.64) than the humerus, as in most paravians (e.g., *Aurornis* = 0.49; *Anchiornis* = 0.55; *Eosinopteryx* = 0.63) (Xu et al., 2002) and lies parallel to the dorsal vertebral series as in *Archaeopteryx* and *Mei* (Lefèvre et al., 2014). The scapula is gently convex caudoventrally whereas it is straight in *Aurornis, Eosinopteryx, Xiaotingia, Microraptor, Mei,* and *Anchiornis* (Godefroit et al., 2013a; Godefroit et al., 2013b; Lefèvre et al., 2014; Xu et al., 2011; Xu et al., 2003). The scapula is thicker on the lateroventral edge of the proximal part of the bone and lacks the distal groove near the glenoid fossa at the ventral side of the scapula, as is the case in *Xiaotingia* (Xu et al., 2011). The acromial process is not strongly laterally everted contrary to the condition seen in *Xiaotingia* (Xu et al., 2011). The angle between the scapula and the coracoid is less than 90° as in *Microraptor, Zhongjianornis,* and *Sapeornis* (Ji et al., 1998; Xu et al., 2009b; Xu et al., 2003). The coracoid is subrectangular as in *Eosinopteryx, Archaeopteryx* and *Anchiornis*, (Godefroit et al., 2013b; Zhou & Zhang, 2003). The biceps tubercle is well-developed and distinctly more detached from the lateral margin of the coracoid in comparison with other paravians (e.g., *Aurornis, Eosinopteryx, Microraptor, Jeholornis*). As in *Xiaotingia* and *Eosinopteryx*, the proximal end of the coracoid is narrower than the distal one (Godefroit et al., 2013a; Xu et al., 2011). The lateral process is thickened in a rounded bump, a unique feature among basal Avialae. This feature cannot be viewed as a result of compression during fossilisation because the coracoid is a flat bone which is less inclined to be strongly deformed during the diagenesis process unlike long bones where their surfaces are largely cracked and shattered due to high pressure (i.e., the surface of the coracoid is not altered or scarified. This bone can be considered as relatively unaffected by distortion). Unlike *Anchiornis*, the ventral surface of the subrectangular coracoid is smooth, not sculpted by numerous small pits (Hu et al., 2009). The boomerang-shaped furcula is more robust than those of most other non-avialan theropods, with an interclavicular angle of about 110° (Xu et al., 2011). As in

Xiaotingia, *Anchiornis*, and *Archaeopteryx*, each proximal end bears a small acromial process revealed in this specimen by X-ray (Hu et al., 2009; Xu et al., 2011). Each furcular ramus is about one third of the femoral length (0.28), as in *Anchiornis*. No hypocleideum is developed at the junction of the two rami.

Total length of forelimbs remains unknown due to missing parts in the phalangeal region (Fig. S3.12). As in *Xiaotingia*, *Aurornis*, and *Eosinopteryx* the humerus of PMOL-AB00200 is slightly shorter than the femur (0.9), whereas this bone is distinctly longer in *Archaeopteryx* (1.12-1.24) (Godefroit et al., 2013a; Godefroit et al., 2013b; Zhou & Zhang, 2003). The deltopectoral crest is about one-quarter the length of humerus as in *Anchiornis*, scansoriopterygids, some dromaeosaurids and basal troodontids (Hu et al., 2009; Xu et al., 2003). Both radius and ulna are straight along their length as in scansoriopterygids, *Anchiornis*, *Eosinopteryx*, and *Aurornis*, but they do not tightly contact each other. Metacarpal I is about one third the length of metacarpal II, and is distinctly slender, a condition also encountered in *Aurornis* and *Eosinopteryx*. Metacarpal II and III are not fused proximally in contrast with more crownard avialans (e.g. *Jeholornis*, *Sapeornis*, *Confuciusornis*) (Feo et al., 2015). Phalanx I-1 extends beyond the distal end of metacarpal II as in *Anchiornis*, *Aurornis*, and *Eosinopteryx*.

The dorsal margin of the ilium is gently convex along its entire length as in other basal paravians (Xu et al., 2011), except in *Aurornis* where the dorsal margin remains subhorizontal (Godefroit et al., 2013a). As in *Aurornis*, the anterior margin of the ilium is quadrangular. The posterodorsal margin of the ilium is caudoventrally oriented, the postacetabular process tapering posteriorly as in *Microraptor*, *Sinornithosaurus*, *Sinovenator*, and basal birds (Leng & Yang, 2003; Zhu et al., 2005b). The obturator process (= dorsodistal process) of the ischium is blunt, not acuminate as in *Anchiornis*, *Rahonavis* and unenlagiines. This condition is similar to *Aurornis* and *Eosinopteryx*. The ventrodistal process is strongly deflected caudodorsally, a unique character among paravians (Fig. S3.6).

The femur is slightly bowed anteriorly in lateral view as in *Aurornis*, *Anchiornis*, and *Archaeopteryx* (Godefroit et al., 2013a; Hu et al., 2009; Zhou & Zhang, 2003). The femoral mid-shaft is significantly thinner than both the proximal and the distal ends. The tibia (140% of femoral length) is proportionally shorter than in *Anchiornis* (160%) and comparable to those of *Eosinopteryx* (140%) and *Archaeopteryx* (142%) and distinctly more elongate than in more crownward avialans (e.g., *Jeholornis* (117%), *Confuciusornis* (117%)). The fibula is slender with a well-developed proximal end whereas the distal end does not reach the calcaneum. Metatarsals are not fused proximally as in *Anchiornis* and metatarsal III is transversely compressed, suggesting a sub-arctometatarsalian condition as in *Aurornis*, *Eosinopteryx*, *Anchiornis*, *Microraptor* and some dromaeosaurids and troodontids (Godefroit et al., 2013a; Godefroit et al., 2013b; Hu et al., 2009; Xu et al., 2011) (Fig. S3.13). Unlike troodontids, metatarsal IV is not more robust than metatarsal II and III (Xu et al., 2003). As in *Mei*, *Anchiornis*, and some dromaeosaurids, the distal articulation of

metatarsal II is merely as wide as that of metatarsal III (Xu et al., 1999). Metatarsal V is preserved and reach one-third the length of metatarsal IV. Pedal digit I is relatively short and lies on the medioplantar side of metatarsal II as in *Archaeopteryx* and *Aurornis*. Pedal digit II lacks the specialised morphology of deinonychosaur-grade paravians. The phalanges of pedal digit III and IV are slender and do not significantly increase in length proximodistally.

Additional information on feather preservation in *Serikornis sungei*

The plumage of PMOL-AB00200 is exceptionally well-preserved as imprints. Pennaceous feathers are present on the body, limbs and along the tail. Due to the opisthotonic posture of *Serikornis*, feathers from the neck, the back and the pelvic region are overlapping, hiding details from the feather structure. However, two body feathers from the back region are well-exposed and show a well-defined rachis with clearly detached barbs (see Fig. 3.3B). Elongated pennaceous feathers present along the hindlimbs were recovered after a supplementary preparation of the fossil. Although this secondary preparation was performed as accurate as possible, total number of tibial and metatarsal feathers remains impossible to determine. The total number of forelimb remiges remains also unclear due to the overlap of the feathers in the anterior region. However, feathers are distinct enough in their distal region to observe a thin straight rachis which does not narrows abruptly towards the distal end, unlike in *Archaeopteryx* (Foth et al., 2014; Wellnhofer, 2009). All remiges from forelimbs and pennaceous feathers from hindlimbs present an identical configuration in having a well-defined rachis and well-preserved barbs. In all pennaceous feathers vanes are symmetric with an angle between rachis and barbs that varies between 10.1° and 20.8° (for comparison, the angle between rachis and barbs in *Archaeopteryx* varies between 22° and 25°) (Foth et al., 2014). As in *Anchiornis*, anterior remiges are short, symmetrical, and straplike, with slender rachises, and there is no significant difference in length between the coverts and the remiges (Longrich et al., 2012). Considering this configuration, *Serikornis* is closer to *Anchiornis* than *Archaeopteryx* in possessing a more primitive wing feather arrangement. Width of the tibial feathers is comparable to that of anterior remiges (respectively 3.18 mm and 3.85 mm).

Feathers of the tail are plumulaceous and composed of bundles of filaments that are joined together proximally and remain nearly parallel as they extend distally, as in *Aurornis* and *Eosinopteryx*. In the proximal third, filaments are relatively long (29 mm) and rapidly decrease in length to reach their minimal length in the middle part of the tail (13.5 mm). The distal part of the tail is completely devoid of true pennaceous rectrices as in *Aurornis* but is covered by short tectrices.

Close examination under binocular magnifier and SEM microscope of all these pennaceous feathers has failed to find barbules, a conclusion also confirmed by the absence of basal expansions on the barbs at the *pennula* (i.e., the insertion point of the barbules) (Lucas & Stettenheim, 1972b). In living birds, the basal width of barbules (from dorsal flange to ventral rim) is taxonomically variable: 23 ± 1 µm in the

common shelduck (D'Alba et al., 2014) up to 80 µm in the Single Comb White Leghotn Chicken (Lucas & Stettenheim, 1972a). The absence of barbules in *Serikornis* can be regarded as a real feature rather than a taphonomic artefact since long and slender integumentary structures have been found on the neck region of this specimen, having a mean width of 43 ± 2 µm (Fig. S3.13).
This find suggests that the close arrangement of vanes present in some maniraptorans (e.g., *Protarcheopteryx*, *Anchiornis*) cannot be considered as an evidence of barbules (Ji et al., 1998; Xu et al., 2003).

Aerodynamic performance of *Serikornis sungei*

One of the main prominent characters associated with flight in modern birds is the elongated asymmetrical primary feathers of the wing which are composed with a trailing vane that is wider than the leading vane (Feo et al., 2015). This asymmetry in the primaries allows a stabilization of the feathers at an effective angle of attack (Longrich et al., 2012; Lucas & Stettenheim, 1972c) and permits a twist of the leading vane on the precedent trailing vane in order to form a continuous airfoil surface (Longrich et al., 2012). *Serikornis sungei* bears symmetrical remiges on forelimbs and hindlimbs, making them impossible to resist to the air pressure created during hypothetical power flight. However this assumption can be ruled out whether the feathers extend parallel to the airstream. In this case, they are not subject to a torsional moment about their long axis and does not need to be asymmetrical. Remiges of *Serikornis* are not as sophisticated or as efficient as those of *Archaeopteryx* and derived birds but they could have played a role during a glide flight.
The apparent absence of barbules on the primaries does not allow them to hold ramis together when air pressure is applied on the vanes during a power flight (Lucas & Stettenheim, 1972c) but the relative stiffness of the vanes could have be used to resist the air pressure during a glide flight.
The total number of tibial and metatarsal feathers remain unknown even if an accurate preparation was performed on PMOL-AB00200. These feathers are symmetric as it is the case for pennaceous feathers of anterior wings. The uncovered tibial feather is at least 64 mm long whereas the length of the metatarsal pennaceous feathers is indeterminable. Contrary to *Microraptor* which shows possible aerodymanic adaptations in having asymmetric metatarsal feathers longer than twice the length of the tibial feather (Foth et al., 2014), *Serikornis sungei* should use these feathers not in relation to flight, but for other functions (e.g. display, breeding, protection) as in *Archaeopteryx*, *Anchiornis* and, *Sapeornis* (Godefroit et al., 2013a; Godefroit et al., 2013b; Ji et al., 1998).

Laminography on *Serikornis*

This technique is based on the relative motion of the X-ray source, the detector and the object (Gondrom et al., 1999). The X-ray source and the detector are moved synchronously in opposite directions (Gondrom et al., 1999). This non-destructive

technique is generally used for inspection of large flat components (e.g., mounted electronic device). To the best of our knowledge, this technique has never been applied in palaeontology.

SEM investigation and EDS analysis

Two samples were collected on the tibial feather (Fig. S3.14). They both were studied under Scanning Electron Microscopy (SEM – gold-coated, 5 kV) and Energy-Dispersive X-ray analysis (EDS – 15kV) in order to determine their elemental composition. Sample 1 has been analyzed on nine different points located beneath the surface whereas elemental mapping was performed on sample 2 in order to compare the composition of dark (barbs) and lighter (sediment) areas (Fig. S3.7) of the posterior remige.

According to SEM and EDS analyses, feather samples mostly contain (Al-rich) phyllosilicates, but pyrite framboids and carbonate crystals have also been observed (Fig. S3.15A, B). Elongate imprints have been observed in Sample 1 (Fig. S3.15C, D): they are densely packed and randomly oriented, as it has already been observed for melanosome-like microbodies (Li et al., 2012a; Lindgren et al., 2015). It is difficult to differentiate them from microbodies like bacteria or melanosomes at this stage of the study. Other microbodies - spherical ones - are observed in the same specimen (Fig. S3.15E). EDS analyses show they do not contain carbon but, in some cases, high amounts of iron and oxygen. They probably correspond to iron oxide crystals (Zhu et al., 2005b).

Carbon was not detected in sample 1 and the analysed areas contain high levels of O, Si and Al, indicating Al-rich phyllosilicates (probably kaolinite). Some areas are particularly rich in iron (34 to 55%) but lack sulphur. Therefore, they do not contain pyrite or other sulfide and sulfates, but their shape indicates they might rather represent iron oxide pseudomorphs after pyrite. Carbon has been detected in each analysed area of sample 2. Mapping shows that elemental distribution is rather homogenous for all elements, except for O, C, and Ca (Table S3.4). Oxygen-rich and carbon-rich areas appear as elongate parallel structures (Fig. S3.16), while calcium-rich zones appear in small patches. Carbon-containing areas roughly follow the barb imprints, suggesting that these structures are enriched in C compared to the rest of the feather sample. Indeed, they contain abundant C, nearly 40% (in mass). Those C-enriched areas could, therefore, support the preservation of soft tissues in *Serikornis*. Phyllosilicates, pyrite and other minerals could have played a role in the particularly good preservation of *Serikornis* plumage (Leng & Yang, 2003; Zhu et al., 2005b).

Phylogenetic nomenclature

We adopt, in this paper, the following definition of higher-level theropod taxa (Godefroit et al., 2013a).

- Coelurosauria, the most inclusive clade containing *Passer domesticus* Linnaeus, 1758 but not *Allosaurus fragilis* Marsh 1877, *Sinraptor dongi* Currie and Zhao, 1993, and *Carcharadontosaurus saharicus* Depéret and Savornin, 1927.
- Paraves, the most inclusive clade containing *Passer domesticus* Linnaeus, 1758 but not *Oviraptor philoceratops* Osborn 1924.
-Eumaniraptora, the most inclusive clade containing *Passer domesticus* Linnaeus, 1758 but not *Anchiornis huxleyi* (Xu et al., 2009a).
- Avialae, the most-inclusive clade containing *Passer domesticus* Linnaeus, 1758 but not *Dromaeosaurus albertensis* Matthew and Brown, 1922 or *Troodon formosus* Leidy, 1956.
- Deinonychosauria, the most-inclusive clade containing *Dromaeosaurus albertensis* Matthew and Brown, 1922 but not *Passer domesticus* Linnaeus, 1758.
- Dromaeosauridae, the most-inclusive clade containing *Dromaeosaurus albertensis* Matthew and Brown, 1922 but not *Passer domesticus* Linnaeus, 1758 or *Troodon formosus* Leidy, 1956 (according to our phylogenetic analysis).
- Troodontidae, the most-inclusive clade containing *Troodon formosus* Leidy, 1956 but not *Passer domesticus* Linnaeus, 1758 or *Dromaeosaurus albertensis* Matthew and Brown, 1922.

Phylogenetic analysis

The data matrix (1732 characters for 130 Operational Taxonomic Units) was analysed using the TNT software package (Goloboff et al., 2008). The stem-archosaur *Euparkeria* and the basal theropods *Herrerasaurus* and *Tawa* were used as outgroups, with the former rooting the analyses. We performed 100 "New Technology search" analyses with default settings, then explored the shortest tree islands found during first analyses by tree-bisection-reconnection, holding all shortest trees found. Bremer support was assessed by computing decay indices with TNT, version 1.5.

Analysis with TNT recovered 96 shortest trees each of 5743 steps in length. The strict consensus of the shortest trees recovered is well-resolved (Fig. S3.10). In all recovered shortest trees, *Serikornis* is found as sister-taxon of *Eosinopteryx*; they form a clade with *Aurornis* and *Pedopenna* placed among basal paravians, which, in turn, is sister group of the node including *Anchiornis* and Eumaniraptora.

Unambiguous synapomorphies of the main paravian nodes resulted by the analysis of the first phylogenetic dataset (numeration refers to the character statement in Godefroit et al., 2013a):

Paraves: 154.0: marginal teeth crowns asymmetrical (curved apicodistally); 252.0: scapula shorter than 90% humerus; 272.1: humerus mid-shaft width comparable to femur mid-shaft; 333.1: manual ungual flexor tubercles prominent; 353.1: middle-caudal neural spines absent; 360.1: proximal caudal centra box-like; 378.0: ilium shorter than 60% femur; 386.0: postacetabular surface reduced; 395.1: processus supratrochantericus present; 503.1: penultimate phalanx on 3rd toe elongate; 560.1: mt IV shaft uncompressed; 1362.1: lacrimal ventral process inset; 1435.1: preantorbital ramus of maxilla shallow; 1505.1: pedal ungual flexor tubercles prominent; 1688.1;

metatarsal pennaceous feathers present; 1719.1: scapula glenoid extended laterally; 1725.1: caudal neural spines I-V abruptly reduced.

Unnamed node ("*Aurornis*-like forms" + (*Anchiornis* + Eumaniraptora)): 107.1: ascending ramus of quadratojugal short; 421.1: ischium shorter than 60% pubis; 494.0: 2nd toe shorter than 4th; 505.1: 2nd pedal ungual enlarged; 832.1: anterior chevrons flattened; 1147.1: distal caudal centra laterally excavated; 1659.1: maxillary fenestra enlarged; 1697.1: distal carpal 3 fused to medial carpals.

Unnamed node ((*Aurornis* + *Pedopenna*) + (*Eosinopteryx* + *Serikornis*)): 76.1: frontals anterior margin triangular; 478.0: length of metatarsal III less than half tibia; medial distal crest on femur present; anterior margin of ilium straight; posterodorsal process of lacrimal forms more than 1/3 of lacrimal height.

Unnamed node (*Aurornis* + *Pedopenna*): pedal phalanx P1-IV not shorter than pedal phalanx P1-II; metatarsal IV not shorter than metatarsal III; pedal phalanx P1-II shorter than ¼ of metarsal II.

Unnamed node (*Eosinopteryx* + *Serikornis*): gracile metacarpal I (width less than ¼ length); no more than 27 caudal vertebrae; pubic peduncle of ilium longer than acetabulum.

Unnamed node (*Anchiornis* + Eumaniraptora): 394.1: pubic peduncle of ilium deeper than ischiatic; 513.1: rectrices present; 542.1: obturator process of ischium acuminate; 617.1: distal end of pedal phalanx P1-II expanded.

Eumaniraptora: 56.1: ventral ramus of lacrimal anterodorsally oriented; 238.1: dorsal parapophyses stalked; 420.0: ischium straight; 682.0: dentary lateral groove short; 807.1: ulna bowed; 1250.1: remiges asymmetrical.

Avialae: 50.1: subnarial process of nasal absent; 80.0: parietals unfused; 124.1: subotic recess present; 154.1: maxillary/dentary teeth not curved mesiodistally; 154.1: maxillary/dentary teeth lacking carinae; 188.0: posterior surangular foramen small; posterior dorsal pleurocoels present; no more than 27 caudal vertebrae; 390.1: pubic peduncle of ilium longer than acetabulum; 398.1: preacetabular process of ilium longer than postacetabular; 548.1: pedal ungual I not smaller than unguals III and IV; 587.1: axial neural spine broadly convex; 603.1: cuppedicus fossa confluent with pubic peduncle; 683.1: basipterygoid processes lateroventrally directed; 1104.1: scapular only sharply rimmed posterodorsally; 1375.1: scapular acromion lacking coracoid facet; 1384.1: furcula robust; 1585.1: proximodorsal process of ischium trapezoidal; 1688.1: pennaceous feathers on metatarsus absent; 1732.0: metacarpals II-III shafts contact not extended distally.

Deinonychosauria: 3.0: anteroventral margin of premaxilla blunt; 34.1: cheek teeth small and >75; 272.0: humerus mid-shaft width smaller than femur; 381.0: supracetabular crest reduced; 441.1: distal femur not wider than long; 503.0: penultimate phalanx on 3rd toe short; 545.1: mt II trochlea placed more proximally; 687.1: pedal P1-I less than 25% mt II; 931.1: distinct brachial fossa on humerus; 1111.1: distal ulna flattened; 1113.1: cnemial crest prominent; 1659.0: maxillary fenestra reduced in size.

Feather evolution among Coelurosauria

We mapped the distribution of plumage features among coelurosaurian theropods, using the strict consensus of the shortest trees found by the phylogenetic analysis. Ambiguous character states were optimised using the delayed transformation option (i.e., assuming the minimum number of reversals necessary to explain the distribution of the character states).

Thickened "rachis-like" feathers are optimised as a maniraptoriform synapomorphy, being them reported in ornithomimosaurs (Zelenitsky et al., 2012), therizinosaurs (Xu et al., 2003) and pennaraptorans (Xu et al., 2003). Elongation of forearm feathers is optimised as a maniraptoran synapomorphy, pending the discovery of more complete feathers in ornithomimosaurs (Zelenitsky et al., 2012). The absence of true pennaceous feathers in *Serikornis*, *Eosinopteryx* and scansoriopterygids may indicate that the shared presence of rectrices and remiges in oviraptorosaurs (Ji et al., 1998) and eumaniraptorans (Xu et al., 2003) is due to convergence. The evolution of elongate feathers covering both tibiotarsus and metatarsus (tetrapterygian condition) is optimised as a paravian synapomorphy. Scansoriopterygids secondarily lost the tetrapterygian condition; together with the presence of a patagium with aerodynamic function in these theropods (Xu et al., 2015), this combination of feature indicates that feathers were not selected for an aerodynamic purpose among the first paravians with scansorial adaptations. The presence of asymmetrical pennaceous remiges is optimised as a synapomorphy of Eumaniraptora, and further suggests that the evolution of aerodynamic function in the feathers is an adaptation exclusively of deinonychosaurs and birds, absent in more basal paravians. Avialans are characterised by the loss of metatarsal feathers (this features is optimised as a secondary re-gain among *Sapeornis* and is reported in some enantiornithines (Zheng et al., 2013b). Tibial feathers are also optimised as secondarily lost in jeholornithids and ornithothoracines. Thus, the origin of avialans (the "*Archaeopteryx* node") among Paraves is characterised, in the plumage, by the progressive reduction and loss of the tetrapterygian condition (Zheng et al., 2013b), and in the skeleton by the elongation of the forelimb relative to the hindlimb: this combination supports the origin of the avian-like flight style (i.e., exclusively forelimb-based) among the early birds, but not among more basal paravians. The alula evolved convergently among ornithothoracine birds and microraptorines, in combination with the evolution of a relatively shorter first manual digit in both groups (Xu et al., 2003).

Character optimisation indicates that *Eosinopteryx* and *Serikornis* share the secondary loss of thickened forearm rachises: this supports the scenario suggested by Godefroit et al. (2013a) on secondary reduction of plumage among early paravians. Alternatively, this may indicate that thickened rachises in these taxa were an ontogenetically-controlled feature present exclusively among mature individuals, as suggested for ornithomimosaurs (Zelenitsky et al., 2012).

Chapter 4

This chapter is based on: Cincotta et al., *to be included in a paper*

Synchrotron micro X-ray fluorescence (μ-XRF) and absorption spectroscopy (μ-XANES) suggest the presence of eumelanin pigment in the feathers of *Kulindadromeus zabaikalicus* (Middle Jurassic of Siberia)

Abstract

Since the first discoveries of feathers closely associated with the skeletons of non-avian theropod dinosaurs, it is widely recognised that the ancestors of birds also possessed feathers. More recently, elongated integumentary structures interpreted as primitive feathers have been reported in ornithischian dinosaurs, the clade not related to birds. The study of epidermal appendages in non-theropod dinosaurs brings new data about the origin and evolution of feathers. Here, we investigate the chemical composition of the elongate filaments from the basal neornithischian dinosaur *Kulindadromeus zabaikalicus* (Middle Jurassic of Siberia) using synchrotron μ-XRF elemental mapping and μ-XANES spectroscopy. μ-XRF mapping shows that these structures interpreted as primitive feathers are enriched in Cu, and to a lesser extent in Ca, compared to the surrounding sedimentary matrix. μ-XANES performed at the Cu K-edge reveals that their Cu-coordination chemistry is similar to organic Cu in modern bird feathers and in natural eumelanin, as previously reported for Cretaceous and Eocene fossil bird feathers. This would indicate that the feathers of *Kulindadromeus* were pigmented by eumelanin, suggesting that primitive feathers could preserve evidence of pigments in other basal dinosaurs.

1. Introduction

Preservation of tissue morphology does not imply that tissues retain their original organic compounds. Fossil soft tissues exhibit different modes of preservation, such as carbonaceous remains (e.g., Li et al., 2010; Lindgren et al., 2015), calcium phosphate (Allison & Briggs, 1993; Briggs et al., 1993), pyrite (Briggs et al., 1991; Farrell et al., 2013a; Leng & Yang, 2003), clay minerals (Gabbott et al., 2001; Martin et al., 2004), aluminosilicates (Butterfield et al., 2007) or a combination of these minerals (Wilby et al., 1996). In many, if not most, cases, most of the original organic compounds in soft tissues are lost due to their diagenetic transformation into authigenic minerals. Kerogenisation – transformation to kerogen - of organic matter leads to the alteration and loss of labile organic functions, with generally first a loss of oxygen-bearing functions (e.g., Meyers & Ishiwatari, 1993). The cross-linking by hydrogen bonds and the formation of long hydrocarbon chains are common processes in the kerogenisation of organic material. The transformation of organic compounds into kerogen essentially consists of the depolymerisation of macromolecules and their recondensation. Long, heavy, molecules are segmented into shorter molecules. These mono- or oligomers condense with other substances to form longer, more stable, and insoluble polymers (De Leeuw & Largeau, 1993). The organic compounds are eventually transformed into kerogens, the insoluble fraction of the organic matter. Selective preservation of the most resistant compounds was alternatively proposed for the formation of kerogens (Tegelaar et al., 1989). Highly resistant macromolecules, such as lignin and sporopollenin (De Leeuw & Largeau, 1993), may be selectively preserved during diagenesis and, therefore, constitute a significant part of the kerogen composition. In some cases, however, traces of original organic molecules may be preserved in the fossil and detected by accurate methods. The high brightness and tenability of the synchrotron beam makes synchrotron-based X-ray spectroscopy and imaging methods unique, non-invasive and very sensitive tools to characterize major-to-trace elemental composition, including concentrations as low as tens of ppm, of fossils at the microscale (Bergmann et al., 2012; Gueriau et al., 2016). Particularly, μ-XANES has proved its worth in determining the speciation of elements in molecules and therefore allowing discrimination between inorganic and organic molecules (Bergmann et al., 2012; Gueriau et al., 2016).

Here, we analyse the chemical composition of fossil integumentary structures belonging to a small neornithischian dinosaur, *Kulindadromeus zabaikalicus* (Godefroit et al., 2014), from the Middle Jurassic of Siberia (see Chapter 5). The aim of this study is to obtain new data about the chemical composition of fossil feathers - especially from a non-theropod dinosaur - and to discuss the preservation of ancient molecules in fossil soft tissues. Micro X-ray fluorescence (μ-XRF) is applied to collect information on the elemental composition of the feathers, whereas micro X-ray absorption near-edge spectroscopy (μ-XANES) provides data on the chemical speciation of copper.

2. Material and methods

The Kulinda locality, situated in Transbaikal region (Siberia, Russia), yielded abundant remains of a primitive neornithischian dinosaur, *Kulindadromeus zabaikalicus* (Fig. 4.1). Traces of well-preserved skin, scales, and three types of integumentary structures all interpreted as primitive feathers were found closely associated with bones. Dating of the Kulinda locality indicates that this taxon lived during the Bathonian (Middle Jurassic) (see Chapter 5). Three successive monospecific bone beds were excavated at Kulinda but soft tissues were preserved in the lowest layer only. The fossil material, including bones and the soft tissues, was enclosed in an iron-rich volcaniclastic matrix. Petrological studies showed that the locality likely consists of several successive mud and grain flows that transported disarticulated carcasses on an alluvial plain. The bone bed that bears soft tissues shows a somehow different depositional setting. There, articulated carcasses were probably quickly recovered by mud flows, allowing their exceptional preservation. The analysed integumentary structures consist of monofilaments that were connected to the abdominal part of the skeleton of *Kulindadromeus zabaikalicus* (Fig. 4.2). These filaments are relatively thin, with a constant width of about 400 µm, and a length of at least 15 mm. As the filaments are embedded partially within the slab it was not possible to assess their total length, we therefore consider filaments being up 15 mm long. They present a discontinuous pattern probably linked to the preferential preservation of chemically more resistant portions of the feathers.

Scanning electron microscopy (SEM)

SEM analyses of the *Kulindadromeus* feathers were performed under low vacuum with an environmental QUANTA 200 (FEI) scanning electron microscope (RBINS, Brussels) at potentials of 20-30 kV and using working distances ranging between 8 and 15 mm. EDS analyses of single points and areas were performed using an environmental QUANTA 200 (30 kV, working distance of 10 mm).

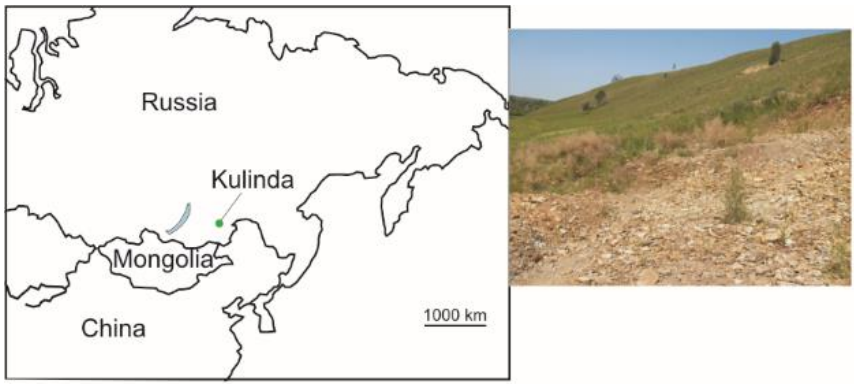

Figure 4.1. Location of the Kulinda locality (Transbaikal region, Russia). The picture on the right shows the hill slope on which three bone beds have been excavated and yielded remains of the small basal neornithischian dinosaur *Kulindadromeus zabaikalicus*.

Synchrotron micro X-ray fluorescence (μXRF)

μ-XRF maps were collected at the DiffAbs beamline of the SOLEIL synchrotron (Gif-sur-Yvette, France), using an excitation energy of 9.7 keV, selected for excitation of K-lines from phosphorus to zinc. The X-ray beam was collimated by two bendable mirrors, monochromatised using a Si (111) double-crystal monochromator (energy resolution of 0.7 eV) and focused using Kirkpatrick-Baez mirrors down to a spot size of 9×6 μm^2 (H×V, full width at half maximum, fwhm). The sample was mounted on a xyz scanner stage, allowing ± 12 mm movements with micrometre accuracy. The sample was oriented at 45° to the incident beam and at 45° to the XRF detector, a four element silicon drift detector (SDD, Vortex ME4, total active area: 170 mm^2) placed in the horizontal plane. Counting time per pixel was set to 250 ms to attain good statistics on trace elements at this energy. All the elemental distributions presented herein have been reconstructed from a full spectral decomposition performed with the PyMCA data-analysis software (Solé et al., 2007) using batch-fitting procedure, Pseudo-Voigt peak shape and polynomial baseline subtraction. Semi-quantitative concentrations were obtained in the process using experimental parameters, considering corrections for a claystone matrix reabsorption (defined as follows based on XRD measurements: SiO_2 48%, $Al_2Si_2O_5$ 19%, $KAlSi_3O_8$ 16.6%, et FeO(OH) 17%), and a photon flux of 1.4×10^9 photons.s^{-1} (estimated by using [Fe] as an internal standard). In order to extract the elemental concentrations for the feathers and the surrounding sedimentary matrix separately (Table 4.1), the Cu map (under the control of an optical view of the sample) was manually segmented to divide two sets of pixels corresponding to the feathers and sediment, respectively.

Figure 4.2. Elongate integumentary structures from *Kulindadromeus zabaikalicus*, interpreted as feathers (Godefroit et al., 2014). Synchrotron analyses were performed on the area delineated by the white box.

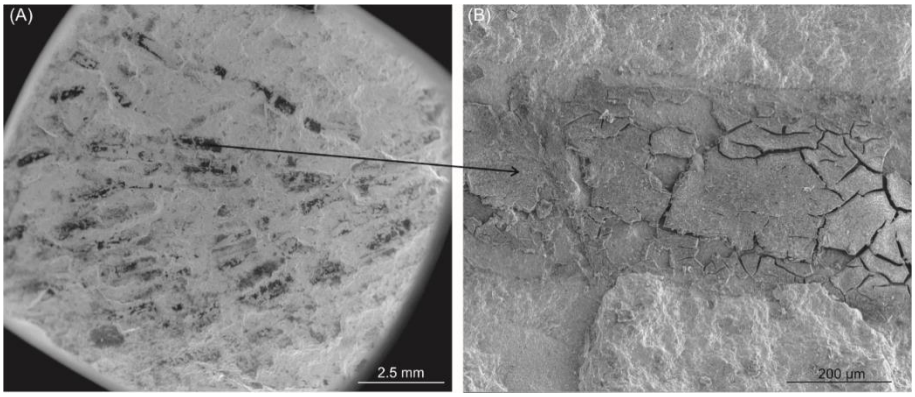

Figure 4.3. Scanning electron microscope (SEM) images of elongate epidermal structures from *Kulindadromeus*. (A) the elongate integuments are not homogeneously preserved but rather form discontinuous structures, (B) close up of the dark part of a filament showing an altered organic layer, well-differentiated from the embedding sedimentary matrix.

Micro X-ray absorption near-edge spectroscopy (µXANES)

µ-XANES measurements at the Cu K-edge were performed in the 8945–9135 eV range with 0.5 eV step size in the XANES region (8955–9015 eV), using the same geometry and beam size of 9×7 μm^2 (H×V fwhm). The counting time was 5s per energy step. Energy calibration was performed by setting the first edge inflection point of a copper foil at 8979 eV. Spectra were normalised and processed with the Athena software (Ravel & Newville, 2005), and the copper foil spectrum was corrected from self-absorption.

3. Results

Structure of *Kulindadromeus* feathers

Scanning electron microscopy (SEM) images of the elongate filaments show that they are preserved as a thin dark layer on the surface of the rock sample (Fig. 4.3A,B). Energy dispersive spectroscopy (EDS) indicate that these monofilaments are likely preserved as carbonaceous residues (Fig. 4.4A,B). Traces of sulfur were also detected, although no sulphur-containing minerals, such as pyrite, were observed. Filaments are not preserved on their whole surface, only short dark segments are preserved and separated by lighter areas where the sedimentary matrix is visible, only, and where no carbonaceous film is visible. The carbonaceous layer presents a discontinuous, altered surface (Fig. 4.3B), under which it is possible to observe, in some places, clusters of small granules, tightly packed together (Fig. 4.5).

Chemical composition

µ-XRF analysis of the monofilaments of *Kulindadromeus* reveals the presence of Ca and transition metals in the sample (Fig. 4.6). The µ-XRF maps (Fig. 4.7) display the relative concentration of copper, iron and manganese in the fossil and its embedding

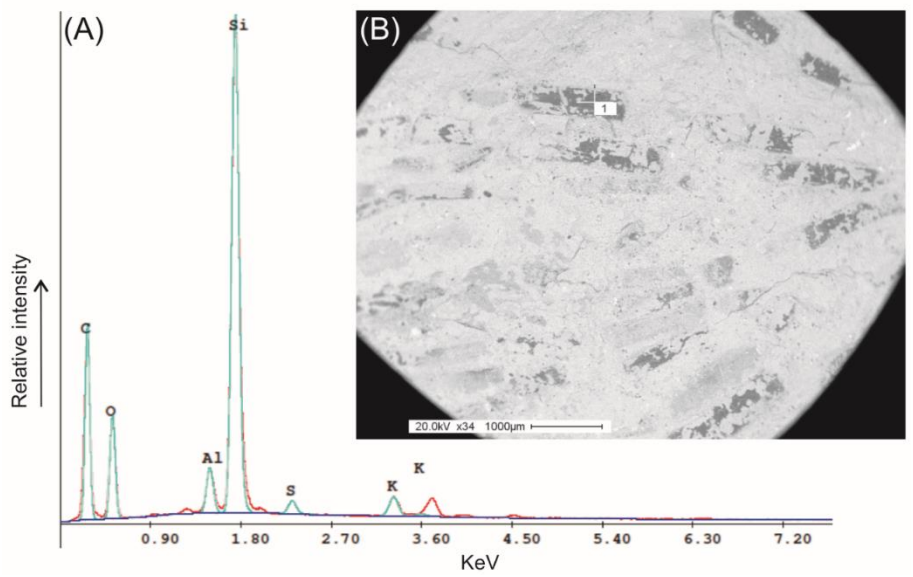

Figure 4.4. Energy X-ray spectroscopy (EDX) of elongate integumentary structures from *Kulindadromeus*. (A) the spectrum shows that carbon is present in the soft tissue, as well as sulfur. The silicon signal is linked to the contribution of the underlying sediment. (B) location of the analysis point.

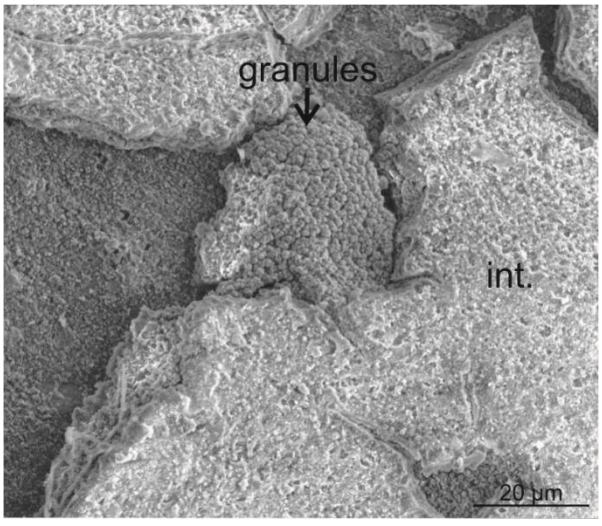

Figure 4.5. SEM image of the surface of one elongate integumentary structure (int.) showing the spherical granules located just underneath the surface, visible in altered areas.

matrix. The false colour map clearly shows a particular enrichment in copper in the preserved soft tissues, and not in the sediment. The elongate morphology of the filaments is easily recognisable due to their higher content in Cu. Among the other detected elements, only Ca is also more concentrated in the filaments than in the

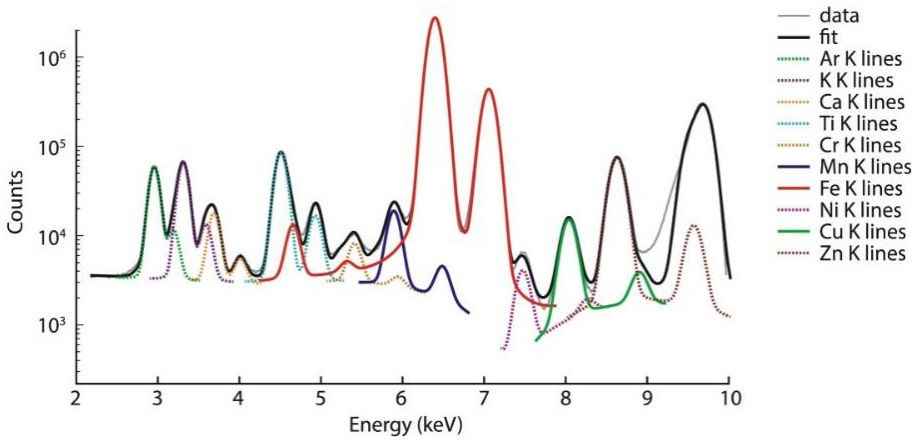

Figure 4.6. Mean Synchrotron XRF spectrum collected from the box area shown in Fig.4.2, displaying its elemental composition.

sediment (Table 4.1) and follows, yet to a lesser extent, the same concentration pattern as Cu (Fig. 4.8). As already revealed by XRD quantifications, Fe and K predominate, Ca, Ti and Zn are minor elements, and V, Cr, Mn, Ni and Cu are present at trace levels (tens to hundreds of ppm; Table 4.1).

The μ-XANES of the elongate filaments was performed at the Cu K-edge due to the particular enrichment of Cu in the fossil and its known properties as a chelator in melanin (e.g., Cesarini, 1996; Hong et al., 2004; Szpoganicz et al., 2002). The technique measures the absorption of the incident photon beam at different energies - typically ranging between 8945 and 9135eV for Cu - in the fossil. The peaks further observed on μ-XANES spectra are limited to specific ranges of energy, which reflect a specific chemical environment for the studied element. Here, the resulting Cu K-edge μ-XANES spectrum of the feathers of *Kulindadromeus* (Fig. 4.9) shares strong similarities with spectra showing Cu-coordination in organic compounds, in this case, natural eumelanin (Wogelius et al., 2011). Comparison with other Cu-containing compounds from literature have not shown any resemblance with inorganic Cu-coordination.

Table 4.1. Comparison between elemental concentrations obtained from laboratory technique and synchrotron-based µ-XRF quantifications (wt% or ppm)

analytical technique	sample	K	Ca	Ti	V	Cr	Mn	Fe	Cu	Zn
XRD	sed	2.30%						10.70%		
SEM-EDX	sed	5%								
µ-XRF	**feat.**	5.06%	0.55%*	1.12%	221ppm	113ppm	608ppm	12.78%	202ppm*	0.12%
µ-XRF	sed	4.87%	0.27%	1.07%	174ppm	101ppm	541ppm	10.12%	89ppm	914ppm

°mean semi quantitative concentrations from 1413 pixels of the 75x75 µm² pixel size map (see Fig.4.8 for location of the pixels); °°mean semi quantitative concentrations from 12258 pixels of the 75x75 µm² pixel size map (see Fig.4.8 for location of the pixels); * significantly higher concentrations in the feathers than in the sediment (2.04x and 2.27x for [Ca] and [Cu] respectively.

4. Discussion

Spherical microbodies have been observed by SEM within the structure of the elongate integumentary structures of Kulindadromeus. Carbon and sulphur have been detected by EDS, in addition to elements characterising the underlying sedimentary matrix (i.e., Si, Al, and K).

Similar spherical structures were observed in fossil ink sacs and were interpreted as eumelanin granules (Glass et al., 2013; Glass et al., 2012b). The current state of this work does not allow to certify - with the SEM - whether these granules are preserved eumelanosomes, or authigenic minerals. The presence of sulfur in the feathers may be related to its abiogenic incorporation into organic matter during kerogenisation of the

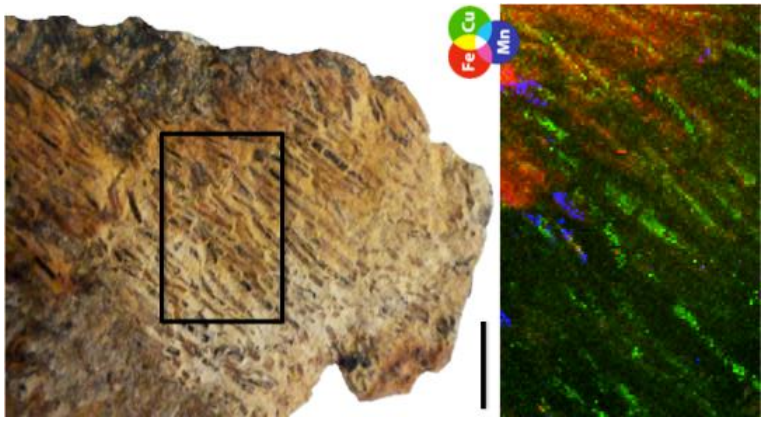

Figure 4.7. Synchrotron XRF mapping of trace elements contained in the fossil feathers. False color map displays the relative concentration of Fe, Cu, and Mn in the black box area. Scale bar = 5 mm.

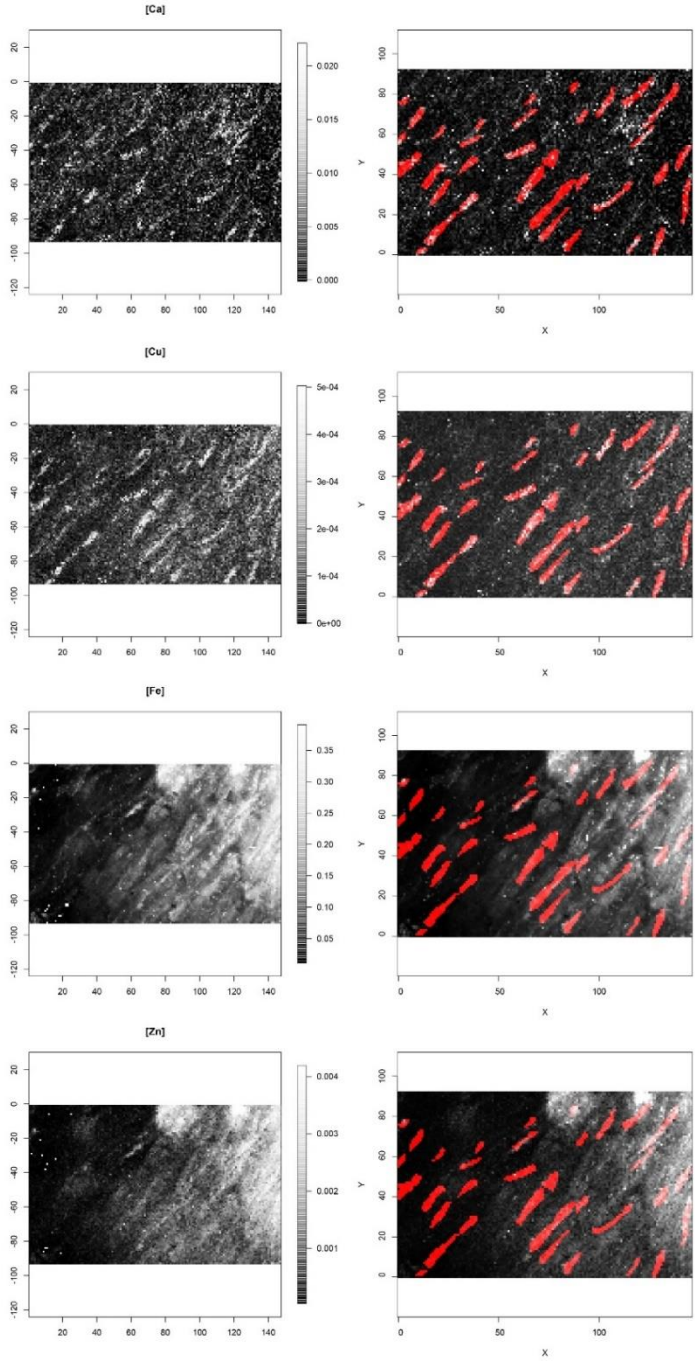

Figure 4.8. Synchrotron XRF concentration maps of Ca, Cu, Fe, and Zn. On the right, the red mask shows the location of the pixel considered to correspond to the integuments. Cu provides the best fit for the elongate filaments.

soft tissues (Sinninghe-Damsté & De Leeuw, 1990; Sinninghe-Damsté et al., 1989).

This process is known as "sulfurisation" and occurs during early diagenesis. Sulfur is also a significant trace element present in the structure of phaeomelanin, the red-yellow pigment. An alternative hypothesis to explain its presence in the feathers of the dinosaur might be that it corresponds to preserved traces of phaeomelanin. Further work needs, however, to be conducted in an attempt to study the extensive chemical composition of these granules and to precise their origin. It has been shown that melanin has a particular affinity for certain monovalent and divalent metal ions. Among these cations, Pb^{2+} and Cu^{2+}, respectively, represent the two preferentially bound elements in melanin (Larsson & Tjälve, 1978). These trace elements are likely incorporated in the free carboxyl groups of the pigment.

In figure 4.9, one can see that the position of the maximum intensity peak in the µ-XANES spectra is either shifted or does not fit at all (see the arrows) with those of inorganic compounds, whereas it fits well with that of a modern bird feather. It suggests that Cu-coordination in the fossil is rather close to Cu-coordination in modern feathers, where it is related to the eumelanin (Hong et al., 2004; Wogelius et al., 2011). The preferential enrichment of metals, and in particular copper, has

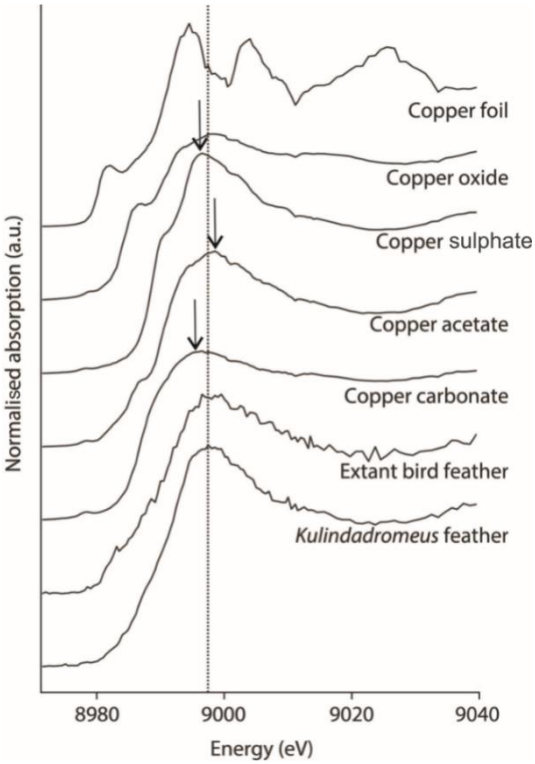

Figure 4.9. µ-XANES spectra at the Cu K-edge for the fossil elongate structures from *Kulindadromeus*, and a modern bird feather. Spectra have also been collected from five inorganic compounds for comparative purpose. The maximum peak intensity is indicated by the vertical dashed line.

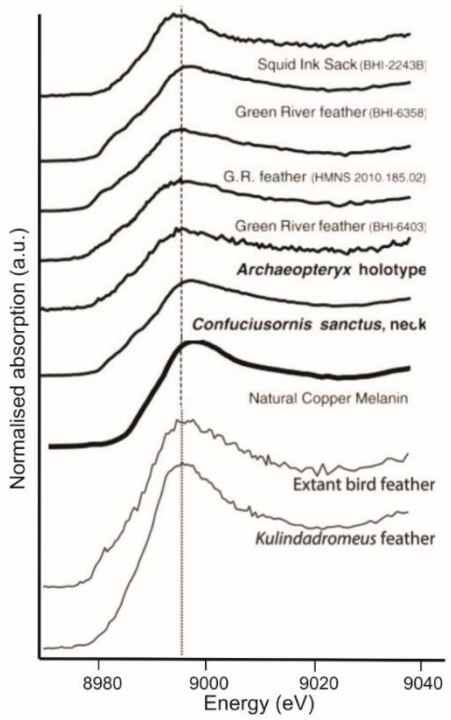

Figure 4.10. Comparison of the μ-XANES spectra at the Cu K-edge for the fossil feathers of *Kulindadromeus* with those from natural melanin and fossil bird's feather (from Wogelius et al., 2011).

previously been reported in fossil feathers from the Cretaceous bird *Confuciusornis sanctus* from the Jehol biota and isolated Eocene bird feathers from the Green River Formation (Wogelius et al., 2011). In their paper, the authors show, using comparable techniques (i.e., μ-XRF and μ-XANES) and protocol, that the Cu-coordination in the fossil bird feathers is similar to that of natural eumelanin (Wogelius et al., 2011). μ-XANES spectrum of *Kulindadromeus* feathers is similar to that of natural melanin and feathers of fossil birds (Fig. 4.10). The affinity of Cu for melanin is well known (Larsson & Tjälve, 1978; Hong et al., 2004; Szpoganicz et al., 2002). Then, the enrichment of Cu in the feathers, and not in the host sediment, may indicate that Cu was incorporated preferentially in melanin-containing structures. Due to their chelator properties, metals might be preserved in fossils even after melanin degradation and could therefore be used as biomarkers for ancient pigments. Further investigation should show whether Cu is authochtonous (linked to melanin *in vivo*) or was incorporated diagenetically in the feathers because of its affinity for melanin. For that purpose, tissues that do not contain animal melanin (e.g., plants) should be analysed using the same methodology. Here, synchrotron μ-XRF, together with μ-XANES, permitted to analyse and map trace elements contained in the fossil sample. This work

provided promising data about the preservation degree of the oldest feather structures found so far. The advantages of the methods we used is to analyse tissues using non-destructive methods, which does not require any sample preparation prior to analysis.

5. Conclusion

Substantial amount of carbon has been detected by SEM and EDS in the elongate integumentary appendages of *Kulindadromeus zabaikalicus* and not in the sediment, suggesting that there are preserved as carbonaceous thin films. Traces of sulfur, possibly of abiogenic origin, has been detected as well. Our results show that the feathers from the Jurassic dinosaur *Kulindadromeus zabaikalicus* are greatly enriched in copper relative to the surrounding sedimentary matrix. μ-XANES performed at the Cu K-edge reveals that their Cu-coordination chemistry is similar to organic Cu in modern bird feathers and in natural eumelanin, as previously reported for Cretaceous and Eocene fossil bird feathers (Wogelius et al., 2011). This would indicate that the feathers of *Kulindadromeus* were pigmented by eumelanin, suggesting that a wide range of primitive feathers could already contain pigments.

Section II

The Kulinda locality (Transbaikal region, Siberia) has yielded exceptional fossils that inform on the evolutionary history of feathers in dinosaurs. The remains of a small dinosaur, *Kulindadromeus zabaikalicus*, are associated with soft tissues. *Kulindadromeus* is situated at the base of the neornithischian clade, which is – unlike theropods - not related to birds. This taxon shows, in addition to epidermal scales, elongated appendages interpreted as primitive feathers. This section concerns the dating of *Kulindadromeus* remains with the aim to better constrain the timing of the evolution of feathers. The determination of the source and deposition processes of the bone beds, and the palaeoenvironmental reconstruction of the Kulinda locality, provide important data to understand in what environmental conditions *Kulindadromeus* lived. The state of preservation of the soft tissues is related to the palaeo-environmental conditions that prevailed at time of deposition but also to more recent weathering processes. The geochemistry of the Kulinda deposits is regarded here as a tool to understand the processes that led to the exceptional preservation of the *Kulindadromeus* soft tissues.

Chapter 5

This chapter is based on: Cincotta et al., *to be submitted*

A Middle Jurassic age for the neornithischian *Kulindadromeus zabaikalicus*, the oldest dinosaur with 'feather-like' structures from Siberia

Abstract

Diverse epidermal appendages, including grouped monofilaments, that closely resemble primitive feathers in non-avian theropods, are associated with skeletal elements in the primitive ornithischian dinosaur *Kulindadromeus zabaikalicus* from the Kulinda locality in south-eastern Siberia. This discovery suggests that feather-like structures did not evolve exclusively in theropod dinosaurs, but were instead potentially widespread in the whole dinosaur clade. Dating of the Kulinda locality is therefore particularly important for reconstructing the evolution of feather-like structures in dinosaurs within a chronostratigraphic framework. Here we present the first dating of the Kulinda locality, combining U-Pb radiochronological analyses on zircons and monazites and palynological observations. Concordia ages constrain the maximum age of the volcaniclastic deposits at 172.8 ± 1.6 Ma, corresponding to the Aalenian (early Middle Jurassic). The palynological assemblage collected in the *Kulindadromeus*-bearing volcaniclastic sediments is dominated by bisaccate pollen of *Pseudopicea* and spores of the bryophytes *Stereisporites*, and include taxa that are correlated to Bathonian palynozones from western Siberia, and then constrain the minimum age of the deposits. The new U-Pb ages, together with the palynological data, therefore provide evidence of a Bathonian age – between 168.3 ± 1.3 Ma and 166.1 ± 1.2 Ma - for *Kulindadromeus zabaikalicus*. This is older than the previous Late Jurassic to Early Cretaceous ages tentatively based on local stratigraphic correlations. A Bathonian age is highly consistent with the phylogenetic position of *Kulindadromeus* at the base of the neornithischian clade. *Kulindadromeus* is consequently the oldest known dinosaur with "feather-like" structures discovered so far. However, the presence of feather-like structures both in the ornithischian and theropod clades suggests that their origin dates back to the Middle Triassic.

1. Introduction

In 2010, a new *Konservat-Lagerstätte* was discovered in the Kulinda locality (south-eastern Siberia, Russia) by geologists from the Institute of Natural Resources, Ecology, and Cryology, SB RAS (Chita, Russia). The site has yielded numerous bones and associated integumentary structures belonging to the primitive ornithischian dinosaur, *Kulindadromeus zabaikalicus* (Godefroit et al., 2014). The soft-tissue remains include well preserved skin, epidermal scales, and three types of integumentary filaments all tentatively interpreted as feathers (see the reconstruction of the specimen in Supplementary Fig. S5.1). Monofilaments in ornithischian dinosaurs were previously reported in the basal ceratopsian *Psittacosaurus* (Mayr et al., 2002) and in the heterodontosaurid *Tianyulong* (Zheng et al., 2009b). However, the diversity and complexity of the elongated and compound integumentary structures in *Kulindadromeus* suggest that feather like structures were likely widespread within the whole dinosaur clade and potentially present in their last common ancestor (Godefroit et al., 2014). According to Alifanov and Saveliev (2014, 2015), the dinosaur fauna at Kulinda comprises three new taxa: the 'hypsilophodontian' ornithopods *Kulindapteryx ukureica* and *Daurosaurus olovus* (Alifanov & Saveliev, 2014), and the 'nqwebasaurid' ornithomimosaur *Lepidocheirosaurus natalis* (Alifanov & Saveliev, 2015). However, we consider these three taxa as nomina dubia, and very likely synonym of *Kulindadromeus zabaikalicus* (see the Supplementary Information for a discussion of the composition of the Kulinda dinosaur fauna).

The stratigraphic section at Kulinda belongs to the base of the Ukurey Formation in the Olov Depression. K-Ar radiochronological analyses on basalts and rhyolites from the base of the Ukurey Formation proposed ages between 153–157 Ma (Kimmeridgian) and 147–165 Ma (Callovian-Berriasian), respectively (Sinitsa, 2011a). Palaeoentomological and microfauna comparisons with the Glushkovo Formation in the Unda-Daya Depression also suggested an Upper Jurassic - Lower Cretaceous age for the Ukurey Formation (Sinitsa, 2011b; Sinitsa & Starukhina, 1986). The age of the Kulinda deposits has not been directly investigated so far.

Here, we refine the age of the Kulinda locality using U-Pb absolute dating of detrital zircons and comparisons of the palynomorph and megafloral assemblages collected in the volcaniclastic layers that have also yielded the *Kulindadromeus* fossils. Dating of the Kulinda locality is particularly important for a better timing of the evolutionary history of integumentary structures, including feathers, in dinosaurs. Thus, the oldest well-dated integumentary structures in dinosaurs are from paravian theropods (*Anchiornis*, *Xiaotingia*, *Eosinopteryx*, *Aurornis*, and *Serikornis*, Godefroit et al., 2013a; Godefroit et al., 2013b; Hu et al., 2009; Lefèvre et al., 2017; Xu et al., 2011) and the heterodontosaurid *Tianyulong* (Zheng et al., 2009b) from the Tiaojishan Formation, in the Daxishan section near the town of Linglongta, Jianchang County in western Liaoning Province (China). Recent U-Pb analyses have dated this section as Oxfordian, with an age ranging between 160.254 ± 0.045 Ma and 160.889 ± 0.069 Ma (Chu et al., 2016). The present chapter describes the depositional history of the

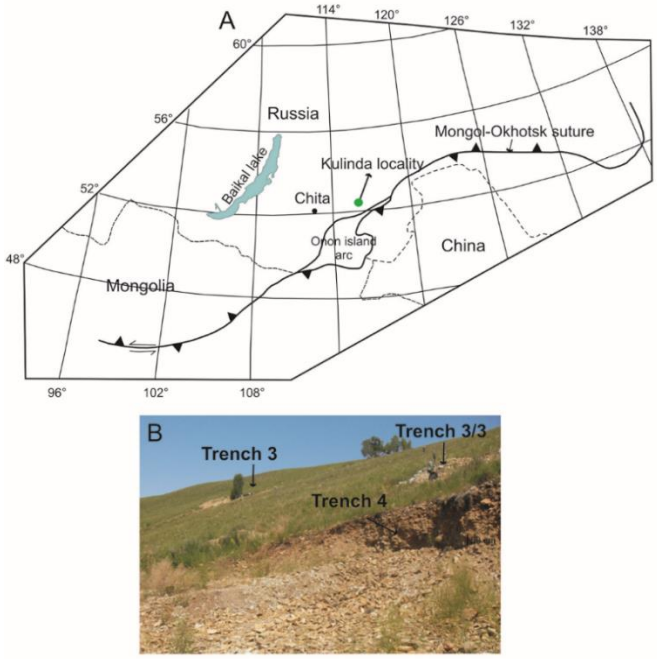

Figure 5.1. Location of the studied area showing, (A) the position of Kulinda locality with respect to the Mongol-Okhotsk suture (modified from Tomurtogoo et al., 2005), (B) the position of the three excavated trenches on the hillslope.

Kulinda section and provides data about the age of the neornithischians and the implication of this for the early evolution of feathers in dinosaurs.

2. Geological setting

The Kulinda locality (Fig. 5.1) is situated between two major fault zones related to the closure of the Mongol-Okhotsk Ocean that likely took place in south-eastern Siberia at the Early-Middle Jurassic boundary (Zorin, 1999; Zorin et al., 2001), or during the early Middle Jurassic (Jolivet et al., 2013) (see also the Supplementary Text). Both fault zones delimit a series of grabens in the area. The excavated sections at Kulinda belong to the lower part of the Ukurey Formation that crops out in the Olov Valley. The Formation is composed of interbedded sandstones, tuffaceous sandstones, conglomerates, tuffaceous conglomerates, siltstones, breccia, andesites, basaltic trachyandesites, basaltic andesites, and tuffs, up to a thickness of 850 metres (Anashkina et al., 1997). The geological map of the Transbaikal region indicates that Upper Jurassic volcaniclastic deposits crop out in Kulinda area (Fig. 5.2). Field work conducted in this area and described in 2011 in a local – unpublished – report identified the remains of a volcanic edifice, named “Pharaoh”, ca. five kilometres south of the Kulinda locality (Kozlov, 2011a). That structure is still clearly visible in

the landscape (see the Supplementary Fig. S5.2). The report notes that trachyandesites from the Pharaoh volcano have been collected on the left bank of the Olov River, and were dated at 180 ± 5 and 188 ± 6 Ma by K-Ar methods (Kozlov, 2011a). In the same report, K-Ar dating of other volcanic rocks, this time collected on the right bank of the Olov River, indicate younger ages (155 ± 5.0 Ma, 104 ± 3.0 Ma, and 103 ± 4.0 Ma). The wide age range reported for the volcanic rocks collected on the Pharaoh complex suggests several volcanic episodes in the area from the Early Jurassic up to the Early Cretaceous.

Felsic igneous rocks are exposed on top of the Kulinda hill and consist of granites, biotite granites, and biotite-quartz monzonites (see Supplementary Table S5.1 and Supplementary Fig. S5.2). These plutonic rocks likely constitute an outcropping part of the basement. Excavations at Kulinda consisted of three parallel trenches located at successive altitudes on the southern slope of a hill (Fig.5.3A). The rock layers dip 20-30° to the south. The trenches are not correlated laterally due to their poor exposure. The vertical stratigraphic distances were therefore estimated by means of rock dip and horizontal distances between the trenches, and correspond to ca. 11–17 m between trench 4 and trench 3/3, and ca. 36–58 m between trench 3/3 and trench 3. Deposits from trench 4 are considered as the oldest, being deposited on the lowest part of the slope (altitude 680 m), deposits from trench 3/3 are intermediate (alt. 690 m), and those from trench 3 are located higher up on the hill (alt. 720 m). Trench 4 and trench 3 are laterally separated by about 130 meters (Fig.5.3B). The Kulinda

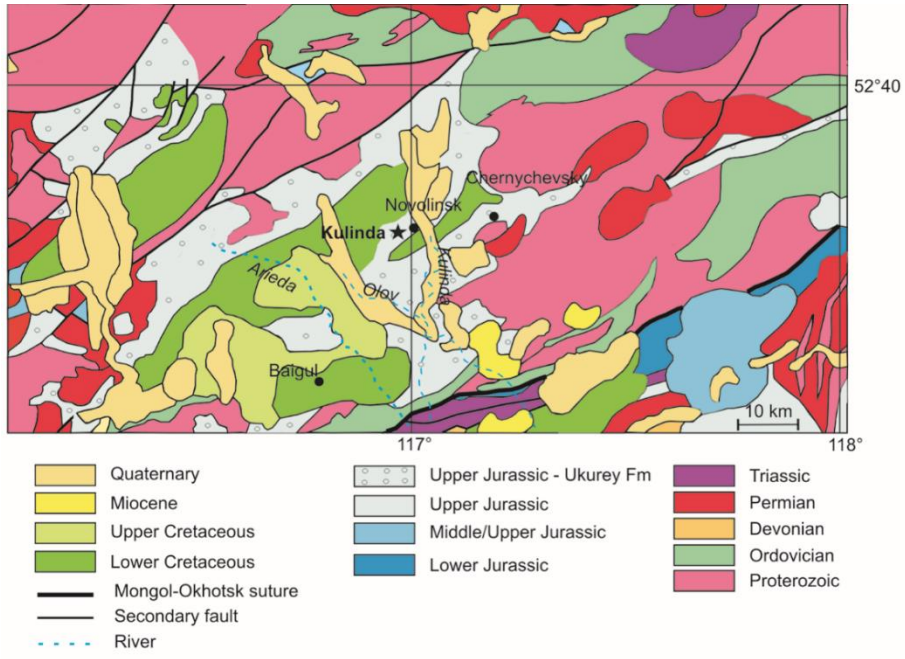

Figure 5.2. Geological map of the Kulinda region. According to the map, Kulinda is situated in the Upper Jurassic Ukurey Formation.

stratigraphical section mainly consists of a succession of volcaniclastic deposits. It comprises: (1) thinly laminated mudstones, (2) a single layer of tuffaceous siltstones showing glass shards, (3) lithic arenites (sandstones) including reworked fragments mainly of volcanic origin, (4) greywackes (matrix-supported) and feldspathic arenites (grain-supported) of silt- and sand-sizes, and (5) coarse- grained to brecciated sandstones mainly composed of automorph quartz and feldspars (see Supplementary Figs. S5.3 and S5.4).

3. Methods

Geochronology

Zircons and monazites were sampled from volcaniclastic deposits: (1) in the lowest part of trench 4, beneath bone bed 4, (2) in the medial part of trench 3, beneath bone bed 3, and (3) in granites cropping out on top of the hill (see Fig. 5.3). The samples were prepared for mineral separation at the Laboratoire G-Time (Université Libre de Bruxelles, Brussels). Rocks have been previously fragmented by Selfrag® high voltage pulse to liberate intact zircon grains. Zircons were then separated by standard methods using heavy liquids, hand-picked under a binocular microscope, mounted on epoxy resin, and eventually polished.

Uranium, thorium and lead isotope analyses were carried out by laser ablation - inductively coupled plasma - mass spectrometry (LA-ICP-MS) at the Goethe University of Frankfurt (GUF), using a slightly modified method, described in Gerdes and Zeh (2006, 2009). A ThermoScientific Element 2 sector field ICP-MS was coupled to a Resolution S-155 (Resonetics) 193 nm ArF Excimer laser (CompexPro 102, Coherent) equipped with two-volume ablation cell (Laurin Technic, Australia). The laser was fired with 5.5 Hz at a fluence of about 2-3 J.cm-2. The above configuration, with a spot size of 30 µm and depth penetration of 0.6 $\mu m.s^{-1}$, yielded a sensitivity of 11000-14000 cps/ppm ^{238}U. Raw data were corrected offline for background signal, common Pb, laser induced elemental fractionation, instrumental mass discrimination, and time-dependent elemental fractionation of Pb/U using an in-house MS Excel© spread-sheet program (Gerdes & Zeh, 2006, 2009). Laser-induced elemental fractionation and instrumental mass discrimination were corrected by normalisation to the reference zircon GJ-1 (0.0982 ± 0.0003; ID-TIMS GUF value).

Repeated analyses of the reference zircon Plesovice and BB-1670 during the same analytical session yielded an accuracy of better 1%. All uncertainties are reported at the 2 SD level.

Palynology

A total of eleven samples were chosen for palynological analyses, one from trench 3, four from trench 3/3, and six from trench 4 (Fig. 5.6). First, 25 g of sediment were separated from each sample, washed under water and crushed into gravel-sized fragments (about 2 mm), exposed in 15% HCl, followed by 30% HF, and finally in

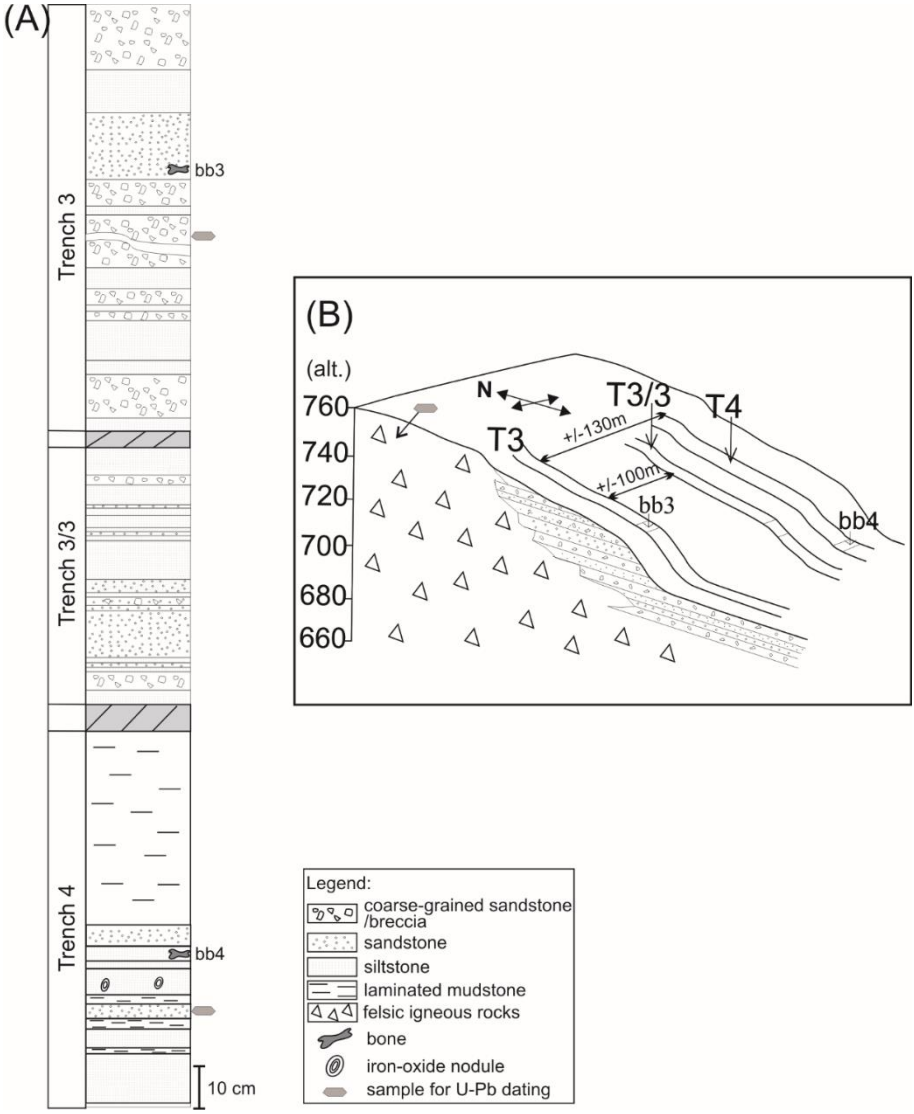

Figure 5.3. Lithological section of the Kulinda dinosaur locality in the Ukurey Formation. (A) composite stratigraphic log of the three trenches and the position of the bone beds, (B) schematic location of the trenches on the hillslope.

warm 10% HCl. A 12 µm filter was used to isolate the palynomorphs from the coarser grains. Palynological preparations for palynofacies were directly mounted on slides, although samples for organic preparations were further exposed in HNO_3 for two minutes. Observation of palynological preparations was done using a Zeiss optical microscope and microphotographs were taken with an Infinity X (Lumenera) camera using Deltapix software.

4. Results

U-Pb geochronology

$^{206}Pb/^{238}U$ data obtained for the granite and two volcaniclastic samples (see Fig. 5.3) are given in Supplementary Table S5.2. $^{206}Pb/^{238}U$ ages of individual zircons and monazites range between 171.1 ± 1.5 Ma and 189.3 ± 1.5 Ma, with the highest age probability around 172–173 Ma (Fig.5.4). Two age populations are recognized in the volcaniclastic deposits: (1) 183.8 ± 1.8–189.3 ± 1.5 Ma, and (2) 171.1 ± 1.5–177.6 ± 1.7 Ma. The granite has one age population, at 172.8 ± 1.6 Ma, which is interpreted as its crystallization age. Results of $^{206}Pb/^{238}U$ dating of the three samples have been plotted on three distinct concordia curves (Fig.5.5). Analyses of single zircons from T4-3, T3-7, and the granite yield mean $^{206}Pb/^{238}U$ ages of: (1) 173.0 ± 1.6 Ma (mean square of weighted deviates, MSWD = 0.89), (2) 172.8 ± 1.5 Ma (MSWD = 1.1), and (3) 172.5 ± 1.6 Ma (MSWD = 0.95), respectively.

Palynology and palaeobotany

The distribution of palynological taxa is shown in Figure 5.6. Two samples collected from trench 3/3 and two samples from trench 3 (Fig. 5.6, G, I, K, and L) do not contain palynomorphs. This probably represents a taphonomic bias partly related to the coarse-grained character of the deposits, less favorable to the accumulation of thin-walled spores and pollen grains (e.g., Batten, 1996; Traverse, 1988a). The eight remaining samples contain spore-pollen spectra mostly represented by gymnosperm pollen of poor preservation. The spore-pollen spectrum from trench 4 is more diverse, and all collected samples contained palynomorphs. Figure 5.7 displays selected palynomorphs from Kulinda deposits and the taxa are listed in Supplementary Table S5.3.

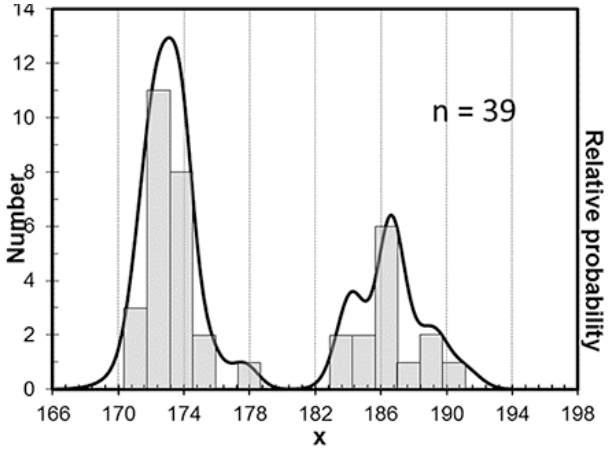

Figure 5.4. Relative U-Pb age probability curve for the Kulinda deposits, based on the LA-ICP-MS data performed on zircons and monazites. Two age populations can be discriminated from the curve.

Bisaccate morphotypes include high percentages of *Pseudopicea* spp. (5-19%), *Pseudopicea variabiliformis* (8-12%), and *Pseudopicea grandis* (3-7%). Pollen morphotypes closer to recent forms are rare and represented by the genera *Piceapollenites* (1-1.5%) and *Pinuspollenites* (1-1.5%). *Alisporites* spp. and *Podocarpidites* spp. are also rare. Common components of the assemblage are *Ginkgocycadophytus* spp. (1-7 %) and *Cycadopites* spp. (0.5-2.5%). *Classopollis* pollen show a rather low diversity at Kulinda (1-5%). Spore abundance is variable but is in general higher than that for pollen. Spores are dominated by *Stereisporites* spp. (1-19%), *Cyathidites australis* (2.5-9%), and *Cyathidites minor* (1.5-4%).

Besides the taxa shown in Figure 5.6, the assemblage also includes rare occurrences of the pollen *Alisporites bisaccus*, *Dipterella oblatinoides*, *Piceites podocarpoides*, *Protoconiferus funarius*, *Protopicea cerina, Protopinus subluteus*, *Pseudopiceae monstruosa*, *Pseudopinus* spp, the conifers *Dacrydiumites* spp., *Pinus divulgata*, *P. incrassata, P. pernobilis*, *P. subconcinua, P. vulgaris*, *Podocarpidites multesimus, P. major*, *Sciadopityspollenites multiverrucosus,* and taxa of uncertain affinity such as *Callialasporites dampieri* and *Podozamites* spp. Rare specimens of spores include the lycopods *Annulispora folliculosa, Densoisporites velatus*, *Leptolepidites verrucatus, Neoraistrickia aff. taylorii, Perotrilites sp., Polycingulatisporites triangularis, Retitriletes subrotundus, Undulatisporites pflugii, U. fossulatus, Uvaesporites scythicus, the ferns Dictyophyllidites equiexinus, Eboracia granulosa, Gleicheniidites sp., Leiotriletes nigrans, L. pallescens, L. selectiformis, L. subtilis, Osmunda papillata, Osmundacidites jurassicus, Salvinia sp.,* the bryophytes *Stereisporites infragranulatus,* the horsetail *Equisetites variabilis,* and *Acanthotriletes spp.* and *Punctatosporites scabratus,* both of unclear affinities. The assemblage also contains very rare trilete, zonate spores of rather simple morphology resembling the genera *Couperisporites, Kraeuselisporites,* or the taxa *Aequitriradites norrisii* (see Figure 5.7-21).

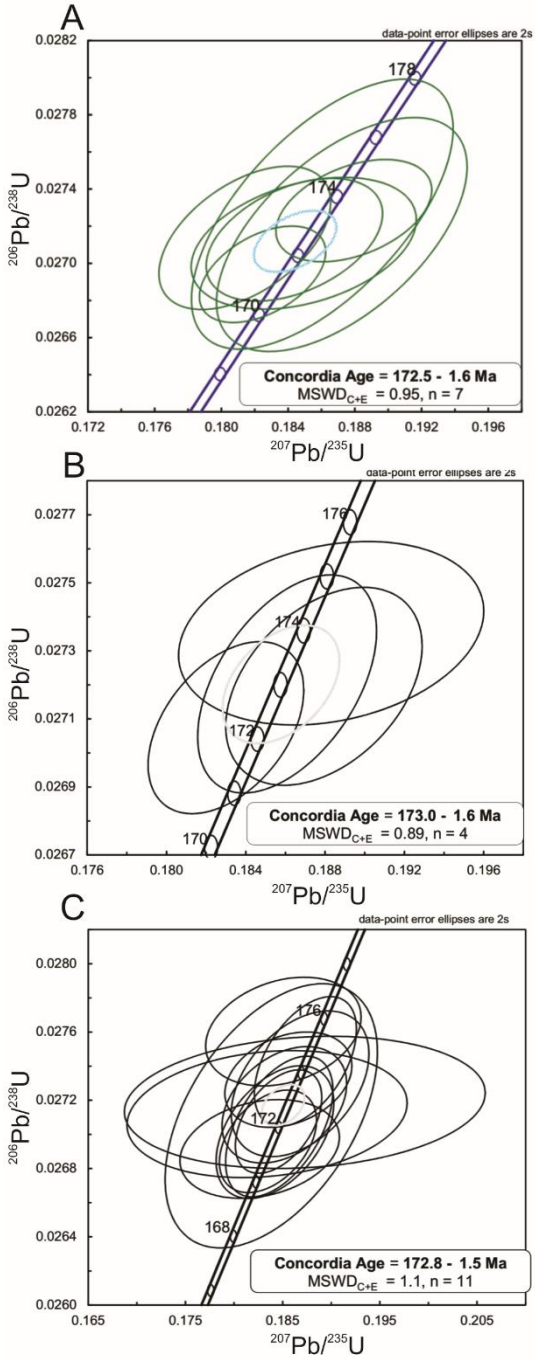

Figure 5.5. Concordia diagrams for (A) zircons and monazites collected from the granite, (B) zircons collected from a sample situated below bb4 in trench 4, and (C) zircons collected from a sample situated above bb3 in trench 3.

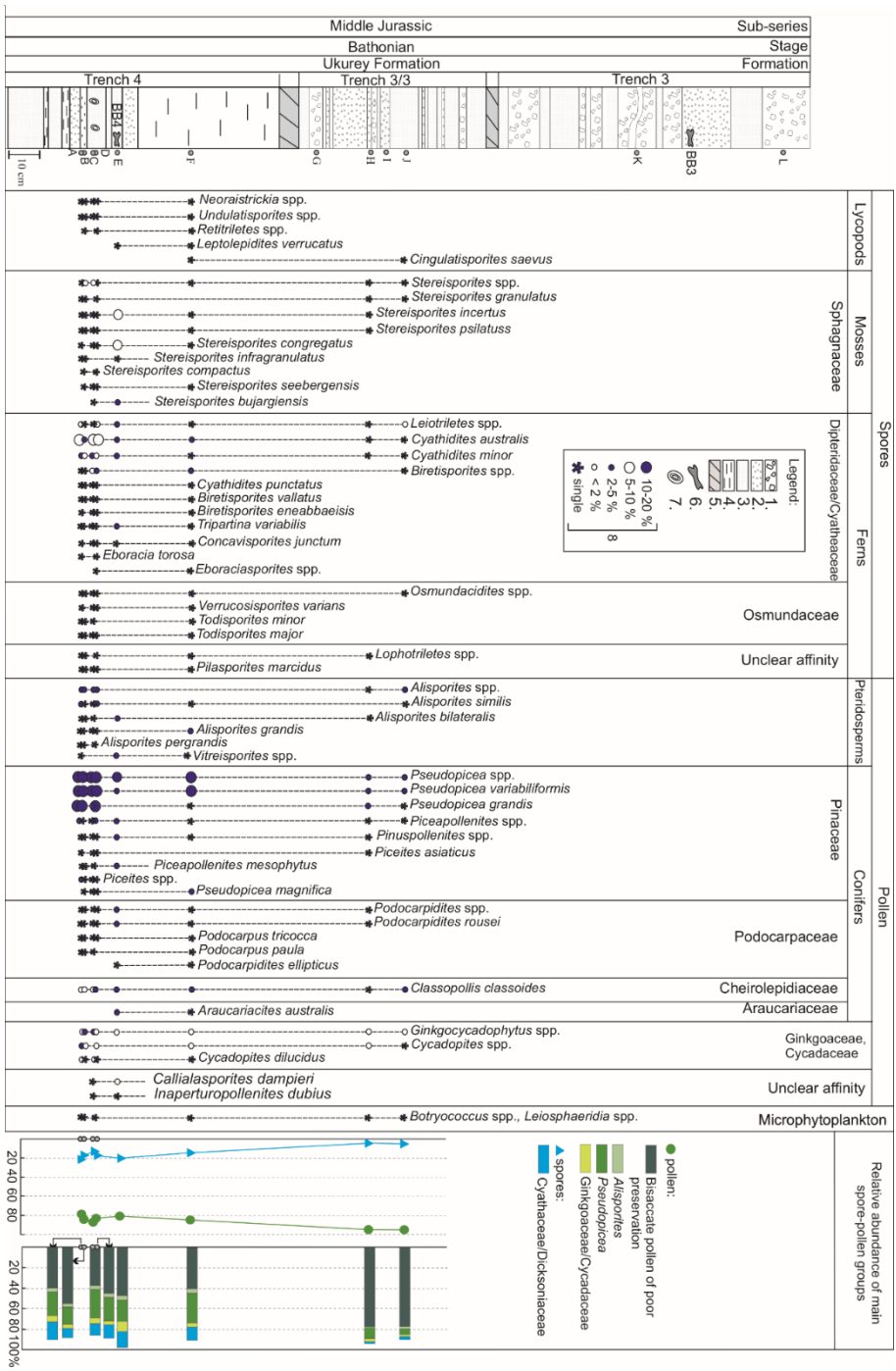

Figure 5.6. Palynomorph distribution in Kulinda deposits. Legend: 1 – coarse sandstone/breccia, 2 – sandstone, 3 – siltstone, 4 – laminated mudstone, 5 – non-correlated parts of the stratigraphic section, 6 – bone bed, 7 – iron-oxide nodules, 8 – palynomorph abundances.

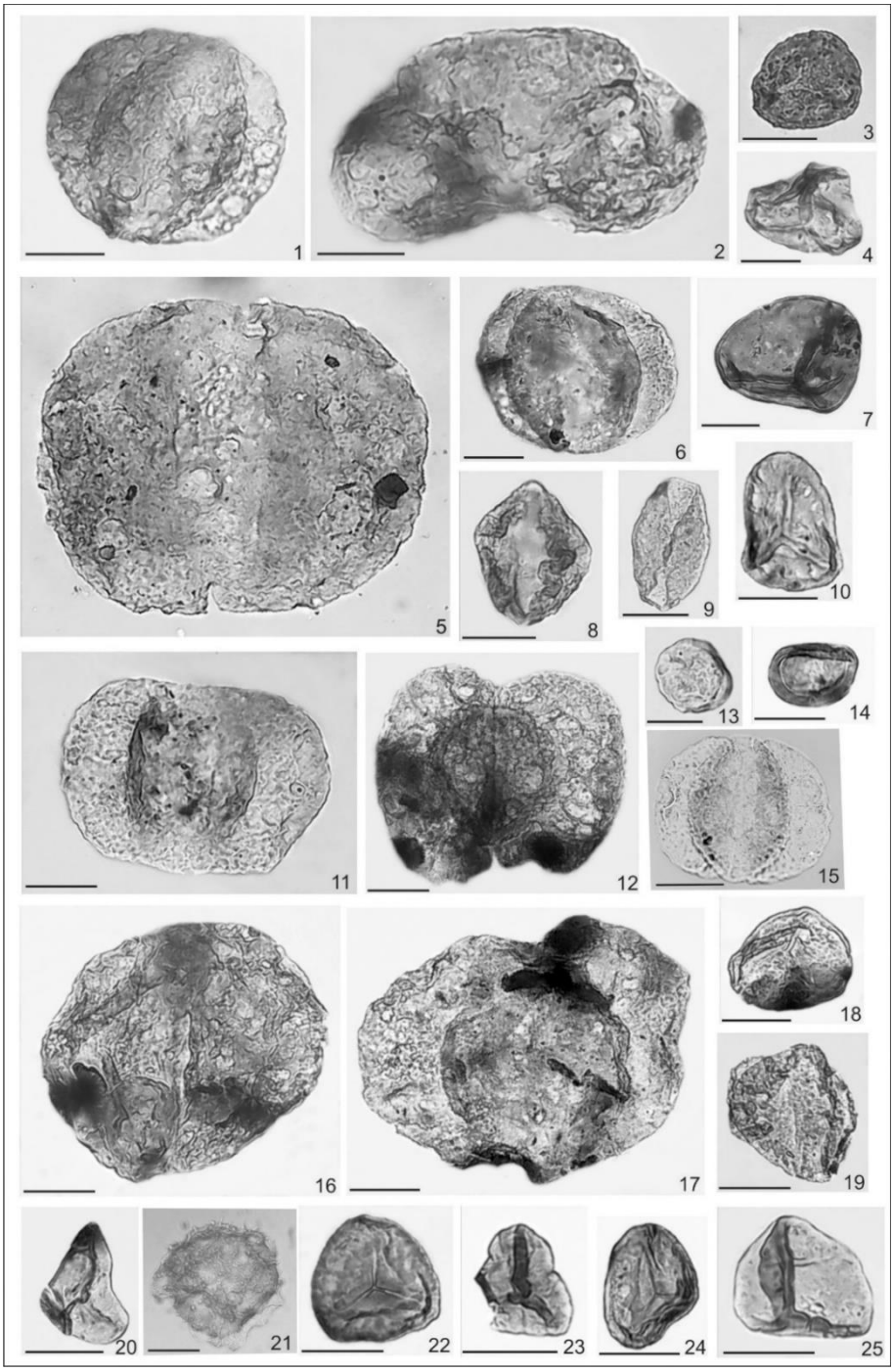
1
2
3
4
5
6
7
8
9
10
11
12
13
14
15
16
17
18
19
20
21
22
23
24
25

Figure 5.7. Selected palynomorphs from Kulinda deposits, trench 4. Scale bars = 20 μm, 1) *Alisporites similis* (Balme) Dettmann, 2) *Piceapollenites mesophyticus* (Bolchovitina) Petrosjanz, 3) *Osmundacidites jurassicus* (Kara-Mursa) Kuzitschkina, 4) *Cyathidites minor* Couper, 5) *Protopinus subluteus* Bolchovitina, 6*) Pseudopicea variabiliformis* Bolchovitina, 7) *Biretisporites eneabbaensis* Backhouse, 8) *Podocarpidites rousei* Pocock, 9) *Ginkgocycadophytus* sp., 10) *Stereisporites bujargiensis* (Bolchovitina) Schulz, 11) *Pseudopicea grandis* (Cookson) Bolchovitina, 12) *Podocarpus tricocca* (Maljavkina) Bolchovitina, 13) *Leiosphaeridia* sp., 14) *Classopollis classoides* Pflug, 15) *Alisporites bisaccus* Rouse, 16) *Protoconiferus funarius* (Naumova) Bolchovitina, 17) *Pseudopicea magnifica* Bolchovitina, 18) *Stereisporites granulatus* Tralau, 19) *Pinus divulgata* Bolchovitina, 20) *Leiotriletes subtilis* Bolchovitina, 21) undetermined spore taxa, 22) *Stereisporites* sp., 23) *Tripartina variabilis* Maljavkina, 24) *Stereisporites incertus* (Bolchovitina) Semenova, 25) *Leiotriletes* sp.

5. Discussion

The Kulinda deposits were previously regarded as Upper Jurassic to Early Cretaceous, based on palaeontological comparisons and on the relative position of the section within the Ukurey Formation (Kozlov et al., 1998; Rudenko & Starchenko, 2010). The new U-Pb radiochronological investigations obtained here from Kulinda deposits provide direct evidence that can constrain the age of the locality.

The concordia ages for zircons and monazites recovered from both the volcaniclastics and the granite suggest an Aalenian age. We interpret the older age population in the volcaniclastic sediments as possibly representing inherited zircons from the granite or detrital zircons coming from another granitic source not sampled here. Chemical analyses (more information available in the Supplementary Methods) performed on rock samples collected from the stratigraphic section shows that the sedimentary deposits are very similar in composition (see Supplementary Table S5.4 and Supplementary Fig. S5.5), indicating a similar source for all the deposits. This is also evidenced by the rare earth element (REE) pattern between the deposits and the granitic basement (see Supplementary Fig. S5.5). Even if no zircon older than 173.4 ± 3.7 Ma has been sampled in the present study in the granite, our data suggest that the deposits at Kulinda, including the bone beds, are composed of material reworked from the nearby granitoids, cropping out on top of the hill. When only looking at the youngest zircon population, the three samples display concordant age within error at 172.5 ± 1.6; 173.0 ± 1.6 and 172.8 ± 1.5 Ma (Fig. 5.5). This also emphasizes the genetic relationship between the granite and the volcaniclastic sediments from the bone beds. Consequently, the average age of 172.8 ± 1.6 Ma indicates the maximum age of the volcaniclastic sediments, which corresponds to the Aalenian.

The volcaniclastic origin of the deposits at Kulinda, together with the chemical and age for the granites suggest that the Kulinda deposits accumulated from the reworking of that igneous source at the site of deposition. We cannot exclude that another igneous source yielded the older population of zircon, but this source must be chemically similar to the granites in any case.

Because of the volcaniclastic nature of the Kulinda deposits, palynological information provides an essential complement to the radiochronological data for refining the age of the deposits. Most of the palynomorphs recovered at Kulinda are

characterised by a wide stratigraphic range and were observed both in Jurassic and Cretaceous deposits (e.g., Cornet et al., 1973; Ercegovac, 2010; Filatoff, 1975; Higgs & Beese, 1986; Ilyina, 1986; Kujau et al., 2013; Lebedeva & Pestchevitskaya, 2012; Li & Batten, 2004; Markevich, 1995; Markevich & Bugdaeva, 2009; Norris, 1965; Pestchevitskaya, 2007; Ribecai, 2007; Zhang et al., 2014). The spore and pollen taxa observed in Kulinda deposits are reported in Middle Jurassic palynozones that are calibrated to ammonite biozones from marine sections (Ilyina, 1986) and palaeofaunas from continental strata (Mitta et al., 2012). In northern Siberia, the appearance of *Pinus divulgata* is attested in the Bajocian but the taxon is common elsewhere, from the Triassic through the Cretaceous; *Alisporites bisaccus* and *Podocarpidites rousei* are both reported in Bajocian deposits from Siberia and western Canada (Ilyina, 1986), although *A. bisaccus* has a much wider stratigraphic range and *P. rousei* is typical for the Bathonian of western Siberia and the Kansk-Achinsk Basin in south-western Siberia (Krasnoyarsk region) (Smokotina, 2006). The stratigraphically important taxa recovered from Kulinda deposits are *Podocarpidites rousei*, *Eboracia torosa*, and *Gleicheniidites* spp. These species are typical for the Bathonian in southern and northern regions of western Siberia (Ilyina, 1985; Shurygin et al., 2010) and Kansk-Achinsk Basin (Smokotina, 2006). The palynozone 10 from these regions includes *Cyathidites* spp., *Sciadopityspollenites macroverrucosus*, *Eboracia torosa*, *Classopollis*, and a local palynozone includes *Eboracia torosa*, *Quadraequlina limbata*, *Classopollis*. The strong domination of *Pseudopicea variabiliformis* is a characteristic feature of Bathonian assemblages, although this pollen is also abundant in lower, and then older, strata. Note that in western Siberia, the stratigraphic position of the palynozones is controlled by ammonites and foraminifers, and is therefore considered as robust. Small pollen grains resembling *Podocarpidites rousei* are reported in assemblages from the middle part of the Bajocian of northern Siberia (Ilyina, 1985), but it is a characteristic pollen taxon for Bathonian deposits in southern Siberia. *Eboracia torosa* is a Bathonian species in western Siberia (Ilyina, 1985), although the possibility that the taxon appeared earlier in other regions cannot be excluded. *Gleicheniidites* is an important component of the Kulinda assemblage, its lowermost occurrences are defined in Bathonian sediments dated by macro- and microfauna in the East-European Platform (Mitta et al., 2012). Another key feature is the low abundance of *Classopollis* spp., which exclude a Callovian age, characterised by high percentages of this pollen in the Siberian palaeofloristic region (Ilyina, 1985; Shurygin et al., 2010; Smokotina, 2006). It is interesting to note the presence of trilete zonate spores resembling *Aequitriradites norrisii*, which is an important species for the Middle Jurassic of Australia. Its oldest occurrences there are in the Bathonian, where the eponymous zone is defined for the middle part of this stage (Sajjadi & Playford, 2002). Nevertheless, an accurate determination of this taxon is not possible in the Kulinda material due to poor preservation. Combination of these data suggest that the taxa recovered from Kulinda deposits have a Bathonian age.

The macrofloral assemblages from Kulinda are similar in the different horizons where they were collected. Their taxonomic composition is characteristic for the Middle Jurassic-Early Cretaceous time range in Siberia, but do not provide more precise information about the age of the deposits (see Supplementary Information for a complete description of the macroflora).

6. Conclusions

The deposits from the Kulinda section belong to the lower part of the Ukurey Formation, which crops out in several isolated depressions in central and south-eastern Transbaikal region (Rudenko & Starchenko, 2010; Starchenko, 2010). The age of the Ukurey Formation was previously regarded as Late Jurassic to Early Cretaceous, based on biostratigraphic comparisons and local correlations. Previous radiochronological studies of volcanic rocks from the formation (with no clear sampling location) indicated a Late Jurassic age (Rudenko & Starchenko, 2010; Starchenko, 2010). Our new results, combining absolute dating and palynological observations, place, for the first time, age constraints on the dinosaur-bearing volcaniclastics at Kulinda. The absolute dating of igneous and volcaniclastic rocks at Kulinda indicate a maximum Aalenian age (172.8 ± 1.6 Ma). Palynological data support a Bathonian age for the deposits, corresponding to an age ranging between 168.3 and 166.1 Ma (Gradstein et al., 2012), hence giving a minimum age. The stratigraphic range of the Ukurey Formation is therefore wider than it was previously assumed, its lower part extending to the Middle Jurassic. However, this new observation does not contradict the general geological framework of the region, characterised by marine deposits until the early Middle Jurassic, followed by continental sedimentation in grabens (Mushnikov et al., 1966; Rudenko & Starchenko, 2010; Starchenko, 2010).

A Middle Jurassic age for *Kulindadromeus* is consistent with its phylogenetic position (Fig. S5.7). A consistent and pectinate scheme of Middle Jurassic Asian basal neornithischians, including *Agilisaurus louderbacki*, *Hexinlusaurus multidens* and *Kulindadromeus zabaikalicus*, form a stem lineage culminating in Cerapoda (Godefroit et al., 2014): *Parasaurolophus walkeri* Parks, 1922, *Triceratops horridus* Marsh, 1889, their most recent common ancestor and all descendants (Butler et al., 2008). *Agilisaurus* and *Hexinlusaurus* were discovered in the lower member, the Shaximiao Formation of Dashanpu, Sichuan Province, China (Barrett et al., 2005), and should therefore be Bajocian-Bathonian in age (Li et al., 2011). *Yandusaursaurus hongheensis*, from the upper member of the Shaximiao Formation of Dashampu (Bathonian-Callovian; Li et al., 2011) is not included in this analysis, but is also regarded as closely related to *Agilisaurus* and *Hexinlusaurus* (Boyd, 2015). In this phylogenetic scheme, *Kulindadromeus* is regarded as the sister-taxon of the vast clade Cerapoda. Cerapodan dinosaurs were particularly successful during the Cretaceous, being e.g. represented by pachycephalosaurs, ceratopsians, and iguanodontians (including the 'duck-billed' hadrosaurs). The earliest records of cerapodans are the

dryosaurid iguanodontian *Callovosaurus leedsi*, from the Callovian of England (Ruiz-Omeñaca et al., 2006), and the basal ceratopsian *Yinlong downsi*, from the Oxfordian of Junggar Basin, Xinjiang, China (Xu et al., 2006). The calibrated phylogeny of ornithischian dinosaurs therefore suggests that cerapodans originated in Asia during the Middle Jurassic, from a common ancestor that closely looked like *Kulindadromeus*, then rapidly migrated to Europe, North America and Africa at the end of the Middle Jurassic and during the Upper Jurassic.

Kulindadromeus is therefore the oldest known dinosaur with "feather-like" structures. The other Jurassic formations that have also yielded fossils of 'feathered' dinosaurs are younger. Recent U-Pb zircon CA-ID-TIMS data from Jianchang support a post-Middle Jurassic, Oxfordian (~160 Ma), age for the Yanliao Biota preserved in the Lanqi/Tiaojishan Fm in western Liaoning (China) (Li et al., 2011). Based on strong similarities of the fauna, together with available radioisotopic age evidence, it is generally accepted that the Lanqi Fm in Ningcheng (southeastern Inner Mongolia), and the Tiaojishan Fm in northern Heibei should be coeval with the Lanqi/Tiaojishan Fm in Jianchang (Liu et al., 2012b; Sullivan et al., 2014; Zhou et al., 2010), thus also Oxfordian in age (Li et al., 2011). The lithographic limestones from Solnhofen and adjacent areas in South Germany that yield *Archaeopteryx* are early Tithonian in age (Schweigert, 2007).

The discovery of elongated and compound integumentary structures in the Middle Jurassic basal ornithischian *Kulindadromeus* will undoubtedly orient future researches on the origin of feathers, which should be sought in much older deposits. If it can definitely be demonstrated that those structures are homologous to the feathers in theropods, the origin of feathers can be tracked back to the common ancestor of both dinosaur lineages (Godefroit et al., 2014) that most likely lived, regardless of the phylogenetic scenario considered for the relationships of the major dinosaur clades, during the Middle Triassic (Baron et al., 2017).

Supplementary material for: "A refined age for *Kulindadromeus*, the oldest dinosaur with 'feather-like' structures from Siberia"

Supplementary Tables

Sample	Quartz (wt %)	K-feldspars (wt %)	Biotite (wt %)	Albite (wt %)	Kaolinite (wt %)	total
Granite 1	38	21.3	9.3	25.7	5.8	100.1
Granite 2	39.4	32	/	28.5	/	99.9
Granite 3	6	59	9.5	21.7	3.4	99.6
Granite 4	15.9	34.7	16.9	32.5	/	100

Supplementary Table S5.1. X-ray diffraction based compositions of the four igneous rock samples that crop out on top hill. The four samples have a rather similar overall composition (with quartz, feldspars, biotite, and kaolinite), but differ by the relative abundance of their components.

	Ratio												Age					
Sample/ grain	**^{207}Pb[a] (cps)**	**U[b] (ppm)**	**Pb[b] (ppm)**	**Th[b] / U**	**^{206}Pbc[c] (%)**	**$^{206}Pb/^{238}U$[d]**	**±2s (%)**	**$^{207}Pb/^{235}U$[d]**	**±2s (%)**	**$^{207}Pb/^{206}Pb$[d]**	**±2s (%)**	**rho[e]**	**$^{206}Pb/^{238}U$**	**±2s (Ma)**	**$^{207}Pb/^{235}U$**	**±2s (Ma)**	**$^{207}Pb/^{206}Pb$**	**±2s (Ma)**
granite																		
A06*	78,043	5607	173	0.69	5.3	0.0273	2.2	0.1861	3.4	0.0495	2.7	0.63	173	3.7	173	5.5	172	62
A07*	72,763	4978	148	0.20	4.8	0.0272	1.9	0.1872	3.3	0.0500	2.7	0.58	173	3.2	174	5.3	196	62
A08*	11,508	1710	339	31.4	0.4	0.0273	0.8	0.1879	2.0	0.0499	1.9	0.41	173	1.4	175	3.3	194	43
A09	2600	60	1.6	1.27	2.4	0.0271	1.2	0.1814	2.3	0.0485	2.0	0.50	173	2.0	169	3.6	124	47
A10	2316	63	1.7	1.43	1.9	0.0271	1.0	0.1844	2.3	0.0493	2.1	0.43	172	1.7	172	3.7	163	50
A11	2550	87	2.3	1.42	1.1	0.0271	1.1	0.1849	3.0	0.0495	2.8	0.36	172	1.8	172	4.7	171	65
A12*	24,260	1457	519	62.6	0.0	0.0269	0.8	0.1825	1.7	0.0491	1.5	0.46	171	1.3	170	2.7	154	35
T3-7b																		
A13	2701	111	2.9	1.25	0.6	0.0269	0.9	0.1826	3.7	0.0492	3.6	0.24	171	1.5	170	5.8	159	83
A14	4712	34	0.9	1.37	13.5	0.0271	2.3	0.1838	4.9	0.0492	4.3	0.48	172	4.0	171	7.7	157	100
A15	1830	48	1.4	0.61	2.1	0.0293	0.9	0.2026	2.1	0.0500	1.9	0.43	186	1.7	187	3.7	199	45
A16	1014	26	0.7	1.24	3.2	0.0272	1.2	0.1872	8.1	0.0499	8.0	0.14	173	2.0	174	13.1	194	186
A17	3604	120	3.2	0.22	0.7	0.0274	1.1	0.1872	2.2	0.0496	1.9	0.51	174	1.9	174	3.5	174	44
A19	3093	89	2.5	0.93	3.6	0.0293	1.0	0.1991	3.3	0.0494	3.2	0.31	186	1.9	184	5.6	166	74
A20	4030	57	1.6	1.09	1.2	0.0294	0.8	0.1968	2.5	0.0486	2.4	0.31	187	1.5	182	4.2	129	57
A21	2752	28	0.8	1.43	3.3	0.0295	0.9	0.2071	3.1	0.0509	2.9	0.30	188	1.7	191	5.3	235	67
A22	4986	195	5.2	1.24	0.3	0.0273	0.8	0.1855	2.9	0.0493	2.8	0.29	174	1.4	173	4.6	161	64
A23	1514	61	1.6	1.48	0.4	0.0272	1.0	0.1851	2.2	0.0494	1.9	0.47	173	1.7	172	3.4	169	45
A24	2279	74	2.1	1.86	1.5	0.0292	1.2	0.1997	2.9	0.0496	2.6	0.43	186	2.3	185	4.9	176	60
A25	3341	137	3.6	1.35	0.2	0.0270	0.9	0.1844	2.0	0.0495	1.8	0.45	172	1.5	172	3.2	170	42
A26	1685	53	1.4	1.61	1.2	0.0270	1.2	0.1846	2.4	0.0495	2.1	0.51	172	2.1	172	3.9	173	49
A27	1905	57	1.5	1.19	1.5	0.0270	1.2	0.1841	2.7	0.0495	2.4	0.44	172	2.0	172	4.2	170	56
A28	1430	49	1.3	1.15	1.6	0.0272	1.1	0.1836	3.7	0.0491	3.6	0.30	173	1.9	171	5.9	151	83
A29	2039	76	2.2	1.99	0.5	0.0297	1.0	0.2044	2.3	0.0498	2.1	0.43	189	1.8	189	4.0	187	48
A30	3865	131	3.8	1.13	0.4	0.0294	0.9	0.2012	2.2	0.0497	2.0	0.43	186	1.7	186	3.7	182	46
A31	1649	27	0.7	1.20	1.0	0.0279	1.0	0.1902	4.2	0.0494	4.1	0.23	178	1.7	177	6.9	168	96

A32	1623	29	0.8	1.68	0.3	0.0270	0.9	0.1834	2.2	0.0494	2.0	0.41	172	1.5	171	3.5	166	47
A39	6094	152	4.3	1.21	4.9	0.0290	0.8	0.1977	4.9	0.0494	4.8	0.16	184	1.4	183	8.2	167	113
A40	2885	49	1.3	1.52	5.6	0.0273	1.3	0.1868	3.1	0.0496	2.8	0.41	174	2.2	174	5.0	179	66
A41	2387	40	1.1	1.48	0.5	0.0276	0.9	0.1851	3.5	0.0486	3.4	0.26	175	1.6	172	5.6	131	80
T4-3b																		
A42	6099	251	7.2	1.88	0.0	0.0294	0.8	0.2032	1.7	0.0502	1.6	0.45	187	1.4	188	3.0	205	36
A43	4124	161	4.6	1.81	0.2	0.0290	0.8	0.1985	1.9	0.0497	1.7	0.41	184	1.4	184	3.2	183	40
A44	4346	164	4.8	1.11	0.5	0.0298	0.8	0.2052	2.6	0.0499	2.5	0.31	189	1.5	190	4.6	194	58
A45	1154	49	1.3	1.23	0.3	0.0272	1.0	0.1861	2.0	0.0496	1.7	0.48	173	1.6	173	3.2	178	40
A46	4039	163	4.4	1.05	0.7	0.0274	0.8	0.1883	3.3	0.0499	3.2	0.24	174	1.4	175	5.4	193	75
A47	938	30	0.8	0.78	1.7	0.0291	1.5	0.2002	2.7	0.0499	2.2	0.57	185	2.8	185	4.5	191	51
A48	6697	245	7.0	1.22	0.4	0.0294	0.8	0.1992	2.0	0.0492	1.9	0.38	187	1.4	184	3.4	157	44
A49	8148	333	8.9	1.22	0.8	0.0272	0.9	0.188	2.1	0.0501	2.0	0.40	173	1.5	175	3.5	201	46
A50	5682	265	7.0	1.06	0.5	0.0271	0.8	0.1831	1.7	0.0490	1.6	0.43	172	1.3	171	2.8	150	37
A51	4730	155	4.4	1.30	1.2	0.0289	1.0	0.1971	1.9	0.0494	1.6	0.51	184	1.8	183	3.2	168	38

[a] within run background-corrected mean ^{207}Pb signal in cps (counts per second).
[b] U and Pb content and Th/U ratio were calculated relative to GJ-1 reference zircon
[c] percentage of the common Pb on the ^{206}Pb. b.d. = below dectection limit.
[d] corrected for background, within-run Pb/U fractionation (in case of $^{206}Pb/^{238}U$) and common Pb using the Pb composition model in Stacey and Kramers (1975) and subsequently normalised to GJ-1 (ID-TIMS value/measured value); $^{207}Pb/^{235}U$ calculated using $^{207}Pb/^{206}Pb/(^{238}U/^{206}Pb*1/137.88)$
[e] rho is the $^{206}Pb/^{238}U/^{207}Pb/^{235}U$ error correlation coefficient.

Supplementary Table S5.2. La-ICP-MS data and ages for zircons and monazites (the latter are marked by an *) collected from Kulinda deposits.

Spores

Annulispora folliculosa (Rogalska) de Jersey, 1959
Biretisporites eneabbaensis Backhouse, 1978
Biretisporites vallatus Sajjadi et Playford, 2002
Cingulatisporites saevus Balme, 1957
Concavisporites junctus (Kara-Mursa) Semenova, 1970
Cyathidites australis Couper, 1953
Cyathidites minor Couper, 1953
Cyathidites punctatus (Delcourt et Sprumont) Delcourt, Dettmann et Hughes, 1963
Densoisporites velatus Weyland et Kreiger, 1953
Dictyophyllidites equiexinus (Couper) Dettmann, 1963
Dictyophyllidites harrisii Couper, 1958
Eboracia granulosa (Tralau) Timochina, 1977
Eboracia torosa (Sachanova et Iljina) Timochina, 1977
Equisetosporites variabilis (Vinogradova) Glushko et Strepetilova, 1994
Gleicheniidites sp.
Leiosphaeridia sp.
Leiotriletes nigrans Naumova, 1953
Leiotriletes pallescens Bolchovitina, 1956
Leiotriletes selectiformis Bolchovitina, 1953
Leiotriletes subtilis Bolchovitina, 1953
Leptolepidites verrucatus Couper, 1953
Neoraistrickia aff. *taylorii* Playford et Dettmann, 1965
Osmunda papillata Bolchovitina, 1953
Osmundacidites jurassicus (Kara-Mursa) Kuzitschkina, 1963
Pilasporites marcidus Balme, 1957
Polycingulatisporites triangularis (Bolchovitina) Playford et Dettmann, 1965
Punctatosporites scabratus (Couper) Norris, 1953
Retitriletes subrotundus (Kara-Mursa) E. Semenova, 1970
Stereisporites bujargiensis (Bolchovitina) Schulz, 1966
Stereisporites compactus (Bolchovitina) Iljina, 1985
Stereisporites congregatus (Bolchovitina) Schulz, 1970
Stereisporites granulatus Tralau, 1968
Stereisporites incertus (Bolchovitina) Semenova, 1970
Stereisporites infragranulatus Schulz, 1970
Stereisporites psilatus (Ross) Pflug, 1953
Stereisporites seebergensis Schulz, 1970
Todisporites major Couper, 1958
Todisporites minor Couper, 1958
Tripartina variabilis Maljavkina, 1949

Undulatisporites fossulatus Singh, 1971
Undulatisporites pflugii Pocock, 1970
Uvaesporites scythicus Semenova, 1970
Verrucosisporites varians Volkheimer, 1971

Pollen

Alisporites bilateralis Rouse, 1959
Alisporites bisaccus Rouse, 1959
Alisporites grandis (Cookson) Dettmann, 1963
Alisporites pergrandis (Bolchovitina) Iljina, 1985
Alisporites similis (Balme) Dettmann, 1963
Araucariacites australis Cookson ex Couper, 1953
Callialasporites dampieri (Balme) Sukh-Dev, 1961
Classopollis classoides Pflug, 1953
Cycadopites dilucidus (Bolchovitina) Ilyina, 1985
Dipterella oblatinoides Maljavkina, 1949
Ginkgocycadophytus sp.
Inaperturapollenites dubius Potonie et Venitz, 1934
Piceapollenites mesophyticus (Bolchovitina) Petrosjanz, 1971
Piceites asiaticus Bolchovitina, 1956
Piceites podocarpoides Bolchovitina, 1956
Pinus divulgata Bolchovitina, 1956
Pinus incrassata Bolchovitina, 1953
Pinus pernobilis Bolchovitina, 1956
Pinus subconcinua Bolchovitina, 1953
Pinus vulgaris (Naumova) Bolchovitina, 1953
Podocarpidites ellipticus Cookson, 1947
Podocarpidites multesimus (Bolchovitina) Pocock, 1970
Podocarpidites rousei Pocock, 1970
Podocarpus major (Maljavkina) Bolchovitina, 1953
Podocarpus paula Bolchovitina, 1956
Podocarpus tricocca (Maljavkina) Bolchovitina, 1953
Protoconiferus funarius (Naumova) Bolchovitina, 1956
Protopicea cerina Bolchovitina, 1956
Protopinus subluteus Bolchovitina, 1956
Pseudopicea grandis (Cookson) Bolchovitina, 1961
Pseudopicea magnifica Bolchovitina, 1956
Pseudopicea monstruosa Bolchovitina, 1956
Pseudopicea variabiliformis Bolchovitina, 1956
Sciadopityspollenites multiverrucosus (Sahanova et Iljina) Iljina, 1985

Supplementary Table S5.3. List of spore and pollen taxa from the Kulinda locality.

Rock type	Granitoids				Deposits trench 3						
Sample	1	2	3	4	bb	1F	1C	4	7	10F	10C
SiO_2	69.7	78.4	67.7	68.7	75.9	76.9	68.9	77.8	73.5	57.1	58.4
TiO_2	0.47	0.05	0.44	0.41	0.85	0.73	0.37	0.77	0.38	1.421	0.67
Al_2O_3	15.7	12.4	17	16	14.6	13.2	16.6	13.6	16.6	22.22	28.8
Fe_2O_3	2.34	0.24	1.91	1.72	DL	DL	2.88	DL	0.13	0.3	0.01
MnO	0.05	0.01	0.03	0.03	0.01	0.0	0.03	0.004	0.004	0.003	0.07
MgO	0.43	0.03	0.32	0.38	0.14	0.11	0.04	0.11	0.05	0.11	0.08
CaO	1.61	0.49	1.44	1.55	0.18	0.11	0.06	0.13	0.14	0.52	0.08
Na_2O	4.12	3.33	4.24	4.3	0.07	0.07	0.28	0.07	0.24	0.03	0.07
K_2O	3.9	5.17	4.9	4.34	1.41	1.62	3.96	1.91	3.23	0.88	1.15
P_2O_5	0.17	DL	0.25	0.17	0.05	0.1	0.12	0.11	0.1	3.75	0.15
LOI	1.43	0.19	1.59	1.28	7.02	5.38	5.18	5.36	4.91	10.26	10.6
Total	**100**	**100**	**100**	**99.4**	**100**	**98.5**	**98.5**	**100**	**99.3**	**96.6**	**100**
Sc	3	<1	3	3	3	3	5	3	2	8	4
Be	3	5	3	4	4	3	4	4	3	24	5
V	39	<5	38	33	59	34	46	41	26	79	65
Cr	20	<20	20	20	130	90	40	110	80	150	90
Co	4	1	7	3	2	2	7	2	2	1	2
Ni	<20	<20	<20	<20	20	<20	30	<20	30	<20	<20
Cu	10	<10	30	<10	40	40	10	30	50	30	<10
Zn	50	<30	60	40	<30	<30	80	<30	40	30	<30
Ga	21	18	22	22	28	25	18	25	14	40	23
Ge	1.4	2.2	1.7	1.7	2.1	1.9	1.9	2.1	2.1	4.1	1.8
As	23	11	20	18	29	12	149	15	18	24	42
Rb	139	277	156	157	55	60	116	65	95	32	38
Sr	346	37	346	329	345	426	468	382	313	>10,000	584
Y	13.2	2.2	11.6	7.7	20.2	14.8	8.9	20.6	6.6	109	7.9
Zr	407	14	369	338	199	288	241	298	219	142	243
Nb	11.7	2.6	11	10.7	11.7	8.8	7.5	8.7	5.1	20.3	9.8
Mo	<2	<2	<2	<2	5	7	48	4	3	15	9
Ag	1.2	<0.5	1.3	1.3	4.4	0.9	0.8	1	0.9	0.8	0.8
In	<0.1	<0.1	<0.1	<0.1	0.1	<0.1	<0.1	<0.1	0.1	0.1	<0.1
Sn	4	<1	6	2	3	3	1	2	3	4	2
Sb	0.8	0.7	0.8	0.7	5.3	3	6.4	4.1	3.2	14.4	10.4
Cs	6.2	13.8	5.1	4.4	2.4	2.1	1.7	2	1.4	0.9	0.7
Ba	547	64	784	597	304	298	665	322	500	1978	168
Hf	11.6	0.9	11.2	10.4	5.5	9.3	6.6	8.6	6.1	5.9	7.3
Ta	1.43	0.71	1.37	1.51	1.34	0.96	0.94	1	1.51	1.55	0.83
W	2.2	1.7	2.2	2.1	10.4	4.6	3.3	5.4	4.4	11.1	7.2
La	30.2	8.09	31.8	22.4	35.9	36.7	31.1	35.7	19.8	888	27.1
Ce	125	11.8	98.2	76.4	48.3	73.6	65.5	64.6	44.9	1790	47.4
Pr	5.7	1.68	6.03	3.62	6.46	8.02	7.15	6.85	5.35	190	4.83
Nd	19	5.42	19.8	11.2	22.2	28.7	26.5	25.3	21.2	705	17.9
Sm	3.51	0.49	3.69	2.02	3.69	5.09	4.53	4.24	3.73	117	2.9
Eu	0.72	0.14	0.73	0.52	0.92	1.09	0.88	1.05	0.83	23.9	0.75
Gd	2.35	0.33	2.31	1.3	3.21	3.47	3.02	3.79	2.27	73.8	2.19

Tb	0.38	0.06	0.41	0.21	0.5	0.45	0.42	0.57	0.31	8.35	0.3
Dy	2.38	0.38	2.52	1.31	2.8	2.53	2.06	3.2	1.44	32.8	1.53
Ho	0.47	0.08	0.47	0.28	0.56	0.5	0.38	0.63	0.24	4.18	0.27
Er	1.47	0.25	1.35	0.94	1.57	1.38	1.05	1.85	0.66	8.73	0.79
Tm	0.25	0.05	0.25	0.19	0.23	0.23	0.15	0.29	0.1	0.88	0.12
Yb	1.91	0.39	1.76	1.46	1.47	1.54	0.99	1.95	0.64	4.59	0.78
Lu	0.299	0.064	0.283	0.23	0.226	0.243	0.166	0.309	0.106	0.602	0.134
Tl	0.67	1.15	0.68	0.71	DL	0.27	0.8	0.28	0.45	0.15	0.19
Pb	23	44	26	26	24	22	34	24	24	542	44
Bi	0.1	0.1	0.1	0.1	<0.1	<0.1	0.3	<0.1	<0.1	0.2	0.3
Th	32.3	11.3	29.5	28.6	8.63	14.2	11.1	14.6	8.73	107	9.56
U	1.97	0.99	2.59	2.21	11.3	32.6	15.7	17	4.94	160	27.1
Th/U	16.4	11.41	11.39	12.94	0.76	0.44	0.71	0.86	1.77	0.67	0.35
∑ REE	193.64	29.23	169.60	122.08	128.05	163.55	143.90	150.33	101.58	3847.84	106.99
LREE/HREE	25.119	21.185	22.113	24.604	15.332	21.379	24.966	15.051	26.131	59.414	24.785
Eu/Eu*	1.18	1.67	1.17	1.51	1.26	1.22	1.12	1.23	1.35	1.209	1.4

Supplementary Table S5.4. Major (wt %), trace (ppm), and rare earth element (ppm) concentrations of Kulinda deposits. Part I. Samples from the basement and trench 3. DL, value below the detection limit.

Rock type	Deposits trench 3/3				Deposits trench 4						
Sample	5F	5C	7	8	bb	3F	3C	8	9F	9G	11
SiO_2	79.6	72.7	73.5	72.2	53.5	76.0	65.4	75.0	78.7	72.3	68.6
TiO_2	0.74	0.38	0.90	0.58	0.59	0.88	0.75	0.14	0.73	0.45	0.79
Al_2O_3	12.4	19.0	16.2	17.0	10.7	13.3	20.5	14.5	12.3	17.6	16.8
Fe_2O_3	DL	0.11	0.25	0.13	21.1	0.01	1.34	1.25	DL	DL	0.16
MnO	0.01	0.01	0.00	0.01	0.655	0.01	0.05	0.06	0.01	0.01	0.01
MgO	0.11	0.05	0.17	0.09	0.41	0.19	0.06	0.04	0.13	0.08	0.31
CaO	0.15	0.08	0.16	0.09	0.29	0.21	0.47	0.15	0.19	0.16	0.35
Na_2O	0.07	0.13	0.05	0.14	0.08	0.09	0.08	0.31	0.08	0.14	0.08
K_2O	1.37	1.98	1.46	2.22	2.42	1.51	2.92	4.38	2.19	3.16	2.81
P_2O_5	0.13	0.08	0.11	0.12	0.32	0.06	0.33	0.1	0.12	0.12	0.18
LOI	6.02	6.27	7.31	6.32	9.16	6.65	7	3.87	5.63	5.94	8.99
Total	**101**	**101**	**100**	**99.4**	**100.3**	**99.6**	**99.3**	**100**	**100**	**100**	**99.4**
Sc	4	2	5	3	18	3	5	4	5	3	5
Be	4	4	5	4	7	4	3	3	3	3	7
V	51	27	63	45	147	60	52	34	58	40	67
Cr	100	90	110	80	60	90	40	80	60	40	80
Co	3	2	1	4	9	3	33	10	2	3	7
Ni	<20	<20	30	20	40	<20	50	40	<20	<20	40
Cu	40	<10	30	10	20	30	20	40	30	20	40
Zn	<30	<30	<30	40	180	40	150	60	<30	<30	60
Ga	23	12	20	20	16	27	22	15	21	15	22
Ge	1.5	1.7	1.8	1.9	1.8	1.3	1.2	1.9	1.3	1.3	1.6
As	29	17	21	17	94	62	105	63	45	38	41
Rb	55	62	60	69	95	63	105	119	84	99	115
Sr	662	464	483	569	710	141	200	490	432	341	575
Y	9.1	4.1	11.2	8.1	37.9	7.5	12.1	7.1	9.5	5.6	14.7
Zr	190	161	181	186	201	127	265	137	202	234	207
Nb	8.8	5.8	9.3	6.7	9.9	9.2	8.4	4.8	10	6	9.2
Mo	3	3	<2	5	11	7	11	23	5	6	3
Ag	3.3	0.6	0.6	0.6	0.9	6.7	0.9	0.7	5.6	1	0.8
In	<0.1	0.1	0.1	<0.1	0.1	<0.1	<0.1	<0.1	<0.1	0.1	0.1
Sn	3	1	2	2	2	2	2	3	3	2	3
Sb	4	2.5	2.1	1.9	2.2	5.6	4.2	4.4	5.2	3.1	1.9
Cs	3.1	1.2	3.2	1.6	3	5	0.9	1.5	3	1.6	4.8
Ba	273	271	264	413	389	249	160	758	293	346	409
Hf	5.5	5.8	4.9	4.9	5.6	3.9	8	4.3	5.4	6.8	6.5
Ta	1.28	0.58	1.04	0.75	0.83	1.08	0.67	0.59	1.2	0.63	0.97
W	7.8	3.7	5.8	4.2	4.3	10.2	4.8	3.8	8.8	3.7	5
La	43.4	22.2	34.3	35.9	50.2	14.9	30.1	30	39.3	27.3	53.5
Ce	88.5	44.7	69.4	70.3	138	24.3	53.4	54.1	67.5	46.8	112
Pr	9.43	4.84	7.44	7.32	17.1	2.3	5.4	6.04	6.74	4.52	12.1
Nd	34	17.3	26.8	26.9	70.1	7.14	19.2	21.8	22.3	15.6	43.7
Sm	5.88	3.17	4.69	4.79	12.1	1.03	3.31	3.32	3.23	2.2	8.4
Eu	1.36	0.79	0.99	0.99	2.39	0.36	0.88	0.81	0.83	0.59	1.55
Gd	4.26	2.17	3.13	3.13	9.97	0.8	2.28	2.22	2.11	1.42	5.28

Tb	0.49	0.27	0.4	0.39	1.28	0.13	0.36	0.33	0.27	0.19	0.69
Dy	2.15	1.12	1.9	1.79	6.73	0.88	2.24	1.74	1.47	1.09	3.2
Ho	0.31	0.16	0.36	0.29	1.22	0.18	0.44	0.28	0.28	0.21	0.5
Er	0.83	0.41	1.07	0.78	3.32	0.59	1.21	0.72	0.82	0.57	1.34
Tm	0.11	0.06	0.17	0.12	0.47	0.1	0.16	0.10	0.13	0.09	0.20
Yb	0.8	0.47	1.15	0.84	2.91	0.7	1.01	0.62	0.94	0.68	1.34
Lu	0.15	0.08	0.16	0.12	0.44	0.12	0.14	0.10	0.16	0.11	0.20
Tl	DL	0.24	0.25	0.26	0.46	DL	0.52	1.07	DL	0.33	0.46
Pb	23	15	28	18	51	24	29	29	39	24	27
Bi	<0.1	<0.1	<0.1	<0.1	0.4	<0.1	0.3	0.2	<0.1	<0.1	<0.1
Th	16.2	9.52	14.1	15	13.8	5.75	7.91	7.53	14.5	8.96	21
U	22.3	3.28	16.3	11.1	40.3	10.8	16.7	11.7	9.81	9.96	46
Th/U	0.73	2.90	0.87	1.35	0.34	0.53	0.47	0.64	1.48	0.90	0.46
∑ REE	192	97.8	152	154	316.2	53.5	120	122	146	101	244
LREE/H REE	36.2 10	34.5 92	26.4 56	32.3 92	16.82 1	18.0 08	19.4 06	28.7 69	33.4 01	32.0 37	29.6 09
Eu/Eu*	1.28	1.42	1.21	1.20	1.02	1.86	1.50	1.40	1.50	1.61	1.09

Supplementary Table S5.4. Major (wt %), trace (ppm), and rare earth element (ppm) concentrations of Kulinda deposits. Part II. Samples from the trenches 3/3 and 4. DL, value below the detection limit.

Supplementary Figures

Supplementary Figure S5.1. Reconstruction of *Kulindadromeus zabaikalicus*. The neornithischian dinosaur was reconstructed with its integumentary coverage consisting of epidermal overlapping scales on the tail and the distal part of the tibiae, non-overlapping scales around the manus, tarsus, metatarsus, and pes, monofilaments around the thorax, on the back and skull, clusters of filaments and their basal plate on the humerus and femur, and ribbon-shaped structures on the proximal part of the tibiae. Photo: T. Hubin. Reconstruction: J. Dos Remedios and M. Mohamed.

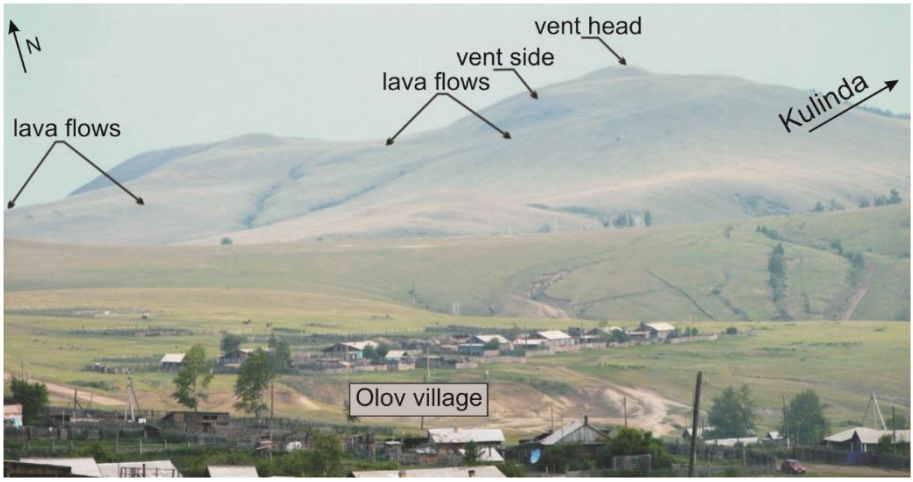

Supplementary Figure S5.2. Photograph of the Pharaoh volcano located in the background of the Olov village, southwest of Kulinda locality (after Kozlov, 2011a). Volcanic rocks (trachyandesites) were observed on the western part of the edifice (see the arrowheads). Radiochronological dating indicates an Early Cretaceous age for these deposits (Kozlov, 2011a).

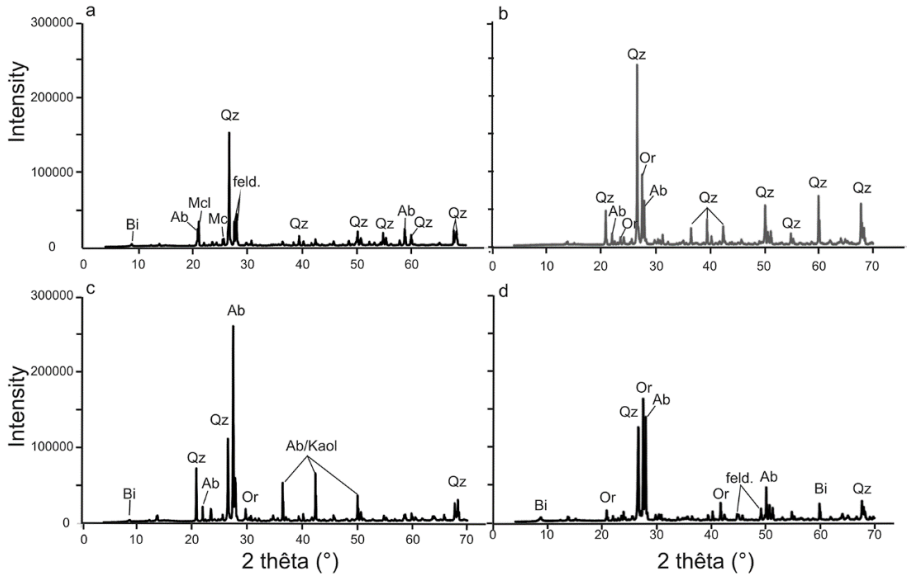

Supplementary Figure S5.3. X-ray diffraction spectra of igneous rock samples from Kulinda. The spectra show the main mineralogical features for four igneous rock samples that crop out on top hill: (a) biotite granite, (b) granite, and (c), (d) quartz-biotite monzonite. All samples contain quartz and feldspars in various, generally high, abundances, together with, less, biotite and kaolinite. The percentage data about the main mineral phases are shown in Supplementary Table S5.1. Abbreviations: Qz, quartz; Ab, albite; Or, orthoclase; Mcl, microcline; feld., feldspars, refer to probable solid solution between albite and orthoclase; Bi, biotite; Kaol., kaolinite.

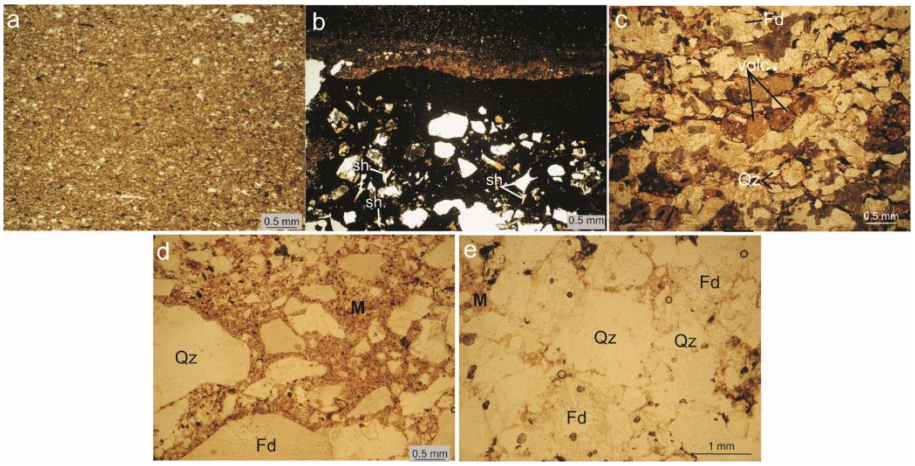

Supplementary Figure S5.4. Microfacies encountered in Kulinda deposits. (a) mudstone from trench 3 (sample T3-3), (b) tuffaceous siltstone from trench 4 (sample T4-5), (c) lithic arenite from trench 4 (sample T4-5), (d) greywacke from trench T3/3 (sample T3/3-5), and (e) brecciated sandstone from trench 3 (sample T3-7). Abbreviations: Qz, quartz; volc, volcanic lithics; sh, glass shards; Fd, feldspars; M, matrix;

Supplementary Figure S5.5. Selected rock samples from Kulinda locality. The photographs show (a) a granite and (b) a biotite granite collected on top hill, (c) and (d) greywackes from trench 4, (e) and (f) breccia and brecciated sandstone from trench 3, (g) very coarse-grained sandstone and (h) mudstone from trench 3/3.

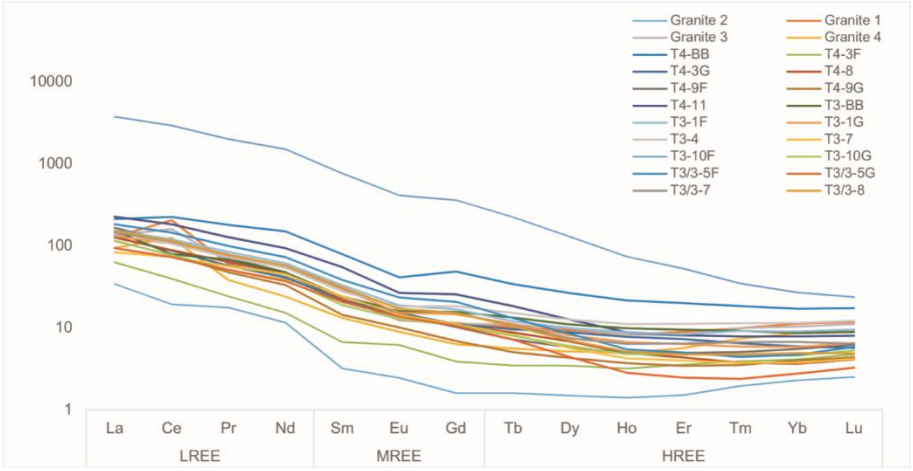

Supplementary Figure S5.6. Rare earth element (REE) chondrite-normalised diagram for Kulinda deposits. The distribution pattern is rather similar for all samples and show an enrichment in light REE (LREE) with respect to the heavy REE (HREE). Values for normalisation were taken from Sun and McDonough (1989).

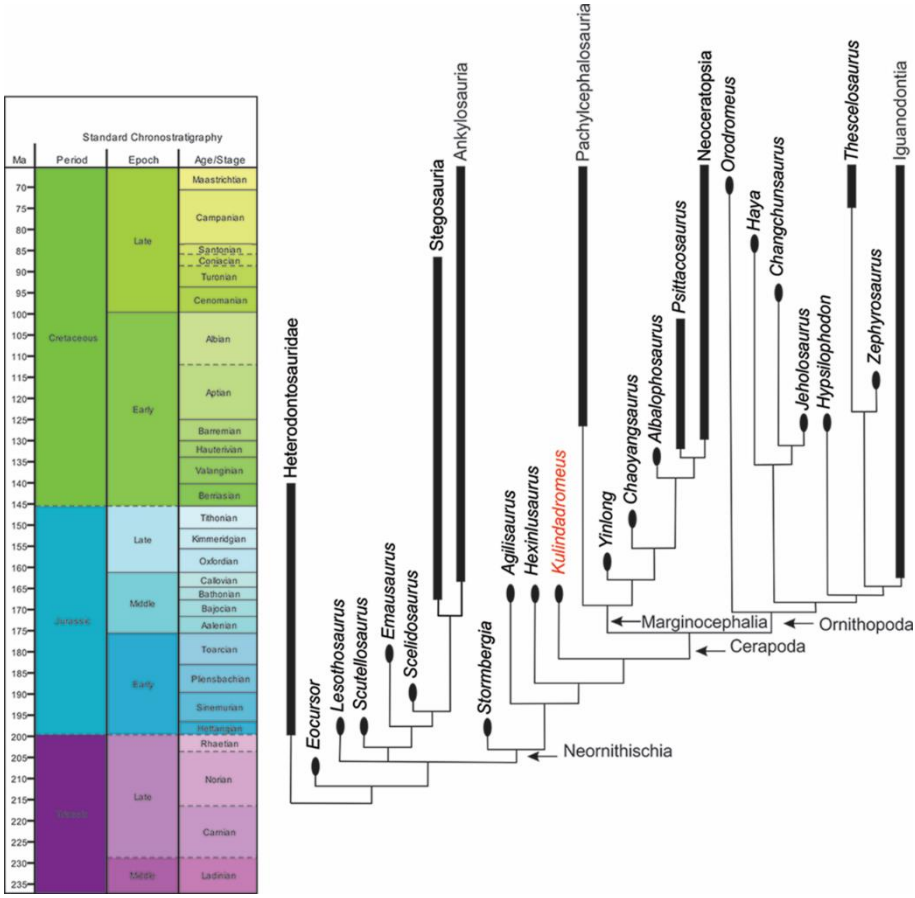

Supplementary Figure S5.7. Time-calibrated phylogeny of basal ornithischian dinosaurs (modified from Godefroit et al., 2014).

Supplementary Text

Methodology

The Kulinda locality is located in the Chernyshevsky District of the Transbaikal region, in south-eastern Siberia (Russia). During the last field campaign conducted in the summer of 2015, two trenches (T4 and T3) - previously excavated on a steep hillside in 2013 (Godefroit et al., 2014) - have been studied, along with a new third trench (T3/3) located at an intermediate elevation, between trenches T4 and T3. The geochemistry of the Kulinda deposits was studied in detail using a total of thirty-six rock samples. Twelve samples have been collected from trench 4, nine from trench 3/3, and eleven from trench 3. In addition, four samples were collected from the plutonic intrusion.

Twenty-two samples (seven from trench 4, four from trench 3/3, and seven from trench 3) were analysed by fusion ICP-AES for major elements and fusion ICP-MS for trace elements (Actlabs, Canada). For this purpose, samples were crushed to a grain size smaller than 125 µm. Ten major elements - Si, Al, Fe, Mn, Mg, Ca, Na, K, Ti, and P -, thirty one trace elements - Sc, Be, V, Cr, Co, Ni, Cu, Zn, Ga, Ge, As, Rb, Sr, Y, Zr, Nb, Mo, Ag, In, Sn, Sb, Cs, Ba, Hf, Ta, W, Tl, Pb, Bi, Th, U -, and the rare earth elements - La, Ce, Pr, Nd, Sm, Eu, Gd, Tb, Dy, Ho, Er, Tm, Yb, Lu - were analysed. Total iron was expressed as Fe_2O_3 (total). Values for major elements and rare earth elements were normalised to chondrites (Sun & McDonough, 1989), and trace elements were normalised to the Upper Continental Crust (UCC) (McLennan, 2001).

The mineralogy of selected rock samples from Kulinda was studied by X-ray diffraction (XRD) analysis using a PANanalytical Empyrean diffractometer (RBINS) with Cu K_α radiation. A tube voltage of 45 kV and a tube current of 40 mA were used. The goniometer scanned from 3° to 69° 2θ for the bulk rock. The semi-quantitative interpretation of data was made using Visual Crystal 6 software.

Geological setting

The Kulinda locality (Transbaikal region, south-eastern Siberia, Russia; GPS coordinates: 52°31'N; 116°42'E) is located at the boundary between the Onon Island Arc and the active margin of Siberia, close to the eastern part of the Mongolia-Okhotsk suture (Kravchinsky et al., 2002; Xu et al., 1997; Zorin, 1999). The Mongol-Okhotsk Orogenic Belt forms the eastern and youngest segment of a major geotectonic unit, the Central Asian Orogenic Belt (Wang et al., 2015a) and is related to the suture of the Mongol-Okhotsk Ocean, a huge segment of the palaeo-Pacific (Zorin et al., 1995) located between Siberia, Onon Island Arc, and the Mongolia-North China continent in the Devonian time (Donskaya et al., 2013; Wang et al., 2015a; Zorin et al., 2001). The subduction of the oceanic lithosphere beneath Siberia and Mongolia since the Early Permian led to the scissor-like eastward collision of the Mongolia-North China and Siberia continental blocks (Xu et al., 1997; Zorin, 1999). The

collision between the two blocks continued from the Late Permian to the Early Jurassic (Donskaya et al., 2013; Zorin, 1999). The exact time of closure is still debated, but it likely occurred during the Late Jurassic-Early Cretaceous (Jolivet et al., 2013; Kravchinsky et al., 2002; Vorontsov et al., 2016; Zorin et al., 2001). However, the closure of the Mongol-Okhotsk Ocean in south-eastern Siberia likely took place at the Early-Middle Jurassic boundary (Zorin, 1999; Zorin et al., 2001), or during the early Middle Jurassic (Jolivet et al., 2013).

Intense magmatism during the Permian, Triassic, and Early Jurassic in south-eastern Siberia was related to the subduction of the Mongol-Okhotsk oceanic plate beneath Siberia (Zorin, 1999; Zorin et al., 2001). Granite and granodiorite plutons are therefore widespread in the region, with calc-alkaline rock suites located in the front part of the active continental margin, and sub-alkaline suites in the back part of the continental margin (Tomurtogoo et al., 2005). Although magmatism dropped in the Jurassic period, probably related to the ending of the subduction (Donskaya et al., 2013), Middle-Late Jurassic granitoids and other various igneous rocks are known in the region of Kulinda (Zorin et al., 2001). Marine sedimentation occurred in central and south-eastern Transbaikalia until the early Middle Jurassic, followed by a period of continental rifting reflected by the formation of grabens in the region (Rudenko & Starchenko, 2010; Starchenko, 2010). Later magmatic events in the region occurred in the Late Jurassic-Early Cretaceous and are the consequence of the post-collisional rifting (Stupak et al., 2016; Zorin, 1999; Zorin et al., 1995).

Discussion on the composition of the Kulinda dinosaur fauna

According to Godefroit et al. (2014), all the ornithischian material discovered at Kulinda belongs to the basal neornithischian *Kulindadromeus zabaikalicus*. An alternative interpretation for the dinosaur fauna at Kulinda was proposed (Alifanov & Saveliev, 2014, 2015), and named three new taxa from this locality: the 'hypsilophodontian' ornithopods *Kulindapteryx ukureica* and *Daurosaurus olovus* (Alifanov & Saveliev, 2014) , and the 'nqwebasaurid' ornithomimosaur *Lepidocheirosaurus natalis* (Alifanov & Saveliev, 2015). Detailed description of the osteology of the dinosaurs from Kulinda is beyond the scope of this paper, but some brief comments are made here.

The authors of this interpretation do not apply modern taxonomic standards for elaborating their classification schemes: in particular, cladistic methods were not used for inferring the phylogenetic relationships between taxa. *Kulindapteryx* and *Daurosaurus* differ only in the structure of their ischia (the only bone that is preserved in both taxa), but those differences can easily be explained by differences in the orientation of the bones: PIN 5434/25a, the holotype of *Kulindapteryx ukureica*, is clearly exposed in dorsal view, not in lateral view as hypothesised by the authors. We therefore consider *Kulindapteryx ukureica* and *Daurosaurus olovus* as nomina dubia, and that the specimens both fall within the *Kulidadromeus zabaikalicus* hypodigm.

In their paper, the authors claimed that the caudal vertebrae and associated scales referred to *Kulindadromeus zabaikalicus* (Godefroit et al., 2014) belong to a new ornithomimosaur, *Lepidocheirosaurus natalis* (Alifanov & Saveliev, 2015). This interpretation is based on analysis of one partially articulated manus and of caudal vertebrae associated by caudal scales. The caudal vertebrae show a spool-shaped centrum, well-developed postzygapophyses and weakly developed neural spine; these features were thought to be characteristic of theropods and to contrast with the vertebrae of bipedal Ornithischia (Alifanov & Saveliev, 2015), characterised by better developed neural spines, a cylindrical centrum and weakly developed postzygapophyses. However, this interpretation is apparently based on direct comparisons with the ornithopod *Hypsilophodon foxii* and lacks a broader phylogenetic context (Alifanov & Saveliev, 2015). For example, caudal vertebrae of more basal ornithischians, e.g., the heterodontosaurid *Tianyulong confuciusi* (see reference Sereno, 2012, fig.25), closely resemble those discovered at Kulinda: from about the tenth vertebra, the centrum is elongated and spool-shaped in lateral view, the neural spines are reduced to a ridge, and both the pre-and postzygapophyses are long, extending beyond the level of the articular surfaces of the centra. Except for the absence of evidence for ossified tendons, the caudal structure in *Tianyulong* is remarkably similar to that in dromaeosaurid theropods (Sereno, 2012). Furthermore, the hand of *Lepidocheirosaurus natalis* from Kulinda closely resembles that of *Tianyulong* (see Sereno, 2012, fig. 27). Combined, these observations strongly indicate a lack of support for the hypothesis that basal ornithomimosaurs were present at Kulinda and that the caudal and manus material described by Alifanov and Saveliev (2015) can be confidently attributed to basal ornithischians, such as *Kulindadromeus zabaikalicus*.

The most parsimonious interpretation of the Kulinda bonebeds is thus that they represent accumulation of a monospecific dinosaur assemblage (Godefroit et al., 2014).

Palaeofloral assemblage

The diversity of the macrofloral assemblage recovered from Kulinda deposits is relatively poor and mostly consists of fossil plants that are widespread in strata from the Siberian palaeofloristic region. Moss sprouts are rare and their remains are most commonly subordinate in the assemblage. They nonetheless comprise remains of the dichotomous mosses *Hepaticites cf. arcuatus* (L. *et* H.) Harris and the cormophytic mosses *Muscites samchakianus* Srebr. Gymnosperms are mainly represented by Coniferales – *Elatides ovalis* Heer, *Pityospermum* sp., *Carpolithes* -, the archaic Pinaceae *Schizolepidopsis*, and Leptostrobales – *Czekanowskia* - trees and shrubs. Ferns, with *Coniopteris* and *Pityophyllum*, horsetail, with *Equisetites*, and Leptostrobales are represented by highly fragmented specimens identifiable at the generic level, only. In trench 4, one can distinguish the following taxa: *Czekanowskia* ex. gr. *rigida*, *Equisetites sp.*, *Elatides ovalis*, *Hepaticites* cf. *arcuatus*,

Schizolepidopsis elegans, and *Algites sp*.; in trench 3/3: *Hepaticites* cf. *arcuatus*, *Carpolithes sp*., and *Algites sp*.; and in trench 3: *Schizolepidopsis sp*., *S. moellerii*, *Hepaticites* cf. *arcuatus*, and *Muscites samchakianus*.

The assemblage is characterised by the predominance of small herbaceous plants represented by the mosses *Hepaticites* cf. *arcuatus* and *Muscites samchakianus*. Such delicate moss stems are generally rare in Jurassic deposits, and their remains are, commonly, not abundant in floral oryctocoenoses (Vakhrameev, 1991). Nevertheless, mosses are widespread in all regions of the world since the Paleozoic, and some species can occupy harsh environments (Bardunov, 1984). It should be noted that, at Kulinda, ferns, arthrophytes, and leptostrobales are only represented by highly fragmented remains and their identification was possible at the generic level, only. Gymnosperms are abundant in some layers, and especially Coniferales and Leptostrobales, which formed trees and bushes. *Czekanowskia* ex gr. *rigida* is a typical Siberian gymnosperm species characterised by a wide stratigraphic extension: it is known from the Lower Jurassic to the Upper Jurassic (Samylina & Kiritchkova, 1993; Vakhrameev, 1991). The moss *Hepaticites arcuatus* was originally found in the Middle Jurassic of Yorkshire (Harris, 1961, 1964). The absence of epidermal structures in the plants from Kulinda allows the definition of this species in the open nomenclature, only. *Elatides ovalis*, *Schizolepidopsis moelleri*, *S. elegans*, *S. levis* are also interpreted as Early-Middle Jurassic species (Mogutcheva, 2009; Vakhrameev, 1970; Vakhrameev, 1991). The modern morphology of conifers was already established in the early Mesozoic (Andrews, 1961). The evolution of the axillary region led to the formation of seeds with spliced scales, which is a typical feature for the group and particularly for the genus *Schizolepidopsis*. The first occurrences of *Schizolepidopsis* are reported from the Triassic of the Fergana Valley in eastern Uzbekistan (Stiksel, 1966). All specimens identified at Kulinda were observed in the Lower Jurassic of Central Asia as well (Turutonova-Ketova, 1950). However, they seem more abundant in the Ukurey Formation, where the presence of unique morphotypes might reflect endemicity. Abundant bifurcate seed scales of *Schizolepidopsis* are typical for the Middle and Upper Jurassic deposits of Siberia (Vakhrameev, 1991). The fern *Coniopteris* appeared in the late Early Jurassic but became common since the Middle Jurassic (e.g., Deng & Lu, 2006; Vakhrameev, 1991). The horsetail *Equisetites*, is here represented by only one species, *E. undense*, which was originally described from the Upper Jurassic of eastern Transbaikal region (Srebrodolskaya, 1983). The Pinaceae *Pityophyllum* cf. *buriensis* is commonly regarded as a characteristic taxon for the Lower Cretaceous, but occurrences of the genus were reported in Middle-Upper Jurassic deposits (Vakhrameev, 1991). *Muscites samchakianus* is reported in Middle-Upper Jurassic deposits from Transbaikal region (Srebrodolskaya, 1980). The taxonomic composition of the paleofloral assemblages from Kulinda locality cannot therefore give a more detailed age than the Middle Jurassic-Early Cretaceous time range for the deposits **.**

Chapter 6

This chapter is based on: Cincotta et al., *in preparation*

Exceptional preservation of soft tissues in the neornithischian dinosaur *Kulindadromeus zabaikalicus* and the reconstruction of the depositional environments

Abstract

The Kulinda locality, in south-eastern Siberia, has yielded abundant remains of the primitive neornithischian dinosaur, *Kulindadromeus zabaikalicus*. The fossil assemblage includes well-preserved soft tissues, including integumentary structures interpreted as primitive feathers. Geochemical studies were made on the stratigraphic section to better understand the origin of the deposits, and the taphonomy of the fossils. The Kulinda locality consists of a succession of immature deposits interpreted as greywackes and arenites, composed of volcanic and plutonic debris derived from nearby igneous sources. They are poorly-sorted, poorly stratified, and contain angular to sub-rounded clasts within a dark fine-grained matrix. The top of the Kulinda section comprises granites, biotite granites and biotite-quartz monzonites. Rare earth element and multiple element diagrams show that the volcaniclastic sediments originate from the reworking of granitoids of similar composition. The granitoids appear to be poorly weathered compared to their derivative volcaniclastic deposits, which are depleted in CaO, Na_2O and, to a lesser extent, K_2O, and enriched in Al_2O_3 and TiO_2. This is reflected by a lack of primary plagioclases but a significant enrichment in clays (in particular, kaolinite).

Two major monospecific bone beds have yielded dinosaur remains depicting different taphonomic histories. The oldest bone bed (bone bed 4), located in the lower part of the section, consists of silty to sandy greywackes and contain bones replaced by iron oxides, together with well-preserved soft tissues. The second bone bed (bone bed 3), located in the upper part of the section, consists of silty mudstones and contains disarticulated and epigenised bones, only. Although they both experienced similar weathering processes, they show diverse types of preservation. In bone bed 3, post-mortem processes probably played a major role in the disarticulation of carcasses prior to deposition and the subsequent fossilisation processes. On the contrary, the good soft tissue preservation observed in bone bed 4 suggests calm depositional conditions. It is likely that dinosaurs found in that layer were swiftly covered by sediment after death, allowing their exceptional preservation. According to their shape, we suggest that the iron oxides found within bone fragments derived from the oxidation of the pyrite. The bones were probably pyritised during early diagenesis, allowing their

initial good preservation. Further leaching of pyrite minerals was accompanied by the dissolution of the bones through the release of acidic fluids.

1. Introduction

The Middle Jurassic deposits of Kulinda, in south-eastern Siberia (Russia), have yielded abundant remains of the primitive neornithischian dinosaur, *Kulindadromeus zabaikalicus* (Godefroit et al., 2014). This taxon is, to date, the oldest known dinosaur with epidermal appendages, which are interpreted as primitive feathers (see chapter 5). The diversity of the fossil assemblage at Kulinda is relatively low: excepting *Kulindadromeus*, only plants and insects have been identified. No other vertebrate remains have been found thus far, except a single theropod tooth (see also chapter 5).

The locality is remarkable due to the mode of preservation of the fossils. Several fossiliferous layers have been excavated, and these display diverse taphonomic modes. The oldest of these layers is the most important because it contains nicely-preserved soft tissues in close association with bones. Fossil soft tissues rarely occur in the geological record (e.g., Allison & Briggs, 1993; Kidwell & Flessa, 1995; Schweitzer, 2011b; Seilacher et al., 1985). Soft parts provide fundamental information about the ecology of extinct organisms, which is otherwise inaccessible. Here, epidermal scales are associated with elongate – isolated or compound – integumentary structures that are reminiscent of primitive feathers in theropod dinosaurs, providing unique information on their early evolution in dinosaurs. The presence of such "feather-like" structures in non-theropod dinosaurs suggests they were more widespread among the Dinosauria, and also that they may have arisen from a common ancestor (Dhouailly et al., 2017; Godefroit et al., 2014; Chapter 5). It is still not completely understood how diagenetic processes affect the morphology and/or chemistry of such delicate tissues and allow their preservation, even after hundreds of million years (e.g., Janvier & Arsenault, 2009). It is likely that the preservation of soft tissues is determined very early after their deposition. Late diagenetic processes (e.g., uplifting of the rock layers, weathering) may also significantly modify the preservation degree of fossil soft tissues.

Here, we aim to determine the nature and depositional setting of the Kulinda deposits, including the two bone beds, to better understand why soft tissues were preserved and which processes led to the preservation of the integumentary structures found associated with the bones of *Kulindadromeus*. In addition, we present data about the taphonomy of the bone beds, and a reconstruction of the palaeoflora. We therefore integrate data obtained through several geological and palaeontological methods, including elemental geochemistry, organic matter analysis (Rock-Eval pyrolysis), microfacies and weathering indices analyses (WIA), palaeofloristic reconstructions, and field observations.

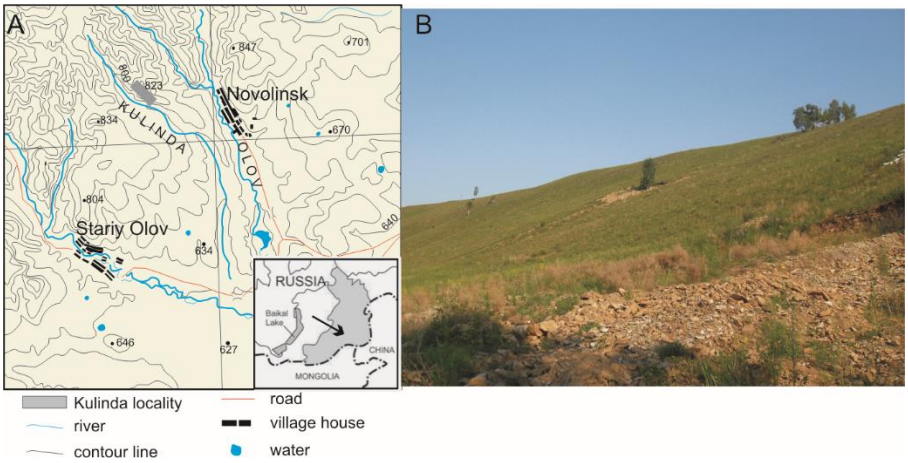

Figure 6.1. Location of Kulinda fossil site. (A) topographic map of the area, showing the location of the site in the Olov Valley (top left), (B) picture of the Kulinda hill with trench 3 in the background (see the tree).

2. Geological setting

The Kulinda fossil locality (GPS coordinates: 52°31'N; 116°42'E) is located in the eastern Transbaikal region (Siberia, Russia) ca. 220 km east of the city of Chita, close to the village of Novolinsk (Fig.6.1A, B). The excavated sections at Kulinda belong to the lower part of the Jurassic Ukurey Formation that crops out in the Olov Valley. The Ukurey Formation is composed of interbedded sandstones, tuffaceous sandstones, conglomerates, tuffaceous conglomerates, siltstones, breccia, andesites, basaltic trachyandesites, basaltic andesites, and tuffs, up to a thickness of 850 meters (Anashkina et al., 1997). Recent U-Pb radiochronological dating performed on detrital zircons and monazites, together with palynological investigations of the volcaniclastic deposits from Kulinda indicate a Middle Jurassic, probably Bathonian, age for the sediments (see Chapter 5). Three trenches – trench 4, trench 3/3 and trench 3 – have been excavated at Kulinda at successive altitudes (Fig.6.2A). The oldest deposits are encountered in the lowermost trench - trench 4 -, whereas the intermediate trench - trench 3/3 - is of intermediate age, and the upper trench - trench 3 – contains the youngest deposits. Trench 4 and trench 3 are laterally separated by about 130 meters (Fig.6.2). Two major bone beds were excavated: bone bed 4 (bb4) is located in trench 4 and contains abundant bones and soft tissue remains, and bone bed 3 (bb3) is located in the upper part of the section in trench 3, and yields bones but not soft tissues. K/Ar dating of trachybasalts collected on the front mouth of an ancient volcanic edifice located at five kilometres southwest of the Kulinda locality were dated at 104 ± 3 Ma (Albian age; Gradstein et al., 2012). Other plutonic rocks located in the same area were dated at 180 ± 5 Ma (Toarcian) and 188 ± 6 Ma (Pliensbachian) (Kozlov, 2011a). This indicates that volcanic activity was recurrent in the Kulinda area at least from the Early Jurassic up to the end of the Early Cretaceous.

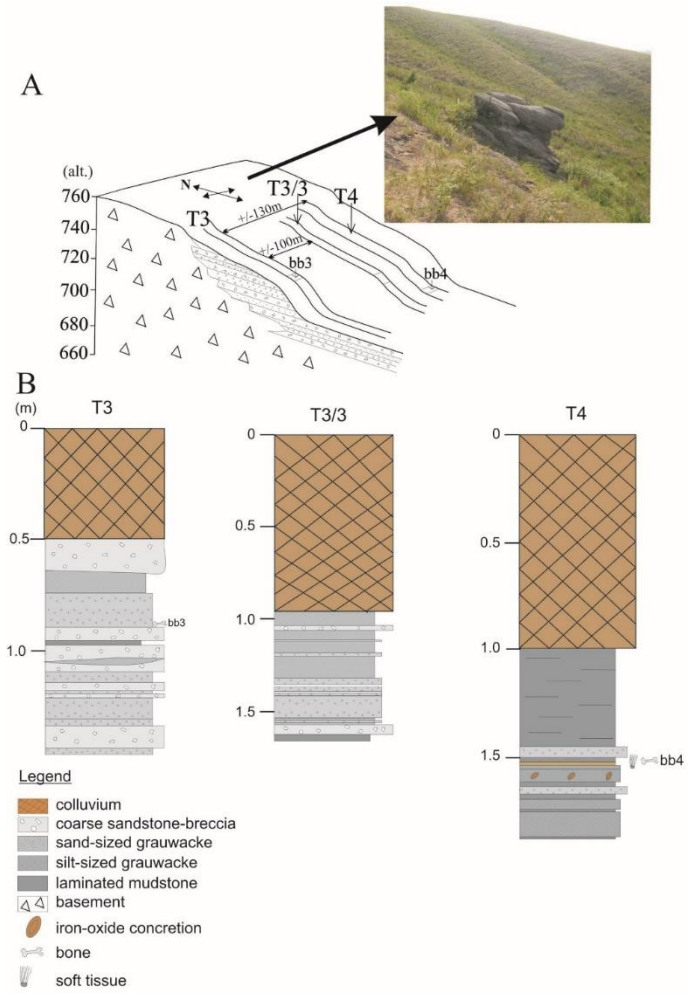

Figure 6.2. Lithological sections at Kulinda locality. (A) schematic location of the three excavated trenches, with the position of the bone beds. Trench 3/3 contain multiple bone layers. The picture shows the granite exposed on top of the hill. (B) Lithological logs of the three trenches and the position of the bone bed 4 (with soft tissues) and bone bed 3 (no soft tissues).

Igneous intrusions and volcanic rocks are widespread in south-eastern Siberia. The collision between the Mongolia-North China and Siberian continents during the Early/Middle Jurassic led to intense magmatic activity in the region throughout the Jurassic period (Delvaux et al., 1995; Stupak et al., 2016; Tomurtogoo et al., 2005; Zorin, 1999).

The Transbaikal region was uplifted in the Early Jurassic, and subsequent erosion of volcanic rocks – rhyolites, andesites, latites, shoshonites, basalts – sedimentary, and igneous material – granites, syenites, granodiorites, quartz diorites, quartz monzonites - (Rutshtein & Chaban, 1992) led to the deposition of continental

molasses in intermontane Basins during the Middle Jurassic (Ruzhentsev & Nekrasov, 2009). Additional magmatic material originated from the post-collisional extension of the crust and the subsequent formation of grabens during the Late Jurassic and Early Cretaceous (Stupak et al., 2016; Wang et al., 2015b).

Magmatism-related ore bodies are widespread in the region and were studied for their high content in trace elements, and especially for gold mineralisation (e.g., Abramov, 2011; Berzina et al., 2013; Chabiron et al., 2003; Kozlov, 2009, 2011b; Prokof ev et al., 2000a; Zorin, 1999). Bone beds and related deposits at Kulinda were thereby deposited in a region that experienced particularly complex geodynamic processes.

3. Material and methods

3.1. Major and trace element composition

During the field campaign conducted in the summer of 2015, two trenches (T4 and T3) (Godefroit et al., 2014) were studied, along with a new third trench (T3/3) located at an intermediate elevation, between T4 and T3 (Fig.6.2A). The petrography and geochemistry of the Kulinda deposits were studied in detail using a total of thirty-six rock samples. Twelve samples were collected from T4, nine from T3/3, and eleven from T3. In addition, four samples were collected from nearby plutonic intrusions. In this paper, all rock samples are named after the trench they were collected from (e.g., sample T4-1 was collected in T4).

Twenty-two samples (seven from T4, four from T3/3, and seven from T3) were analysed by fusion ICP-OES for major elements and ICP-MS for trace elements. For this purpose, samples were crushed into a grain size smaller than 125 µm. Ten major elements - Si, Al, Fe, Mn, Mg, Ca, Na, K, Ti, and P -, thirty one trace elements - Sc, Be, V, Cr, Co, Ni, Cu, Zn, Ga, Ge, As, Rb, Sr, Y, Zr, Nb, Mo, Ag, In, Sn, Sb, Cs, Ba, Hf, Ta, W, Tl, Pb, Bi, Th, U -, and the rare earth elements - La, Ce, Pr, Nd, Sm, Eu, Gd, Tb, Dy, Ho, Er, Tm, Yb, Lu - were analysed. Total iron was expressed as Fe_2O_3 (total). Values for major elements and rare earth elements were normalised to chondrites (Sun & McDonough, 1989), and trace elements were normalised to the Upper Continental Crust (UCC) (McLennan, 2001).

The mineralogy of the fossiliferous layers was estimated by means of X-ray diffraction (XRD) analysis using a PANanalytical Empyrean diffractometer (RBINS) with Cu K_α radiation. A tube voltage of 45 kV and a tube current of 40 mA were used. The goniometer scanned from 3° to 69° 2θ for the bulk rock. The semi-quantitative interpretation of data was made using Visual Crystal 6 software.

3.2. Taphonomy

Samples of soft tissues and bones were collected in the field throughout the different fossiliferous layers, and described *in situ* and in the laboratory. The ultrastructure of the fossil soft tissues and the mineralogy of their surrounding matrix were studied

using scanning electron microscopy (SEM) and Energy Dispersive X-ray spectroscopy (EDS). The samples were studied under low vacuum with an environmental QUANTA 200 (FEI) scanning electron microscope (20–30 kV, working distance 8–15 mm; RBINS). Subsequent EDS analyses (single point and mapping) were performed with the same facilities. For observation of tiny mineralogical structures, samples were mounted on double-sided carbon tape and sputter-coated with gold (Baltec SCD 050).

3.3. Palynofacies and organic matter content

Palynofacies analyses were carried out on four samples disseminated throughout the three stratigraphical sections: one sample bb4 and bb3, and trench 3/3 and trench 3. Each sample was divided in two. One for each pair was processed following standard procedures: gravel-sized fragments (about 2 mm) were dissolved in 15% HCl, in 30% HF, and warm 10% HCl. A 12 µm filter was used to isolate the palynomorphs from the coarser grains. Palynological preparations for palynofacies were mounted directly on slides, although samples for organic geochemistry were placed in HNO_3 for two minutes. Palynological preparations were observed under a Zeiss optical microscope and microphotographs were taken with an Infinity X (Lumenera) camera using Deltapix software. The remaining part of sample was used for Rock-Eval pyrolysis and ground to obtain grains <125 µm in diameter. About 100 mg of powdered rock was analysed with a Rock-Eval 6 apparatus.

3.4. Weathering indices

Six weathering indices were used for evaluating weathering conditions of four samples from the igneous basement and eighteen samples from the complete rock section: the Ruxton Ratio (R; Ruxton, 1968); the Weathering Index of Parker (WIP; Parker, 1970); the Vogt's index (V; Vogt, 1927); the Chemical Index of Alteration (CIA; Nesbitt & Young, 1982); the Chemical Index of Weathering (CIW; Harnois, 1988); and the Plagioclase Index of Alteration (PIA; Fedo et al., 1995). All these indices are calculated on the basis of major element oxides (wt %).

4. Results

4.1. Petrology

4.1.1. General description and composition of the deposits

The lower part of the Ukurey Formation overlies the plutonic basement, but the exact location of the contact could not be observed (Godefroit et al., 2014; Sinitsa & Vil'mova, 2016). The volcaniclastic deposits are (poorly-) exposed in the three

Figure 6.3. Selected samples from the Kulinda lithological sections showing (A) and (B) fine slightly undulating parallel laminations (arrows), (C) sharp boundaries between mudstones and breccia (dashed line), (B) and (D) poorly sorted volcaniclastics with clasts of feldspar and quartz. Abbreviations: cl., clast; md., mudstone; br., breccia.

trenches and are overlain by thick layers (50 cm to 100 cm) of colluvium that contain loose sediment and massive inherited boulders. The bedding structure of the sediments is unclear given the limited lateral exposure of the sections. Beds are massive or show faint planar bedding. No obvious sedimentary structures were identified in the field, although some samples show undulating and plane parallel lamination (Fig.6.3A, B). In the coarsest material (breccias), boundaries between different facies are usually gra dational but sharp boundaries can also occur (Fig.6.3C). Sorting of clasts is moderate to very poor (Fig. 6.3D). Alternation between mud-sized, silt-sized, and sand-sized sediments, and breccias constitutes the main feature at Kulinda. No palaeosol development has been observed.

XRD-analyses of the four granitoid samples collected on the topmost part of the hill show that they mostly contain quartz (6-39 %), K-feldspars (32-59%), plagioclases (22-32 %), and biotite (9-17%) (Fig.6.4). The felsic igneous rocks

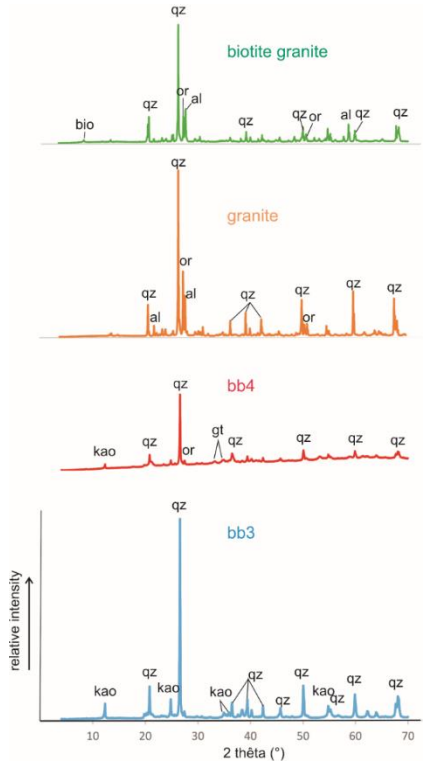

Figure 6.4. X-ray diffractograms of granitic rocks from the basement, and the two main bone beds (bb4 and bb3) from the Kulinda locality. Abbreviations: qz: quartz; or: orthoclase; al: albite; kao: kaolinite; bio: biotite; gt: goethite.

therefore correspond to the following suite: granites, biotite granites, and biotite-quartz monzonites. X-ray analyses and thin section observations of the volcaniclastic deposits indicate that almost all samples have the same mineralogy, consisting of quartz (20–67%), K-feldspars (8–34%), and clay minerals (mainly kaolinite; 19–69%).

Coarse and fine-grained layers do not show differences in their overall composition, but in the relative abundance of these minerals. A single sample, those from the bone bed located in trench 4 - bb4 - shows abundant iron oxides (goethite; 16%), in addition to quartz (48%), K-feldspars (17%), and kaolinite (19%) (Fig.6.4). By comparison, bb3 contains a significant proportion of kaolinite (34%), in addition to high quartz content (57%) and rare orthoclase (8%).

Grain-size is highly variable through the three excavated sections. Trench 4 (T4), in the lower part of the section, contains abundant fine-grained deposits, consisting mainly of mud-grade beds (59%) and siltstones (32%), along with rare sandstones (4–5%). Trench 3/3 (T3/3) contains coarser deposits, with breccia (13%), coarse to fine-

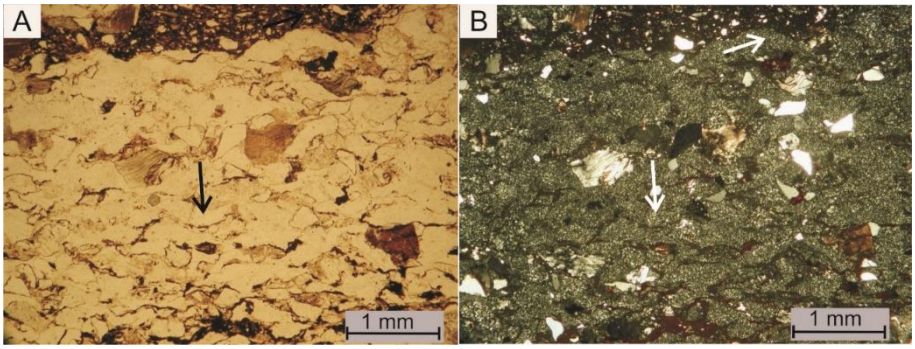

Figure 6.5. Texture of the samples. (A) Most of the minerals (black arrows; plane-polarised light) are replaced by (B) polycrystalline quartz (white arrows; cross-polarised light).

grained sandstones (30%), coarse to medium-grained siltstones (44%) and mudstones (13%). Trench 3 (T3) is characterised by dominant coarse-grained deposits: it comprises mainly very coarse sandstones to breccias (45%) and coarse to fine-grained sandstones (41%), with minor coarse- to medium-grained siltstones (13%) and few mudstones (2–3%). The general trend for the deposits from trench 4 through trench 3 is to coarsen upward, although fining-upward sequences are observed within individual trenches. For example, in trench 4, the layers situated above the bone bed are composed of sandy greywackes overlain by laminated silty mudstones (Fig. 6.2).

4.1.2. Microfacies

Thin sections confirm that all samples have similar mineralogical compositions. The predominant phases are sub-angular to angular quartz and feldspars, muscovite flakes, and kaolinite in a dark silty to clayey groundmass, of microcrystalline quartz. In the coarsest facies, quartz and feldspar grains are cracked and fragmented, and even, in some cases, dislocated. Quartz is mostly monocrystalline with sharp extinction, polycrystalline grains with undulose extinction are relatively rare.

Quartz commonly exhibits embayements with the dissolved cavity replaced by microcrystalline quartz. Feldspars, and, to a lesser extent, biotite are altered to kaolinite at their margin. Biotite is, in most cases, completely altered into kaolinite or chlorite, showing fan-shaped texture and iron-oxide coatings along cleavage planes. In most cases, microcrystalline quartz replaces much of the minerals (Fig. 6.5). This is particularly visible in cross-polarised light (Fig.6.5B).

In addition, samples from trench 4 contain abundant exogenous sub-rounded lithoclasts probably reworked from volcanic rock sources. Other detrital grains are most often angular to sub-angular. The mineralogy is dominated by sub-angular monocrystalline and sub-rounded polycrystalline quartz grains, sub-angular feldspar grains, and kaolinite. In cross-polarised light, quartz phenocrysts can show undulose extinction and polycrystallinity (e.g., in sample T4-2). Resorption features are widespread, especially in coarse-grained sediments. Feldspars are fragmented and weathered, but their primary composition cannot be determined due to secondary

silicification. The matrix consists of < 50 µm grains of quartz, feldspar, muscovite, and kaolinite. Siltstones are coarse-grained, usually poorly sorted and contain quartz and feldspar grains, along with kaolinite. At Kulinda, the finest deposits consist of silt-sized grains floating in a muddy matrix. These very fine-grained siltstones and mudstones are rich in iron oxides and also contain agglutinated plant fragments, algae, and fecal pellets (and lumps). Microfossils were not observed in thin sections. Well-preserved glass shards are present in at least one sample from trench 4 (Fig.6.6). In trench 3/3 deposits are coarser, with breccia (grains > 2 mm), very coarse- to fine-grained sandstones, coarse to medium-grained siltstones, and mudstones. Unlike trench 4, deposits from trenches 3/3 and 3 do not contain allochems, but abundant quartz grains and feldspars. Most samples are matrix-supported with a highly variable proportion among the samples.

Six petrological microfacies (MF) are recognised on the basis of the grain-size and mineralogy (Fig.6.6). These MFs are indistinctly present in the three trenches. Boundaries between successive microfacies can be either smooth or sharp:

Microfacies 1: Very coarse sandstone/breccia (Fig.6.6A)

Microfacies 1 is grain-supported and is characterised by feldspars and quartz that have generally grain sizes up to 2 mm, rarely up to 10 mm, floating in a clastic groundmass of similar composition. Quartz grains are sub-angular to sub-rounded, and usually monocrystalline, but rarely are polycrystalline or show undulose extinction. Feldspars are sub-angular to sub-rounded and show very thin exsolution lamellae and twinning. Sorting is poor and flow textures are observed: the finest-grained minerals show a preferential orientation within the groundmass, which seems deformed by coarser grains.

Microfacies 2: Lithic arenite (Fig.6.6B)

This microfacies is restricted to rock samples from trench 4. MF 2 is grain-supported and contains quartz and feldspar clasts, abundant lithic fragments, and is moderately sorted. The autochthonous crystals of quartz and feldspar are highly fragmented and most feldspars show a “cloudy” texture in plane-polarised light. In cross-polarised light, quartz and feldspars are recrystallised and composed of microcrystalline quartz. Kaolinite prismatic booklets, generally deformed, probably represent weathering products of biotites. Sand-sized grains make up most of the microfacies, and include more than 50% alloclasts, predominantly of volcanic origin, with some minor clasts of sedimentary and metamorphic origin. Most of the volcanic clasts correspond to sub-rounded andesitic fragments that display a typical texture consisting of lath-shaped or rectangular plagioclase crystals with a preferred orientation. The mesostase of these clasts is very fine and probably consists of devitrified volcanic glass. Many volcanic clasts are stretched and show flow textures.

Microfacies 3: Arkosic arenite (Fig.6.6C, D)

Contrasting with the previous microfacies, MF 3 does not contain significant lithic grains, but rather feldspars and quartz of silt- and sand-sizes, although some coarser

grained clasts are also observed. The groundmass is essentially composed of microcrystalline quartz (Fig.6.6D). Flow texture is developed around phenocrysts. Iron oxides are present in coatings around and in the structure of the minerals. The term "arkosic" used here characterises a siltstone/sandstone-like lithology dominated by angular feldspars and quartz, and with little matrix (<15%) (Dott, 1964). MF 3 also contains fecal pellets in the form of individual pellet or lumps.

Microfacies 4: Silty/sandy greywacke (Fig.6.6E)

MF 4 is dominated by a silicate matrix with subordinate silt and sand-sized clasts of similar composition: mostly quartz, feldspars and deformed kaolinite. Lithic clasts of unclear (sedimentary or volcanic) origin are rare. The term greywacke is applied here to unsorted rocks with angular clasts and relatively high proportion of matrix ("matrix-supported"), where free clasts seem to be "floating".

Microfacies 5: silty claystone to clayey siltstone (Fig.6.6F)

The general texture consists of a silica groundmass containing silicate clasts and mica flakes, of silt size, with few coarser (sand-sized) clasts. Fecal pellets are present and generally form clusters of closely packed, rounded, particles that are not cemented. Small bioturbated lenses are observed and erase the original texture of the rock. Plattened plant fragments are common and show parallel orientation to the bedding. Algal remains are rare.

Microfacies 6: iron-stained tuffaceous sandstone (Fig.6.6G)

This microfacies is encountered in a single sample from trench 4 (T4-5). It consists of clasts of medium sand-size along with abundant, slightly finer, arciform glass shards, both highly impregnated by iron oxides. Identification of mineral grains is difficult due to the coating of iron oxides: however some quartz grains show undulose extinction. Given the sample pervasive precipitation of iron oxides, it was not possible to verify whether the tuff was reworked or deposited *in situ*.

4.2. Elemental geochemistry

4.2.1. Major elements

The concentrations of the major elements (in weight %) in the Kulinda deposits are reported in Table S5.4 (see also the Supplementary information of Chapter 5). The plutonic basement consists of granites, biotite granites, and biotite-quartz monzonites. These "granitoids" are characterised by relatively high SiO_2 contents (ranging from 68 to 78 %), along with high alkali ($Na_2O + K_2O$) content, generally higher K_2O than Na_2O, low CaO abundances, and high Al_2O_3 values. Two groups of granitoids are discriminated on the basis of their major elements. Group I, which includes finely grained (micro-) granites, presents relatively high SiO_2 (78.4 %) and high K_2O (5.17 %), but has values well below the mean SiO_2 values ranging from 67.7 to 69.7 %, close to those of the UCC. Granite groupe II, which includes biotite granites and biotite-quartz monzonites, has SiO_2 values ranging from 67.7 % to 69.7 %, close to those of the UCC.

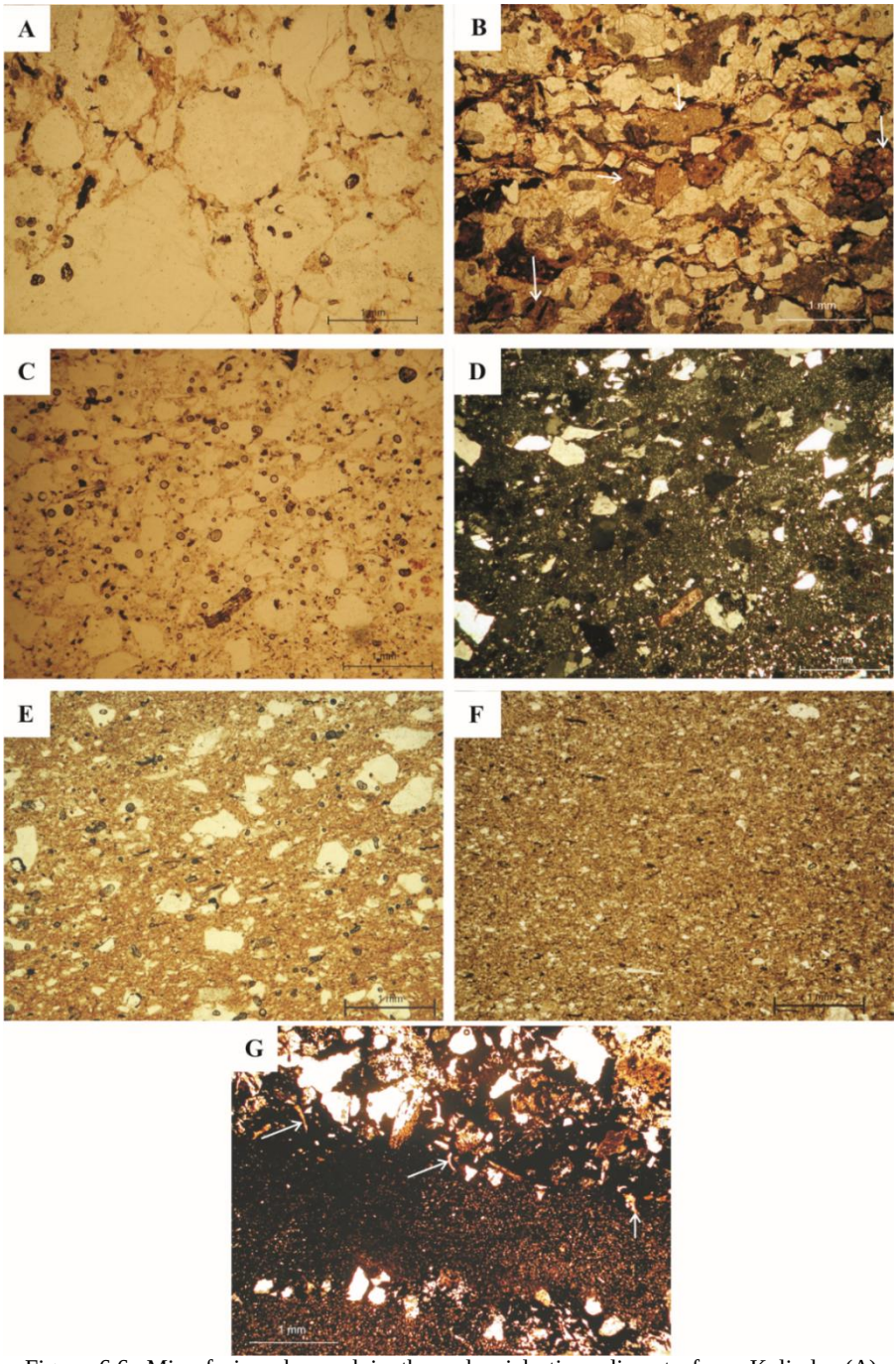

Figure 6.6. Microfacies observed in the volcaniclastic sediments from Kulinda. (A) breccia, (B) lithic arenite with volcanic clasts (white arrows), (C) arkosic arenite, (D) arkosic arenite in cross-polarized light showing the texture of the matrix and the silicification of most grains, (E) silty claystone, (F) greywacke, and (G) tuffaceous siltstone, containing arcuate glass shards (white arrows).

Values for the major elements in the overlying volcaniclastic deposits do not vary significantly, except those of SiO_2 that vary from 53.5 % (for bb4) to 79.6 % (sample T3/3-5F in trench 3/3), with a mean concentration of 70.9 % (see Fig. 6.7). Silica is therefore above the mean value for the UCC (Rudnick and Gao, 2003). The fine-grained samples are generally characterised by higher SiO_2 values compared to the coarser-grained. P_2O_5 content is usually close to the mean value of the UCC, except for three samples that show higher concentrations: 0.32 % (bb4), 0.33 % (T4-3C), and 3.75 % (T3-10F). The alkali CaO and Na_2O have very low abundances, with an average of 0.20 % and 0.12 %, respectively. K_2O concentrations are higher, with an average value of 2.25 %. In addition, K_2O and CaO show a positive correlation. Fe_2O_3 values are generally very low within the three trenches, ranging from below the detection limit, up to 2.88 %. Only one sample, the bone bed 4 (T4-BB), presents high Fe_2O_3 content (21.1 %), together with relatively high MnO and MgO values when compared to the other rock layers. MnO and MgO are however always low at Kulinda. Al_2O_3 is highly variable throughout the three sections (Fig. 6.7), ranging from 10.8 % (bb4) to 28.8 % (T3-10C), with a mean value of 16.4 %.

4.2.2. Trace and rare earth elements (REE)

Upper Continental Crust (UCC)-normalised trace elements were reported on a spidergram (Fig.6.8). The plutonic rocks are characterised by different trace elements values and the two granite groups can be distinguished, here, by their abundance in REE. The microgranite is depleted in REE - especially in HREE - with respect to the three other granitoids, and have ∑REE values well below the mean values for the UCC. Volcaniclastics are particularly enriched in As, Mo, Sb, W, Pb, and U. Bone bed 4 shows high proportions of Y, Be and V that are not observed in bone bed 3. The redox-sensitive trace elements - Mn, V, Cr, Co, Ni, Cu, Zn, Mo, Pb, and U - show variable concentration among the three trenches (Table S5.4). Values of Rb are quite high but variable, ranging from 32 to 119 ppm, and seem higher in trench 4 than in trenches 3 and 3/3. Ba content ranges from 160 to 758 ppm, with an abnormally high value - 1,978 ppm – in sample T3-10F. Be, Cr, Ga, Ge, Sr, Y, Nb, Sb, Ba, Pb, Th, and U values are always high in the latter sample.

Values for Mo and U are always high, respectively ranging from 3 to 32 times, and from 1 to 57 times the UCC values. The Th/U ratios are generally very low (<1), except for four samples (see Table S5.4). Mo and U show a positive correlation (Fig.6.9). Mo/U ratios are always below 1 (mean value = 0.66), except for samples T4-8b (1.97) and T3-1G (3.06). In bone bed 4, Mo/U = 0.27, whereas in bone bed 3, Mo/U = 0.44. Redox-sensitive elements are generally below (V, Co, Ni, and Zn) or close to (Cr, Cu) the UCC values. One particular sample from trench 3 (T3-10F) shows very high Sr, Mo, Ba, Pb, Th, and U values (see Fig.6.8), whereas Co and Ni contents are very low.

Distribution of REE in rocks from the locality are shown in Fig.6.10. Granitoids display rather similar chondrite-normalised REE distributions, characterized by a

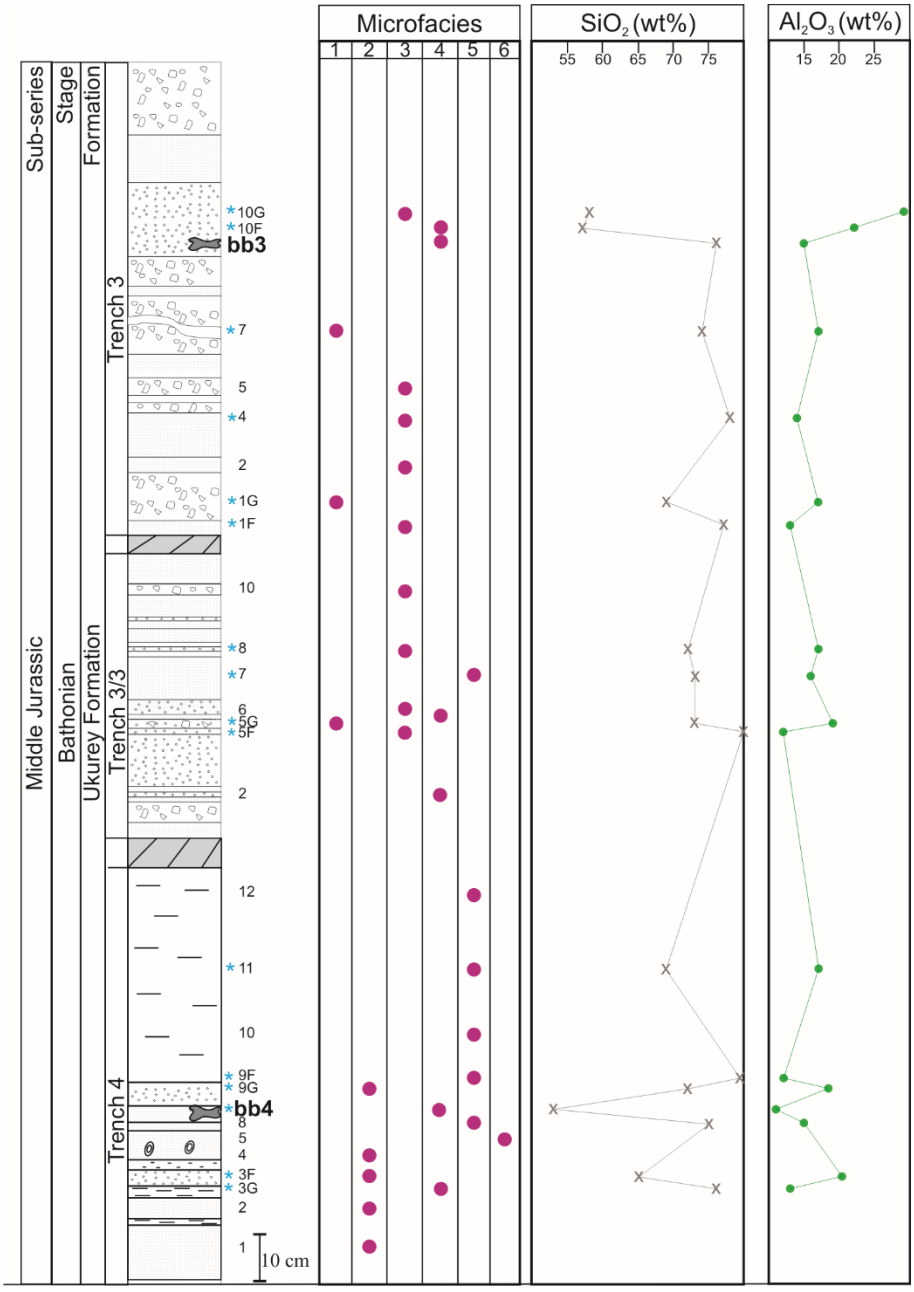

Figure 6.7. Lithological section comprising the three trenches excavated at Kulinda. Six microfacies are discriminated throughout the whole section. Comparison is made with the SiO_2 and Al_2O_3 values (wt%), showing a negative correlation between these two major oxides, except for the bb4. Samples with an * represent those analysed for their geochemical composition.

negative dip, an enrichment in light rare earth elements (LREE) with respect to heavy

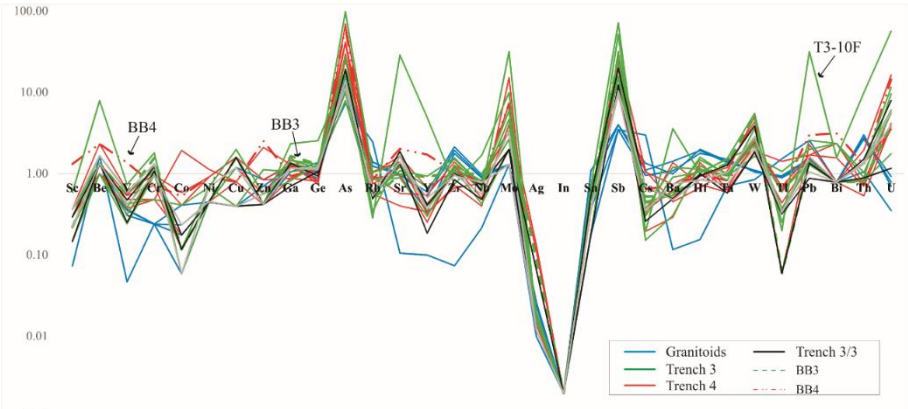

Figure 6.8. Multi-element Spidergram of the volcaniclastic sediments and the granitoids that crop out on top of the hill, at Kulinda. It shows rather similar distribution patterns for the volcaniclastics, reflecting similar source compositions. Values can, however, be highly variable between samples. Distribution pattern for the bone beds 3 and 4, are shown by a black arrow. A sample from trench 3 (T3-10F) shows great enrichments in trace elements (e.g., Sr, Mo, Ba, Pb, Th, U).

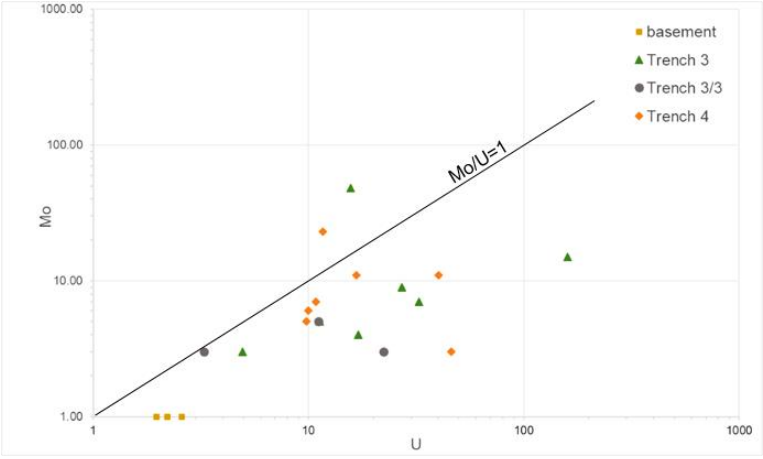

Figure 6.9. Mo versus U diagram showing the positive correlation between the two elements in Kulinda volcaniclastic deposits.

rare earth elements (HREE) and medium rare earth elements (MREE). A Ce enrichment is observed in granites from group II. All volcaniclastic samples show a similar parallel chondrite-normalised REE distribution, with a negative dip and an enrichment in LREE relative to MREE and HREE. Samples have $(Ce/Yb)_N$ ratios ranging from 9.1 to 30.7 (Table S6.4). LREE fractionation is variable, with $(Ce/Sm)_N$ ratios ranging between 2.8 to 5.9, with a mean of 3.9. The HREE show an even more variable fractionation than do the LREE, with $(Gd/Yb)_N$ ratios ranging from 0.9 to 13.3. Eu anomaly $(Eu/Eu^*)_N$ is slightly negative to slightly positive, with values ranging from 0.67 to 1.21.

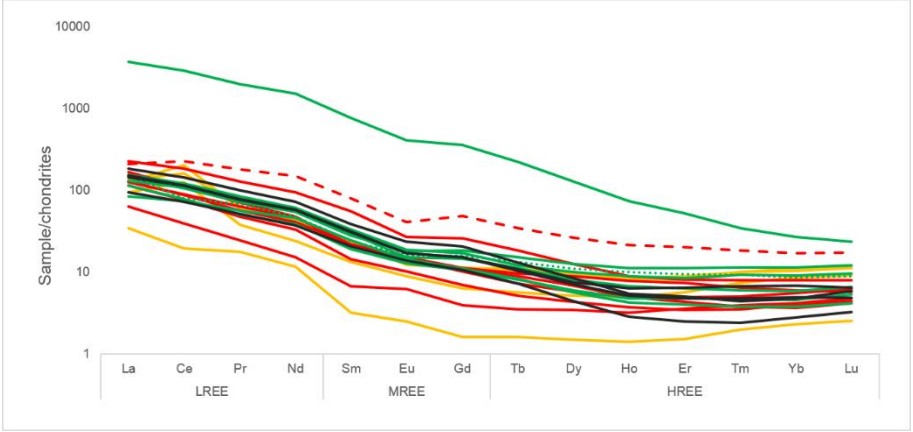

Figure 6.10. Rare Earth Element (REE) chondrite-normalised diagram of the volcaniclastic sediments and granitoids from Kulinda. Legend: yellow plain line: granitoids; red plain line: trench 4; green plain line: trench 3; black plain line: trench 3/3; red dashed line: bb4; green cross line: bb3.

4.3. Weathering indices

Alteration of deposits at Kulinda, and in the bone beds, is partially determined here by the use of weathering indices. Weathering indices are shown in Table 6.1. The granitoids show the lowest values for five indices, R, V, CIA, CIW, and PIA, and the highest values for WIP. The CIA and CIW values are higher than values obtained from "fresh" granites (Harnois, 1988; Morey & Setterholm, 1997; Nesbitt & Young, 1982), whereas the WIP values are lower in the Kulinda basement than in "fresh" granites (Parker, 1970).

These data matched with the mineralogical content and petrographical features, therefore indicating that the granites at Kulinda were exposed to weathering. All the volcaniclastic samples show index values indicating they experienced a much more intense weathering than their granitic source. When we compare the three trenches, the mean index values for each trench are very close to each other, even though slight differences are observed within the trenches. In particular, trench 4 show the lowest mean values for R, V, CIA, CIW, and PIA and has, therefore, the highest mean WIP values. By comparison, the bone bed 3 shows values corresponding to a more intense weathering for that layer. One sample (T3-10C) displays particularly high V and R indices, as well as low WIP index, suggesting that this sample is intensively weathered. The greatest diversity of values among weathering indices appears for the Vogt's index, ranging from 19.9 to 136.4. Moreover, fine-grained deposits (e.g., T4-3F, T4-9F) display index values that are different from the coarser-grained deposits (e.g., T4-3C, T4-9C). It suggests that coarse-grained rocks, like sandstones, were more intensively weathered due to their higher porosity. Data show that weathering probably occurred top down, as it is usually expected. Volcaniclastic deposits from the top section - trench 3 - have been highly weathered, whereas those from the bottom

Table 6.1. Weathering indices for selected samples from volcaniclastic deposits and granitoids. R: Ruxton Ratio, WIP: Weathering Index of Parker, V: Vogt's index, CIA: Chemical Index of Alteration, CIW: Chemical Index of Weathering, PIA: Plagioclase Index of Alteration.

Sample	R	WIP	V	CIA	CIW	PIA
Biotite granite	22.52	57.2	3.18	61.98	73.26	67.31
Leucogranite	15.88	61.12	4.57	58.05	76.51	65.55
Qz-biotite monzonite	25.12	65.84	3.65	61.65	74.97	68.07
Qz-biotite monzonite	23.21	61.93	3.26	61.03	73.18	66.51
T3-1 fine	17.20	13.64	51.21	88.02	98.66	98.47
T3-1 coarse	24.15	33.41	54.24	79.47	98.00	97.39
T3-4	17.48	15.99	50.03	86.57	98.55	98.32
T3-7	22.56	27.47	46.09	82.13	97.76	97.23
T3-10 fine	38.90	8.08	35.00	93.95	97.58	97.49
T3-10 coarse	49.43	9.79	136.36	95.69	99.48	99.46
bb3	19.23	12.09	41.05	89.79	98.32	98.14
T3/3-5 fine	15.55	11.70	41.64	88.61	98.25	98.04
T3/3-5 coarse	26.13	16.75	80.65	89.66	98.91	98.78
T3/3-8	23.55	18.79	60.09	87.41	98.67	98.47
T4-3 fine	17.47	13.11	3018	88.01	97.79	97.51
T4-3 coarse	31.34	24.56	38.41	85.53	97.39	96.97
T4-8	19.38	37.07	37.84	75.03	96.93	95.67
T4-9 fine	15.63	18.39	36.23	83.33	97.85	97.40
T4-9 coarse	24.33	26.40	54.61	83.56	98.32	97.96
bb4	20.13	20.69	16.90	79.41	96.68	95.75

section - trench 4 - have been less extensively weathered. Here, weathering indices constitute good indicators of the recent weathering processes that occurred on site.

4.4. Taphonomy

Description of the bone beds

The fossils unearthed between 2010 and 2012 were briefly described by Godefroit et al. (2014), but new discoveries since 2013, mainly in trench 3/3, require additional explanation. Hundreds of dinosaur bones have been excavated from those three bone beds. Excepting very few algal remains, no aquatic organisms have been recovered from Kulinda deposits. Except for a single shed tooth from a medium-sized theropod (which was found in bb3), Godefroit et al. (2014) hypothesised that the three bone beds contain exclusively bones and soft-tissues from the neornithischian *Kulindadromeus zabaikalicus* and can therefore be regarded as monospecific (*sensu* Eberth et al., 2007): detailed analysis of the skeletal elements (in particular, the partially articulated remains) preserved within and between the bone beds reveals no evidence for multiple taxa of basal ornithischians in the Ukurey Formation of the

Kulinda locality. Each individual skeletal element is represented by a single morphotype; all the observed minor differences can easily be explained by ontogenetic and normal intraspecific variations. Alifanov and Saveliev (2014, 2015) proposed an alternative interpretation for the dinosaur fauna at Kulinda and named three new taxa from this locality: the 'hypsilophodontian' ornithopods *Kulindapteryx ukureica* and *Daurosaurus olovus* (Alifanov & Saveliev, 2014), and the 'nqwebasaurid' ornithomimosaur *Lepidocheirosaurus natalis* (Alifanov & Saveliev, 2015). However, Godefroit et al. (in prep) refute in detail Alifanov and Saveliev's (2014, 2015) hypothesis of a diversified dinosaur fauna at Kulinda. The majority of the *Kulindadromeus* fossils belongs to juveniles or sub-adults; larger individuals are rare. The overrepresentation of younger individuals in the bone beds could suggest an attritional accumulation of carcasses leading to the formation of the bone beds and not recurrent catastrophic event (Lyman, 1994). Confirmation of this hypothesis requires a detailed age-frequency distribution of the long bones and further palaeo-histological investigation.

Unfortunately, the complicated excavation conditions in the field (access to the site is extremely difficult for bulldozers or heavy excavators, in any case not available in this area) did not allow precise 3D mapping and orientation of the collected skeletal elements. Because of the hardness of the sediments, bone bed slabs had to be removed from the hillside and subsequently cleaved into thinner layers, revealing the presence of fossils.

Bone bed 4, in trench 4, consists of one thin (about 5 cm) lens, made of iron-oxide rich hard siltstones and contains abundant organic remains (palynomorphs, plant macro-remains, pellets, and dinosaur remains). This lens is not continuous at the scale of the excavation, but dislocated into decimetric slabs by numerous faults filled up by a mixture of eroded sediment, probably resulting of post-depositional tectonic processes that lead to the formation of the Kulinda hill. *Kulindadromeus* fossils are particularly abundant in this lens and consist of accumulations of fragmentary, but still articulated, carcasses. It is here hypothesised that the dislocation of *Kulindadromeus* carcasses within bb4 at least partly resulted from the post-depositional dislocation of the lens. Most of the bones excavated in this layer are highly weathered and, in most cases, only the three-dimensional external moulds are visible within the rock matrix (Fig.6.11A). It implies that original bones have been dissolved after sediment compaction, possibly recently. Skin and integumentary structures such as scales and feathers are, nonetheless, exquisitely preserved and connected to the poorly-preserved, but articulated, bones (Fig.6.11B). Details of the skin, scales and filaments are finely preserved. Bones from bb4 are impregnated by iron-oxides, such as the host sediment.

In contrast, bone bed 3, in trench 3, consists of several centimetre-scale discrete bone-hosted layers located in the upper part of the section (Fig.6.2B), within coarser volcaniclastic deposits. Fine-grained siltstones contain well-preserved bones with few articulated elements (Fig.6.11C), and soft-tissues are absent. Lighter cranial elements

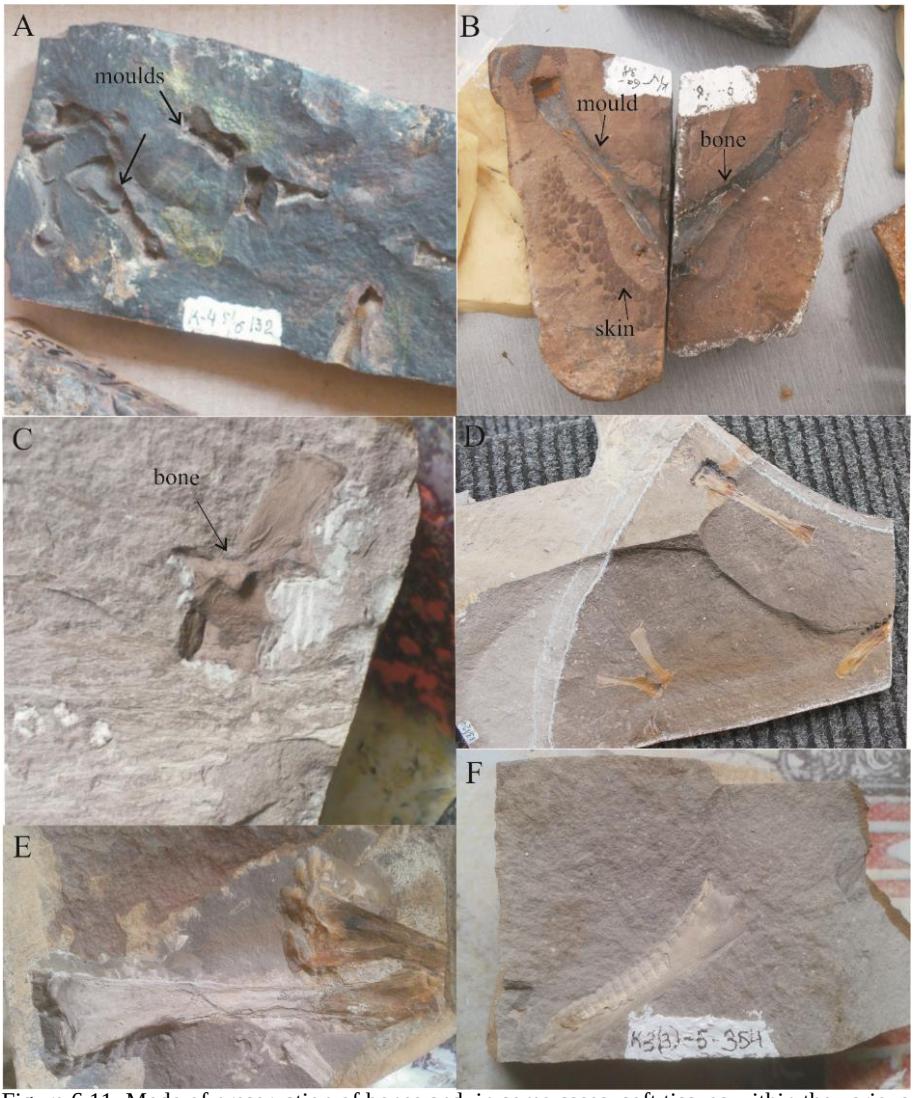

Figure 6.11. Mode of preservation of bones and, in some cases, soft tissues within the various excavated trenches. (A) moulds of *Kulindadromeus* bones in the oxidized bb4, (B) print and counterprint of a tibia associated with scaly skin from bb4 (C) and (D) bone impressions from trench 3, with no soft tissues, (E) bone impressions and (F) soft tissue traces from trench 3/3.

are rare, whereas more massive bones (especially tibiae, humeri, scapulae, and ilia) are well represented. Bones are preserved in two dimensions and they have experienced complete recrystallisation. EDS analyses show that bones have the same chemical composition as the embedding siliciclastic matrix and that original hydroxyapatite is not preserved. These “bones” look rather like bone impressions.

In addition to the two major bone beds, the intermediate section (trench 3/3) contains isolated remains disseminated in several (at least seven) discrete layers

(Fig.6.11E). Rare soft-tissues, including 'feather-like' structures, small epidermal scales, and granular skin, accompany the bone remains (Fig.6.11F). The dominant remains are vertebrae, limb bones, and ilia. Diverse insect remains (Trichoptera) are also present.

Composition of the bone beds

Scanning electron Microscopy (SEM) and Energy dispersive X-ray spectroscopy (EDS) were performed on a bone mould and elongate integumentary structures from bb4, as well as a bone impression from bb3. SEM images of the bone mould and its embedding matrix reveal that hundreds of spheroidal minerals cover the internal wall of the mould (Fig.6.12A). Each sphere is composed of a multitude of smaller rounded structures. The elemental composition of these spheres mostly consists of iron and oxygen (Fig.6.12A), likely indicating the presence of iron oxides in the form of framboids, which is generally typical for pyrites (i.e., iron sulphides). The filament preserves thin discontinuous layer containing relatively high carbon and iron contents, together with less sulfur (Fig.6.12B). The filament does not contain iron sulfides or other automorphic minerals. Rather, the integumentary appendages display relatively smooth, amorphous, surfaces. The other analysed elements – Si, Al, Ca, and K - are characteristic of the embedding alumino-silicate matrix. The bone from bb3 shows a homogeneous surface, not distinguished from the embedding sediment. EDS analyses indicate that both the bone and its matrix contain the same elements (mainly Si, Al, O; Fig.6.12C). No particular features have been observed on the bone, except several minute carbon-rich areas (Fig.6.12C). X-ray diffraction (XRD) spectra of the bone beds (Fig.6.4) show that kaolinite is an essential component of the sedimentary matrix, especially in bb3. Iron oxides are abundant in the matrix of bb4 only. These features may have resulted in the distinct degree of preservation observed in the bone beds.

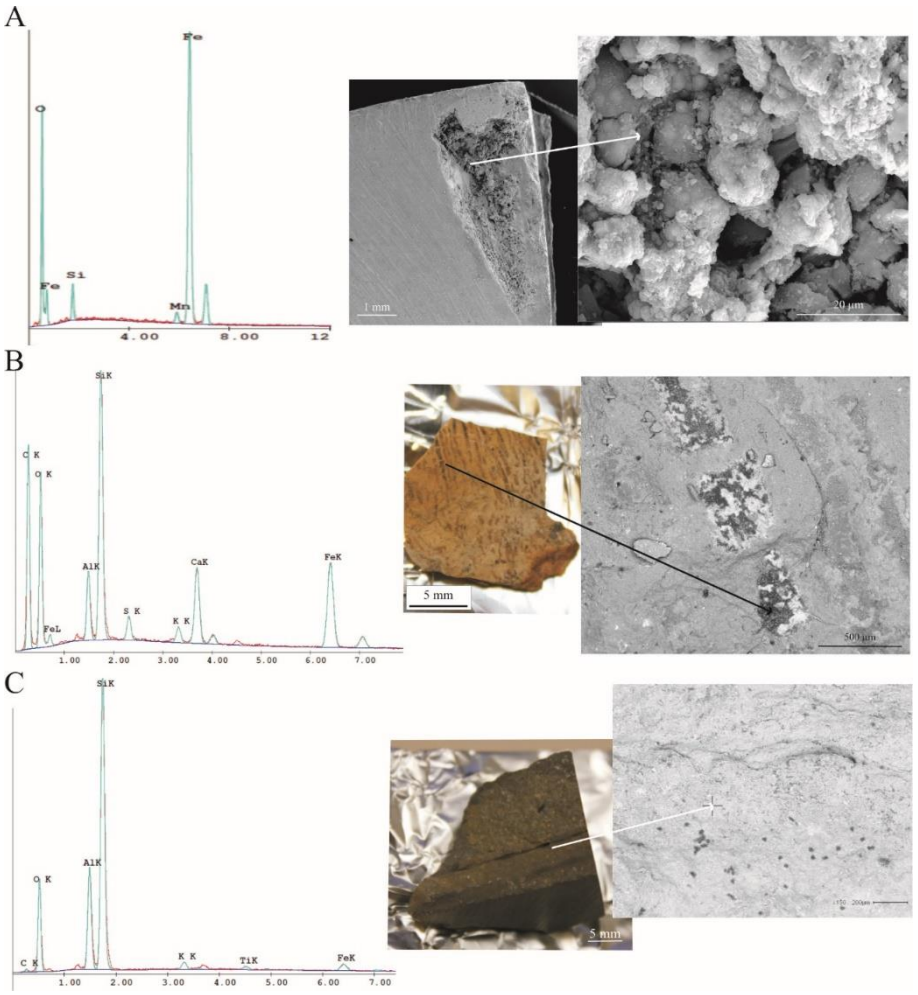

Figure 6.12. Energy dispersive X-ray spectroscopy (left) and scanning electron microscopy (right) of (A) a bone mould from bb4, (B) an elongate integumentary structure from bb4, and (C) a bone "impression" from bb3. Images and elemental compositions indicate that the two bone beds are characterized by two different types of preservation.

4.5. Palynology and palaeobotany

The spore-pollen assemblage contains high quantities of poorly preserved bisaccate pollen of conifers, together with species that were widespread in Siberia and other boreal regions during the Middle Jurassic (e.g., *Pseudopicea variabiliformis*, *P. rotundiformis*, *Dipterella oblatinoides*, *Piceites asiaticus*; Ilyina, 1985; Shurygin et al., 2010; Smokotina, 2006). Pollen of cheirolepidiaceous conifers (*Classopollis* spp.) are rare (1.5–3.0%). Ferns are represented by relatively abundant (3.5–15%) cyatheaceae/dipteridaceae, such as *Cyathidites-Biretisporites* spores. Spores of osmundaceous ferns (*Osmundacidites* and *Todisporites*) are less abundant (1–1.5%). In addition, we spores of lycopods (*Lycopodiumsporites*, *Neoraistrickia*, *Uvaesporites*, and some others) and sphagnaceous mosses (*Stereisporites*, 1.5–4%) are present. Few freshwater microfossils have been observed in the samples: the green algae *Botryococcus* spp. and rounded morphotypes of simple morphology, which can be assigned to the formal genus *Leiosphaeridia* spp.

The macrofloral assemblage collected at Kulinda is relatively poor and consists of:

(1) Algae, with *Algites* sp., represented by small (<1 mm wide and 2 cm long) bent threads indicating that the plants were tender in life-time.

(2) Mosses, with dichotomous thalli of 2 mm wide (Fig.6.13A). The specimens resemble the thalli of *Hepaticites arcuatus* (L. et H.) Harris from the Middle Jurassic deposits of Yorkshire (England), and some bear a median vein. The epidermal structure of the species is well known, but is not preserved. Thereby, the specimens are determined as *Hepaticites cf. arcuatus* (L. et H.) Harris. Cormophytic mosses (Fig.6.13B) are represented by the leafed shoots of *Muscites samchakianus* Sebr. They are branched at the apex and can reach 1 mm wide. The lateral branches deviate from the main stem with a sharp angle (about 45°) and extra-thin leaves are observed on one branch. They are distichously arranged in two vertical ranks on opposite sides of the axis, located on the stem, suggesting that they were probably spirally-disposed in their life-time. The leaves measure 3 mm long and deviate from the shoot at a sharp angle, and their apexes are directed upwards.

(3) Anthophytes are represented by fragmented leaf sheaths of *Equisetites sp*., on which three free drip tips pressed to stem are observed. A stem fragment from *E. undense* shows a clear internode, which is characteristic of this species.

(4) Ferns are represented by isolated pinnate leaves of *Coniopteris sp*. showing characteristic venations (Fig.6.13C), and by leaf fragments of *Peltiphyllum cf buriensis*.

(5) Czekanowskiales (Leptostrobales), represented by fragments of small linear leaves of *Czekanowskia ex gr. rigida* Heer (Fig.6.13D). One can trace a median vein and dichotomy on individual specimens. These specimens resemble *Algites sp*., which forms bulk burials in the Ukurey Formation. Leaves of *Czekanowskia ex gr. rigida* Heer differ from the latter in their stiffness.

(6) Coniferales (Fig.6.13E) are represented by cones with well-preserved diamond-shaped scales attributed to *Elatides ovalis* Heer (Fig.6.13F). Unlike standard

Figure 6.13. Palaeofloral assemblage from the Kulinda locality, including: (A) the moss *Hepaticites arcuatus*?, (B) the cormophytic moss *Muscites samchakianus*, (C) the fern *Coniopteris*, (D) the Czekanowskiale *Czekanowskia ex gr rigida*, (E) and (F) the coniferales *Elatides ovalis* and (G) *Schizolepidopsis moelleri*, and (H) unidentified gymnosperms.

samples from the Ust-Balei locality (in Transbaikal region), the tips are here somewhat truncated. In Russia, *Elatides ovalis* is known in the Early Jurassic of the Irkutsk Basin (Akulov et al., 2015) and the Upper Jurassic of the Bureya Basin (Krassilov, 1973). Winged seeds of *Pityospermum sp*., characterised by large asymmetrical fructification, occur with cones (*Pityostrobus*). The seed-bearing fructification is 13 mm long and 6 mm wide. The exterior margin is bent, though the interior is straight. The apex is not preserved, whereas an ovoid seed (3 mm x 2 mm) is observed at the base. The nucleus of *Pityospermum cf. maakiana* is ovoid, is 4 mm long and 5 mm wide, with a slight tapering down to the tip. Isolated, forked scales of *Schizolepidopsis moelleri* (Fig.6.13G) and *S. elegans* cones are also observed. Cone scale of *S. elegans* is sessile, wedge-shaped, and is 4 mm long and 5 mm wide. The median incision is deep, forming three-quarters of the total length of the scale. It divides the scale into two symmetric lobes measuring 2 mm wide and having subacute apexes. The interior edge of the lobe is less convex than the exterior one. The insertion of seeds and the sculptures on the scale surface were not preserved. The lobes of *S. cf. levis* scales are triangular and asymmetric.

(7) Unidentified gymnosperms represented by small ovoid seeds (3 mm x 2 mm) were observed as well (Fig.6.13H). They might be related to the genus *Carpolithes*.

The distribution of these taxa in the three trenches is as followed: trench 4 contains leaf sheaths of the horsetail *Equisetites*, thalli of the moss *Hepaticites*, leaves of the Czekanowskiale *Czekanowskia*, cones of the conifers *Schizolepidopsis*, and the small algae *Algites*. In trench 3/3, mosses, seeds of gymnosperms (*Carpolithes*), and algae (*Algites*) dominate the plant assemblage. In trench 3, the assemblage is poor and consists of cormophytic mosses and cones of conifers (*Schizolepidopsis*).

4.6. Sedimentary organic matter

The Rock-Eval pyrolysis reveals relatively low but variable total organic carbon (TOC) contents (<1 wt %), ranging from 0.34% to 0.90%. The highest TOC values are observed in bone bed 3 and in a barren sample from trench 3/3. Bone bed 4, which contains well-preserved soft-tissues but weathered bones, has nonetheless the lowest TOC values (0.34-0.35 %). The Hydrogen Index (HI) varies from 60 to 260 mgHC.g^{-1} TOC. The Oxygen Index (OI) is abnormally high in bb4 (951-1000), whereas it is much lower in bb3 (117-127) and sample T3/3-7 (101-110). The OI and HI values plotted on a modified van Krevelen diagram (Fig.6.14A) shows that the organic matter from bb4 is a type IV kerogen (highly oxidised organic matter), although the other analysed samples are kerogen type III (terrestrial organic matter). Mean T^{max} values of the pyrolysed samples are 450 °C in bb4, 444°C in T3/3-7, and 438°C in bb3, indicating that organic matter is thermally mature (Fig.6.14B).

Organic matter from bb4 is dominated by figured elements such as light brown gymnosperm pollen grains and spores, and brown or black phytoclasts (Fig.6.15A). The latter consist of blade-shaped and equant ligneous particles, in some cases

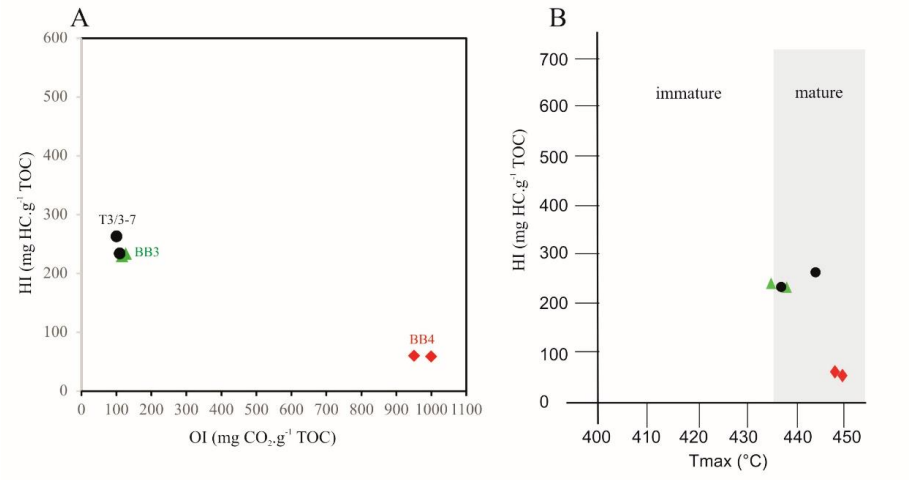

Figure 6.14. Characterisation of the organic matter from bone beds 3 and 4, and a third sample from trench 3/3. (A) Modified Van Krevelen diagram and (B) HI versus T_{max} diagram, showing the specific nature of organic matter from bb4.

showing bordered pits, and translucent cuticles. Woody debris shows various grain sizes, ranging from small (25 μm) to large (>200 μm) particles. Amorphous organic matter (A.O.M.) is rare and generally consists of large brown "fluffy" particles. Phytoclasts and palynomorphs are frequently embedded in the A.O.M. Amber is common, and algal remains - *Botryococcus* – are rare (Fig.6.15B). By contrast, A.O.M. dominates the organic content in bb3, which is primarily constituted of small clusters of light brown granular particles (Fig.6.15C). Rare small (20-40 μm) black, equant or acicular, woody debris are present. No other microfossils have been observed. For comparison, in trench 3/3, the studied sample is dominated by flaky brown amorphous organic matter (Fig.6.15D). Small black woody debris are scarce. This palynofacies is rather similar to that observed in bb3.

The abundance and state of preservation of the figured elements varies greatly among the samples. In trench 4, palynomorphs are abundant and vary in preservation, from well-preserved to badly-preserved. Abundant teratomorphic – with abnormal morphologies – palynomorphs are observed. Bisaccate pollen grains usually show poorer preservation than the other pollens, and spores (see Fig.6.15A). In trenches 3 and 3/3, when present, palynomorphs are rather well-preserved. The pollen and spore assemblages is described in detail in Chapter 5.

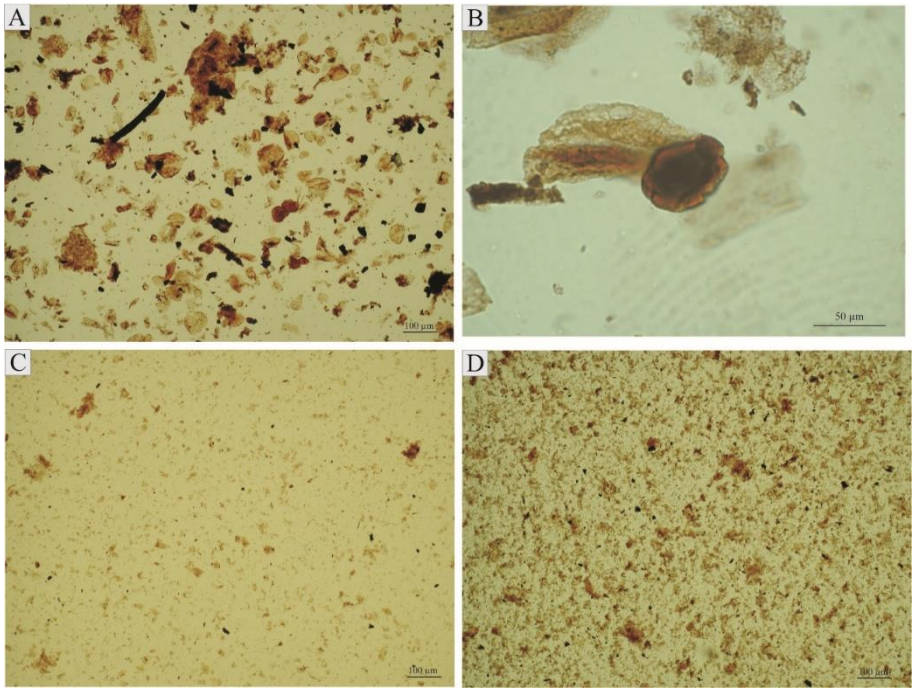

Figure 6.15. Palynofacies from Kulinda deposits showing the degree of preservation of the palynomorphs and other figurated elements. (A) abundant well-preserved figurated elements in bb4, (B) possible *Botryococcus* algae, (C) few figurated elements and dispersed amorphous organic matter from bb3, and (D) abundant flocculate amorphous organic matter from sample T3/3-7 in the intermediate trench.

5. Discussion

Source of the igneous material

Our data show that the finely-grained granite collected on top of Kulinda hill is enriched in silica and is depleted in Ca, Ba, Sr, Eu, Ti, P, and REE, suggesting a greater degree of differentiation with respect to the other granitoids samples. These depleted elements are generally contained in Ca-plagioclases, Ti-oxides and apatite that formed early in the magmatic chamber and are removed from the residual magmatic liquid, then leading to a depleted liquid. Accurate U-Pb dating of the Kulinda granites have shown that they are Aalenian – early Middle Jurassic - in age (see Chapter 5). This granite and the other granitoids samples from Kulinda have major and trace element abundances comparable to other Middle-Late Jurassic intrusions reported in eastern Transbaikalia (Kozlov, 2009). Our data show that the granitoids at Kulinda may be either part either of a complex of rare-metal intrusions known as the Kukul'bei complex or of the Shakhtama plutons (Kozlov, 2009, 2011b). Both complexes are regarded as post-collisional (Spiridonov et al., 2006). According to the dating of these two complexes, the Kulinda granitoids may be part of the Middle-Late Jurassic Shakhtama complex, rather than the Late Jurassic Kukul'bei complex (Rutshtein & Chaban, 1997). The weak negative Eu anomalies in the granitoids from Kulinda was also observed in granitoids from nearby localities in eastern Transbaikalia and might be related to a poor differentiation of the early magmatic liquids (Kozlov, 2009). Our granites and monzonites are similar in composition to other acidic plutons from eastern Transbaikal, and in particular from the Kulinda area (Kozlov, 2009). Our data, nonetheless, suggest that the Kulinda granitoids were emplaced in two different tectonic settings: active continental margin and passive settings. The geodynamic context in Siberia during the Mesozoic may explain these two different origins (Delvaux et al., 1995; Tomurtogoo et al., 2005; Zorin, 1999). We can hypothesise that the biotite granites and quartz monzonites were emplaced first, as a result of felsic magmatism related to the subduction of the Mongol-Okhotsk oceanic lithosphere beneath Siberia during the Early-Middle Jurassic. The finely-grained granites - which display characteristic features of anorogenic granites - may have been emplaced thereafter, during the post-orogenic phase. The two zircon age populations observed in the Kulinda deposits and their granitic source (see Chapter 5) also suggests that two different, successive, magmatic episodes emplaced granitoids in the area, one during the Pliensbachian (between 189.3 ± 1.5 Ma and 183.8 ± 1.8 Ma) and the second during the Toarcian-Aalenian (between 177.6 ± 1.7 Ma and 171.1 ± 1.5 Ma). Tuffs are present in the section but there is no direct evidence that these deposits were produced by volcanic activity contemporaneous with their accumulation. It should, however, be noted that volcanic debris are usually rapidly weathered and that their primary texture is rapidly lost during alteration.

The volcaniclastic deposits from Kulinda are, at different extents, enriched in trace elements and particularly in REE. The mean crustal Th/U ratio ranges around 4

(Sun & McDonough, 1989), reflecting the typical difference in the mobility of these two elements. Here, most of Kulinda samples (including bb4 and bb3) show Th/U ratios below 1, suggesting a preferential enrichment of U. The positive correlation between P_2O_5 and U (and REE) suggests that the enrichment in U (and REE) in some samples is related to the presence of phosphate minerals, such as apatite and monazite.

Alternatively, rare earth and trace elements may originate from their concentration in organic phosphates, such as in coprolites and bones (e.g., Williams et al., 1997; Owocki et al., 2012; Polet & Orban, 2001; Trueman et al., 2007; Trueman, 1999; Trueman & Tuross, 2002). This would explain why the bb4 (and sample T3-10F) displays a greater enrichment in both phosphates and REE, relative to the other samples.

Weathering indices are not correlated with REE abundances, likely indicating that REE enrichment is not related to weathering processes. The particular richness in trace elements is most probably related to the source of the sediments. The mineralogy of the deposits is similar to weathered granites, as indicated by the lack of unstable minerals such as plagioclases and biotite, but a large amount of their alteration products (kaolinite) (e.g., Irfan, 1996; Morey & Setterholm, 1997; Wilson, 2004). In addition, REE-normalised diagrams displayed similar distribution patterns for both the granitoids and the volcaniclastic deposits. This implies that the latter mostly derived from the same igneous material, similar in composition to the "granitoids" that crop out on top of Kulinda hill (see also Chapter 5).

Due to its high content in the volcaniclastic sediments and its nearly absence in their granitoid source, kaolinite is interpreted here as the weathering product of biotite and feldspars (e.g., Gilkes & Suddhiprakarn, 1979; Irfan, 1996; Jeong, 1998; Mitsuda, 1960; Wilson, 2004). Kaolinite forms when cations are constantly removed from feldspars, during intense water flow (Irfan, 1996), but can also form from biotite weathering (Gilkes & Suddhiprakarn, 1979; Irfan, 1996). The high kaolinite contents in most samples suggest their rather intense alteration. The relative amount of kaolinite in the volcaniclastics is similar to what is observed in residual soils derived from a granitic protolith (Irfan, 1996). The kaolinite content is also positively correlated to the degree of weathering indicated by the weathering indices. In particular, bb3 has higher kaolinite content than bb4 and show more intense weathering.

Origin of the volcaniclastic deposits

The lack of sorting, as observed in Kulinda volcaniclastic deposits is a typical feature of debris or mud flows (e.g., Bertran & Texier, 1999). Unlike deposits originating from fluvial processes, debris flows do not segregate particles with respect to their size, but are rather transported together in the flow, resulting in poorly-sorted deposits. Debris flows have a high sediment content, which generates the characteristic viscosity of these flows. Highly viscous, non-Newtonian, fluids can suspend large particles. In general, in such flows, elongate debris are oriented in the direction of the

flow (Lorenzini & Mazza, 2004). Debris flows are defined as flows containing more than 50% of coarse-grained debris, together with fine-grained particles. Mud flows typically contained finer-grained material (Lorenzini & Mazza, 2004; Varnes, 1978).

Sediment immaturity, i.e., greywackes and arenites, is a common features in orogenic settings, where detitritus from volcanic and plutonic basement feed the adjacent basins (Dickinson, 1970). Andesitic and granitic rocks are common material providers in back-arc sedimentary basins. Debris flows are not rare near orogenic belts, which generally constitute the main source for the clasts (Dickinson, 1970; Floyd et al., 1990; Webby, 1959). The variability in sediment grain size in adjacent rock layers may be explained by sporadic sedimentation that was only sporadic, probably reflecting seasonality, such as in debris flows (Fastovsky et al., 1995). The absence of palaeosol and root traces in the deposits suggest that sedimentation rates were too fast for the establishment of stable plant communities and pedogenesis. The palaeofloral reconstruction is in good agreement with these data, as pioneer plants dominate the assemblage.

Preservation of the soft tissues

Weathering seems to be a key element in the recent taphonomic history of the Kulinda deposits. Comparison of weathering indices for the two major bone beds shows that bb4 has experienced less weathering than bb3. This is consistent with their respective, bottom and top, location on the hillslope.

The taphonomic processes that allowed the preservation of dinosaur remains in the different levels of the volcaniclastic deposits are varied. The first difference consists in the presence or absence of soft tissues accompanying the bones in the bone beds. Soft tissues are abundant in bb4 (they are rarely observed in trench 3/3) but are not present in bb3. Secondly, the articulation of the bones and their connection with soft tissues is restricted to the bb4. The original organisation of the delicate integumentary structures is, in many cases, preserved in that bone bed. It means that the carcasses of the dead animals did not suffer from significant post-mortem transport, reworking and aerial exposure prior to their deposition (e.g., Behrensmeyer, 1975; Voorhies, 1969). It also suggests that scavengers and predators were absent from the area or had no time to feed on the remains prior to their burial (Behrensmeyer, 1975). In any case, the carcasses were deposited in a very calm environment with rapid sedimentation, quickly after the death of the animals. It was, obviously, not the case in the other bone beds. As for bb3, the paucity of articulated elements in trench 3/3 suggests that the *Kulindadromeus* carcasses were already dislocated before their subsequent reworking as a bone layer (Voorhies, 1969). However, the presence of plant remains, insects, and (although rare) delicate integumentary structures in trench 3/3 indicate that the elements were transported over shorter distances and were subsequently deposited in a calm environment. The presence of several discrete layers indicates recurrent, possibly seasonal, reworking episodes leading to the formation of these bone-bearing deposits. The mixture of bones of various shapes and sizes in the

same layers from trench 3 is not consistent with a fluvial sorting (Behrensmeyer, 1975). It rather indicates that bones were transported together to the depositional environment. The complete absence of soft tissues in bb3, as well as the sorting of the bones and the paucity of articulated elements, suggest that this bone bed consist of transported elements accumulated in a lag deposit. In any case, the scattered remains suggest that carcasses were already disarticulated and decayed prior to deposition, as stressed by Voorhies (1969).

In bone bed 4, bone remains are additionally coated by iron-oxides, whereas soft tissues contain carbon, sulfur, and show less iron-oxide precipitation. Here, we propose that iron-oxides (goethite) formed as a secondary mineralisation, resulting from the early oxidation of sulfate minerals such as primary pyrite. Pyrite is commonly involved in the early mineralation of soft tissues from decaying carcasses, induced by sulphate-reducing bacteria in anoxic environmental conditions (Berner, 1984; Allison, 1988; Taylor & Macquaker, 2000). Pyrite has been found in association with numerous well-preserved fossils (Allison & Briggs, 1991; Briggs et al., 1991; Leng & Yang, 2003; Wang et al., 2012; Farrell et al., 2013b; Gutiérrez-Marco et al., 2017; Schwimmer & Montante, 2007). Given the framboidal shape of the iron oxides observed within bones and soft tissues from bb4, they are considered as weathering products of early diagenetic pyrites. Pyrite preferentially formed on the dinosaur tissues (bones) where a reducing microenvironment promoted its precipitation. Soft tissues were therefore swiftly mineralised and protected from further degradation. The early replacement of the tissues' structure by diagenetic pyrite, probably promoted their exquisite preservation. Such preservation patterns implying pyrite and its subsequent oxidation have been observed elsewhere (Briggs et al., 1995; Zhu et al., 2005a; Schwimmer & Montante, 2007; Williams et al., 2008; Barling et al., 2015; Gutiérrez-Marco et al., 2017). We can also argue that iron sulphides have been oxidised due to meteoric fluids that have migrated within bb4 due to tectonic parameters. Fissures that dislocated bb4 may have drained these fluids, resulting in the oxidation of the pyrite accumulated in the structure of the dinosaur remains. Alternatively, the early replacement of original inorganic and organic materials from bones and soft tissues by minerals may have been triggered by hydrothermal fluid migrations, as hydrothermally related ores are known in the area and are related to the regional geodynamic context (e.g., Prokof ev et al., 2000b; Seltmann et al., 2010; Spiridonov et al., 2010). Nonetheless, further analyses need to be done to confirm whether that process is involved in the silicification of the deposits at Kulinda.

It is possible that bioapatite degradation was the result of its dissolution by acid fluids released during the oxidation of pyrite (e.g., Lowson, 1982; Nordstrom, 1982; Kraal et al., 2009). Epidermal structures, such as feathers, are much less influenced by oxidation and acid alteration due to their insoluble properties (e.g., Fraser et al., 1972; Goddart & Michaelis, 1934; McKittrick et al., 2012). The differential preservation of soft tissues and bones in an acidic environment is particularly well illustrated in Iron-Age peat bogs where bones of a man were completely lost but the

skin, hair, nails and clothing were still preserved (Glob, 1969). Here, the absence (or scarcity) of soft tissues accompanying remains in bb3/3 and bb3, and therefore the absence of iron sulphides, may explain the different types of preservation and mineralogy observed at Kulinda.

Sedimentary organic matter

Rock-Eval analyses show that sedimentary organic matter in Kulinda deposits is terrestrial (kerogen type III), therefore essentially derived from land plants. Low total organic carbon (TOC) values - less than 1 wt% - indicate that the rocks are poor in organic matter. Although bb4 contains abundant and exceptionally preserved soft tissues, the organic matter content in the embedded rock is the lowest from the sampled sediments. The TOC content is related to the organic content in the sediment, but not to that of the fossils. The two data should therefore be regarded separately. The low organic carbon content may be due to: a low degree of vegetation cover; high degradation rates of the organic material in the environment (Jennings et al., 2011); a high sedimentation rate; or possibly the combination of these phenomena. The rapid burial of the carcasses after their deposition may have stopped or lowered the decomposition processes. It is yet probable that the fossil soft tissues do not contain – or in very little quantities - organic matter anymore, and that they were predominantly epigenised (replaced by authigenic minerals) during diagenetic processes. Samples bb3 and T3/3-7 have close moderate TOC, HI and OI values, and present similar organic matter contents. These data probably reflect similar, oxygen-poor – dysoxic - depositional environments. In bb4, the extremely high OI values indicate severe oxidation of the organic matter in the sediment and are therefore consistent with a high degradation rate. This is also reflected by the low amount of A.O.M. present in the palynological sample. Pollen grains and phytoclasts are, by contrast, preferentially preserved. This is probably related to the relatively high resistance of these particles to degradation (Tegelaar et al., 1989). An intense oxidation of the bb4 is also in agreement with the mineralogical data showing the replacement of primary pyrites by iron oxides. Palynofacies assemblages bring additional information about the depositional environment of the fossiliferous layers. The distribution of palynomorphs in the sediments is partly related to processes that, similarly distribute sediment of diverse grain sizes in different depositional environments (Traverse, 1988b). The diversified assemblage both constituted of particles of low (amber and algae) and high buoyancy (spores, pollen grains, woody debris) from bb4 suggests a short transport and a deposition in a low-energy environment (Batten & Stead, 2005). The relatively poor palynological assemblage of bb3, constituted of granular A.O.M. and rare small phytoclasts, contrasts with that from bb4, likely indicating a different depositional environment. The low diversity, together with a high degree of sorting and a small size for the particles, rather indicates a higher-energy environment for the bb3 (Batten & Stead, 2005). These data are in good agreement with the petrographic and taphonomic observations, which, altogether, indicate very calm deposition conditions

for bb4, and more energetic – but still restricted - conditions implying the transport of disarticulated bones for bone layers in trenches 3/3 and 3.

Palaeo-environmental reconstruction

The spore-pollen assemblage from the lower part of the lithological section is diversified and indicates that the neighbouring areas were occupied by coniferous forests with an admixture of pteridosperms, podocarpaceans and ginkgoaleans. Ginkgoleans might also grow in wet areas as reported by Bugdaeva et al. (2006). Cheirolepidiacea (*Classopollis*), typical of hot and arid climates, are relatively scarce at Kulinda. Cyathaceae and Osmundaceae are more abundant and characterize humid and drained habitats. This palynological assemblage suggests a temperate and humid climate. The low diversity of palynological assemblages from the trench 3/3 apparently results from their poor preservation. The general composition of this assemblage shows an upward increase in bisaccate coniferous pollen and a decrease of spores and pollen produced by moisture loving plants (pteridosperms, cyatheaceous/dipteridaceous ferns, ginkgoaleans). This trend is possibly related to less wet conditions.

In general, floral oryctocoenoses from Kulinda have a similar taxonomic composition throughout the section. The diversity of plant taxa at the Kulinda suggests that plants were transported from different habitats prior to their deposition. Hence, they are derived from different plant communities that preclude accurate floristic reconstructions. Algal threads indicate humid, possibly aquatic, environments. Wet habitats and floodplains can be reconstructed based on the presence of abundant thalli of liverworts (*Hepaticites arcuatus*) and mosses (*Muscites samchakianus*) in floral assemblages. It is the specific feature of floral oryctocoenoses of the Kulinda locality, which has not been observed elsewhere in the Jurassic of Transbaikalia. Wet environments were also favourable for horsetails (*Equisetites* sp., *Equisetites* cf. *undense*), which are the common water-related plants preferring the areas located nearby water sources. Abundant leafs of leptostrabaleans (*Czekanowskia*) confirm the occurrence of wet and possibly waterlogged environments. Krassilov (1972) suggested that plant communities dominated by leptostrabaleans grew in the river floodplains and marshlands near lakes, or occupied lake beaches. Coniferous plants were apparently confined to the uplands and slopes.

The botanical composition of megafloral assemblages, which reflect the local vegetation, and palynological assemblages, which also reflects the surrounding vegetation, is generally considerably different. Spores and pollen are easily carried to the place of deposition by wind and water flows. Only small fragments of waterside plants are present in Kulinda deposits, and large remains of terrestrial plants from inner land areas are lacking.

6. Conclusions: proposed scenario for the formation of the Kulinda bone beds

The lithological sections observed at Kulinda represent a succession of immature volcaniclastic deposits, including greywackes, arenites and breccia, together with mudstones. These deposits depict debris and mud flows in intermountain basins. The volcaniclastics derived from nearby acidic igneous sources that were weathered, eroded, and transported to the deposition locality at the occasion of seasonal rain falls or other climatic/natural events. Several monospecific bone beds of the basal neornithischian dinosaur *Kulindadromeus zabaikalicus* are intercalated within these deposits.

During the Middle Jurassic, the south-eastern Transbaikal region was characterised by intense magmatic and volcanic activities related to the closure of the Mongol-Okhotsk Ocean. *Kulindadromeus zabaikalicus* lived in an environment consisting of intermountain basins with steep slopes, on which grew upland forests mainly composed of conifers, pteridosperms, and ginkgoales. In the basins, the floodplains developed a pioneer vegetation, including mosses, liverworts and horsetails. The absence of palaeosol and root traces in the deposits and the over-representation of pioneering plants in the macrofloral assemblage suggest a sedimentation rate too fast for the establishment of stable plant communities. This harsh and unstable environment may also explains the low diversity of the vertebrate fauna at Kulinda.

The bone beds record two main taphonomic histories. First, in trench 4, the complete carcasses of dead (or even possibly living) juvenile individuals were recovered by mud flows, transporting fragments of the eroded acidic igneous rocks. The carcasses, rich in organic matter originating from the bones and soft tissues, were swiftly replicated by authigenic pyrite, enhancing their preservation potential. The presence of bone moulds in association with well-preserved soft-tissues in that bone bed probably relates the recent oxidation of the layer by meteoric fluids, which resulted in the pseudomorphisation of pyrite by iron oxides and the subsequent release of acid fluids. The latter are responsible for the dissolution of most of bones but have not similarly impacted the soft tissues, which are, in certain conditions, much more resistant to acids than phosphates.

The bone beds from the trenches 3/3 and 3 are characterised by a different mode of preservation: it is likely that the already completely disarticulated carcasses of *Kulindadromeus* were transported and scattered in mud flows. The bones (and scarce soft tissues) were then completely remineralised into alumina-silicates during the diagenesis, leading to the complete loss of their original features. There are at least seven bone bed episodes in trench 3/3, showing that the mud flow episodes occurred frequently and regularly.

Section III

Besides the taphonomy of soft tissues that bring valuable data about the biology of extinct organisms, the study of bone beds – even those with no preserved soft tissues – gives additional, complementary, data about the composition of ancient communities, such as how the organisms died, the degree of transport of the dead carcasses, the way carcasses or disarticulated bones were buried in the sediment, the diagenetic processes, etc. Inter- and intraspecific behavioral aspects may also be considered when examining bone assemblages (e.g., predation, sexual dimorphism, adaption to a specific living environment).

In this section, the taphonomy of three distinct bone beds from a single Late Cretaceous locality (Velaux-La Bastide Neuve, south-eastern France) is reviewed in detail. The paper examines the bone remains buried in riverine – channel, levee, and floodplain – deposits. The reconstruction of the palaeo-environment constitutes another important aspect of the work.

Chapter 7

This chapter is based on: Cincotta et al., 2015, *published in PLoS ONE*

Integrated palaeoenvironmental reconstruction and taphonomy of a unique Upper Cretaceous vertebrate-bearing locality (Velaux, Southeastern France)

Abstract

The Velaux-La Bastide Neuve fossil-bearing site (Bouches-du-Rhône, France) has yielded a diverse vertebrate assemblage dominated by dinosaurs, including the titanosaur *Atsinganosaurus velauciensis*. We here provide a complete inventory of vertebrate fossils collected during two large-scale field campaigns. Numerous crocodilian teeth occur together with complete skulls. Pterosaur, hybodont shark and fish elements are also represented but uncommon. Magnetostratigraphic analyses associated with biostratigraphic data from dinosaur eggshell and charophytes suggest a Late Campanian age for the locality. Lithologic and taphonomic studies, associated with microfacies and palynofacies analyses, indicate a fluvial setting of moderate energy with broad floodplain. Palynomorphs are quite rare; only three taxa of pollen occur: a bisaccate taxon, a second form probably belonging to the Normapolles complex, and another tricolporate taxon. Despite the good state of preservation, these taxa are generally difficult to identify, since they are scarce and have a very minute size. Most of the vertebrate remains are well preserved and suggest transport of the carcasses over short distances prior to their accumulation in channel and overbank facies, together with reworked Aptian grains of glauconite, followed by a rapid burial. The bones accumulated in three thin layers that differ by their depositional modes and their taphonomic histories. Numerous calcareous and iron oxides-rich palaeosols developed on the floodplain, suggesting an alternating dry and humid climate in the region during the Late Campanian.

1. Introduction

Late Cretaceous continental deposits are widely exposed in southern France and have yielded numerous and diverse vertebrate remains (Allain & Suberbiola, 2003) especially in the Aix-en-Provence Basin (e.g., Tabuce et al., 2013; Valentin et al., 2012; Vila et al., 2012). However, few studies of both sedimentology (including lithofacies, microfacies, and palynofacies) and vertebrate taphonomy have been conducted at these localities (e.g., Thouand, 2004). The Velaux-La Bastide Neuve site (Fig. 7.1) was discovered in 1992 by one of us (X.V.) and hundreds of vertebrate remains have been collected during an initial survey (2002) and two large scale field campaigns (2009 and 2012). The vertebrate assemblage represents a highly diverse fauna including chelonian, crocodilian, dinosaur and pterosaurs. Among the dinosaurs, a new titanosaur genus, *Atsinganosaurus velauciensis*, was described based on partially articulated skeletons (Garcia et al., 2010). The present paper aims to describe the sedimentological and taphonomic context of the Velaux locality and to reconstruct its palaeoenvironment, using lithofacies, microfacies, palynofacies associated with taphonomy and fossil descriptions, and also provide a complete inventory of the vertebrate taxa found in this area.

2. Geological setting and stratigraphy

The Velaux-La Bastide Neuve fossil-bearing site is located in the western part of the Aix-en-Provence Basin (Bouches-du-Rhône department, southeastern France), an east-west oriented syncline of about 400 km^2 (Westphal & Durand, 1989). The basin fill is composed of fluvio-lacustrine deposits dating from Santonian to Lutetian age (Cojan et al., 2003) that were deposited following an episode of epeirogeny at the end of the Santonian (Plaziat, 1981). The age of the site is based on continental biostratigraphic data such as charophytes and dinosaur eggshell. The continental layers exposed in Velaux-La Bastide Neuve site were previously attributed to the "Begudian" local stage (Fig.7.1), correlated to the Late Campanian (Garcia & Vianey-Liaud, 2001). Two charophyte biozones have been recognised at Velaux-La Bastide

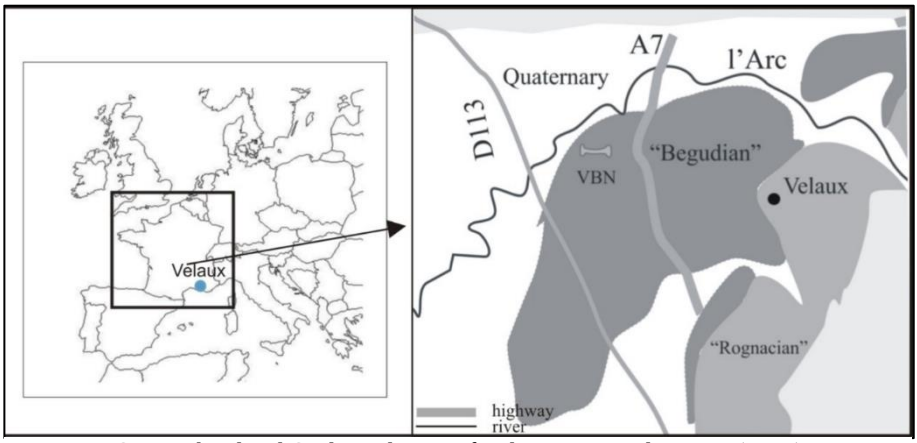

Figure 7.1. Geographical and Geological maps of Velaux-La Bastide Neuve (VBN) area. VBN is located in southeastern France, between Marseille and Aix-en-Provence. Our fossil-bearing locality is indicated by the bone, between two major roads (D113 and A7). The site belongs to the "Begudian" local stage.

Neuve. The *Peckichara pectinate* biozone is correlated to the middle-early Late Campanian, and the *Peckichara cancellata* biozone to the Late Campanian (Thouand, 2004). In addition, dinosaur eggshell from this locality belong to the *Megaloolithus aureliensis* biozone, correlated to the Late Campanian (Garcia & Vianey-Liaud, 2001).

3. Material and methods

During the two field campaigns a surface of 375 m^2 to a depth of 1.2 m was excavated, which resulted in 100 m^3 of overburden and matrix. During the first campaign (2009), several small areas separated from the main fossil-bearing layer were worked. In 2012, two large sections were excavated to complete the previous sampling. A total of 308 fossil specimens were inventoried during the two field campaigns - they are housed at the Moulin seigneurial Museum and at the Henri-Ricard Archaeological repository, both located in Velaux. Rock samples for sedimentological analyses were collected from each layer of the sedimentological section (Fig.7.2).

Sampling for several types of analysis was performed at the same time; 18 samples were collected for magnetostratigraphic analyses. Forty one samples were used to study the lithofacies; among these, eight were used for palynological processing, and thirteen were used to prepare thin sections for microfacies analysis. Palynological samples were prepared using standard methods (Schnyder et al., 2009). Two samples (VBN-18 and VBN-20A) collected from sandy horizons were used for isotopic dating using standard K-Ar methods (Gradstein et al., 2012).

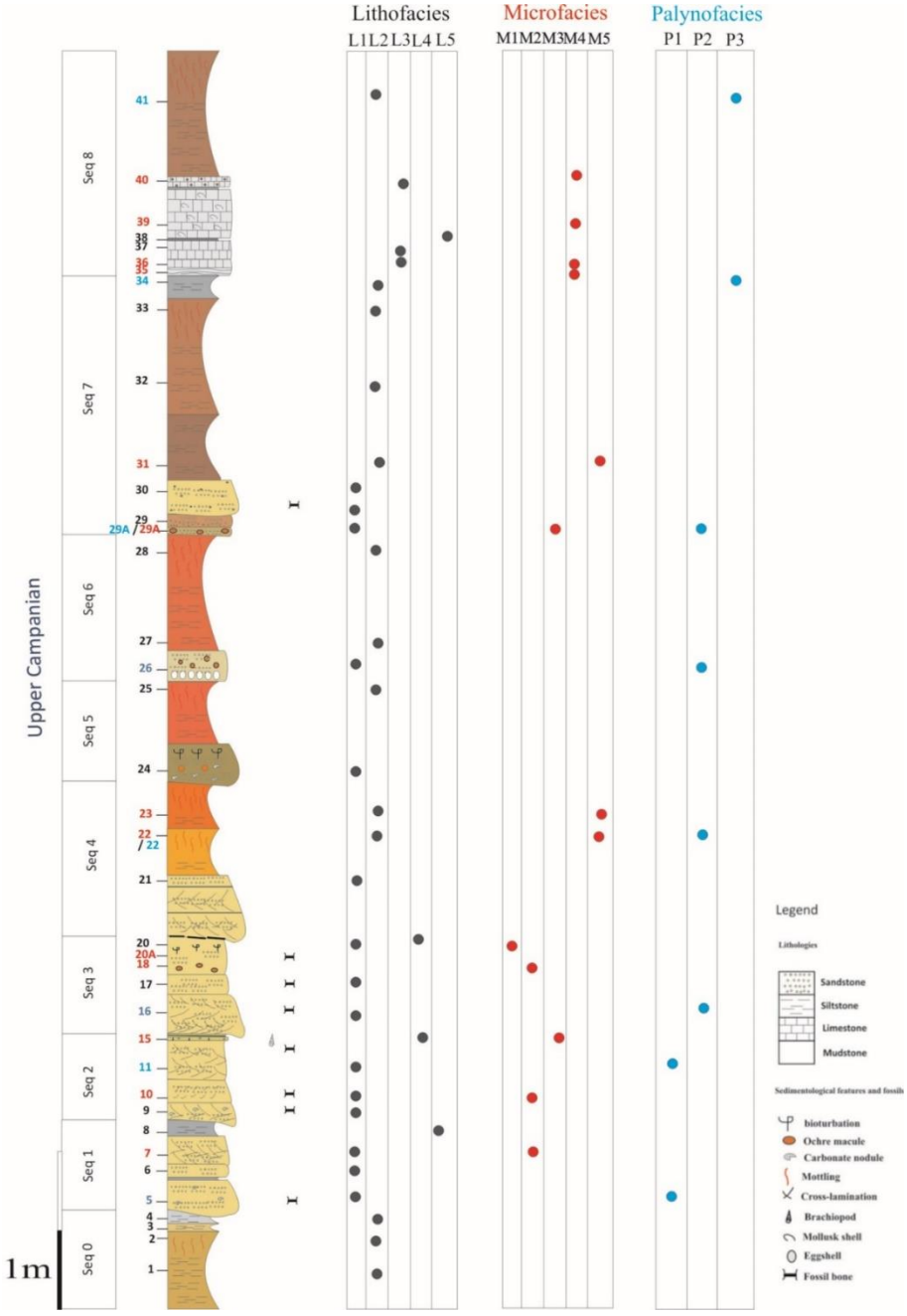

Figure 7.2. Sedimentological succession of Velaux-La Bastide Neuve locality. Three vertebrate-bearing layers are present: in the sequences 1, 2 and 3. Numbers on the left side correspond to samplings; blue numbers are palynofacies samples; red numbers are microfacies samples and black ones are lithofacies samples. The three tables on the right discriminate the different facies for these samples. Location of magnetostratigraphic samples are indicated by arrows, and the letters MA.

3.1. Magnetostratigraphy

Oriented block samples were collected from 27 stratigraphic levels in the 16.3 m thick section. The palaeomagnetic analyses were carried out at the Laboratory of the iPHEP (University of Poitiers). The intensity and direction of remanent magnetisation were measured with a JR6 spinner magnetometer using four position standard specimen holders.

3.2. Taphonomy

The position of each bone collected during the 2009 and 2012 field seasons was mapped (see Fig.7.3). Data were also collected as to the nature, dimensions and orientations in the case of elongate bones. The fossil-bearing area covers a surface of about 140 m^2.

Features of the bones (weathering stage, fractures) were studied in laboratory (University of Poitiers and IRSNB), in order to document the taphonomy of the locality. Stereonet free program was used for drawing bidirectional rose diagrams and the nonparametric Rayleigh's test was performed for testing uniformity of the data.

4. Results

4.1. Magnetostratigraphy

Only one paleomagnetic component could be recognised in the studied samples (Fig.7.4a, b). The greater part of remanent magnetisation was removed at 60 mT, which may indicate that magnetite is the main carrier. The average directions were determined after tilt correction (Fig.7.4c): the mean direction of the characteristic

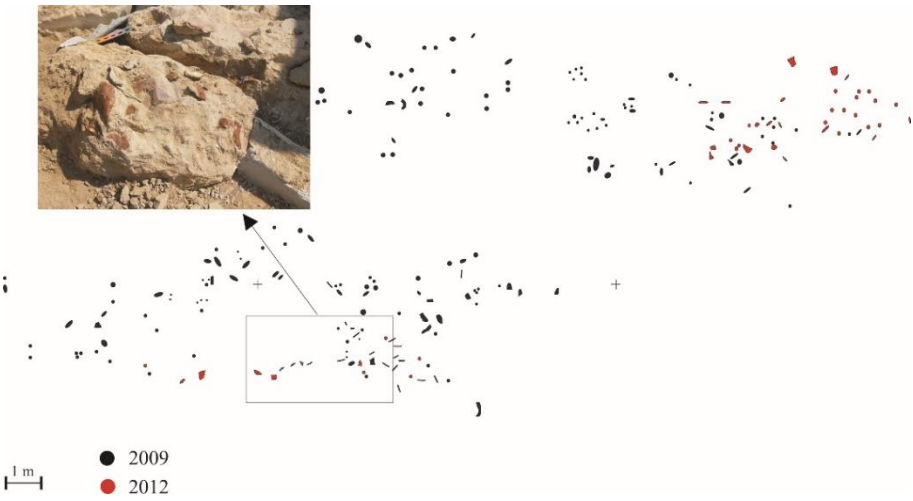

Figure 7.3. Map of the fossil-bearing site at Velaux-La Bastide Neuve. Two zones were explored, during the two field campaigns (2009 and 2012) on a total surface of about 140 m^2. The three taphonomic modes (TM) are represented by three colors—TM1 in green, TM2 in black, and TM3 in red—, which represent the three successive deposits.

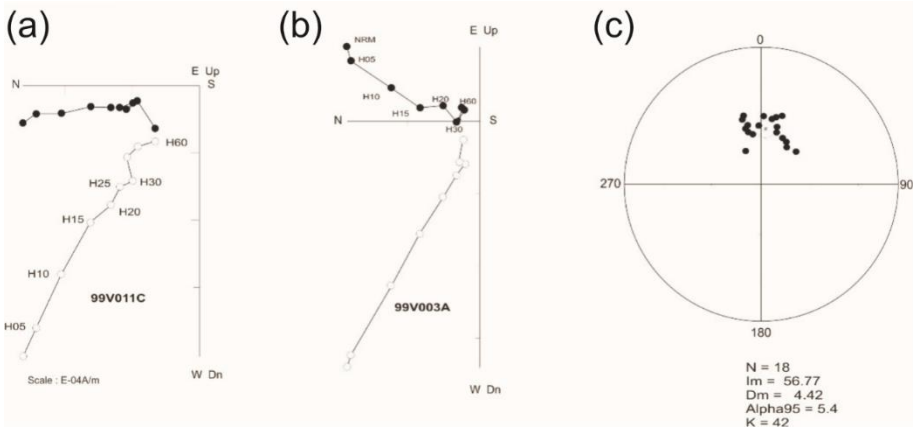

Figure 7.4. Zijderveld diagrams. (a) and (b) representative Zijderveld diagrams of the samples (c) equal-area stereographic projection of characteristic direction.

components is (I = 56.7, D = 4.42, a = 5.4, kappa = 42; n = 18). The mean direction is different from the present day magnetic field at the sampling site suggesting a primary remanence of magnetisation. The rocks exhibit a single normal polarity. According to the biochronological data, the correlation with the Geomagnetic Polarity Time Scale (GPTS) could be done with the normal chron of the chron C32 (C32n.1n, C32n.2n or C32r.1n). Accordingly, an age of between 70.9 and 73.3 Ma, or an adjusted age of between 71.6 and 74.0 Ma (Gradstein et al., 2012), can be assigned to the Velaux-La Bastide Neuve section.

4.2. Section, sequences, and facies

The studied section has a thickness of 16.3 m from the basal level located below the lowermost bone-bed to the top of the upper limestone bed. The section can be divided into nine depositional sequences (Fig.7.2).

The lower contact of each sequence is erosional and each sequence fines upward. Four sequences are characterised by the same facies succession: sandstones at the base followed by calcareous siltstones. Only the uppermost sequence contains limestones, indicating a different sub-environment. Oxidised glauconite grains were found in sandstones from sequence 3 (samples VBN-18 and VBN-20A) and were dated using K-Ar analysis. Results provide ages of 122.2 ± 3.2 Ma and 123.6 ± 3.4 Ma (Table 7.1), corresponding to the early Aptian stage (Gradstein et al., 2012; Steiger & Jäger, 1977).

Table 7.1. Radiometric results on glauconite grains belonging to two sandstone samples.

Sample	K (%)	^{40}Ar rad (nl/g)	^{40}Ar air (%)	Age (Ma)
VBN-18	1.68	8.073	37.5	122.2 ±3.2
VBN-20A	1.69	8.265	48.3	123.6 ±3.4

The entire succession comprises five dominant lithofacies: sandstones (Fig.7.5a, b), siltstones (Fig.7.5c, d), limestones (Fig.7.5e, f), mudstones (Fig.7.5f) and lignite layers. The sedimentological section is dominated by variegated siltstones (52% of the section thickness) and sandstones (34%; Fig.7.2). There are five microfacies: bioclastic micro-conglomerate (Fig 7.6a), bioclastic sandstone (Fig.7.6b), bioclastic siltstone (Fig.7.6c, d), micritic wackestone (Fig.7.6e) and azoic oxidized siltstone (Fig.7.6f). Palynological analysis allow discrimination of three palynofacies: a high diversity palynofacies (Fig.7.7a, b), a charcoal-rich palynofacies (Fig.7.7c, d) and a phytoclast-rich palynofacies (Fig.7.7e, f). Lithofacies are associated with microfacies and palynofacies to specify the nature of sub-environments. Nonetheless, some of the same microfacies and palynofacies are associated with different, but related, sub-environments:

- **Facies 1**. Facies 1 predominantly corresponds to sandstone deposits that in all cases overlie an erosional base (Fig.7.5a). The facies is composed of yellow to grey sandstones and displays various grain sizes, from conglomeratic to coarse-grained sandstones. Bed thickness varies from 5 cm to 80 cm. Sandstones exhibit small-scale planar cross-stratification and horizontal lamination. At the base of sequence 7 (Fig.7.2), a thin clast-supported intraformational conglomerate is present. Sandstones are in some cases interstratified with thin layers of lignite. Sandstone abundance decreases from the base of the section to the top. Thin black lignite laminae are interstratified within sandy beds, especially at the top of sequences 2 and 3 (Fig.7.2). Fossil trunk wood traces are also found in these layers. Facies 1 comprises two distinct microfacies.

The first one is the coarsest, represented by a micro-conglomerate composed of subangular to subrounded quartz and feldspar grains. It contains micritic grains as algal balls, glaebules, peloids, calcareous intraclasts (Fig.7.6a), fragments of mollusc shells (Fig.7.6b), “algae” and foraminifera. The second microfacies is a bioclastic sandstone that contains the same skeletal elements but is matrix-supported. The palynological assemblage comprises abundant phytoclasts (rounded charcoal grains and various lignitic debris), bisaccate pollen grains, fungal spores (Fig.7.7a) and fungal hyphae (Fig.7.8a).

- **Facies 2**. The deposits of facies 2 are characterised by medium to coarse-grained sandstones (Fig.7.5b). The sandstones are in some cases variegated, contain mollusc shells, calcareous nodules and, locally, orange mud clasts. Sediments are mixed with reworked debris, including marine invertebrate fossils (foraminifera and "red algae"). Feldspar grains, foraminifera, Microcodium (calcite prisms induced by biogenic processes (Kabanov et al., 2008; Murru et al., 2003), freshwater fossils as Characeae gyrogonites, algal balls, mud coated grains and stromatolites are also present in these deposits. Skeletal grains are in some cases highly micritised and not easily identifiable (Fig.7.6c). The palynofacies contains the same palynomorphs as facies 1; including phytoclasts, abundant charcoal and bisaccate pollen grains (Fig.7.8b), fungal hyphae and fungal spores.
- **Facies 3**. The third facies consists of variegated and fine-grained siltstones. The siltstones are bioclastic and contain mollusc shells, foraminifera, Microcodium, algal balls, mud-coated grains and stromatolites (Fig.7.6d). Skeletal grains are highly micritised. The palynological material constitutes mostly phytoclasts, mainly with charcoal and lignitic debris (Fig.7.7e); but fungal hyphae are also present. Pollen grains (Fig.7.7f) are rare. Charcoal grains are less abundant than in the facies 1. Tracheid fragments are bigger and better preserved than charcoal.
- **Facies 4**. Sediments of facies 4 are variegated, but mostly reddish and fine-grained siltstones. No sedimentary structures are present in these siltstones, but pedogenic features, such as carbonate nodules are well developed. Skeletal elements are also lacking (Fig.7.6f). There are only rare reworked glauconite grains, and mineral grains are coated by iron oxides. The corresponding palynofacies contains nearly the same organic particles as facies 1 and 2, although fungal hyphae (Fig.7.7c) are absent. Charcoal grains are very abundant and lignitic debris is less common although less degraded than in facies 3. A few bisaccate (Fig.7.8b), tricolporate (Fig.7.8c) and monosulcate (Fig.7.8e) pollen grains, and also some Normapolles (Fig.7.8d) occur.
- **Facies 5**. The fifth facies is only present in sequence 8 (Fig.7.2) and consists of resistant limestone beds interstratified with thin greyish mudstones. The limestones reach 1.2 m in thickness, and include very fine-grained beds containing mollusc shells and ostracod valves. Undulatory laminae are present at the base of the lowermost bed (Fig.7.5f). Upper beds are massive without any sedimentary structure. Very few mudstone layers occur in this facies; where present, they are horizontally laminated. Limestones are overlain by reddish siltstones presenting colour mottling.

The microfacies is a fine micritic limestone, containing abundant Microcodium (Fig.7.6e) but also charophyte gyrogonites and some ostracods. Microcodium are in some cases wrapped in thin mud layers. No detrital grains are present in this facies, but only a fine micritic mud with a wackestone texture including Microcodium features and shells dispersed in a micritic matrix.

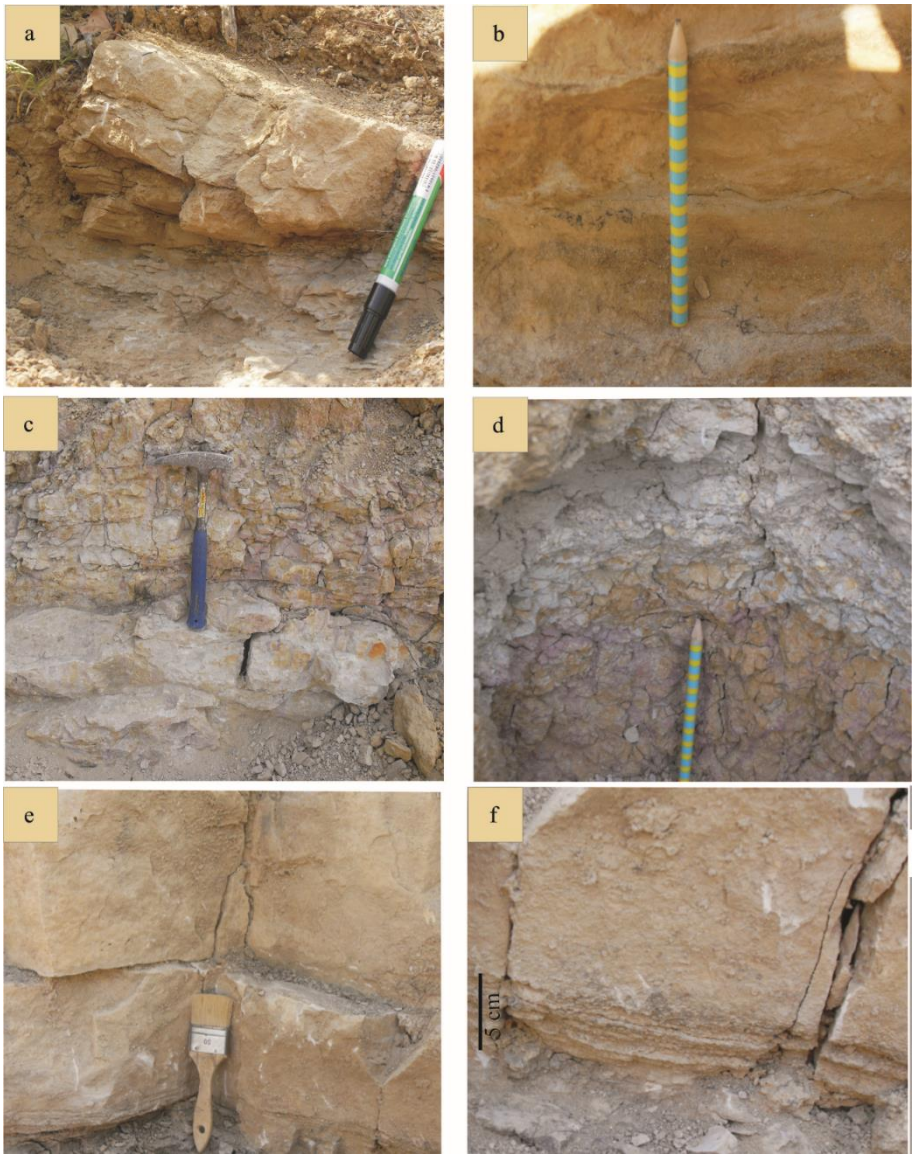

Figure 7.5. Lithofacies. (a) small-scale cross-laminated sandstones (seq. 1), (b) beige fine-grained sandstones showing no sedimentary features (seq. 3), (c) variegated siltstones overlying grey sandstones (seq. 6), (d) blue-grey siltstones overlaying variegated siltstones (seq. 7), (e) both first beds from the massive limestone of the sequence 8, and (f) thin muddy layers below the lower limestone bed, and the undulated limestone layer at the base of the lower bed (seq. 8).

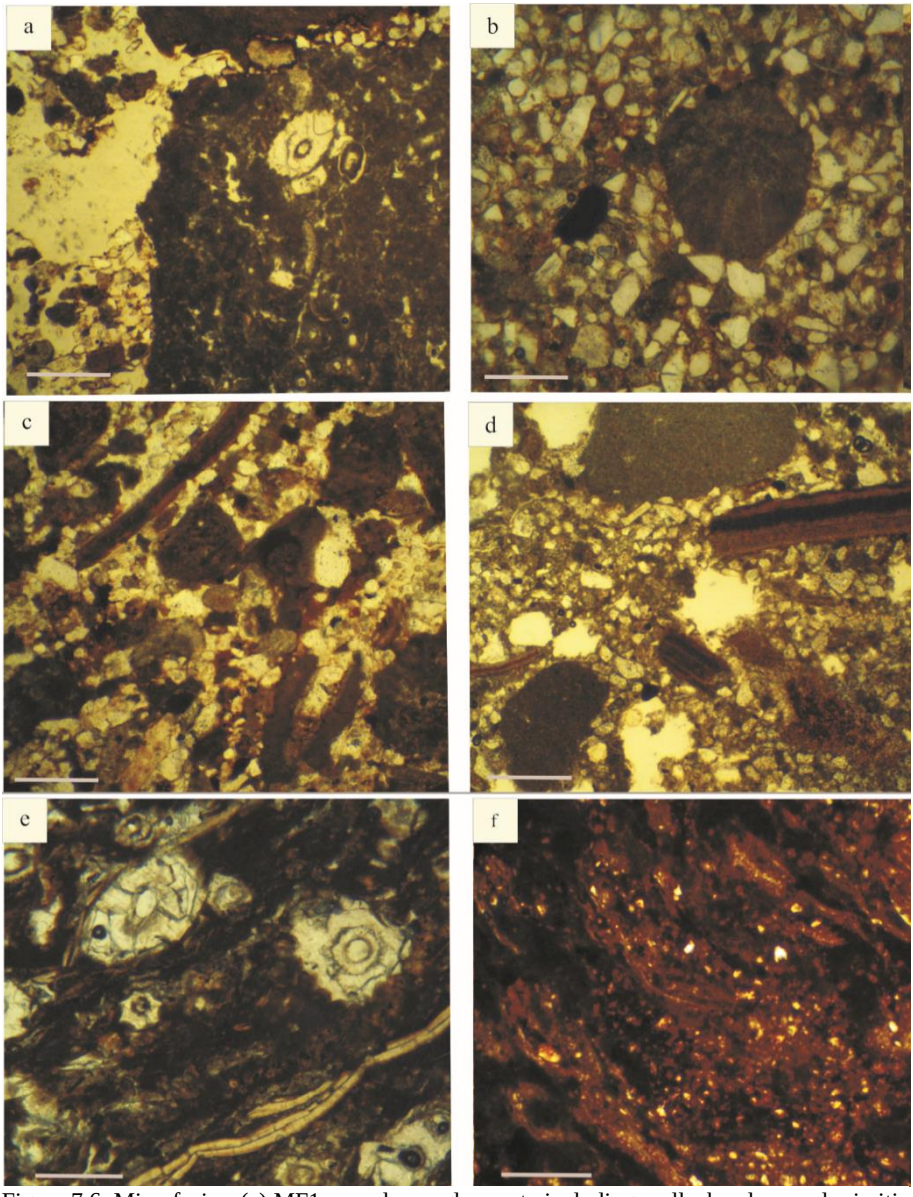

Figure 7.6. Microfacies. (a) MF1—sandy conglomerate including mollusk valves and micritic grains, (b) MF1—carbonated intraclast including Microcodium, (c) MF2—fine-grained sandstone with algal ball and mollusc shells, (d) MF3—coarse-grained siltstone including micritic grains and mollusc shells, (e) MF4—micritic limestone including Microcodium and shells (f) MF5—fine-grained siltstone coated with iron oxides. Scale bars = 500 μm.

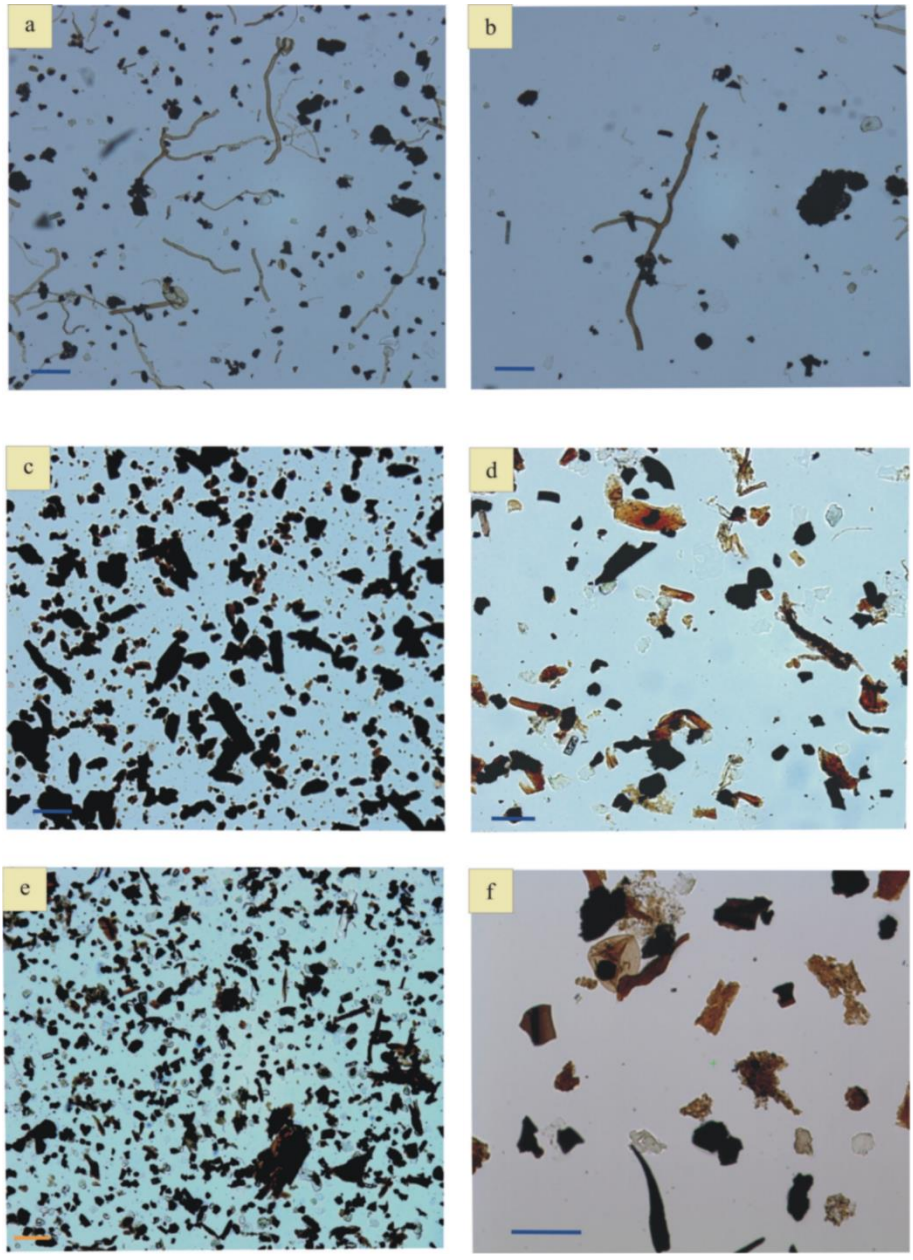

Figure 7.7. Palynofacies preparations from the Velaux-La Bastide Neuve sedimentological succession. (a) PF1—high diversity section with lignitic debris, charcoal and abundant fungal hyphae (scale bar = 100 µm), (b) PF1—fungal hyphae showing septae, lignitic debris, charcoal and amorphous organic matter (scale bar = 50 µm), (c) PF2—numerous rectangular and rounded charcoal grains, and lignitic debris (scale bar = 50 µm), (d) PF2—A.O.M., charcoal and pollen grain (scale bar = 50 µm), (e) PF3—charcoal and tracheid fragments, and (f) PF3—fungal spore, diverse plant debris (e.g. tracheid fragments), charcoal and A.O.M. (scale bar = 50 µm).

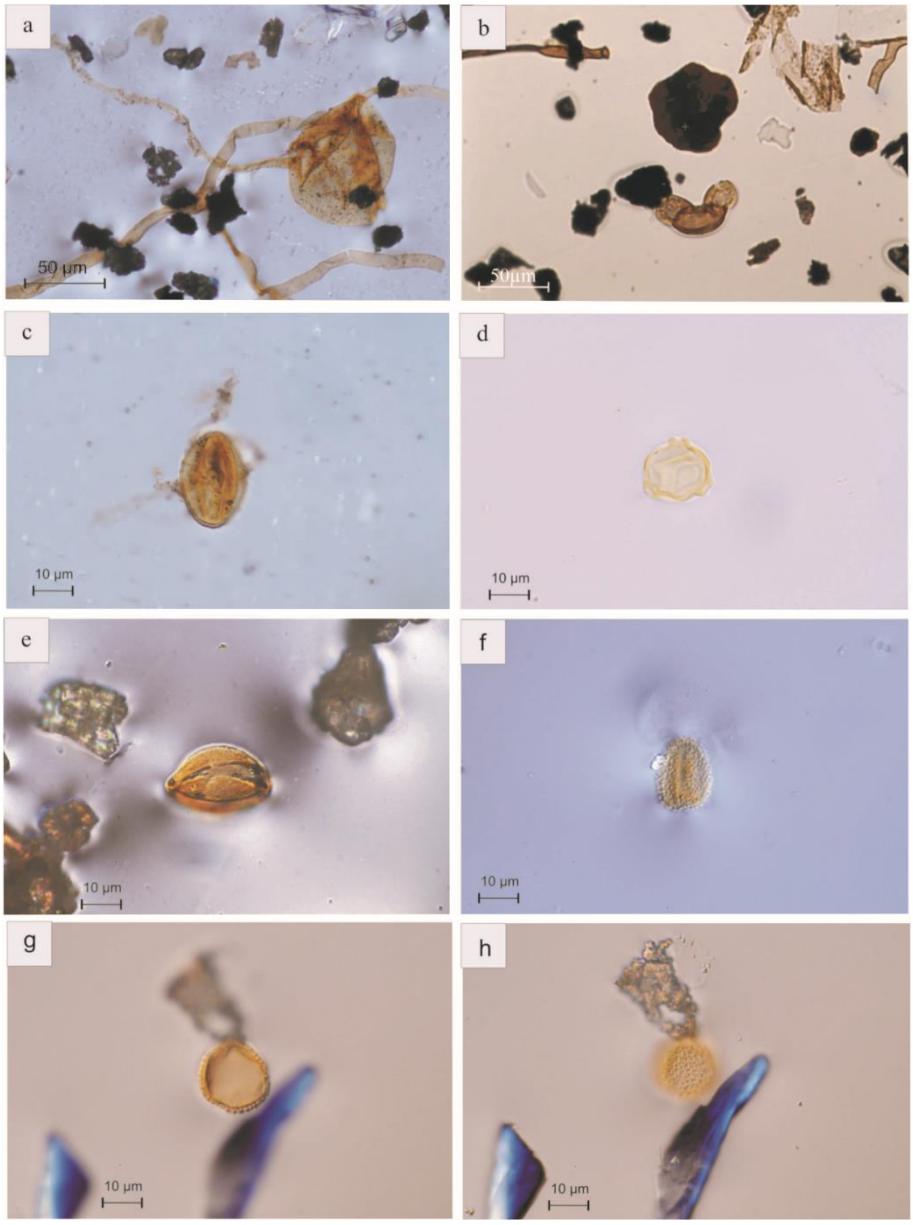

Figure 7.8. Fungal hyphae, spores and palynomorphs. (a) fungal spore with thin wall and folds and connected to an hypha (Paleomycites?) (12-VBN-05; sequence 1), (b) bisaccate pollen grain among coalified plant debris and hyphae (arrow) (12-VBN-05; sequence 1), (c) prolate tricolporate pollen grain in meridian view, (d) pollen grain probably belonging to the Normapolles complex (polar view), (e) monoaperturate pollen grain, probably monosulcate pollen grain, (f) semitectate, reticulate, probably monosulcate pollen grain, and (g) and (h) monosulcate pollen grain; same taxon in median (g) and high (h) focus.

4.3. Taphonomy

Taxonomic and skeletal composition. Three hundred and eight vertebrate fossils - including bones, plates, osteoderms, and teeth - belonging to several taxa were inventoried at Velaux during the two field-campaigns. Dinosaur remains dominate the vertebrate fossils (Fig.7.9—top), representing over 38% of the total assemblage collected during the 2009 and 2012 campaigns. Crocodilian elements are particularly abundant (16%), and mainly represented by shed teeth (Fig.7.9—bottom right). Numerous crocodilian (non-shed) teeth occur together with incomplete juvenile skulls and one complete adult skull (MMS/VBN-12-10A). Chelonian carapace and plastron parts are abundant (64 specimens collected so far), representing 22% of the assemblage. Pterosaur, hybodont shark and fish elements are also represented in the assemblage although they are rather rare (17, 10 and 4 elements, respectively). Among the identifiable dinosaur remains, ornithopod (39%) elements are the most abundant. Various ankylosaur (24.5%) elements were found including osteoderms, long bones and one scapula. Titanosaur elements (22.4%) comprise vertebrae and long bones. Theropods (14%) are mainly known from isolated teeth, with few long bones and vertebrae. Small fossils are numerous, dominated by teeth and chelonian shell parts. Fragile bones such as ribs, chevrons or cranial elements are under-represented (Fig.7.9—bottom left).

Accumulation modes

The vertebrate fossils of the Velaux-La Bastide Neuve site occur in three thin layers with different accumulation modes reflecting different depositional histories. Investigations were concentrated on the three vertebrate-bearing layers (Fig.7.3), located in the lower part of the sedimentological section in sequences 1, 2 and 3

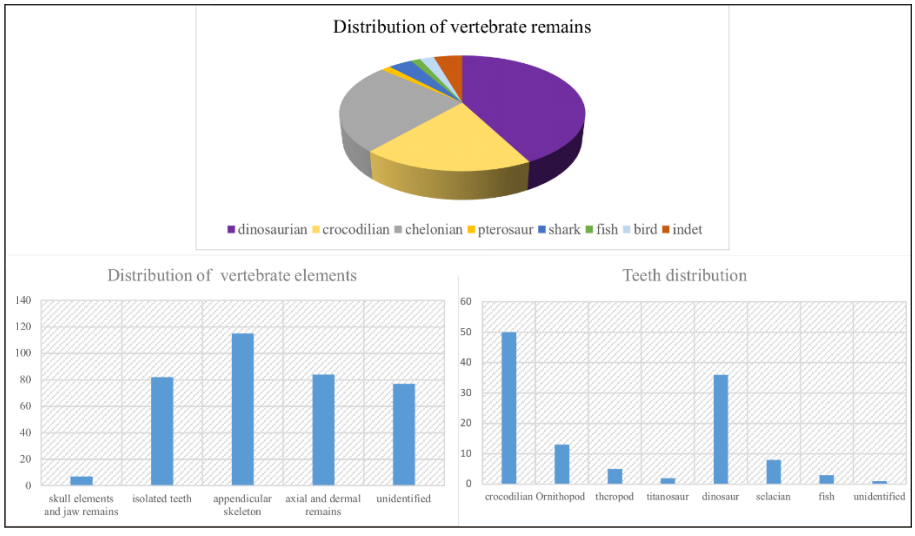

Figure 7.9. Vertebrate remains distribution and bone nature. Dinosaurs and chelonians dominate the fossil assemblage. Elements as teeth or plates are particularly abundant. Data were taken during two field campaigns, in 2009 and 2012.

(Fig.7.2). Bones are particularly abundant in the second fossiliferous layer, which consists of fine to coarse-grained sandstone. Isolated and disarticulated elements belonging to a single taxon were found in variegated coarse-grained siltstones from sequence 1, and were interpreted as an overbank facies. Two long (>2m) fragile but very well preserved parallel bones were found in 2009 in these variegated siltstones, in association with skin impressions. These elements can be identified as sauropod cervical ribs (Koen Stein, pers. comm.). The lowermost fossiliferous layer cannot be regarded as a bone bed, in the current state of excavation, as all the elements possibly belong to a single individual (Behrensmeyer, 2007).

The second fossiliferous layer is represented by a multitaxic accumulation of elements included in coarse-grained conglomeratic sandstones from sequence 2. The following elements are represented in this multitaxic bone bed; ornithopod bones and teeth, bones and teeth from the titanosaur *Atsinganosaurus velauciensis* (Garcia et al., 2010), theropod teeth, crocodilian teeth, isolated bones, skulls (Fig.7.10a) and one osteoderm, chelonians carapace and plastron elements and long bones belonging to two different taxa - *Solemys* (Fig.7.10b) and *Polysternon* -, hybodont shark teeth, fish teeth and pterosaur bones. Most of bones are disarticulated, except partially articulated titanosaur skeletons (Garcia et al., 2010). Elements, presenting various sizes and shapes, are mixed together and are often entangled in the sandy matrix. Long bones in this layer tend to be aligned along a NW-SE axis (Fig.7.11). Predation marks are extremely rare, they are even absent on titanosaur bones, although crocodilian shed teeth are rather abundant. A single deep tooth mark is present near the ocular fenestrae of a complete adult crocodilian skull discovered in 2012 in this bone bed (Fig.7.10a). Trample marks have not been identified in this material; these are characterised by shallow, sub-parallel scratch striae on the bone surfaces (Blasco et al., 2008; Fiorillo, 1991a).

A third taphonomic mode consists of disarticulated bones (Fig.7.10d, e), plates, and abundant teeth found in sequence 3. The bones are more dispersed than in the other modes and belong to several taxa. Ankylosaur long bones and osteoderms are only present in this silty sandstone layer. Theropod teeth, ornithopod teeth, crocodilian osteoderms and teeth, and chelonian plates belonging to both *Solemys* and *Polysternon* (Fig.7.10c) occur. Neither predation marks nor tramples marks are present. The chelonian remains are very well preserved and usually less degraded than dinosaur bones. Long bones (mostly belonging to the ankylosaur) are mostly oriented NE-SW but other elements present orientations that are quite varied (Fig.7.11).

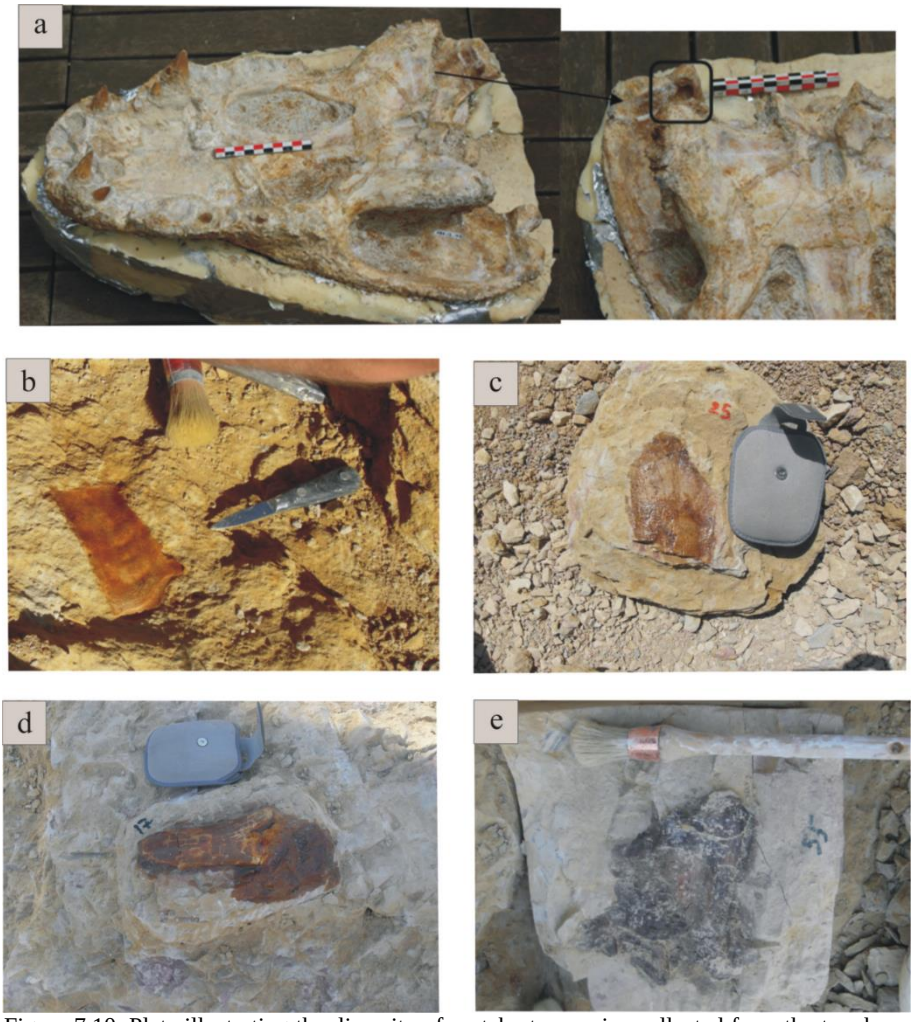

Figure 7.10. Plate illustrating the diversity of vertebrate remains collected from the two bone beds of Velaux-La Bastide Neuve. (a) complete crocodilian skull (MMS/VBN-12-10A) from an adult specimen that shows a deep tooth pit near the ocular fenestra (square) (b) ornamented chelonian plate attributed to the genus Solemys (c) non-ornamented chelonian plate attributed to the genus Polysternon (d) indetermined dinosaur phalanx (e) dinosaur vertebra.

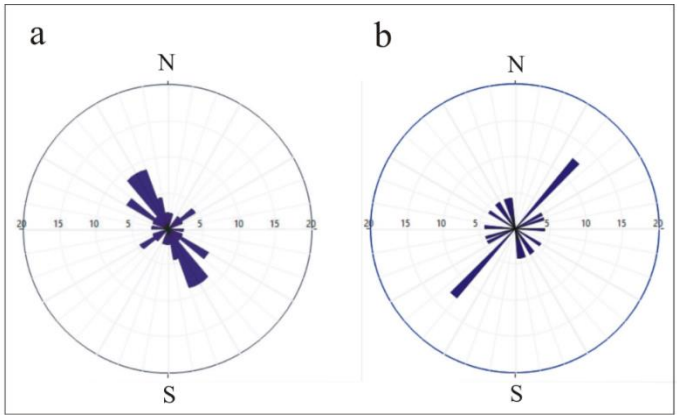

Figure 7.11. Rose diagrams showing the long-axis orientation for bones collected at Velaux-La Bastide Neuve. (a) represents the south-east/north-west trend for long bones from the second taphonomic layer (BB1; n = 23); and (b) shows the orientation pattern for long bones of the third taphonomic layer (BB2; n = 12). Statistical analyses show that the null hypothesis of uniformly distributed data can be rejected for (a) but cannot be rejected for (b); Rayleigh's test, (a) $z = 2.969$, $p < 0.05$; (b) $z = 0.661$, $p > 0.05$.

5. Discussion

5.1. Paleoenvironment: integrated litho-, micro-, and palynofacies

The observed lithologies, microfacies and palynomorphs documented in the nine depositional sequences exposed at Velaux-La Bastide Neuve indicate several alluvial sub-environments, ranging from channel lag to floodplain.

- **Facies 1**. Conglomeratic beds (e.g. sequence 2) correspond to the basal deposits in a stream channel, whereas all finer sandstones are interpreted as channel levee deposits or crevasse splay deposits. The presence of small-scale planar cross-stratification indicates low-energy sedimentation (Smoot, 1991; Stewart, 1981), whereas horizontal bedding corresponds to upper flow regime conditions (Stewart, 1981; Viseras et al., 2006). Mud clasts could indicate reworking of channel banks within the river (Fiorillo, 1991b) or basal scour during channel incision. Lignite layers are interpreted as organic matter accumulations introduced by bank erosion into the river channel, collected by the river stream and then deposited along with bedload sand during lower flow regime conditions (Fiorillo, 1991b). Glauconite grains dated from 122.2 ± 3.2 Ma and 123.6 ± 3.4 Ma are interpreted as reworked grains probably originating from Aptian marine limestones, widespread in this area (e.g. Guyonnet-Benaize et al., 2010). Foraminifera observed in thin sections are also probably reworked from older carbonate rocks. *Microcodium* (Kabanov et al., 2008) may also be reworked. Broken and rounded grains occur in the upper flow regime sediments, resulting from deposition in the channel or in a crevasse play. Phytoclasts and in particular lignitic debris reflect the presence of vascular plants in the environment,

Sample	01	02	22	23	25	27	28	31	32	33	41
$CaCO_3$ (%)	23.8	24.3	48.5	93.4	38	30.9	34.1	50	32.7	29.7	38.1

Table 7.2. Carbonate concentration of palaeosol samples. The table displays the $CaCO_3$ content of calcareous siltstones. All samples are particularly rich in carbonates. See Fig 8.2 for correlation with these samples.

either from riparian forests (if found in channel deposits) or other remote forests. The roundness of most charcoal indicates a prolonged transportation of these particles in the river channel. Fungal hyphae indicate recycling of wood debris from surrounding soils (Scott et al., 2000).

- **Facies 2**. Facies 2 is interpreted as levee deposits. Because feldspar crystals are unstable and quickly weathered, their presence in the sandstones reflects rapid transport and deposition from the sediment source (e.g. do Nascimento et al., 2015). The micritisation of many skeletal elements reveals shallow water conditions (Srivastava, 2006; Védrine et al., 2007). The rounded shape of charcoal still indicates a prolonged transportation from the plant source. These charcoal grains potentially reflect different stages of organic matter maturity. Indeed, they are common features in palynological assemblages, corresponding to charring states of diverse organic debris; they may be a result of wild fires. Vegetation in levee facies was likely abundant, suggesting rare inundation episodes (Brierley et al., 1997).
- **Facies 3**. The presence of colour mottling, in addition to the absence of stratification, in the fine-grained siltstones of facies 3 suggests soil formation, resulting from periods of subaerial exposure (e.g. Pimentel et al., 1996; Wright, 1992). The palaeosol profiles are particularly rich in carbonates (Table 7.2). Broken mollusc shells and other skeletal grains indicate that they were transported by relatively high currents before deposition within fine sediments. Moreover, mud coated grains reflect rather shallow water conditions (Srivastava, 2006; Védrine et al., 2007). Charcoal grains are less abundant than in the previous facies. The large size of tracheid fragments suggests better preservation conditions, and/or the proximity of source plants to the depositional site, and/or low hydrodynamic conditions. The presence of both broken skeletal elements and well preserved phytoclasts in fine-grained sediments indicate an intermediate sub-environment, intermediate between the active channel and surrounding floodplain. Therefore, this facies is tentatively interpreted as a proximal floodplain environment.
- **Facies 4**. Facies 4 is the finest grained, consisting predominantly of siltstones and mudstones. It is interpreted as a low-energy alluvial plain facies rather far from the active channel, according to the size of the grains, the oxide-coated grains, the quantity of mud, and the lack of bioclasts. Deposits are variegated, probably indicating local changes from oxidising to reducing conditions (Wright, 1992). The silty

sediments were exposed subaerially and subject to soil-forming processes leading to palaeosol formation in a well-drained floodplain as it is shown by mottled sediments, and calcareous nodules (e.g. Csiki et al., 2010). The mudstones are horizontally laminated, and are interpreted as a result of settling of suspended sediment in overbank areas during flood events (Ghosh et al., 2006). The low amount of lignitic particles in palynological assemblages, although they are well preserved, suggests long-range transportation from the source.

- **Facies 5**. Undulatory laminae at the base of the lowermost limestone bed (Fig.7.5f) suggest deposition in a shallow lake with bottom currents (Stewart, 1981). Upper beds are massive without sedimentological structure. Because of its very fine texture and the presence of ostracods, this calcareous facies may be interpreted as freshwater limestone deposits within an alluvial setting (Armenteros et al., 1997). Lake formation could have resulted from avulsion when channels were abandoned (Blasco et al., 2008). During periods of high discharge, flows can spread out onto the floodplain and then fill abandoned channel to form a lake (Nichols & Fisher, 2007). On the other hand, such a lake could have been formed independently from the fluvial system. Absence of any form of sedimentary structure in the upper carbonate beds probably represents low-energy lake sedimentation with high biogenic productivity (Csiki et al., 2010; Stewart, 1981). These micritic limestones correspond to autochthonous deposition of carbonate mud. The microfacies reveal very fine matrix and the presence of freshwater "algae", mollusc shells and ostracod valves (Türkmen et al., 2007). The fine-grained sediments reflect a very calm depositional environment without channel sediment contribution. Moreover, the presence of fossils and the homogeneous texture of the lacustrine wackestone indicate a shallow low-energy depositional context (Tófalo & Pazos, 2010; Wright et al., 1997), as well as the decrease in the detrital input.

5.2. Taphonomy

The vertebrate assemblage collected in 2009 and 2012 includes two chelonians, *Solemys* and *Polysternon* (de Lapparent de Broin & Murelaga, 1996), which are freshwater taxa that lived in fluvial environments (Marmi et al., 2012; Marmi et al., 2009). Chelonian specimens are abundant within the different taphonomic modes and are usually well preserved (Fig.7.9), suggesting a local source for the turtle carcasses. The crocodilian skull and a mandible probably belonging to a basal Alligatoroïdae are similar to a specimen from this crocodilian family (Delfino et al., 2008) previously found in Romanian pond deposits, suggesting that they lived in lacustrine habitats (Marmi et al., 2012). The excellent preservation of several crocodilian specimens in fluvial deposits from the Velaux-La Bastide Neuve locality also indicates short transport followed by a rapid burial at the local site and suggests that this crocodilian could also live in fluvial environments. The presence of teeth of the hybodont shark *Meristonoides* (Gilles Cuny, pers. com.) is rather unusual. However, hybodont sharks are abundant in freshwater environments during the Cretaceous, although it is difficult

to determine precisely if they lived only or occasionally in freshwater environments (Cuny, 2012). Predation marks are scarce: only one supposed predation mark is observed among the total assemblage. Tooth marks on dinosaur bones are usually attributed to scavenging and prey carcass utilization (Behrensmeyer, 2007; Fiorillo, 1988; Viseras et al., 2006). If so the scarcity of such marks on the bones of Velaux-La Bastide Neuve assemblage might reflect a low incidence of scavenging at the locality. Alternatively, it may also be hypothesised that prey were particularly numerous and that scavengers only ate the fleshy part of carcasses (Eberth & Getty, 2005) or preferred some portions of the skeletal remains (Faith & Behrensmeyer, 2006). Tooth-marked bones are never frequent in dinosaur localities and that theropod dinosaurs did not routinely bite bones during prey carcass utilization (Viseras et al., 2006). Post-mortem fractures are frequent in the fossil assemblage, but bone edges usually remain sharp, indicating that the transport that affected the dead carcasses was rather short (Fiorillo, 1988). However, numerous parallel transverse fractures (perpendicular to bone fibers) represent post-mortem fracturing that affects bones during burial compaction (Kos, 2003), while longitudinal breakages represent weathering, a pre-diagenetic process (Behrensmeyer, 2007). Oblique and in rungs breakages are also common and consist of pre-fossilisation fracturing, revealing fresh bone damage (Eberth & Getty, 2005). Perthotaxic features (bone modification processes active on the land surface (Clark et al., 1967) are not found on the bones inspected here. Weathering of bone surfaces is weak in the assemblage. This indicates that the bones were not exposed subaerially for any significant time before or after reworking and that they were quickly buried. The chelonian remains are very well preserved and usually less degraded than dinosaur bones, suggesting that their transport was of shorter duration and that they lived directly in (or very close to) the area. Most of vertebrate remains are very well preserved in the three fossil-bearing layers. The exceptional preservation of two parallel sauropod cervical ribs, associated with skin impressions in the lowermost layer, reflect rapid burial (Eberth & Currie, 2005) in fine-grained sediments after short transport in the alluvial plain. Associated elements (partially articulated titanosaur skeletons) from the lowermost bone bed are not complete suggesting that the rest of the skeleton was dissociated earlier.

The taxonomic diversity of the two bone beds suggests distinct accumulations of vertebrate remains belonging to individuals that died in different places and/or at different times. Their remains were then transported by river streams from their different habitats, deposited and finally gathered in the same area in a channel. It appears that the lowermost bone bed presents a non-random orientation pattern with a major south-east trend for the elongate elements (Fig.7.11). In this sandy layer elements are heterogeneous with various sizes and shape ranges. This orientation pattern with heterogeneous elements results probably from larger elements acting as obstacles for the other, smaller, elements (Domínguez-Rodrigo et al., 2014). No clear preferential orientation in the uppermost layer probably results from low energy depositional conditions. In this case, currents were probably too weak to orient all the

elements in the same direction. The apparently random orientation in this layer could also originated in the abundance of elements or by their sudden deposition. It has been demonstrated that bones transported in shallow water adopt a parallel orientation to the flow, suggesting a NE-SW direction for the currents that transported these bones (Domínguez-Rodrigo et al., 2014).

5.3. Sedimentology and taphonomy

Sedimentology and taphonomy, together, permit a reconstruction of the palaeoenvironments in Velaux-La Bastide Neuve locality. Interpretations resulting from both sedimentological and taphonomic studies, indicate that the bones were deposited in a fluvial environment. The size of the grains, related to downstream decrease in discharge, is a good indicator for assessing the distance between the depositional environments from the main stream channel. Coarser sediments (conglomeratic and sandy facies) deposited close to the channel, were accompanied by heavier vertebrate elements. Finer sediments were deposited further in the alluvial plain, with lighter elements. Sandy fossil-bearing deposits are interpreted as either channel or crevasse splay facies, while silty deposits are interpreted as overbank facies. Organic particles are typically found in the finer sediments because of their low densities. Thus, organic matter reflects a low energy depositional environment far from the river stream. Numerous charcoal fragments might indicate the presence of wildfires in the palaeoenvironment. Moreover wildfires might intensify landslides and thus influence sedimentation (Brown et al., 2012). On the other hand, charcoal might also be the result of plant debris maturation. Charcoal is common in palynological assemblages. Palynofacies therefore confirm the results of the sedimentological studies. Preservation of charcoal, lignitic debris and other organic particles probably reflect flooding events that concentrated phytoclasts. The scarcity of pollen grains in the sediment is more likely the result of the distance from the vegetation sources than their non-preservation. The vertebrate assemblage discovered at Velaux-La Bastide Neuve clearly represents a mixture of aquatic and terrestrial animals that lived in different habitats. Transported vertebrate carcasses appear to be well preserved both in channel-fills and overbank deposits, due to rather short transport in a low-energy fluvial system. Chelonians and crocodilians were potentially (para) “autochthonous”—their carcasses experienced very little transport inside their life environment-, whereas dinosaurs and sharks were “allochthonous”: the latter did not live directly inside the fluvial realm, but in its vicinity and their remains were transported. During flood events, the river water could overflow channel banks and spread out over the alluvial plain. The finest deposits result from settling of material further from the active channel and accumulated in overbank areas. The river system is interpreted to have had a broad floodplain subjects to periods of soil development. Major vertebrate taxa (dinosaurs, turtles, pterosaurs and crocodiles) lived in this fluvial environment. Palynological analysis confirm that this environment was surrounded by flowering plants and conifers. Repeatedly rainfall could induce

flooding events, which resulted in transport of vertebrate remains and organic matter within the system. Different sub-environments then succeeded in the same area and the sedimentological facies in Velaux record these fluvial deposit successions.

6. Conclusion

The sedimentological record observed in Velaux-La Bastide Neuve site represents a vertical succession of five facies that are interpreted as channel and floodplain deposits in the medial part of a fluvial depositional system; moreover, the section shows evidence for both river and lacustrine environments. There are nine sedimentological sequences dominated by overbank deposits representing successive flooding episodes. Each sequence is characterised by erosive and depositional episodes. Relatively fine-grained sediments and amalgamation of channel-fills suggest a river system surrounded by a floodplain. Lack of floodplain deposits overlying the sandstones in sequences 2 and 3 suggest several episodes in the river channel down cutting within this zone. Palynological study corroborates the environmental model proposed, confirming relatively low hydrodynamic depositional conditions and dry climate alternating with wet periods. Vascular plants were present in the palaeoenvironment. Palynological assemblages show that angiosperms were also represented in the environment. A few triaperturate pollen grains possibly belonging to Normapolles complex indicate that the vegetation from the Velaux region was probably composed of both gymnosperms (Coniferales) and angiosperms. Transported vertebrate carcasses appear to be well preserved both in channel-fills and overbank deposits, due to rather short transport in a low-energy fluvial system.

Conclusions and perspectives

This PhD thesis has focused on the following topics: (1) the type and degree of preservation of fossil feathers and other integumentary structures from different dinosaur taxa, (2) the taphonomy and depositional environment of bone beds from terrestrial Late Cretaceous and Middle Jurassic localities, and (3) the dating of deposits that yielded feathers in non-theropod dinosaurs.
Based upon these three great thematic axes, various types of analyses were performed with different objectives:

- To characterise the ultrastructure and chemical composition of fossil feathers from dinosaurs, and test for the survival of original compounds in these epidermal appendages (i.e., keratin and melanin);
- To reconstruct the living habitats of extinct vertebrates and determine the processes that led to the deposition of their remains;
- To constrain the age of an important dinosaur taxon, *Kulindadromeus zabaikalicus*, in relation with the origin and evolution of feathers within the dinosaur clade.

The first objective was completed by studying the fossil feathers of dinosaurs using the combination of imagery (SEM and TEM) and analytical techniques (FTIR, ToF-SIMS, IBA, CP/MAS ^{13}C NMR, Py-GC-MS). Two distinct studies were done on the same specimen: one aimed at measuring the melanin content in the fossils feathers and the other one aimed at determining the elemental and molecular composition of organic matter preserved in the feathers. They both gave distinct, but complementary, results about the preservation of the fossil feathers.
The second objective required the study of rock samples and the observation of outcrops on the field. The granulometry of the deposits, their texture, the sedimentary structures, and also the palynomorph content allow the reconstruction of ancient, palaeo-, environments. Geochemical analyses of the rock samples provided data about the composition, alteration, and sources of the sediments. Careful examination of the position and orientation of the bone remains within the rock layers allows to determine the hydrodynamic conditions responsible for their transport, and then deposition.
The third objective, i.e. the dating of the neornithischian dinosaur *Kulindadromeus zabaikalicus*, was achieved by using the combination of radiochronology (U-Pb) on minerals from the Kulinda deposits and palynology.
This chapter synthesises the main results obtained during my PhD thesis for each topic cited above and provides an overview of the analytical techniques used here.

1. Modes of preservation of fossil soft tissues

Each method used in this dissertation for characterizing the fossil organic matter brings specific chemical information. Some provide data on the elemental composition of the samples (e.g., X-ray spectroscopy techniques), other on their molecular content (e.g., Py-GC-MS), on the functional groups present in the sample (e.g., vibrational spectroscopy), or on the atom coordination in molecules (e.g., μ-XANES). These methods also work at different spatial scales, delivering information from a millimetric scale to a nanometric scale, for the more accurate ones. The application of a combination of these analytical techniques constitutes a good way to obtain information on the soft tissue preservation. All contribute at a different extent to the determination of the chemical composition of ancient soft tissues, and then to the comprehension of the chemical changes occurring in their molecular structure through time. Table 1 provides an overview of the analytical methods used in the scope of the present thesis, the type of information obtained from each method, and the advantage(s) and disadvantage(s) identified in the analyses made during this thesis.

The plumage of the paravian dinosaur *Anchiornis huxleyi* (YFGP-T5199) has received a particular attention for the characterisation of its chemical composition and the observation of its microscopic structure. For this purpose, a series of spectroscopy and chromatography methodologies were combined. The results have shown that the morphology of pigment organelles – here eumelanosomes – may be preserved in fossils as old as 160 Ma. Large quantities of eumelanosome moulds were also observed, suggesting that a great part of the original organelles was altered. Several analytical techniques used here for the determination of feather chemical composition have produced useful results, although some others did not. For example, ToF-SIMS has revealed data consistent with the presence of eumelanin traces in the feathers. All the analyses nonetheless show that it is difficult to find traces of original compounds in very old organic matter. ^{13}C NMR and Py-GC-MS of *Anchiornis* feathers demonstrated that the chemical structure of soft tissues may have changed considerably during diagenesis. The ion beam analyses (PIXE and EBS), used here for the first time on fossil soft tissues, indicated that carbon is the main element present in the fossil, and that it is preserved only in the proximal part of the fossil feathers. IBA has proved to be a useful method for deciphering the width of the fossil feathers by depth profiling while analysing their elemental composition. Sulfur has also been detected in the samples by the same method. The use of state-of-the-art techniques such as microprobes or synchrotron radiation are useful when searching for minute inhomogeneous traces of original organic compounds. The ion beam analyses (PIXE and EBS), used here for the first time on fossil soft tissues, indicated that carbon is the main element present in the fossil, and that it is preserved only in the proximal part of the fossil feathers.

Method	Type(s) of information	Advantages	Disadvantages
SEM	Topographic image	Direct observation of the ultrastructure of very small soft tissue samples	Requires coating with conductive metal, which does not allow further chemical analyses
BSE	Topographic image and chemical composition	Rapid overlook of the distribution of the different mineral phases in a soft tissue or rock sample	Requires preparation prior to analysis to optimise the results (i.e., polishing)
EDS	Elemental composition	Overall and rapid characterisation of the elemental composition	Requires preparation prior to analysis (polishing); sensitivity limited by the beam size and the sample relief
XRD	Main mineral phases and clay mineral identification	Rapid accurate characterisation of the mineral phases	Requires to grind the sample => loss of material
μ-XRF	Elemental composition, mapping	Extremely sensitive; rapid data acquisition; may be used in combination with other methods	Requires extensive pre-processing preparation; costly
μ-XANES	Chemical coordination of atoms	Idem μ-XRF	Idem μ-XRF
PIXE	Heavy elements contained in a light matrix	Does not require particular preparation; very sensitive; may be used in combination with other methods	Extensive post-processing of the data (need excellent knowledge of the method)
EBS	Light element composition	Idem PIXE	Idem PIXE
ToF-SIMS	Ion content	Does not require particular preparation prior to analysis	Very sensitive to contaminants; provide two sets of data (cations and anions) to analyse
FTIR	Functional group determination	Does not require particular preparation prior to analysis; rapid; give information on both organic and inorganic functions	Requires flat surfaces, which is not always possible with fossils
^{13}C NMR	Molecular environment of ^{13}C atoms => functional groups	Gives easily readable spectra	Requires extensive preparation prior to analysis; destroy the fossil
Py-GC-MS	Molecular composition of macromolecular compounds	Gives molecular information; complementary to ^{13}C NMR	Idem ^{13}C NMR

Table 1. Overview of all the methods used in the present PhD thesis. The table gives the main information obtained from each method, and the advantages/disadvantages encountered in this work.

IBA has proved to be a useful method for deciphering the width of the fossil feathers by depth profiling while analysing their elemental composition. Sulfur has also been detected in the samples by the same method. The use of state-of-the-art techniques such as microprobes or synchrotron radiation are useful when searching for minute inhomogeneous traces of original organic compounds. Other methods used in this thesis commonly give excellent results but difficulties may arise due to the inhomogeneous character of the fossils. Fossil soft tissues are, in most cases, tightly bound to the embedding sediment, providing a "mixed" signal that should be separated from those of the fossils. The scanning electron microscopy (SEM) associated to X-ray spectroscopy (EDS) provide complementary data. Pyrite-like framboidal structures are generally observed in the fossil soft tissues but their composition indicates that they rather are iron oxide pseudomorphs after pyrite. Iron oxide pseudomorphs were observed in *Kulindadromeus* bones and bone moulds and, less, in the soft tissues, but also within the structure of *Anchiornis* and *Serikornis* feathers. It has been proposed that iron oxides are related to recent weathering/alteration of pyrite that may have formed early during diagenesis and played a role in the preservation of the dinosaur carcasses. Additionally, this thesis has shown that – as in the case of *Kulindadromeus* feathers – specific trace elements, here copper, may also be used as biomarkers for melanin in fossils. Copper is a chelator that has an affinity for modern melanin and may therefore be incorporated in melanin-containing structures, such as feathers. Its preferential enrichment in *Kulindadromeus* monofilaments – interpreted as primitive feathers – may be related to the presence of melanin in these primitive epidermal appendages.

2. Taphonomy and depositional environments of fossils

The taphonomy of bone beds was studied in two different localities that have yielded dinosaur remains. The first locality, Velaux-La Bastide Neuve (south-eastern France) consists of a succession of regressive sequences of conglomerates, sandstones, siltstones, and mudstones, including palaeosols. These riverine sequences are topped by micritic limestones characterising the migration of a riverine system through a lacustrine setting. The vertebrate assemblage is relatively diversified and is restricted to the riverine sediments. It comprises remains of pterosaurs, titanosaurids, rhabdodontids, ankylosaurids, chelonians, crocodilians, hybodont sharks, and theropods (shed teeth). Three bone beds were detected, in river channel, overbank and floodplain facies, which record diverse vertebrate assemblages. The Velaux locality therefore represents attritional concentrations of vertebrates originating from different habitats in a low-energy riverine setting.

The taphonomy of bone beds has been studied in the Kulinda locality (south-eastern Siberia, Russia), as well. This fossil-bearing site is characterised by a succession of monotaxic bone beds containing remains of the Jurassic neornithischian dinosaur *Kulindadromeus zabaikalicus*. Two main bone beds (named bb3 and bb4) and seven minor bone layers (bb3/3) have been excavated. They represent distinct

taphonomic processes: the lowermost bone bed (bb4) consists of articulated bones and bone moulds highly impregnated by iron-oxides, along with well-preserved soft tissues - including feathers -, whereas the overlying bone beds (bb3/3 and bb3) only contain scattered bones with very few or no soft tissues. All the bone beds lie in fine-grained (silt- or fine sand-sized) greywackes that derived from the reworking of Early and Middle Jurassic felsic igneous rocks. The articulated character of the bones in bb4 and the presence of soft tissues reflect calm deposition conditions with short transport. The disarticulated character of the bones and the absence or faint traces of soft tissues in the other bone beds (bb3/3 and bb3) suggest disarticulation of the dinosaur carcasses prior to their deposition. Post-mortem processes have certainly played a major role in the disarticulation of the dead corpses in these bone beds.

3. Date constrain on a locality containing fossil soft tissues

Kulindadromeus zabaikalicus from the Siberian locality of Kulinda is of particular importance because that non-theropod dinosaur possessed elongated appendages interpreted as proto-feathers. A major goal of the thesis was therefore to refine the dating of the *Kulindadromeus* bone beds. The dating of the locality was performed by means of laser ablation ICP-MS U-Pb radiochronology on granites and their volcaniclastic derivatives, and palynological investigations. Given the reworked origin of the deposits at Kulinda (like most non-volcanic sediments), the combination of absolute dating and palynology was essential. The U-Pb dating of zircons and monazites collected within the sediments and their granitic source has constrained the maximum age of the Kulinda deposits at 172.8 ± 1.6 Ma, corresponding to the Aalenian (early Middle Jurassic). The palynomorph assemblage mostly contains taxa that have a wide stratigraphic ranges. Several spores and pollen nonetheless present a stratigraphic importance: *Podocarpidites rousei*, *Eboracia torosa*, and *Gleicheniidites* spp. These species are typical for the Bathonian (Middle Jurassic) in southern and northern regions of western Siberia. In addition, the minor amount of the pollen of the extinct Cheirolepidiaceae *Classopollis* excludes a younger, Callovian (late Middle Jurassic), age for the deposits. This work brings new age constraints on the deposits containing the neornithischian dinosaur with feathers, *Kulindadromeus*, which probably lived during the Bathonian (i.e., between 168.3 ± 1.3 Ma and 166.1 ± 1.2 Ma). These important data push back the origin of feathers in dinosaurs (Fig. 24) and provide discussion for research on the first feathers that should be sought in a common ancestor to dinosaurs and pterosaurs.

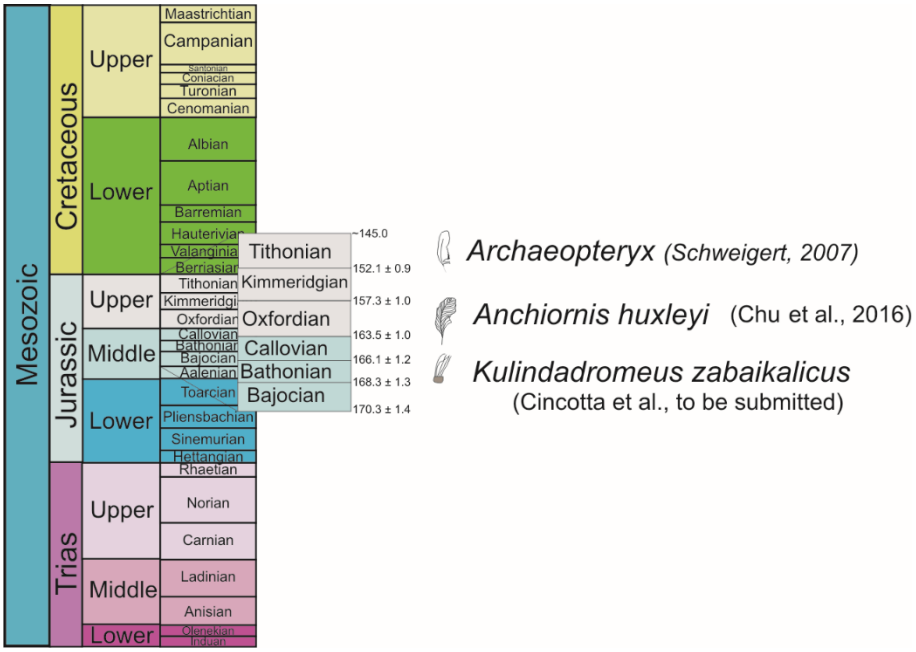

Figure 24. Position of the major feathered fossils relative to the origin of feathers. *Archaeopteryx* is the oldest known Avialae from the Kimmeridgian-Tithonian of Bavaria; *Anchiornis huxleyi* is a paravian feathered dinosaur from the early Oxfordian of China; *Kulindadromeus zabaikalicus* is a neornithischian dinosaur with primitive feathers from the Bathonian of Siberia.

Perspectives

Work needs to be continued, especially on the environmental context of *Kulindadromeus* bone beds. Particularly, the study of the weathering aspects of some mineral phases in relation to the geodynamic context of Siberia during the Middle Jurassic, may bring new data on the origin of the sediments, their depositional setting, and the mode of preservation of the soft tissues and bones. Further excavation at Kulinda will be necessary to find new fossils and refine the taphonomic pathways of *Kulindadromeus* remains.

In the future, the taphonomy of the soft tissue head crest of a pterosaur from the Cretaceous of Brazil will be examined in detail. For that purpose, SEM and TEM should bring important data on the ultrastructure of the pterosaur soft tissues and, in particular, the pycnofibres. The chemical composition (using IBA, FTIR, and ^{13}C NMR) of the soft tissues will be analysed in order to test the survival of keratin and melanin in the fossils. Both structural and chemical analyses will be used in an attempt to reconstruct the colouration pattern of the head crest.

The difficulty of the thesis was to decipher which method to use rather than another. The panel of geochemical analytical tools available for palaeontological studies is enormous and it is therefore necessary to examine which one is more suitable in the

case of a particular study. It is also necessary to focus on the cost and time involved in such analyses. Most of time collaboration with laboratories allow the use of advanced techniques. In some cases, it is also good to test novel methods or to modifiy the analytical protocols. I think that this thesis gathered most of the points mentioned above. Nonetheless, after evaluation of the methodology used here, the use of less methods would have permitted to focus on specific aspect of the preservation of fossil soft tissues. I would have focused on Py-GC-MS and ^{13}C NMR that gave data about the molecular structure of the fossil organic matter, SEM/TEM that permitted to study the ultrastructure of the fossils, and IBA (PIXE and EBS) that has shown its capacity in depth profiling and the determination of the elemental composition of fossil feathers, and is therefore perfectly suited for the study of palaeontological material. This thesis, however, displays a good overview of the possible ways to study the preservation of fossil soft tissues and their depositional environments.

Appendices

A1. Appendice to "Molecular composition and ultrastructure of Jurassic paravian feathers"

Provenance and age of YTGP-T5199

Like most paravian fossils from western Liaoning, YTGP-T5199 was acquired by Yizhou Fossil & Geology Park from a local fossil dealer, who reported that the specimen was recovered from the Yaolugou locality (Jianchang County), not far from the village of Daxishan where *Anchiornis* specimen LPM-B00169 (housed in Liaoning Paleontological Museum) was unearthed1. YTGP-T5199 was prepared by professional technicians at Yizhou Fossil & Geology Park, thus its authenticity and integrity (except for some minor restorations made under strict scientific control) are ensured.

The Tiaojishan Formation crops out in western Liaoning Province (Duan et al., 2009). It is about 130–970 meters thick, and comprises a broad array of siliciclastic rocks, including basalts, andesites, rhyolites, tuffs, tuffaceous sandstones, and conglomerates (Chang et al., 2009). Due to complex local stratigraphic conditions, accurate dating of the Tiaojishan Formation has proven difficult (Zhang et al., 2008). Absolute ages between 165 ± 1.2 and 153 ± 2.0 Ma were obtained by SHRIMP U-Th-Pb dating of samples from the nearby Lanqi Formation (a lateral equivalent to the Tiaojishan Formation) (Yang & Li, 2008; Zhang et al., 2008). Zhang et al. (2008) concluded that the upper boundary of the Lanqi Formation ranges between 156 and 153 Ma, whereas Chang et al. (2009) obtained Ar-Ar ages of 160.7 ± 0.4 and 158.7 ± 0.6 Ma for the lower part of the formation. These estimates indicate that the Tiaojishan Formation spans the Callovian-Kimmeridgian interval of the Middle-Late Jurassic (Gradstein et al., 2004).

Specimen details and taxonomic assignment

Because the holotype (IVPP V14378, housed in the Institute of Vertebrate Paleontology and Paleoanthropology) of *Anchiornis huxleyi* lacks a head (Xu et al., 2009a), cranial comparisons were made primarily with the virtually intact referred specimen LPM-B001691. YFGP-T5199 is about 47 cm long when measured from the tip of the snout to the distal end of the tail, and is thus comparable in size with LPM-B00169 (see Supplementary Table S3 for selected length measurements). The following features indicate that YFGP-T5199 represents a skeletally mature individual (Forster et al., 1998; Gao et al., 2012; Godefroit et al., 2013b; Turner et al., 2012; Xu & Norell, 2004; Zhou & Zhang, 2003): (1) the texture of the bone at the proximal and distal ends of the coracoid, humerus, ulna, pubis, and femur is regular and continuous; (2) the neural arches of the cervical and caudal vertebrae are fused to their corresponding centra; and (3) the frontals are fused along their sagittal line. The

head of YFGP-T5199 is almost complete. As in *Aurornis* and *Eosinopteryx*, it is slightly shorter than the femur (Godefroit et al., 2013a; Godefroit et al., 2013b). In lateral view, the skull is sub-triangular due to its shallow snout and expanded postorbital region. These characteristics are also found in *Aurornis*, *Eosinopteryx* and *Xiaotingia* (Godefroit et al., 2013a; Godefroit et al., 2013b; Xu et al., 2011). Similar to *Eosinopteryx* (but not *Aurornis*; Godefroit et al., 2013b) (Godefroit et al., 2013a), the maxillary process of the premaxilla is short. The external naris extends beyond the rostral border of the antorbital fenestra. This condition is similar to that of *Mei*, but contrasts with the shortened naris in *Aurornis* (Godefroit et al., 2013b). Similar to BMNHC PH828 (a third referred specimen of *A. huxleyi;* Li et al., 2010; but see also below), LPM-B00169, *Aurornis*, and *Eosinopteryx*, the nasal contributes to the posterior margin of the naris. The premaxillary fenestra in YFGP-T5199 is about the same size as in *Xiaotingia*, but distinctly smaller than in Aurornis (Godefroit et al., 2013b; Xu et al., 2011). YFGP-T5199 has a large maxillary fenestra separated from the antorbital fenestra by a narrow interfenestral bar, a condition comparable to that in LPM-B00169 and BMNHC PH828. Additionally, the antorbital fenestra is about half the length of the orbit, and the former cranial opening is as high as long. These features are evident in LPM-B00169, but contrast with those in *Xiaotingia* where the antorbital fenestra is considerably shorter than high (Xu et al., 2011).

In YFGP-T5199, the posterior process of the lacrimal is shorter than the anterior process, a character state comparable to that of *Archaeopteryx* and troodontids (Hwang et al., 2002; Makovicky & Norell, 2004; Xu et al., 2002), but dissimilar to the long posterior process in *Eosinopteryx* and *Aurornis* (Godefroit et al., 2013a; Godefroit et al., 2013b). The dentary is slender and bears a groove that widens posteriorly. It also contains a row of foramina, as in numerous other paravians, including *Archaeopteryx*, *Anchiornis*, *Xiaotingia*, *Eosinopteryx*, *Aurornis*, troodontids, and some basal dromaeosaurids (Gao et al., 2012; Hu et al., 2009; Wellnhofer, 2009; Xu et al., 2011).

The tooth crowns are sharp (but not serrated), and thus unlike the bulbous teeth in *Xiaotingia*2. The premaxillary teeth are densely spaced in the symphyseal region, as in other basal birds (including IVPP V14378, LPM-B00169 and BMNHC PH828) and troodontids (Currie, 1987; Godefroit et al., 2013a; Godefroit et al., 2013b; Makovicky & Norell, 2004; Xu & Norell, 2004). Similar to LPM-B00169, a longitudinal groove is present along the dorsomedial margin of the (slender) sub-orbital ramus of the jugal. This is unlike the condition in BMNHC PH828. This bone is also more robust than in *Aurornis* (Godefroit et al., 2013b).

The gross morphology of the vertebrae in YFGP-T5199 closely resembles those in basalmost Avialae, including the *A. huxleyi* holotype. The middle and posterior dorsal vertebrae are elongated, whereas the anteriormost caudals are significantly shortened. These character states manifest in other specimens assigned to *Anchiornis*, primitive dromaeosaurs, as well as other basal birds (e.g., *Archaeopteryx, Aurornis* and *Eosinopteryx*; Godefroit et al., 2013a; Godefroit et al., 2013b; Hu et al., 2009;

Wellnhofer, 2009; Xu et al., 2009a). In the proximal caudal series, the transverse processes are posterolaterally oriented, longer than their corresponding centra, and slender; features observed elsewhere in the type specimen of *Anchiornis*. As in IVPP V14378 and *Archaeopteryx*, the distal caudals bear a distinct groove on their lateral surface near the junction between the neural arch and vertebral centrum (Hu et al., 2009).

Similar to most troodontids, *Archaeopteryx*, *Aurornis*, *Eosinopteryx*, and all previously described specimens of *Anchiornis* (Elzanowski, 2002; Godefroit et al., 2013a; Godefroit et al., 2013b; Li et al., 2010; Makovicky et al., 2003; Xu et al., 2009a), there is no ossified sternum in YFGP-T5199. The furcula closely resembles that in IVPP V14378 and BMNHC PH828 (Hu et al., 2009; Li et al., 2010). The interclavicular angle is smaller than in *Archaeopteryx*. The scapula is short and slender (approximately 46 % of humeral length), as in IVPP V14378 (65 %), LPM-B00169 (66 %), BMNHC PH828 (58 %), basal dromaeosaurids (e.g., *Microraptor zhaoianus*), and basal avians (e.g., *Aurornis*, where it is 63 %) (Supplementary Table S4; see also Makovicky et al., 2005). The coracoid is sub-rectangular, as in IVPP V14378, LPM-B00169, BMNHC PH828, *Aurornis*, *Eosinopteryx*, and *Archaeopteryx*. There are numerous small pits on its ventral surface, a diagnostic feature observed also in IVPP V14378, but not in the (dorsally exposed) coracoids of BMNHC PH828 and LPM-B00169 (Hu et al., 2009; Li et al., 2010).

Similar to *Anchiornis*, *Aurornis*, *Eosinopteryx*, and *Xiaotingia*, the forelimb/hind limb ratio is below 1.0. The humeri in YFGP-T5199 equal the femora in length (1.0), and are thus comparable to those in the holotype of *A. huxleyi* (0.96) and LPM-B00169 (1.04), but unlike the shorter humeri in *Aurornis* (0.88), *Eosinopteryx* (0.79) and *Xiaotignia* (0.85). The deltopectoral crest is short (about one-fourth of humeral length) as in the *A. huxleyi* holotype, BMNHC PH828, dromaeosaurids, and troodontids (Hu et al., 2009; Li et al., 2010). The ulna is only slightly thicker than the radius and exhibits a gentle posterior curvature, as in IVPP V14378, BMNHC PH828 and *Aurornis*; this contrasts with the virtually straight ulna in *Xiaotingia* and *Eosinopteryx* (Godefroit et al., 2013a; Godefroit et al., 2013b; Xu et al., 2011; Xu et al., 2009a). The radius and ulna closely contact each other, unlike the condition in *Xiaotingia*, *Archaeopteryx*, *Mei*, dromaeosaurids, and *Sinornithoides* (Currie & Zhiming, 2001; Godefroit et al., 2013b). Metacarpal I is about one-third the length of metacarpal II, like *Aurornis*, *Eosinopteryx* and *Xiaotingia* (Godefroit et al., 2013a; Godefroit et al., 2013b; Xu et al., 2011). Contrary to the condition in *Aurornis*, the manual phalanx I-1 is not more robust than the radius (Godefroit et al., 2013b). Also in contrast to *Eosinopteryx* (but similar to BMNHC PH828), metacarpal III is both as long and wide as metacarpal II (Godefroit et al., 2013a; Godefroit et al., 2013b; Li et al., 2010). As in the *A. huxleyi* holotype and *Eosinopteryx*, the long manual phalanx II-1 is

comparable in robustness to the radius (Godefroit et al., 2013a), but it is also thicker than the other manual phalanges (Xu et al., 2009a).

Similar to the holotype of *Anchiornis*, the ilium of YFGP-T5199 is about half the length of the femur (Hu et al., 2009; Xu et al., 2009a). The dorsal margin of the ilium is slightly convex, as in LPM-B00169 and *Xiaotingia*, and contrasts with the sub-horizontal dorsal profile seen in *Aurornis*, and the strongly convex edge found in *Eosinopteryx* (Godefroit et al., 2013a; Godefroit et al., 2013b; Xu et al., 2011). As in *Eosinopteryx*, the postacetabular process does not taper distally. This process remains sub-horizontal, similar to the condition in *Eosinopteryx*, *Aurornis* and *Xiaotingia* (Godefroit et al., 2013a; Godefroit et al., 2013b; Xu et al., 2011). Although the supraacetabular crest and the prominent supratrochanteric process have been crushed during fossilisation, the general shape of the ilium in YFGP-T5199 appears to be virtually identical to that in LPM-B00169 and IVPP V14378. As in LPM-B00169 and *Eosinopteryx*, the ischium is strongly curved posteriorly with an obturator process located close to the midpoint of the element (Godefroit et al., 2013a; Hu et al., 2009); this is contrary to the condition in *Aurornis* where the obturator process is delimited by a hook-like ventral process and a long dorsodistal process of the ischium (Godefroit et al., 2013b). In YFGP-T5199, the dorsodistal process of the ischium is short and blunt, whereas it forms an elongate, tapering blade in IVPP V14378, LPM-B00169 and *Eosinopteryx* (Godefroit et al., 2013a; Hu et al., 2009; Xu et al., 2009a). Pending additional material of *Anchiornis*, we tentatively consider this character state as representing either sexual dimorphism or intraspecific variation, since it by itself is insufficient to warrant the erection of a new species. Unlike dromaeosaurids and *Xiaotingia*, there is no groove running along the anterior margin of the ischium (Xu et al., 2011). The hind limbs in YFGP-T5199 are highly elongate with a femur + tibiotarsus + metatarsal III/trunk length ratio of 2.4, roughly corresponding to that in the *A. huxleyi* holotype (2.0). The distal half of the femur is thicker than the proximal half, a feature also seen in basal avialans, such as *Sapeornis* and *Rahonavis*, as well as in the primitive dromaeosaurid *Buitreraptor* (Forster et al., 1998; Hu et al., 2009; Zhou & Zhang, 2003), but not in *Xiaotingia*, *Aurornis* and *Eosinopteryx*. The tibiotarsus is highly elongate (156 % of femoral length), as in the *Anchiornis* holotype (160 %) and LPM-B00169 (161 %). The bone is relatively longer than in any other non-avian theropod (80 or Mesozoic avialan (Supplementary Table S4).

As in IVPP V14378, LPM-B00169, BMNHC PH828, *Aurornis*, and *Eosinopteryx*, the metatarsals are not fused proximally. Pedal digit I lies medial to metatarsal II, suggesting a non-reversed hallux, as in IVPP V14378 and LPM-B00169 (Hu et al., 2009; Xu et al., 2009a). The sub-arctometatarsalian condition (that is, a transverse compression of metatarsal III) is present in YFGP-T5199, as in some dromaeosaurids and troodontids (Xu et al., 2009a), LPM-B00169, *Aurornis* (Godefroit et al., 2013b), and *Eosinopteryx* (Godefroit et al., 2013a). Metatarsal I is less than one-fourth the length of metatarsal III, as in LPM-B00169 (about 20 % in both specimens), whereas the bone is about 30 % the length of metatarsal III in *Aurornis* (Godefroit et al.,

2013b). As in *Mei* and some dromaeosaurids, the distal articulation of metatarsal II is about as wide as the corresponding surface of metatarsal III1. Similar to *Archaeopteryx*, *Eosinopteryx*, *Aurornis*, *Xiaotingia*, and terrestrial cursorial birds, the pedal phalanges decrease gradually in length proximodistally (Godefroit et al., 2013a; Godefroit et al., 2013b; Wellnhofer, 2009; Xu et al., 2011).

In conclusion, YFGP-T5199 closely resembles both the holotype (IVPP V14378) and referred specimen (LPM-B00169) of *A. huxleyi.* Diagnostic characters of *A. huxleyi* (see Xu et al., 2009a) that also occur in YFGP-T5199 include: (1) numerous small pits on the ventral surface of the coracoid; (2) an extremely reduced ischium (less than one-fourth of femoral length); and (3) an elongate tibiotarsus (roughly 150 % of femoral length). Additionally, measurements and ratios presented in Supplementary Tables S1.3 and S1.4 show that the skeletal and anatomical proportions of YFGP-T5199 are virtually identical to those of IVPP V14378 and LPM-B00169, whereas they differ substantially from those of other paravians from the Tiaojishan Formation. Accordingly, YFGP-T5199 is here assigned to as *A. huxleyi*.

Remarks on the systematic position of BMNHC PH828

In 2010, Li et al. (2010) referred a partial paravian with extensive body coverage (BMNHC PH828) from the Daxishan site to *A. huxleyi*. At that time, only *Anchiornis* was known from the locality (other taxa, including *Xiaotingia*, *Aurornis* and *Eosinopteyx* have since been discovered in the area; Godefroit et al., 2013a; Godefroit et al., 2013b; Xu et al., 2011). This stratigraphical proximity, coupled with compatible body-size (within 5 % that of the *A. huxleyi* holotype) and tibia length, was used to justify the taxonomic assignment.

Nevertheless, we undertook additional comparisons with IVPP V14378, LPM-B00169, and other feathered theropods from Jianchang County: *Aurornis*, *Eosinopteyx* and *Xiaotingia* (Supplementary Table S1.4). These revealed near identical character states, measurements and proportions between these paravians. Thus, a detailed re-examination of BMNHC PH828 is required to confirm its affinity, an undertaking that is beyond the scope of the current study.

SEM imaging of YFGP-T5199 plumage sample S2–S14

The morphological dissimilarity between the microbodies and imprints in sample S1 and those previously reported from the ‘forecrown’ of another presumed specimen (BMNHC PH828) of *A. huxleyi* (Li et al., 2010) - but see also discussion above - prompted an investigation of other parts of the plumage of YFGP-T5199 (Fig. 1.1b). This analysis revealed that the feather traces occur in various states of preservation, ranging from pristine (as in S1) to diffuse, corroded outlines within the clay matrix. Microbodies and/or imprints were found primarily with the tail feathers, and were all oval to elongate in shape (Supplementary Fig. S1.8).

Growth and preparation of eumelanin from *Saccharophagus degradans*

Eumelanin was extracted from *Saccharophagus degradans* strain 2-4081 using the method of Banerjee et al. (2014). Bacteria were grown to late stationary phase in 50 ml of half strength 2216 medium. Black cells were harvested, and the pellet re-suspended in 20 ml 5 % trichloroacetic acid (TCA) for 10 min. The black precipitate was then collected via centrifugation at 8000 × g. After repetition, the pellet was washed twice in 10 ml ethanol-ether 1:1 (v:v), and once with 10 ml ether. After air-drying, the eumelanin was extracted using 50 mM NaCO3 at 95 ºC, and purified via gel filtration using a PD10 desalting column packed with Sephadex G25.

Growth and preparation of pyomelanin from *Vibrio cholerae*

Bacteria belonging to a colony of *Vibrio cholerae* strain SNW2883 were grown aerobically at 37 °C for five days in Lysogeny broth (Sambrook et al., 1989, supplemented with 25 mg of kanamycin per litre solution. Individual cells were removed from the liquid culture by centrifugation at 7500 × g for 15 min at 4 °C. The supernatant was cleared by centrifugation at 50 000 × g for 30 min, resulting in a brown-coloured solution that was stored in the dark at 4 °C. The pigment was purified in milli-Q water using an Amicon® ultra centrifugal filter (3kDa MWCO, Merck Millipore) at 14 000 g for 4 × 10 min.

Preparation of synthetic pyomelanin

Pyomelanin was chemically derived via auto-oxidation of homogentisic acid (HGA) in accordance with the methods of Turick et al. (2002).

Remarks on the IR data

For our IR absorbance measurements, we used two different beamlines: SMIS at SOLEIL, France, and D7, MAX-IV laboratory, Sweden. By utilizing a small area (50 × 50 μm^2) MCT-A single element detector and the superior photon flux at SOLEIL, we were able to identify a few feather regions showing broad-band absorbance consistent with eumelanin (Fig 1.8a). Moreover, the set up enabled measurements of spatially small regions (15 × 15 μm^2), thereby reducing contributions from the sediment. Two distinct peaks at 2850 and 2920 cm^{-1} (Fig. 1.8a) – derived from C-H stretch vibrational modes – were considered representative of melanin and used to produce the IR image in Fig. 1.8c. These bands were not affected by the sediment or a none-linear background (which was more pronounced in our focal plane array detector measurements).

The utility of the C-H stretches to represent residual eumelanin in fossil material is in accordance with published accounts by Glass et al. (2013, 2012b) in contrast to modern *Sepia* melanin, absorbance spectra from fossil ink sac samples exhibit well-defined and intense C-H stretches).

A.2. Appendice to "Chemical taphonomy of morphologically well-preserved dinosaur feathers: a multi-technique approach"

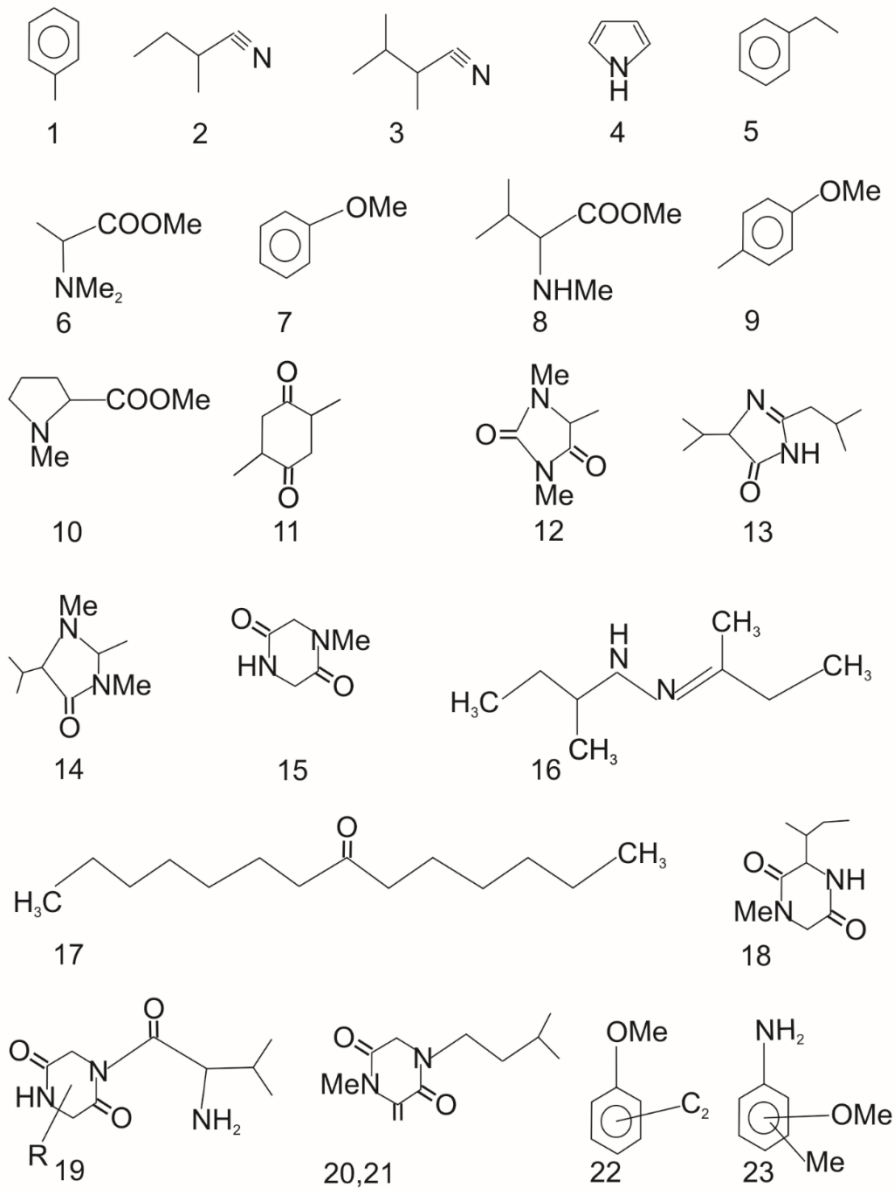

Figure A2.1. Molecular structures of compounds identified in the modern bird feathers. The correspondence with the numbers appears in Table 2.2 and Figure 2.8.

A.3. Appendice to "A new Jurassic theropod from China documents a transitional step in the macrostructure of feathers"

Osteological description

PMOL-AB00200 is about 49 cm long (see Fig. 3.1). Although most of the cranial bones are shattered, the rostral part of the skull is almost well-preserved. The maxillary process of the premaxilla is short and does not exclude the maxilla from the ventral margin of the external naris, as in *Archaeopteryx, Anchiornis*, and most of theropods (e.g. *Saurornithoides*, *Zanabazar*, *Velociraptor*, *Caudipteryx*, *Haplocheirus*, *Monolophosaurus* but not in Ornithomimosauria) (Barsbold, 1974; Choiniere et al., 2010; Godefroit et al., 2013a; Ji et al., 1998; Makovicky et al., 2004; Norell et al., 2009; Osborn, 1924; Wellnhofer, 2009; Zhao and Currie, 1993) (Fig. A3.1). The rostral plate and the maxillary process of the premaxilla are short and robust as in *Eosinopteryx* (Godefroit et al., 2013b). Only the ventral margin of the maxilla is well-preserved with partial shattered portions of the interfenestral bar. The left lacrimal is mostly completely preserved in *Serikornis* and only the proximal part of the right lacrimal is located posteriorly to the left one. The left lacrimal has a long

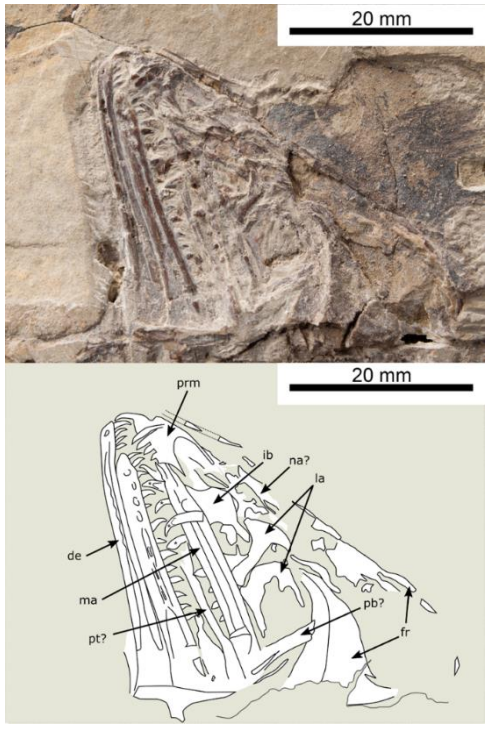

Figure A3.1. Photograph and line drawing of the skull region of *Serikornis*. Abbreviations: de, dentary; fr, frontal; ib, interfenestral bar; la, lachrymal; ma, maxillary; na, nasal; pb, postorbital bar; prm, premaxillary; pt, pterygoid.

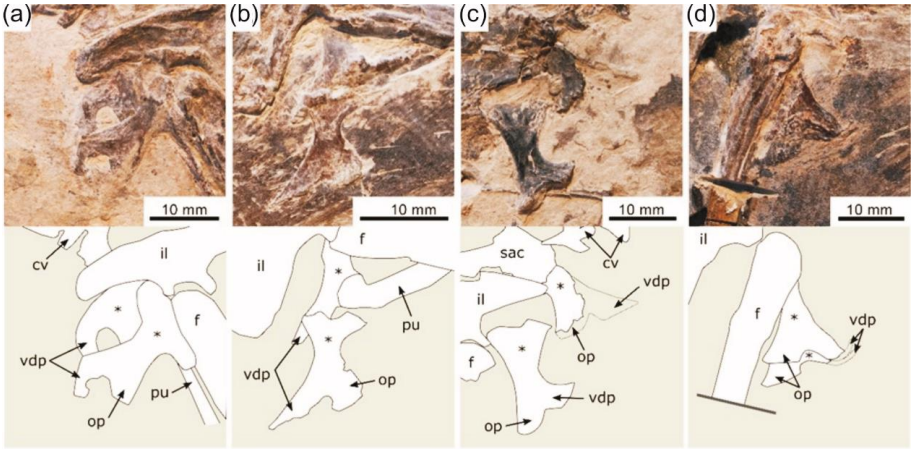

Figure A3.2. Photographs and line drawings of the ischial region among several paravian theropods. (a) *Aurornis*. (b) *Eosinopteryx*. (c) *Anchiornis*. (d) *Serikornis*. Abbreviations: cv, caudal vertebrae; f, femur; il, ilium; op, obturator process; pu, pubis; sac, sacral vertebrae; vdp, ventrodistal process. Ischia are labelled with an asterisk.

and slender anterior process (= rostral process), while the posterior process is shortened. It is virtually impossible to know whether the anterior process contacts the nasal and forms the entire dorsal border of the antorbital fenestra as in all paravians where this bone is known (e.g. *Aurornis*, *Anchiornis*, *Deinonychus*, *Sinornithosaurus*, *Byronosaurus*) (Hu et al., 2009; Makovicky and Norell, 2004; Norell and Makovicky, 2004; Xu and Wu, 2001). Anterior teeth are closely packed as in troodontids (Makovicky and Norell, 2004; Wellnhofer, 2009; Xu et al., 2011). A posteriorly-widening groove extends along the labial surface of the dentary, as in many paravians (Agnolin and Novas, 2013; Godefroit et al., 2013a, 2013b; Hu et al., 2009; Makovicky and Norell, 2004; Xu et al., 2011). The vertebral column is almost complete, although most details of the vertebrae are poorly preserved. Nine cervical vertebrae can be confidently identified. The second, the third and the fourth cervical vertebrae have ossified cervical ribs as long as their corresponding centra. Most of the dorsal portion of the vertebral column is covered by the left humerus and its posterior part is shattered at the junction between two slabs. Only 6 dorsal centra can be identified. Details of the sacral portion is poor due to the junction of four slabs but they appear to be fused. The tail is formed by 27 vertebrae (20 in *Eosinopteryx*, 30 in *Aurornis*, 21-23 in *Archaeopteryx*, 24 in *Anchiornis* YFGP-T5199 (pers. obs.), 22 in *Jeholornis*, at least 26 in *Velociraptor* IGM 100/986) and is 3.9 time the length of the femur (Godefroit et al., 2013a, 2013b; Lindgren et al., 2015; Norell and Makovicky, 1999; Wellnhofer, 2009; Zhou and Zhang, 2002). The scapula is 64% the length of the humerus (selected relative proportions are given in Table S3.4). This bone is thin and ribbon-shaped with a pointed distal end. It is gently convex caudoventrally whereas it is straight in *Aurornis*, *Eosinopteryx*, *Xiaotingia*, *Microraptor*, *Mei*, and *Anchiornis* (Gao et al., 2012; Godefroit et al., 2013a, 2013b, Xu et al., 2011, 2003). The acromion process is not as strongly laterally everted as it is in *Xiaotingia* and oviraptorosaurs

(e.g. *Caudipteryx*) (Osmolska et al., 2004; Xu et al., 2011), more closely resembling the moderately developed and cranially-everted acromion in dromaeosaurids (Ostrom, 1969; Norell and Makovicky, 2004). The coracoid is subrectangular as in most basal paravians (e.g. *Eosinopteryx, Aurornis, Anchiornis,* and *Archaeopteryx*). The biceps tuber of the coracoid is better developed and projects further laterally in *Serikornis* than in other basal paravians and dromaeosaurids; it forms a subglenoid shelf along the caudoventral margin of the coracoid as in dromaeosaurids. The lateral process of the coracoid is thickened distally, forming a ventral rounded bump. The boomerang-shaped furcula is robust as in most other non-avialan theropods (Xu et al., 2011). The humerus of *Serikornis* is slightly shorter than the femur (0.9). Its deltopectoral crest is about one-quarter the length of the humerus, as in other Late Jurassic basal paravians (Table S3.1). The radius and ulna are straight in dorsal view, as in scansoriopterygids, *Anchiornis, Eosinopteryx,* and *Aurornis* (Godefroit et al., 2013a, 2013a, 2013b; Zhang et al., 2002). The distal end of the radius lacks the distinct flange shared by deinonychosaurians and avialans (Zheng et al., 2010). Metacarpals II and III, although partially incomplete, are not fused proximally. The dorsal margin of the ilium is gently convex as in other paravians (Xu et al., 2011) except in *Aurornis,* in which the dorsal margin is subhorizontal (Godefroit et al., 2013a). The obturator process of the ischium is blunt and its ventrodistal process is strongly deflected caudorsally (Fig. A3.2). The femur is slightly bowed anteriorly as in *Aurornis, Anchiornis,* and *Archaeopteryx* (Godefroit et al., 2013a; Hu et al., 2009; Wellnhofer, 2009). The tibia is proportionally shorter (1.41 the length of the femur) than in *Anchiornis* (Table S3.4). The metatarsals are not fused proximally and metatarsal III is transversely compressed as in *Aurornis, Eosinopteryx, Anchiornis, Microraptor*, unenlagiines and all troodontids (Gao et al., 2012; Godefroit et al., 2013a, 2013b; Hu et al., 2009; Makovicky and Norell, 2004; Snively et al., 2004; Xu and Norell, 2004). Metatarsal V is one-third the length of metatarsal IV. Pedal digit II lacks the proximo-dorsally expanded articular trochlea of deinonychosaur-grade paravians (e.g. *Deinonychus, Velociraptor*) and possibly also the Eichstätt specimen of *Archaeopteryx* (Mayr et al., 2005; Norell and Makovicky, 1999; Ostrom, 1969). Pedal phalanges of digit III and IV are slender and successive phalanges do not significantly increase in length proximodistally (see supplementary files for a complete description).

Osteological comparisons

Serikornis differs from other paravians in the following osteological features: the first four maxillary teeth that are twice as large as the others (Figs. S3.3 and S3.4). This anisodonty does not reflect taphonomic factors (i.e., a partial extrusion of first teeth from maxillary sockets) as the maxillary rim recovering the tooth is erased, allowing to observe that the roots are not displaced. X-ray analysis of the skull shows that the posterior maxillary teeth were completely erupted at the moment of the dead (Fig. S3.4). The biceps tuber of the coracoid is strongly developed and well detached from

its lateral margin; the lateral process of the coracoid forms a rounded bump (Fig. S3.5). The ventrodistal process of the ischium is narrow, hook-like, strongly deflected caudodorsally and placed at the distal end of the bone, a unique feature in basal paravians (Fig. A3.2). The shape of the ventrodistal process of the ischium is not the result of a local deformation during the diagenesis because other long bones (humerus, ulna, radius, femur, and tibia) remain straight along their entire length.

Although they share relatively close bone proportions (Table S3.4), several characters clearly distinguish *Serikornis* from *Anchiornis*, also from the Tiaojishan formation, although they share relatively close bones proportion (Table S3.4). The ventral side of the coracoid in PMOL-AB00200 is not sculptured by the numerous small pits, regarded as autapomorphic for *Anchiornis* (Fig. A3.3) (Lindgren et al., 2015; Makovicky & Norell, 2004; Xu et al., 2009a). As this character is present both in the smaller holotype (femur length: 43 mm; Xu et al., 2009a) and in a larger referred specimen (YFGP-T5199, femur length: 70 mm, as in the holotype of *Serikornis*; Lindgren et al., 2015) of *Anchiornis*, the ornamentation of the coracoid is clearly not ontogenetic. The ischium of *Serikornis* also differs from that of *Anchiornis* by its blunt obturator process located more distally than the midpoint of the ischial shaft (Figs. A3.2c, d and S3.6). In *Anchiornis*, the posterodorsal margin of the ischium is gently concave in lateral view (Hu et al., 2009) (pers. obs. on YFGP-T5199). This is the plesiomorphic paravian condition, also shared by *Eosinopteryx* (Godefroit et al., 2013b). The ischium of *Serikornis* is also unique among basal paravians because of its distinct hook-like process on the apical end of its dorsal margin; this process is clearly visible on the left ischium, and as an impression on the slab above the damaged end of the right ischium that closely resembles the process on the left ischium (Fig. A3.2d). In both ischia, the process is more expanded dorsoventrally than anteroposteriorly, resulting in a narrow 'hooked' apex of the bone. *Serikornis* also differs from *Anchiornis* in having a tibiotarsus/femur ratio smaller than 1.5 (1.41 in PMOL-AB00200, >1.55 in all known *Anchiornis* specimens regardless of body size; [Hu et al., 2009; Xu et al., 2009a; pers. obs. on YFGP-T5199, Table S3.3]). This ratio is shared by *Anchiornis* specimens smaller than *Serikornis* (pers. obs. on YFGP-T5199) and individuals subequal in size to the latter (femur length: 66 mm; ratio =1.60; LPM-B00169) (Hu et al., 2009). Therefore, different proportions of the tibia in *Serikornis* and *Anchiornis* likely do not reflect ontogenetic variations.

Serikornis differs from Aurornis in the morphology of its ischium: the postacetabular process tapers distally and the dorsal margin is gently convex, whereas it is not markedly deflected ventrally with a horizontal dorsal margin in *Aurornis*. The ischium also lacks the ventrally-expanded, hook-like ventral process on the distal end that delimits a prominent distal obturator notch in *Aurornis* (Godefroit et al., 2013a).

Serikornis differs from *Eosinopteryx* in the longer rostral plate and larger maxillary process of the premaxilla (although this latter difference may be biased by

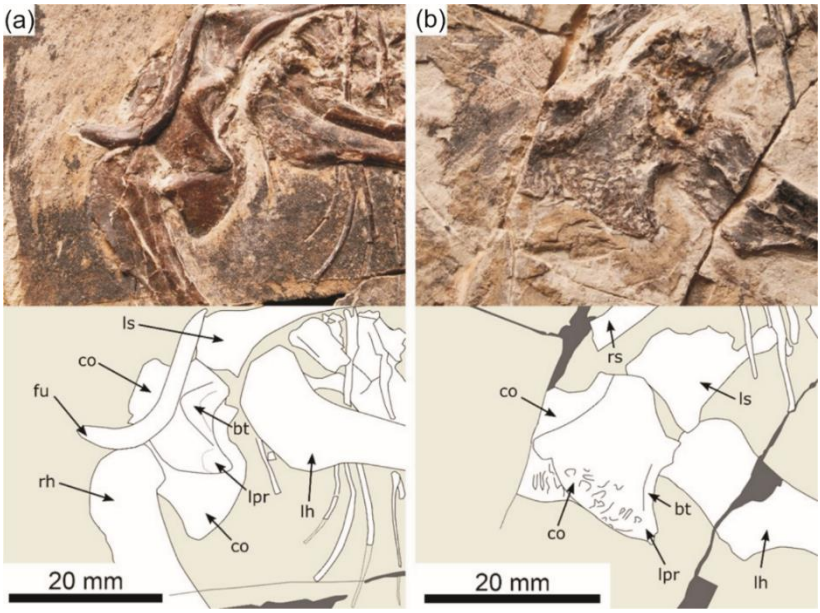

Figure A3.3. Comparison of the scapular girdle in *Serikornis sungei* and *Anchiornis huxleyi* (YFGP-T5199). (a) *Serikornis sungei*. (b) *Anchiornis huxleyi*. Numerous pits are present on the anterior surface of the coracoid of *Anchiornis* that are completely absent in *Serikornis*. Abbreviations. co, coracoids; ct, coracoid tuber; fu, furcula; lh, left humerus; lpr, lateral process of the coracoid; ls, left scapula; rs, right scapula.

the different ontogenetic stages of the type individuals). It also differs by the presence of an anterior process of the lacrimal (the latter is vestigial in *Eosinopteryx*). This feature is likely not an ontogenetic feature as *Serikornis* is a sub-adult specimen whereas *Eosinopteryx* is thought to be an earlier juvenile (Godefroit et al., 2013a).

Serikornis differs from *Pedopenna* in its relatively longer metatarsal I, its metatarsal III longer than metatarsals II and IV, and in the more robust first phalanx of pedal digit I (Xu & Zhang, 2005).

Serikornis differs from *Xiaotingia* in the posterior process of its maxilla that does not exceed in depth the dentary at mid-length, in having a metacarpal III as long as and not more robust than metacarpal II, in the interclavicular angle of its furcula wider than 75° with a slender omal end, and in lacking a strongly laterally everted acromial process on its scapula (Fig. A3.3) that overhangs a groove along the lateral surface of the scapular blade (Xu et al., 2011).

Limb element ratios used to differentiate *Serikornis* may be affected by allometric effects as in other theropods (Christiansen, 1999; Currie, 2003; Gatesy, 1991; Houck et al., 1990). In order to demonstrate that the difference in proportions are due to taxonomy rather than ontogeny, a plot of the limb ratios presented in Table S3.4 versus the femur length (taken as a body size proxy) is presented in Figure A3.4. Trend lines indicate that there is no relationship in regard of each limb proportion ratio. Therefore the differences in limb proportion ratios are due to the taxonomy rather than to the

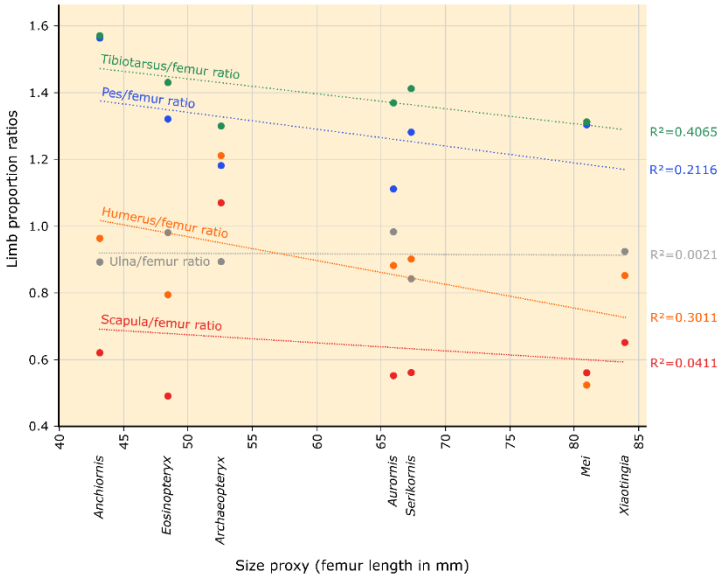

Figure A3.4. Plot of limb proportion ratios versus the length of the femur as a body size proxy in seven paravians. Trendlines and R^2 indicate an absence of relationship between species in regard of each limb proportion ratio.

ontogeny and they can be used in order to discriminate *Serikornis* from other paravian species.

Pneumaticity

Without the presence of recognizable foramina in *Serikornis* due to the crushing of bones during diagenesis, it is impossible to determine whether the bones are pneumatized. Thanks to an X-ray technique called laminography (see supplementary files of Chapter 3), the skull and anteriormost series of cervical vertebrae were digitally sliced with high resolution (Fig. A3.5). At least the anteriormost cervical vertebrae are pneumatized and form numerous small internal chambers (camellate vertebrae). This pattern suggests that a cervical air sac system invades those vertebrae (Sereno et al., 2008) as it is also the case in many theropods (e.g. *Aerosteon*, *Archaeopteryx*, *Rahonavis*, *Deinonychus*, *Velociraptor*, *Anchiornis*) (Britt et al., 1998; Forster et al., 1998; Norell et al., 1999; Ostrom, 1969; Sereno et al., 2008; Xu et al., 2009a).

Phylogenetic analysis

The data matrix consists of 1732 informative characters, including 9 characters describing the plumage and has been scored for 130 Operational Taxonomic Units (OTUs) (see supplementary files of Chapter 3). In order to recover the position of *Serikornis*, the data matrix has been analyzed with the TNT software (Goloboff et al., 2008).

One hundred ‘New Technology search’ runs with default settings have been computed. Then the shortest tree islands found were explored by tree-bisection-reconnection algorithm to only hold the shortest trees. Our analysis recovered 96 shortest trees with each a length of 5743 steps. The consensus tree focused on the paraves clade (Fig. A3.6) shows that the scansoriopterygid lineage is placed at the base of the clade. Here, *Xiaotingia* is recovered as a basal member of the Scansoriopterygidae but its position is highly unstable (Foth et al., 2014; Godefroit et al., 2013a; Godefroit et al., 2013b; Xu et al., 2011) and further investigations are required to fix its position. Several taxa (*Pedopenna*, *Aurornis*, *Eosinopteryx* and *Anchiornis*) previously regarded as basal members of Avialae are now placed in a more basal position outside Eumaniraptora. As in numerous studies, Troodontidae and Dromaeosauridae are grouped within the Deinonychosauria, which is the sister-group of Avialae.

Our phylogenetic analysis places *Serikornis* among basal paravians, outside the Avialae-Deinonychosaurian node (Eumaniraptora) (Figs A3.6 and S3.11), as the sister-taxon of *Eosinopteryx*, and closely related to *Aurornis* and *Pedopenna* (Foth et al., 2014; Godefroit et al., 2013a; Hu et al., 2009; Lefèvre et al., 2014). Our analysis also recovers *Anchiornis* as the sister-taxon of Eumaniraptora.

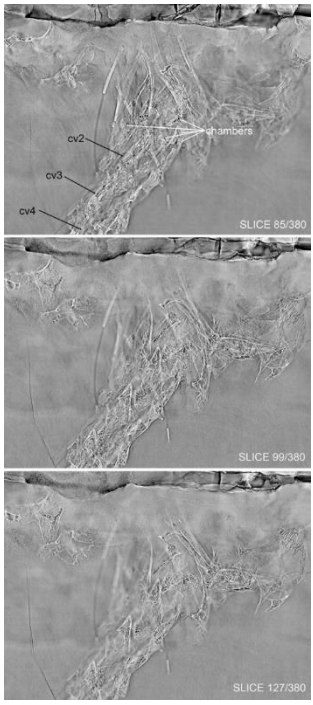

Figure A3.5. Pneumaticity in *Serikornis sungei* by laminography. At least the most proximal portion of the cervical column is highly pneumatized as shown by numerous small chambers revealed under laminography.

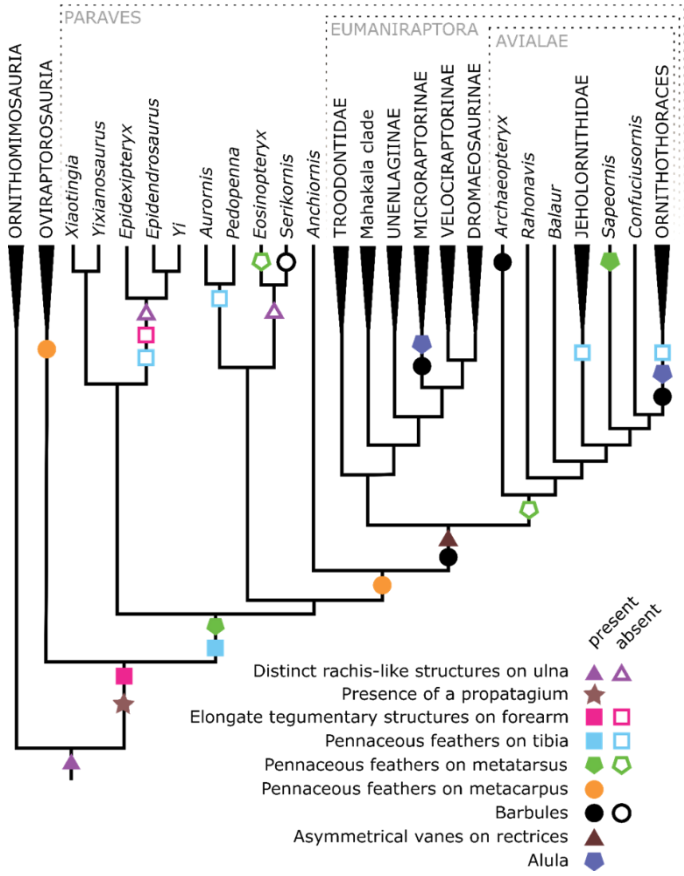

Figure A3.6. Strict consensus tree resulting from the phylogenetic analysis (length = 5743, consistency index = 0.2614, retention index = 0.7386). Major evolutions in the history of birds are mapped on the paraves clade. The complete tree is presented in Supplementary Figure S3.11.

Literature cited

Abramov, B. N. (2011). *Conditions for the formation and ore potential of the fluid-explosive formations of gold deposits in the Eastern Transbaikalian region.* Paper presented at the Doklady Earth Sciences.

Adhyaru, B. B., Akhmedov, N. D., Katritzky, A. R., & Bowers, C. R. (2003). Solid-state cross-polarization magic angle spinning ^{13}C and ^{15}N NMR characterization of *Sepia* melanin, *Sepia* melanin free acid and human hair melanin in comparison with several model compounds. *Magnetic resonance in chemistry, 41*, 466-474. doi:0.1002/mrc.1193

Akulov, N. I., Frolov, A. O., Mashchuk, I. M., & Akulova, V. V. (2015). Jurassic deposits of the Southern part of the Irkutsk sedimentary Basin. *Stratigrafiya Geologicheskaya Korrelyatsiya, 23*(4), 40-63.

Alifanov, V. R., & Saveliev, S. V. (2014). Two new ornithischian dinosaurs (Hypsilophodontia, Ornithopoda) from the Late Jurassic of Russia. *Paleontological Journal, 48*(4), 414-425.

Alifanov, V. R., & Saveliev, S. V. (2015). The most ancient Ornithomimosaur (Theropoda, Dinosauria), with cover imprints from the Upper Jurassic of Russia. *Paleontological Journal, 49*(6), 636.

Allain, R., & Suberbiola, X. P. (2003). Dinosaurs of France. *Comptes Rendus Palevol, 2*(1), 27-44.

Allison, P. A. (1988). Konservat-Lagerstatten: cause and classification. *Paleobiology, 14*(4), 15.

Allison, P. A., & Briggs, D. E. G. (1991). The taphonomy of soft-bodied animals. Pp. 120–140inS. K. Donovan, ed. The processes of fossilization: Columbia University Press, New York.

Allison, P. A., & Briggs, D. E. G. (1993). Exceptional fossil record: Distribution of soft-tissue preservation through the Phanerozoic. *Geology, 21*, 527-532.

Alpert, N. L., Keiser, W. E., & Szymanski, H. A. (1970). *IR: theory and practice of infrared spectroscopy*. New York: Plenum Press.

Anashkina, K. K., Butinm, K. S., Enikeev, F. I., Kineakin, s. V., Krasnov, V. P., Krivenko, V. A., Alekseev, B. I., Pinaeva, T. A., Rutchtein, I. G., Semyonov, V. N., Starukhina, L. N., Chaban, N. N., & Shulika, E. V. (1997). *Geological structure of Chita region. Explanatory note to the geological map at 1:500000 scale, Chita.* Retrieved from Chita:

Andrews, H. N. (1961). *Studies in paleobotany*. New York: Wiley.

Apostolaki, N. E., Rayfield, E. J., & Barrett, P. M. (2015). Osteological and soft-Tissue evidence for pneumatization in the cervical column of the Ootrich (*Struthio camelus*) and observations on the vertebral columns of non-volant, semi-volant and semi-aquatic birds. *PLoS ONE, 10*(12), e0143834.

Arai, K. M., Takahashi, R., Yokote, Y., & Akahane, K. (1983). Amino acid sequence of feather keratin from fowl. *The FEBS Journal, 132*(3), 501-507.

Arai, K. M., Takahashi, R., Yokote, Y., & Akahane, K. (1986). The primary structure of feather keratins from duck (*Anas platyrhynchos*) and pigeon (*Columba*

livia). *Biochimica et Biophysica Acta (BBA)-Protein Structure and Molecular Enzymology*, *873*(1), 6-12.

Armenteros, I., Daley, B., & García, E. (1997). Lacustrine and palustrine facies in the Bembridge Limestone (late Eocene, Hampshire Basin) of the Isle of Wight, southern England. *Palaeogeography, Palaeoclimatology, Palaeoecology*, *128*(1-4), 111-132.

Baas, M., Briggs, D., Van Heemst, J., Kear, A., & De Leeuw, J. (1995). Selective preservation of chitin during the decay of shrimp. *Geochimica et Cosmochimica Acta*, *59*(5), 945-951.

Banerjee, A., Supakar, S., & Banerjee, R. (2014). Melanin from the nitrogen-fixing bacterium Azotobacter chroococcum: a spectroscopic characterization. *PLoS ONE*, *9*(1), e84574.

Barden, H. E., Bergmann, U., Edwards, N. P., Egerton, V. M., Manning, P. L., Perry, S., van Veelen, A., Wogelius, R. A., & van Dongen, B. E. (2014). Bacteria or melanosomes? A geochemical analysis of micro-bodies on a tadpole from the Oligocene Enspel Formation of Germany. *Palaeobiodiversity Palaeoenvironments*, *95*, 33-45.

Barden, H. E., Bergmann, U., Edwards, N. P., Egerton, V. M., Manning, P. L., Perry, S., van Veelen, A., Wogelius, R. A., & van Dongen, B. E. (2015). Bacteria or melanosomes? A geochemical analysis of micro-bodies on a tadpole from the Oligocene Enspel Formation of Germany. *Palaeobiodiversity and Palaeoenvironments*, *95*(1), 33-45.

Barden, H. E., Wogelius, R. A., Li, D., Manning, P. L., Edwards, N. P., & van Dongen, B. E. (2011). Morphological and geochemical evidence of eumelanin preservation in the feathers of the Early Cretaceous bird, *Gansus yumenensis*. *PLoS ONE*, *6*(10), e25494.

Bardunov, L. V. (1984). *Ancient flora on the land [Drevneyshie na sushe]*. Novosibirsk: Nauka.

Barling, N., Martill, D. M., Heads, S. W., & Gallien, F. (2015). High fidelity preservation of fossil insects from the Crato Formation (Lower Cretaceous) of Brazil. *Cretaceous Research*, *52*, 605-622.

Baron, M. G., Norman, D. B., & Barrett, P. M. (2017). A new hypothesis of dinosaur relationships and early dinosaur evolution. *Nature*, *543*(7646), 501-506.

Barone, J. R., Schmidt, W. F., & Liebner, C. F. E. (2005). Thermally processed keratin films. *Journal of Applied Polymer Science*, *97*, 1644-1651. doi:10.1002/app.21901

Barrett, P. M., Butler, R. J., & Knoll, F. (2005). Small-bodied ornithischian dinosaurs from the Middle Jurassic of Sichuan, China. *Journal of Vertebrate Paleontology*, *25*(4), 823-834.

Barrows, C. W. (1981). Roost selection by spotted owls: an adaptation to heat stress. *Condor*, 302-309.

Bartels, T. (2003). Variations in the morphology, distribution, and arrangement of feathers in domesticated birds. *Journal of Experimental Zoology Part B: Molecular and Developmental Evolution*, *298*(1), 91-108.

Barthel, K. (1964). Zur Entstehung der Solnhofener Plattenkalke (unteres Untertithon). *Mitteilungen der Bayerischen Staatssammlung für Paläontologie und Historische Geologie*, *4*, 37-69.

Barthel, K. W., Swinburne, N. H. M., & Morris, S. C. (1990). *Solnhofen*: CUP Archive.

Basiuk, V. A., & Navarro-González, R. (1997). Identification of hexahydroimidazo [1, 2-a] pyrazine-3, 6-diones and hexahydroimidazo [1, 2-a] imidazo [1, 2-d] pyrazine-3, 8-diones, unusual products of silica-catalyzed amino acid thermal condensation and products of their thermal decomposition using coupled high-performance liquid chromatography–particle beam mass spectrometry and gas chromatography–Fourier transform infrared spectroscopy–mass spectrometry. *Journal of Chromatography A, 776*(2), 255-273.

Batten, D., & Stead, D. (2005). Palynofacies analysis and its stratigraphic application. *Applied stratigraphy*, 203-226.

Batten, D. J. (1996). Palynofacies. *Palynology: principles and applications, 3*, 1011-1084.

Baumel, J. J. (1993). *Handbook of avian anatomy: nomina anatomica avium*.

Behrensmeyer, A. K. (1975). *The taphonomy and paleoecology of plio-pleistocene vertebrate assemblages: east of lake Rudolf, Kenya*: Harvard Univ.

Behrensmeyer, A. K. (2007). Bonebeds through time. *Bonebeds: genesis, analysis, and paleobiological significance*, 65-101.

Bendit, E. (1966). Infrared absorption spectrum of keratin. I. Spectra of α-, β-, and supercontracted keratin. *Biopolymers, 4*(5), 539-559.

Benson, R. B., Rich, T. H., Vickers-Rich, P., & Hall, M. (2012). Theropod fauna from southern Australia indicates high polar diversity and climate-driven dinosaur provinciality. *PLoS ONE, 7*(5), e37122.

Benton, M. J. (2004). Origin and relationships of Dinosauria. *The Dinosauria, 2*, 7-19.

Benton, M. J., Zhonghe, Z., Orr, P. J., Fucheng, Z., & Kearns, S. L. (2008). The remarkable fossils from the Early Cretaceous Jehol Biota of China and how they have changed our knowledge of Mesozoic life. *Proceedings of the Geologists' Association, 119*, 209-229.

Bergmann, U., Manning, P. L., & Wogelius, R. A. (2012). Chemical mapping of paleontological and archeological artifacts with synchrotron X-rays. *Annual Review of Analytical Chemistry, 5*, 361-389.

Bergmann, U., Morton, R., Manning, P., Sellers, W., Farrar, S., Huntley, K., Wogelius, R., & Larson, P. (2010). *Archaeopteryx* feathers and bone chemistry fully revealed via synchrotron imaging. *Proceedings of the National Academy of Sciences, 107*(20), 9060-9065.

Berner, R. A. (1984). Sedimentary pyrite formation: an update. *Geochimica et Cosmochimica Acta, 48*(4), 605-615.

Bertran, P., & Texier, J.-P. (1999). Facies and microfacies of slope deposits. *CATENA, 35*(2), 99-121. doi:https://doi.org/10.1016/S0341-8162(98)00096-4

Bertrand, L., Doucet, J., Dumas, P., Simionovici, A., Tsoucaris, G., & Walter, P. (2003). Microbeam synchrotron imaging of hairs from ancient Egyptian mummies. *Journal of synchrotron radiation, 10*(5), 387-392.

Bertsch, A., & Coello, N. (2005). A biotechnological process for treatment and recycling poultry feathers as a feed ingredient. *Bioresource Technology, 96*, 1703-1708. doi:10.1016/j.biortech.2004.12.026

Berzina, A. P., Berzina, A. N., Gimon, V. O., Krymskii, R. S., Larionov, A. N., Nikolaeva, I. V., & Serov, P. A. (2013). The Shakhtama porphyry Mo ore-magmatic system (eastern Transbaikalia): age, sources, and genetic features. *Russian Geology and Geophysics, 54*(6), 587-605.

Biron, K., Derenne, S., Robert, F., & Rouzaud, J. N. (2015). Toward an experimental synthesis of the chondritic insoluble organic matter. *Meteoritics & Planetary Science, 50*(8), 1408-1422.

Blanco, A., Bolaños-Sánchez, U., Lizárraga-Mendiola, L., Hernández-Ávila, J., Ángeles-Trigueros, S., Ambrocio, P., & González-Sandoval, M. (2013). *Microscopic evidences of replacement of iron sulfide by iron oxide in macro fossils: a useful tool for the search of life in Mars?* Paper presented at the Lunar and Planetary Science Conference.

Blasco, R., Rosell, J., Peris, J. F., Cáceres, I., & Vergès, J. M. (2008). A new element of trampling: an experimental application on the Level XII faunal record of Bolomor Cave (Valencia, Spain). *Journal of Archaeological Science, 35*(6), 1605-1618.

Boles, W. E. (1997). Hindlimb proportions and locomotion of Emuarius gidju (Patterson & Rich, 1987)(Aves, Casuariidae). *MEMOIRS-QUEENSLAND MUSEUM, 41*, 235-240.

Bonde, N., & Christiansen, P. (2003). The detailed anatomy of *Rhamphorhynchus*: axial pneumaticity and its implications. *Geological Society, London, Special Publications, 217*(1), 217-232.

Bortolotti, G. R. (2010). Flaws and pitfalls in the chemical analysis of feathers: bad news–good news for avian chemoecology and toxicology. *Ecological Applications, 20*(6), 1766-1774.

Boyd, C. A. (2015). The systematic relationships and biogeographic history of ornithischian dinosaurs. *PeerJ, 3*, e1523.

Bramwell, C. D., & Whitfield, G. (1974). Biomechanics of *Pteranodon*. *Philosophical Transactions of the Royal Society of London B: Biological Sciences, 267*(890), 503-581.

Brierley, G. J., Ferguson, R. J., & Woolfe, K. J. (1997). What is a fluvial levee? *Sedimentary Geology, 114*(1-4), 1-9.

Briggs, D., Kear, A., Martill, D., & Wilby, P. (1993). Phosphatization of soft-tissue in experiments and fossils. *Journal of the Geological Society, 150*(6), 1035-1038.

Briggs, D. E. (2003). The role of decay and mineralization in the preservation of soft-bodied fossils. *Annual Review of Earth and Planetary Sciences, 31*(1), 275-301.

Briggs, D. E., & Wilby, P. R. (1996). The role of the calcium carbonate-calcium phosphate switch in the mineralization of soft-bodied fossils. *Journal of the Geological Society, 153*(5), 665-668.

Briggs, D. E., Wilby, P. R., Perez-Moreno, B. P., Sanz, J. L., & Fregenal-Martinez, M. (1997). The mineralization of dinosaur soft tissue in the Lower Cretaceous of Las Hoyas, Spain. *Journal of the Geological Society, 154*(4), 587-588.

Briggs, D. E. G., Bottrell, S. H., & Raiswell, R. (1991). Pyritization of soft-bodied fossils: Beecher's trilobite bed, Upper Ordovician, New York State. *Geology, 19*(12), 1221-1224.

Briggs, D. E. G., Kear, A. J., Baas, M., Leeuw, J. W., & Rigby, S. (1995). Decay and composition of the hemichordate *Rhabdopleura*: implications for the taphonomy of graptolites. *Lethaia, 28*(1), 15-23.

Britt, B. B. (1993). *Pneumatic postcranial bones in dinosaurs and other archosaurs.* Geology and Geophysics, University of Calgary.

Britt, B. B., Makovicky, P. J., Gauthier, J., & Bonde, N. (1998). Postcranial pneumatization in Archaeopteryx. *Nature, 395*(6700), 374.

Brown, R. E., Baumel, J. J., & Klemm, R. D. (1994). Anatomy of the propatagium: the great horned owl (Bubo virginianus). *Journal of morphology, 219*(2), 205-224.

Brown, S. A., Scott, A. C., Glasspool, I. J., & Collinson, M. E. (2012). Cretaceous wildfires and their impact on the Earth system. *Cretaceous Research, 36*, 162-190.

Bugdaeva, E. V., Volynets, E. B., Golozubov, V. V., Markevich, V. S., & Amel'chenko, G. L. (2006). Flora i geologicheskie sobytiya serediny melovogo perioda (Alchanskii bassein, Primor'e). *Flora and Geological Events of the Mid Cretaceous Time (Alchan River Basin, Pri morye)), Vladivostok: Dalnauka*.

Burdelnaya, N., Bushnev, D., Mokeev, M., & Dobrodumov, A. (2014). Experimental study of kerogen maturation by solid-state 13C NMR spectroscopy. *Fuel, 118*, 308-315. doi:http://dx.doi.org/10.1016/j.fuel.2013.11.003

Butler, R. J., Barrett, P. M., & Gower, D. J. (2009). Postcranial skeletal pneumaticity and air-sacs in the earliest pterosaurs. *Biology Letters, 5*(4), 557-560.

Butler, R. J., Upchurch, P., & Norman, D. B. (2008). The phylogeny of the ornithischian dinosaurs. *Journal of Systematic Palaeontology, 6*(1), 1-40.

Butterfield, N. J., Balthasar, U., & Wilson, L. A. (2007). Fossil diagenesis in the Burgess Shale. *Palaeontology, 50*(3), 537-543.

Campbell, J., Boyd, N., Grassi, N., Bonnick, P., & Maxwell, J. (2010). The Guelph PIXE software package IV. *Nuclear Instruments and Methods in Physics Research Section B: Beam Interactions with Materials and Atoms, 268*(20), 3356-3363.

Carney, R. M., Vinther, J., Shawkey, M. D., D'alba, L., & Ackermann, J. (2012). New evidence on the colour and nature of the isolated *Archaeopteryx* feather. *Nature Communications, 3*, 637.

Carrillo, F., Macanás, J., Colom, X., Cañavate, J., Molins, G., Álvarez, M., & Garrido, N. (2012). *Use of chicken feathers waste for the fabrication of composite materials.* Paper presented at the 15th European conference on composite materials, Venice.

Centeno, S. A., & Shamir, J. (2008). Surface enhanced Raman scattering (SERS) and FTIR characterization of the sepia melanin pigment used in works of art. *Journal of Molecular Structure, 873*(1), 149-159.

Cesarini, J. P. (1996). Melanins and their possible roles through biological evolution. *Advances in space research, 18*(12), 35-40.

Chabiron, A., Cuney, M., & Poty, B. (2003). Possible uranium sources for the largest uranium district associated with volcanism: the Streltsovka caldera (Transbaikalia, Russia). *Mineralium Deposita, 38*(2), 127-140.

Chang, S.-c., Zhang, H., Renne, P. R., & Fang, Y. (2009). High-precision $^{40}Ar/^{39}Ar$ age constraints on the basal Lanqi Formation and its implications for the

origin of angiosperm plants. *Earth and Planetary Science Letters, 279*(3), 212-221.

Chedekel, M. R., Smith, S. K., Post, P. W., Pokora, A., & Vessell, D. L. (1978). Photodestruction of pheomelanin: role of oxygen. *Proceedings of the National Academy of Sciences, 75*(11), 5395-5399.

Chiappe, L. M., Ji, S.-A., Ji, Q., & Norell, M. A. (1999). Anatomy and systematics of the Confuciusornithidae (Theropoda, Aves) from the late Mesozoic of northeastern China. Bulletin of the AMNH; no. 242.

Chinsamy, A., Chiappe, L. M., Marugán-Lobón, J., Chunling, G., & Fengjiao, Z. (2013). Gender identification of the Mesozoic bird Confuciusornis sanctus. *Nature Communications, 4*, 1381.

Choi, S.-S., Kim, M.-C., & Kim, Y.-K. (2013). Formation of methoxybenzenes from cellulose in the presence of tetramethylammonium hydroxide by pyrolysis. *Bulletin of the Korean Chemical Society, 34*(2), 649-652.

Christiansen, P. (1999). Long bone scaling and limb posture in non-avian theropods: evidence for differential allometry. *Journal of Vertebrate Paleontology, 19*(4), 666-680.

Christiansen, P., & Bonde, N. (2004). Body plumage in *Archaeopteryx*: a review and new evidence from the Berlin specimen. *C. R. Palevol, 3*, 20. doi:10.1016/j.crpv.2003.12.001

Chu, Z., He, H., Ramezani, J., Bowring, S. A., Hu, D., Zhang, L., Zheng, S., Wang, X., Zhou, Z., & Deng, C. (2016). High-precision U-Pb geochronology of the Jurassic Yanliao Biota from Jianchang (western Liaoning Province, China): Age constraints on the rise of feathered dinosaurs and eutherian mammals. *Geochemistry, Geophysics, Geosystems, 17*(10), 3983-3992.

Cincotta, A., Yans, J., Godefroit, P., Garcia, G., Dejax, J., Benammi, M., Amico, S., & Valentin, X. (2015). Integrated paleoenvironmental reconstruction and taphonomy of a unique Upper Cretaceous vertebrate-bearing locality (Velaux, southeastern France). *PLoS ONE, 10*(8), e0134231.

Claessens, L. P., O'Connor, P. M., & Unwin, D. M. (2009). Respiratory evolution facilitated the origin of pterosaur flight and aerial gigantism. *PLoS ONE, 4*(2), e4497.

Clark, J., Beerbower, J. R., & Kietzke, K. K. (1967). *Oligocene sedimentation, stratigraphy, paleoecology and paleoclimatology: in the Big Badlands of South Dakota* (Vol. 5): Field Museum of Natural History.

Clarke, J. A., Ksepka, D. T., Salas-Gismondi, R., Altamirano, A. J., Shawkey, M. D., D'Alba, L., Vinther, J., DeVries, T. J., & Baby, P. (2010). Fossil evidence for evolution of the shape and color of penguin feathers. *Science, 330*(6006), 954-957.

Cojan, I., Renard, M., & Emmanuel, L. (2003). Palaeoenvironmental reconstruction of dinosaur nesting sites based on a geochemical approach to eggshells and associated palaeosols (Maastrichtian, Provence Basin, France). *Palaeogeography, Palaeoclimatology, Palaeoecology, 191*(2), 111-138.

Colleary, C., Dolocan, A., Gardner, J., Singh, S., Wuttke, M., Rabenstein, R., Habersetzer, J., Schaal, S., Feseha, M., & Clemens, M. (2015). Chemical, experimental, and morphological evidence for diagenetically altered melanin in exceptionally preserved fossils. *Proceedings of the National Academy of Sciences, 112*(41), 12592-12597.

Cope, E. D. (1877). *On a gigantic saurian from the Dakota epoch of Colorado*.

Cornet, B., Traverse, A., & McDonald, N. G. (1973). Fossil spores, pollen, and fishes from Connecticut indicate Early Jurassic age for part of the Newark Group. *Science, 182*(4118), 1243-1247.

Csiki, Z., Grigorescu, D., Codrea, V., & Therrien, F. (2010). Taphonomic modes in the Maastrichtian continental deposits of the Haţeg Basin, Romania—Palaeoecological and palaeobiological inferences. *Palaeogeography, Palaeoclimatology, Palaeoecology, 293*(3), 375-390.

Cubo, J., & Casinos, A. (2000). Incidence and mechanical significance of pneumatization in the long bones of birds. *Zoological Journal of the Linnean Society, 130*(4), 499-510.

Cuny, G. G. R. (2012). Freshwater hybodont sharks in Early Cretaceous ecosystems: a review *Bernissart dinosaurs and Early Cretaceous terrestrial ecosystems* (pp. 518-529): Indiana University Press.

Currey, J. D., & Alexander, R. (1985). The thickness of the walls of tubular bones. *Journal of Zoology, 206*(4), 453-468.

Currie, P. J. (1987). Bird-like characteristics of the jaws and teeth of troodontid theropods (Dinosauria, Saurischia). *Journal of Vertebrate Paleontology, 7*(1), 72-81.

Currie, P. J. (2003). Allometric growth in tyrannosaurids (Dinosauria: Theropoda) from the upper Cretaceous of North America and Asia. *Canadian Journal of Earth Sciences, 40*(4), 651-665.

Currie, P. J., & Zhiming, D. (2001). New information on Cretaceous troodontids (Dinosauria, Theropoda) from the People's Republic of China. *Canadian Journal of Earth Sciences, 38*(12), 1753-1766.

D'Alba, L., Van Hemert, C., Spencer, K. A., Heidinger, B. J., Gill, L., Evans, N. P., Monaghan, P., Handel, C. M., & Shawkey, M. D. (2014). Melanin-based color of plumage: role of condition and of feathers' microstructure: The Society for Integrative and Comparative Biology.

Davis, J. A. (1984). Complexation of trace metals by adsorbed natural organic matter. *Geochimica et Cosmochimica Acta, 48*(4), 679-691. doi:https://doi.org/10.1016/0016-7037(84)90095-4

Davis, P. G., & Briggs, D. E. (1995). Fossilization of feathers. *Geology, 23*(9), 783-786.

de Lapparent de Broin, F., & Murelaga, X. (1996). Une nouvelle faune de chéloniens dans le Crétacé supérieur européen. *Comptes rendus de l'Académie des sciences. Série 2. Sciences de la terre et des planètes, 323*(8), 729-735.

De Leeuw, J. W., & Largeau, C. (1993). A review of macromolecular organic compounds that comprise living organisms and their role in kerogen, coal, and petroleum formation *Organic Geochemistry* (pp. 23-72): Springer.

Delevoye, C., Giordano, F., Marks, M. S., & Raposo, G. (2011). Biogenesis of melanosomes. *In Melanins and melanosomes: Biosynthesis, structure, physiological and pathological functions*, 247-294.

Delfino, M., Codrea, V., Folie, A., Dica, P., Godefroit, P., & Smith, T. (2008). A complete skull of Allodaposuchus precedens Nopcsa, 1928 (Eusuchia) and a reassessment of the morphology of the taxon based on the Romanian remains. *Journal of Vertebrate Paleontology, 28*(1), 111-122.

Delvaux, D., Moeys, R., Stapel, G., Melnikov, A., & Ermikov, V. (1995). Palaeostress reconstructions and geodynamics of the Baikal region, Central Asia, Part I. Palaeozoic and Mesozoic pre-rift evolution. *Tectonophysics, 252*(1-4), 61-101.

Deng, S., & Lu, Y. (2006). The Mesozoic Dicksoniaceous ferns: characteristics, distribution, origin and evolutionary trends. *Glob Plant Lett, 1*, 9-29.

Dennis, L. W., Maciel, G. E., Hatcher, P. G., & Simoneit, B. R. (1982). 13 C Nuclear magnetic resonance studies of kerogen from Cretaceous black shales thermally altered by basaltic intrusions and laboratory simulations. *Geochimica et Cosmochimica Acta, 46*(6), 901-907.

Desmond, A. J. (1979). Designing the dinosaur: Richard Owen's response to Robert Edmond Grant. *Isis, 70*(2), 224-234.

Dhouailly, D., Godefroit, P., Martin, T., Nonchev, S., Caraguel, F., & Oftedal, O. (2017). Getting to the root of scales, feather and hair: as deep as odontodes? *Experimental Dermatology*.

Dickinson, W. R. (1970). Relations of andesites, granites, and derivative sandstones to arc-Trench tectonics. *Reviews of Geophysics, 8*(4), 813-860.

do Nascimento, D. R., Sawakuchi, A. O., Guedes, C. C., Giannini, P. C., Grohmann, C. H., & Ferreira, M. P. (2015). Provenance of sands from the confluence of the Amazon and Madeira rivers based on detrital heavy minerals and luminescence of quartz and feldspar. *Sedimentary Geology, 316*, 1-12.

Domínguez-Rodrigo, M., Uribelarrea, D., Santonja, M., Bunn, H., García-Pérez, A., Pérez-González, A., Panera, J., Rubio-Jara, S., Mabulla, A., & Baquedano, E. (2014). Autochthonous anisotropy of archaeological materials by the action of water: experimental and archaeological reassessment of the orientation patterns at the Olduvai sites. *Journal of Archaeological Science, 41*, 44-68.

Donskaya, T. V., Gladkochub, D. P., Mazukabzov, A. M., & Ivanov, A. V. (2013). Late Paleozoic – Mesozoic subduction-related magmatism at the southern margin of the Siberian continent and the 150 million - year history of the Mongol-Okhotsk Ocean. *Journal of Asian Earth Sciences, 62*, 79-97.

Dott, R. H. (1964). Wacke, graywacke and matrix: what approach to immature sandstone classification? *Journal of Sedimentary Research, 34*(3), 625-632.

Dove, C. J., Rijke, A. M., Wang, X., & Andrews, L. S. (2007). Infrared analysis of contour feathers. The conservation of body heat radiation in birds. *Journal of Thermal Biology, 32*, 42-46.

Duan, Y., Zheng, S.-L., Hu, D.-Y., Zhang, L.-J., & Wang, W.-L. (2009). Preliminary report on Middle Jurassic strata and fossils from Linglongta area of Jianchang, Liaoning. *Global Geology, 28*(2), 143-147.

Duff, G. A., Roberts, J. E., & Foster, N. (1988). Analysis of the structure of synthetic and natural melanins by solid-phase NMR. *Biochemistry, 27*, 7112-7116.

Duncker, H.-R. (1971). The lung air sac system of birds. *Advances in Anatomy, Embryology, and Cell Biology, 45*, 1-171.

Dutta, S., Hartkopf-Fröder, C., Mann, U., Wilkes, H., Brocke, R., & Bertram, N. (2010). Macromolecular composition of Palaeozoic scolecodonts: insights into the molecular taphonomy of zoomorphs. *Lethaia, 43*(3), 334-343.

Dymov, A., Zhangurov, E., & Hagedorn, F. (2015). Soil organic matter composition along altitudinal gradients in permafrost affected soils of the Subpolar Ural Mountains. *CATENA*, *131*, 140-148.

Eaton, G. F. (1910). Osteology of Pteranodon. Connecticut Acad. Arts and Sciences, Mem: Yale University Press.

Eberth, D., & Getty, M. (2005). Ceratopsian bonebeds: occurrence, origins, and significance,. 501-536 In PJ Currie and EB Koppelhus (eds.) Dinosaur Provincial Park: a spectacular ancient ecosystem revealed: Bloomington: Indiana University Press.

Eberth, D. A., & Currie, P. J. (2005). Vertebrate taphonomy and taphonomic modes. *Dinosaur Provincial Park: a spectacular ancient ecosystem revealed. Edited by PJ Currie and EB Koppelhus. Indiana University Press, Bloomington, IN*, 453-477.

Eberth, D. A., Rogers, R. R., Fiorillo, A. R., Rogers, R. R., Eberth, D. A., & Fiorillo, A. J. (2007). A practical approach to the study of bonebeds. *Bonebeds: genesis, analysis, and paleobiological significance*, 265-331.

Edwards, N., Barden, H., Van Dongen, B., Manning, P., Larson, P., Bergmann, U., Sellers, W., & Wogelius, R. (2011). Infrared mapping resolves soft tissue preservation in 50 million year-old reptile skin. *Proceedings of the Royal Society of London B: Biological Sciences*, *278*(1722), 3209-3218.

Edwards, N. P., Manning, P. L., & Wogelius, R. A. (2014). Pigments through time. *Pigment cell & melanoma research*, *27*(5), 684-685.

Egerton, V. M., Wogelius, R. A., Norell, M. A., Edwards, N. P., Sellers, W. I., Bergmann, U., Sokaras, D., Alonso-Mori, R., Ignatyev, K., & van Veelen, A. (2015). The mapping and differentiation of biological and environmental elemental signatures in the fossil remains of a 50 million year old bird. *Journal of Analytical Atomic Spectrometry*, *30*(3), 627-634.

Elzanowski, A. (2002). Archaeopterygidae (Upper Jurassic of Germany). *Mesozoic birds: above the heads of dinosaurs*, 129-159.

Ercegovac, M. D. (2010). The age of the Dinaride Ophiolite Belt: Derived olistostrome melange at the northern slope of Moračka Kapa (Montenegro). *Geoloski anali Balkanskoga poluostrva*(71), 37-51.

Eusterhues, K., Rumpel, C., Kleber, M., & Kögel-Knabner, I. (2003). Stabilisation of soil organic matter by interactions with minerals as revealed by mineral dissolution and oxidative degradation. *Organic Geochemistry*, *34*(12), 1591-1600.

Faith, J. T., & Behrensmeyer, A. K. (2006). Changing patterns of carnivore modification in a landscape bone assemblage, Amboseli Park, Kenya. *Journal of Archaeological Science*, *33*(12), 1718-1733.

Fajardo, R., Hernandez, E., & O'Connor, P. (2007). Postcranial skeletal pneumaticity: a case study in the use of quantitative microCT to assess vertebral structure in birds. *Journal of anatomy*, *211*(1), 138-147.

Farrell, Ú. C., Briggs, D. E., Hammarlund, E. U., Sperling, E. A., & Gaines, R. R. (2013a). Paleoredox and pyritization of soft-bodied fossils in the Ordovician Frankfort Shale of New York. *American Journal of Science*, *313*(5), 452-489.

Farrell, Ú. C., Briggs, D. E. G., Hammarlund, E. U., Sperling, E. A., & Gaines, R. R. (2013b). Paleoredox and pyritization of soft-bodied fossils in the Ordovician

Frankfort Shale of New York. *American Journal of Science, 313*(5), 452-489.

Fastovsky, D., Clark, J., Strater, N., Montellano, M., & Hopson, J. (1995). Depositional environments of a Middle Jurassic terrestrial vertebrate assemblage, Huizachal Canyon, Mexico. *Journal of Vertebrate Paleontology, 15*(3), 561-575.

Fedo, C. M., Nesbitt, H. W., & Young, G. M. (1995). Unraveling the effects of potassium metasomatism in sedimentary rocks and paleosols, with implications for paleoweathering conditions and provenance. *Geology, 23*(10), 921-924.

Feduccia, A. (1993). Evidence from claw geometry indicating arboreal habits of *Archaeopteryx*. *SCIENCE-NEW YORK THEN WASHINGTON-, 259*, 790-790.

Feduccia, A., & Czerkas, S. A. (2015). Testing the neoflightless hypothesis: propatagium reveals flying ancestry of oviraptorosaurs. *Journal of Ornithology, 156*(4), 1067-1074.

Feo, T. J., Field, D. J., & Prum, R. O. (2015). Barb geometry of asymmetrical feathers reveals a transitional morphology in the evolution of avian flight. *Proceedings of the Royal Society of London B: Biological Sciences, 282*(1803), 20142864.

Filatoff, J. (1975). Jurassic palynology of the Perth Basin, western Australia. *Palaeontographica Abteilung B*, 1-113.

Fiorillo, A. R. (1988). Taphonomy of Hazard Homestead Quarry (Ogallala Group), Hitchcock County, Nebraska. *Rocky Mountain Geology, 26*(2), 57-97.

Fiorillo, A. R. (1991a). Prey bone utilization by predatory dinosaurs. *Palaeogeography, Palaeoclimatology, Palaeoecology, 88*(3-4), 157-166.

Fiorillo, A. R. (1991b). Taphonomy and depositional setting of Careless Creek Quarry (Judith River Formation), Wheatland County, Montana, USA. *Palaeogeography, Palaeoclimatology, Palaeoecology, 81*(3-4), 281-311.

Floyd, P., Leveridge, B., Franke, W., Shail, R., & Dörr, W. (1990). Provenance and depositional environment of Rhenohercynian synorogenic greywackes from the Giessen Nappe, Germany. *Geologische Rundschau, 79*(3), 611-626.

Forster, C. A., Sampson, S. D., Chiappe, L. M., & Krause, D. W. (1998). The theropod ancestry of birds: new evidence from the Late Cretaceous of Madagascar. *Science, 279*(5358), 1915-1919.

Foth, C. (2012). On the identification of feather structures in stem-line representatives of birds: evidence from fossils and actuopalaeontology. *Paläontologische Zeitschrift, 86*(1), 91-102.

Foth, C., Tischlinger, H., & Rauhut, O. W. (2014). New specimen of *Archaeopteryx* provides insights into the evolution of pennaceous feathers. *Nature, 511*(7507), 79-82.

Fraser, R., MacRae, T., Parry, D., & Suzuki, E. (1971). The structure of feather keratin. *Polymer, 12*(1), 35-56.

Fraser, R. D. B., & MacRae, T. P. (2012). *Conformation in fibrous proteins and related synthetic polypeptides*: Elsevier.

Fraser, R. D. B., MacRae, T. P., & Rogers, G. E. (1972). *Keratins: their composition, structure, and biosynthesis*. Springfield, U.S.: Thomas.

Fraser, R. D. B., & Parry, D. A. D. (1996). The molecular structure of reptilian keratin. *International Journal of Biological Macromolecules, 19*(3), 207-211.

Gabbott, S., Norry, M., Aldridge, R., & Theron, J. (2001). Preservation of fossils in clay minerals; a unique example from the Upper Ordovician Soom Shale, South Africa. *Proceedings of the Yorkshire Geological Society, 53*(3), 237-244.

Gabbott, S. E., Xian-Guang, H., Norry, M. J., & Siveter, D. J. (2004). Preservation of Early Cambrian animals of the Chengjiang biota. *Geology, 32*(10), 901-904.

Galletti, G. C., & Mazzeo, R. (1993). Pyrolysis/gas chromatography/mass spectrometry and Fourier-transform infrared spectroscopy of amber. *Rapid communications in mass spectrometry, 7*(7), 646-650.

Gallois, N., Templier, J., & Derenne, S. (2007). Pyrolysis-gas chromatography-mass spectrometry of the 20 protein amino acids in the presence of TMAH. *Journal of Analytical and Applied Pyrolysis, 80*, 216-230. doi:10.1016/j.jaap.2007.02.010

Gao, C., Morschhauser, E. M., Varricchio, D. J., Liu, J., & Zhao, B. (2012). A second soundly sleeping dragon: new anatomical details of the Chinese troodontid *Mei long* with implications for phylogeny and taphonomy. *PLoS ONE, 7*(9), e45203.

García, B., Mogollón, J. L., López, L., Rojas, A., & Bifano, C. (1994). Humic and fulvic acid characterization in sediments from a contaminated tropical river. *Chemical Geology, 118*(1), 271-287. doi:http://dx.doi.org/10.1016/0009-2541(94)90181-3

Garcia, G., Amico, S., Fournier, F., Thouand, E., & Valentin, X. (2010). A new titanosaur genus (Dinosauria, Sauropoda) from the Late Cretaceous of southern France and its paleobiogeographic implications. *Bulletin de la Société géologique de France, 181*(3), 269-277.

Garcia, G., & Vianey-Liaud, M. (2001). Dinosaur eggshells as biochronological markers in Upper Cretaceous continental deposits. *Palaeogeography, Palaeoclimatology, Palaeoecology, 169*(1), 153-164.

Gardinier, A., Derenne, S., Robert, F., Behar, F., Largeau, C., & Maquet, J. (2000). Solid state CP/MAS 13 C NMR of the insoluble organic matter of the Orgueil and Murchison meteorites: quantitative study. *Earth and Planetary Science Letters, 184*(1), 9-21.

Gatesy, S. M. (1991). Hind limb scaling in birds and other theropods: implications for terrestrial locomotion. *Journal of morphology, 209*(1), 83-96.

Ghosh, P., Sarkar, S., & Maulik, P. (2006). Sedimentology of a muddy alluvial deposit: Triassic Denwa Formation, India. *Sedimentary Geology, 191*(1), 3-36.

Gilkes, R., & Suddhiprakarn, A. (1979). Biotite alteration in deeply weathered granite. I. Morphological, mineralogical, and chemical properties. *Clays and Clay Minerals, 27*(5), 349-360.

Giraldo, L., & Moreno-Piraján, J. C. (2013). Exploring the use of rachis of chicken feathers for hydrogen storage. *Journal of Analytical and Applied Pyrolysis, 104*, 243-248.

Glass, K., Ito, S., Wilby, P. R., Sota, T., Nakamura, A., Bowers, C. R., Miller, K. E., Dutta, S., Summons, R. E., & Briggs, D. E. (2013). Impact of diagenesis and

maturation on the survival of eumelanin in the fossil record. *Organic Geochemistry, 64*, 29-37.

Glass, K., Ito, S., Wilby, P. R., Sota, T., Nakamura, A., Bowers, C. R., Vinther, J., Dutta, S., Summers, R., Briggs, D. E. G., Wakamatsu, K., & Simon, J. D. (2012a). Direct chemical evidence for eumelanin pigment from the Jurassic period. *PNAS, 109*(26), 10218-10223.

Glass, K., Ito, S., Wilby, P. R., Sota, T., Nakamura, A., Bowers, C. R., Vinther, J., Dutta, S., Summons, R., & Briggs, D. E. (2012b). Direct chemical evidence for eumelanin pigment from the Jurassic period. *Proceedings of the National Academy of Sciences, 109*(26), 10218-10223.

Glassford, S. E., Byrne, B., & Kazarian, S. G. (2013). Recent applications of ATR FTIR spectroscopy and imaging to proteins. *Biochimica et Biophysica Acta (BBA)-Proteins and Proteomics, 1834*(12), 2849-2858.

Glob, P. V. (1969). *The bog people: the Iron Age man preserved*. Ithaca, N.Y.: Cornell University Press.

Goddart, D. R., & Michaelis, L. (1934). A study on keratin. *Journal of Biological Chemistry, 106*, 605-614.

Godefroit, P., Cau, A., Dong-Yu, H., Escuillié, F., Wenhao, W., & Dyke, G. (2013a). A Jurassic avialan dinosaur from China resolves the early phylogenetic history of birds. *Nature, 498*(7454), 359-362.

Godefroit, P., Demuynck, H., Dyke, G., Hu, D., Escuillié, F., & Claeys, P. (2013b). Reduced plumage and flight ability of a new Jurassic paravian theropod from China. *Nature Communications, 4*, 1394.

Godefroit, P., Sinitsa, S. M., Dhouailly, D., Bolotsky, Y. L., Sizov, A. V., McNamara, M. E., Benton, M. J., & Spagna, P. (2014). A Jurassic ornithischian dinosaur from Siberia with both feathers and scales. *Science, 345*, 6.

Goloboff, P. A., Farris, J. S., & Nixon, K. C. (2008). TNT, a free program for phylogenetic analysis. *Cladistics, 24*(5), 774-786.

Gondrom, S., Zhou, J., Maisl, M., Reiter, H., Kröning, M., & Arnold, W. (1999). X-ray computed laminography: an approach of computed tomography for applications with limited access. *Nuclear engineering and design, 190*(1), 141-147.

Gradstein, F., Ogg, J., & Smith, A. (2004). *A geologic time scale*. Cambridge: Cambridge University Press.

Gradstein, F. M., Ogg, J. G., Schmitz, M., & Ogg, G. (2012). *The geologic time scale 2012*: Elsevier.

Gregg, K., & Rogers, G. E. (1986). Feather keratin: composition, structure and biogenesis. In M. A. G. Bereiter-Hahn J., Richards K.S. (Ed.), (Vol. 2, pp. 666-694): Springer Berlin Heidelberg.

Gueriau, P., Bernard, S., & Bertrand, L. (2016). Advanced synchrotron characterization of paleontological specimens. *Elements, 12*(1), 45-50.

Gueriau, P., & Bertrand, L. (2015). Deciphering exceptional preservation of fossils through trace elemental imaging. *Microscopy Today, 23*(3), 2-6.

Guggenberger, G., Zech, W., Haumaier, L., & Christensen, B. T. (1995). Land-use effects on the composition of organic matter in particle-size separates of soils: II. CPMAS and solution 13C NMR analysis. *European Journal of Soil Science, 46*(1), 147-158.

Gupta, N. S., Cambra-Moo, O., Briggs, D. E., Love, G. D., Fregenal-Martinez, M. A., & Summons, R. E. (2008). Molecular taphonomy of macrofossils from the Cretaceous Las Hoyas Formation, Spain. *Cretaceous Research, 29*(1), 1-8.

Gupta, N. S., Cody, G. D., Tetlie, O. E., Briggs, D. E., & Summons, R. E. (2009). Rapid incorporation of lipids into macromolecules during experimental decay of invertebrates: Initiation of geopolymer formation. *Organic Geochemistry, 40*(5), 589-594.

Gupta, N. S., Michels, R., Briggs, D. E., Collinson, M. E., Evershed, R. P., & Pancost, R. D. (2007a). Experimental evidence for the formation of geomacromolecules from plant leaf lipids. *Organic Geochemistry, 38*(1), 28-36.

Gupta, N. S., Tetlie, O. E., Briggs, D. E., & Pancost, R. D. (2007b). The fossilization of eurypterids: a result of molecular transformation. *Palaios, 22*(4), 439-447.

Gurbich, A. (2016). SigmaCalc recent development and present status of the evaluated cross-sections for IBA. *Nuclear Instruments and Methods in Physics Research Section B: Beam Interactions with Materials and Atoms, 371*, 27-32.

Gutiérrez-Marco, J. C., García-Bellido, D. C., Rábano, I., & Sá, A. A. (2017). Digestive and appendicular soft-parts, with behavioural implications, in a large Ordovician trilobite from the Fezouata Lagerstätte, Morocco. *Scientific Reports, 7*, 39728.

Guyonnet-Benaize, C., Lamarche, J., Masse, J.-P., Villeneuve, M., & Viseur, S. (2010). 3D structural modelling of small-deformations in poly-phase faults pattern. Application to the Mid-Cretaceous Durance uplift, Provence (SE France). *Journal of Geodynamics, 50*(2), 81-93.

Han, G., Chiappe, L. M., Ji, S.-A., Habib, M., Turner, A. H., Chinsamy, A., Liu, X., & Han, L. (2014). A new raptorial dinosaur with exceptionally long feathering provides insights into dromaeosaurid flight performance. *Nature Communications, 5*, 4382.

Harms, F. (2002). Steine erzählen Geschichte (n): Ursache für die Entstehung des Messel-Sees gefunden. *Natur und Museum, 132*(1), 1-4.

Harnois, L. (1988). The CIW index: a new chemical index of weathering. *Sedimentary Geology, 55*(3-4), 319-322.

Harrap, B. S., & Woods, E. F. (1964). Soluble derivatives of feather keratin. 1. Isolation, fractionation and amino acid composition. *Biochemical journal, 92*(1), 8.

Harris, T. M. (1961). The Yorkshire Jurassic Flora. I. thallophyta-Pteriodophyta. Brit. Mus. *Nat. Hist.), London. 212pp. Pteridophyta, Palaeo (PMBD, 185305195)*.

Harris, T. M. (1964). *The Yorkshire Jurassic Flora. II. Caytoniales, Cycadales & Pteridosperms*: British Museum (Natural History).

Hecht, E. (1999). Energie de rayonnement: la lumière. In D. B. Université (Ed.), *Physique* (First ed.). Bruxelles.

Heimhofer, R., & Martill, D. (2007). The sedimentology and depositional environment of the Crato Formation *The Crato fossil beds of Brazil: window into an ancient world*: Cambridge University Press.

Hemsley, A. R., Scott, A. C., Barrie, P. J., & Chaloner, W. G. (1996). Studies of Fossil and Modern Spore Wall Biomacromolecules using13C Solid State NMR.

Annals of Botany, 78(1), 83-94. doi:http://dx.doi.org/10.1006/anbo.1996.0099

Hendricker, A. D., & Voorhees, K. J. (1996). An investigation into the Curie-point pyrolysis-mass spectrometry of glycyl dipeptides. *Journal of Analytical and Applied Pyrolysis, 36*(1), 51-70.

Higgs, K., & Beese, A. P. (1986). A Jurassic microflora from the Colbond Clay of Cloyne, County Cork. *Irish Journal of Earth Sciences*, 99-109.

Hirschler, A., Lucas, J., & Hubert, J.-C. (1990). Bacterial involvement in apatite genesis. *FEMS Microbiology Letters, 73*(3), 211-220.

Hollingworth, N. T., & Barker, M. J. (1991). Colour pattern preservation in the fossil record: taphonomy and diagenetic significance *The Process of Fossilization* (pp. 105-119).

Hong, L., Liu, Y., & Simon, J. D. (2004). Binding of Metal Ions to Melanin and Their Effects on the Aerobic Reactivity¶. *Photochemistry and Photobiology, 80*(3), 477-481.

Horsfield, B. (1989). Practical criteria for classifying kerogens: Some observations from pyrolysis-gas chromatography. *Geochimica et Cosmochimica Acta, 53*(4), 891-901. doi:http://dx.doi.org/10.1016/0016-7037(89)90033-1

Hou, L.-h., Zhou, Z., Martin, L. D., & Feduccia, A. (1995). A beaked bird from the Jurassic of China. *Nature, 377*(6550), 616.

Houck, M. A., Gauthier, J. A., & Strauss, R. E. (1990). Allometric scaling in the earliest fossil bird, Archaeopteryx lithographica. *Science, 247*(4939), 195-198.

Hu, D., Houl, L., Zhang, L., & Xu, X. (2009). A pre-*Archaeopteryx* troodontid theropod from China with long feathers on the metatarsus. *Letters*. doi:10.1038/nature08322

Hwang, S. H., Norell, M. A., Qiang, J., & Keqin, G. (2002). New specimens of *Microraptor zhaoianus* (Theropoda: Dromaeosauridae) from northeastern China. *American Museum Novitates*, 1-44.

Ichida, J. M., Krizova, L., LeFevre, C. A., Keener, H. M., Elwell, D. L., & Burtt, E. H. (2001). Bacterial inoculum enhances keratin degradation and biofilm formation in poultry compost. *Journal of Microbiological Methods, 47*(2), 199-208.

Ilyina, V. I. (1985). *Jurassic Palynology of Siberia*. Moscow: Nauka.

Ilyina, V. I. (1986). Subdivision and correlation of the marine and non-marine Jurassic sediments in Siberia based on palynological evidence. *Review of Palaeobotany and Palynology, 46*, 357-364.

Irfan, T. (1996). Mineralogy, fabric properties and classification of weathered granites in Hong Kong. *Quarterly Journal of Engineering Geology and Hydrogeology, 29*(1), 5-35.

Jain, D., Stark, A. Y., Niewiarowski, P. H., Miyoshi, T., & Dhinojwala, A. (2015). NMR spectroscopy reveals the presence and association of lipids and keratin in adhesive gecko setae. *Scientific Reports, 5* (9594). doi:10.1038/srep09594

Janvier, P., & Arsenault, M. (2009). La conservation exceptionnelle des fossiles du parc national de Miguasha. *Le Naturaliste Canadien, 133*, 78-83.

Jeong, G. Y. (1998). Formation of vermicular kaolinite from halloysite aggregates in the weathering of plagioclase. *Clays and Clay Minerals, 46*(3), 270-279.

Jeynes, C., Bailey, M. J., Bright, N. J., Christopher, M. E., Grime, G. W., Jones, B. N., Palitsin, V. V., & Webb, R. P. (2012). "Total IBA" - Where are we? *Nuclear Instruments and Methods in Physics Research B, 271*, 107-118. doi:10.1016/j.nimb.2011.09.020

Jeynes, C., Barradas, N., Marriott, P., Boudreault, G., Jenkin, M., Wendler, E., & Webb, R. (2003). Elemental thin film depth profiles by ion beam analysis using simulated annealing-a new tool. *Journal of Physics D: Applied Physics, 36*(7), R97.

Ji, Q., Currie, P. J., Norell, M. A., & Ji, S.-A. (1998). Two feathered dinosaurs from northeastern China. *Nature, 393*(6687), 753.

Ji, Q., & Ji, S. (1996). On the Discovery of the earliest fossil bird in China (*Sinosauropteryx* gen. nov.) and the origin of birds. *Chinese Geology, 233*, 6.

Ji, Q., Luo, Z.-X., Yuan, C.-X., Wible, J. R., Zhang, J.-P., & Georgi, J. A. (2002). The earliest known eutherian mammal. *Nature, 416*(6883), 816-822.

Ji, Q., Norell, M. A., Ke-Qin, G., Shu-An, J., & Ren, D. (2001). The distribution of integumentary structures in a feathered dinosaur. *Nature, 410*(6832), 1084.

Jolivet, M., Arzhannikov, S., Chauvet, A., Arzhannikova, A., Vassallo, R., Kulagina, N., & Akulova, V. (2013). Accomodating large-scale intracontinental extension and compression in a single stress-field: a key example from the Baikal Rift System. *Gondwana Research, 24*, 918-935.

Jones, T. P. (1994). Ultrastructural and chemical studies on Oligocene fossil wood from Bovey Tracey, Devon, UK. *Review of Palaeobotany and Palynology, 81*(2), 279-288. doi:http://dx.doi.org/10.1016/0034-6667(94)90112-0

Kabanov, P., Anadón, P., & Krumbein, W. E. (2008). Microcodium: an extensive review and a proposed non-rhizogenic biologically induced origin for its formation. *Sedimentary Geology, 205*(3), 79-99.

Kamal, G. M., Wang, X., Bin, Y., Wang, J., Sun, P., Zhang, X., & Liu, M. (2016). Compositional differences among Chinese soy sauce types studied by 13C NMR spectroscopy coupled with multivariate statistical analysis. *Talanta, 158*, 89-99. doi:http://dx.doi.org/10.1016/j.talanta.2016.05.033

Kaye, T. G., Gaugler, G., & Sawlowicz, Z. (2008). Dinosaurian soft tissues interpreted as bacterial biofilms. *PLoS ONE, 3*(7), e2808.

Kazarian, S. G., & Chan, K. A. (2013). ATR-FTIR spectroscopic imaging: recent advances and applications to biological systems. *Analyst, 138*(7), 1940-1951.

Kelemen, S., Afeworki, M., Gorbaty, M., Sansone, M., Kwiatek, P., Walters, C., Freund, H., Siskin, M., Bence, A., & Curry, D. (2007). Direct characterization of kerogen by X-ray and solid-state 13C nuclear magnetic resonance methods. *Energy & Fuels, 21*(3), 1548-1561.

Kellner, A. W., Wang, X., Tischlinger, H., de Almeida Campos, D., Hone, D. W., & Meng, X. (2010). The soft tissue of Jeholopterus (Pterosauria, Anurognathidae, Batrachognathinae) and the structure of the pterosaur wing membrane. *Proceedings of the Royal Society of London B: Biological Sciences, 277*(1679), 321-329.

Kellner, A. W. A., & de Almeida Campos, D. (2002). The function of the cranial crest and jaws of a unique pterosaur from the Early Cretaceous of Brazil. *Science, 297*, 389-392.

Kidwell, S. M., & Flessa, K. W. (1995). The Quality of the Fossil Record: Populations, Species, and Communities. *Annual Review of Ecology and Systematics, 26*(1), 269-299. doi:10.1146/annurev.es.26.110195.001413

Klein, C., Dutrow, B. D., & James Dwight, K. (2007). *The 23rd edition of the manual of mineral science:(after James D. Dana)*.

Knight, T. K., Bingham, P. S., Lewis, R. D., & Savrda, C. E. (2011). Feathers of the Ingersoll shale, Eutaw Formation (Upper Cretaceous), eastern Alabama: the largest collection of feathers from North American Mesozoic rocks. *Palaios, 26*(6), 364-376.

Kögel-Knabner, I. (1997). 13C and 15N NMR spectroscopy as a tool in soil organic matter studies. *Geoderma, 80*(3-4), 243-270.

Kos, A. M. (2003). Characterisation of post-depositional taphonomic processes in the accumulation of mammals in a pitfall cave deposit from southeastern Australia. *Journal of Archaeological Science, 30*(6), 781-796.

Kozlov, S. A. (2011a). *Report on the results of field work on facility no.5 "GDP-200, sheet N50-XXXII, -XXXIII" (Vershino-Darasunsky area)*. Chita.

Kozlov, V. D. (2009). Rare-earth elements as indicators of ore sources and the degree of differentiation and ore potential of rare-metal granite intrusions (eastern Transbaikalia). *Russian Geology and Geophysics, 50*(1), 29-42.

Kozlov, V. D. (2011b). Trace-element composition and origin of granitoids from the Shakhtama complex and Kukul'bei rare-metal complex (Aga zone, Transbaikalia). *Russian Geology and Geophysics, 52*(5), 526-536.

Kraal, P., Slomp, C. P., Forster, A., Kuypers, M. M. M., & Sluijs, A. (2009). Pyrite oxidation during sample storage determines phosphorus fractionation in carbonate-poor anoxic sediments. *Geochimica et Cosmochimica Acta, 73*(11), 3277-3290.

Krassilov, V. A. (1972). *Palaeoecology of terrestrial plants (Paleoecologiya nazemnykh rasteniy)*. Vladivostok: Far East Scientific Center of AS USSSR.

Krassilov, V. A. (1973). Climatic changes in eastern Asia as indicated by fossil floras. I. Early Cretaceous. *Palaeogeography, Palaeoclimatology, Palaeoecology, 13*, 261-273.

Kravchinsky, V. A., Cogné, J.-P., Harbert, W. P., & Kuzmin, M. I. (2002). Evolution of the Mongol-Okhotsk Ocean as constrained by new palaeomagnetic data from the Mongol-Okhotsk suture zone, Siberia. *Geophysical Journal International, 148*(1), 34-57.

Kreplak, L., Doucet, J., Dumas, P., & Briki, F. (2004). New aspects of the α-helix to β-sheet transition in stretched hard α-keratin fibers. *Biophysical journal, 87*(1), 640-647.

Kricheldorf, H. R., & Müller, D. (1984). Secondary structure of peptides 16th. Characterization of proteins by means of ^{13}C NMR CP/MAS spectroscopy. *Colloid & Polymer Science, 262*, 856-861.

Kruh, J. (1989). *Biochimie: études médicales et biologiques. 2. Métabolismes*. Paris: Hermann.

Kujau, A., Heimhofer, U., Hochuli, P. A., Morales, C., Adatte, T., Föllmi, K., Ploch, I., & Mutterlose, J. (2013). Reconstructing Valanginian (Early Cretaceous) mid-latitude vegetation and climate dynamics based on spore-pollen assemblages. *Review of Paleobotany and Palynology, 197*, 50-69. doi:10.1016/j.revpalbo.2013.05.003

Larsson, B., & Tjälve, H. (1978). Studies on the melanin-affinity of metal ions. *Acta Physiologica, 104*(4), 479-484.

Larter, S., & Horsfield, B. (1993). Determination of structural components of kerogens by the use of analytical pyrolysis methods *Organic Geochemistry* (pp. 271-287): Springer.

Leavitt, J. A., McIntyre, L. C., & Weller, M. R. (2010). Backscattering spectrometry. In Q. Wang, and Nastasi, M. (Ed.), *Handbook of modern ion beam material analysis.* Warrendale: Material Research Society.

Lebedeva, N. K., & Pestchevitskaya, E. B. (2012). Reference Cretaceous spore-pollen succession of West Siberia: evolutionary stages, facies, and correlations. *Journal of Stratigraphy, 36*(2), 193-212.

Leefmann, T., Heim, C., Siljeström, S., Blumenberg, M., Sjövall, P., & Thiel, V. (2013). Spectral characterization of ten cyclic lipids using time-of-flight secondary ion mass spectrometry. *Rapid communications in mass spectrometry, 27*(5), 565-581.

Lefèvre, U., Cau, A., Cincotta, A., Hu, D., Chinsamy, A., Escuillié, F., & Godefroit, P. (2017). A new Jurassic theropod from China documents a transitional step in the macrostructure of feathers. *The Science of Nature, 104*(9-10), 74.

Lefèvre, U., Hu, D., Escuillié, F., Dyke, G., & Godefroit, P. (2014). A new long-tailed basal bird from the Lower Cretaceous of north-eastern China. *Biological Journal of the Linnean Society, 113*(3), 790-804.

Leng, Q., & Yang, H. (2003). Pyrite framboids associated with the Mesozoic Jehol biota in northeastern China: implications for microenvironment during early fossilization. *Progress in Natural Science, 13*(3), 206-212.

Li, J., & Batten, D. J. (2004). Early Cretaceous palynofloras from the Tanggula Mountains of the northern Qinghai-Xizang (Tibet) Plateau, China. *Cretaceous Research, 25*(4), 531-542.

Li, K., Yang, C., & Hu, F. (2011). Dinosaur assemblages from the Middle Jurassic Shaximiao Formation and Chuanjie Formation in the Sichuan-Yunnan Basin, China. *Volumina Jurassica, 9*(9), 21-42.

Li, Q., Clarke, J. A., Gao, K.-Q., Zhou, C.-F., Meng, Q., Li, D., D'alba, L., & Shawkey, M. D. (2014). Melanosome evolution indicates a key physiological shift within feathered dinosaurs. *Nature, 507*(7492), 350.

Li, Q., Gao, K.-Q., Meng, Q., Clarke, J. A., Shawkey, M. D., D'Alba, L., Pei, R., Ellison, M., Norell, M. A., & Vinther, J. (2012a). Reconstruction of Microraptor and the evolution of iridescent plumage. *Science, 335*(6073), 1215-1219.

Li, Q., Gao, K.-Q., Vinther, J., Shawkey, M. D., Clarke, J. A., D'Alba, L., Meng, Q., Briggs, D. E. G., & Prum, R. O. (2010). Plumage color patterns of an extinct dinosaur. *Science, 327*, 1369-1372. doi:10.1126/science.1186290

Li, Q., Gao, K. Q., Meng, Q., Clarke, J. A., Shawkey, M. D., D'Alba, L., Pei, R., Ellison, M., Norell, M. A., & Vinther, J. (2012b). Reconstruction of *Microraptor* and the evolution of iridescent plumage. *Science, 335*, 1215. doi:10.1126/science.1213780

Lindgren, J., Sjövall, P., Carney, R. M., Cincotta, A., Uvdal, P., Hutcheson, S. W., Gustafsson, O., Lefèvre, U., Escuillier, F., Heimdal, J., Engdahl, A., Gren, J. A., Kear, B. P., Wakamatsu, K., Yans, J., & Godefroit, P. (2015). Molecular

composition and ultrastructure of Jurassic paravian feathers. *Scientific Reports, 5*(13520). doi:10.1038/srep13520

Lindgren, J., Sjövall, P., Carney, R. M., Uvdal, P., Gren, J. A., Dyke, G., Schultz, B. P., Shawkey, M. D., Barnes, K. R., & Polcyn, M. J. (2014). Skin pigmentation provides evidence of convergent melanism in extinct marine reptiles. *Nature, 506*(7489), 484.

Lindgren, J., Uvdal, P., Sjövall, P., Nilsson, D. E., Engdahl, A., Schultz, B. P., & Thiel, V. (2012). Molecular preservation of the pigment melanin in fossil melanosomes. *Nature Communications, 3*, 824.

Lingham-Soliar, T., Bonser, R. H., & Wesley-Smith, J. (2009). Selective biodegradation of keratin matrix in feather rachis reveals classic bioengineering. *Proceedings of the Royal Society of London B: Biological Sciences*, rspb20091980.

Lingham-Soliar, T., & Murugan, N. (2013). A new helical crossed-fibre structure of β-keratin in flight feathers and its biomechanical implications. *PLoS ONE, 8*(6), e65849.

Liu, Y.-Q., Kuang, H.-W., Jiang, X.-J., Peng, N., Xu, H., & Sun, H.-Y. (2012a). Timing of the earliest known feathered dinosaurs and transitional pterosaurs older than the Jehol Biota. *Palaeogeography, Palaeoclimatology, Palaeoecology, 323-325*, 1-12. doi:10.1016/j.palaeo.2012.01.017

Liu, Y.-Q., Kuang, H.-W., Jiang, X.-J., Peng, N., Xu, H., & Sun, H.-Y. (2012b). Timing of the earliest known feathered dinosaurs and transitional pterosaurs older than the Jehol Biota. *Palaeogeography, Palaeoclimatology, Palaeoecology, 323*, 1-12.

Liu, Y., Hong, L., Wakamatsu, K., Ito, S., Adhyaru, B., Cheng, C. Y., Bowers, C. R., & Simon, J. D. (2005). Comparison of structural and chemical properties of black and red human hair melanosomes. *Photochemistry and Photobiology, 81*, 135-144.

Longbottom, T. L., Hockaday, W. C., Boling, K. S., Li, G., Letourmy, Y., Dong, H., & Dworkin, S. I. (2016). Organic structural properties of kerogen as predictors of source rock type and hydrocarbon potential. *Fuel, 184*, 792-798. doi:https://doi.org/10.1016/j.fuel.2016.07.066

Longrich, N. R., Vinther, J., Meng, Q., Li, Q., & Russell, A. P. (2012). Primitive wing feather arrangement in *Archaeopteryx lithographica* and *Anchiornis huxleyi*. *Current Biology, 22*(23), 2262-2267.

Lorenzini, G., & Mazza, N. (2004). *Debris flow: Phenomenology and rheological modelling*: Wit Press.

Lowson, R. T. (1982). Aqueous oxidation of pyrite by molecular oxygen. *Chemical reviews, 82*(5), 461-497.

Lubnow, E. (1963). Melanine bei Vögeln und säugetieren. *Journal of Ornithology, 104*(1), 69-81.

Lucas, A., & Stettenheim, P. (1972a). *Avian anatomy—Integument, part II* (Vol. 362).

Lucas, A., & Stettenheim, P. (1972b). Structure of feathers. *Avian anatomy: integument. Washington (DC): US Department of Agriculture*, 341-419.

Lucas, A. M., & Stettenheim, P. R. (1972c). Avian anatomy *Avian anatomy: Integuments* (September 1972 ed., Vol. 2, pp. 380). Washington D.C.: U.S. Department of Agriculture in cooperation with Michigan Agricultural Experiment Station.

Lyman, R. L. (1994). *Vertebrate taphonomy*: Cambridge University Press.

Makovicky, P., & Norell, M. A. (2004). Troodontidae. *The Dinosauria, 2*, 184-195.

Makovicky, P. J., Apesteguía, S., & Agnolín, F. L. (2005). The earliest dromaeosaurid theropod from South America. *Nature, 437*(7061), 1007.

Makovicky, P. J., Norell, M. A., Clark, J. M., & Rowe, T. (2003). Osteology and relationships of Byronosaurus jaffei (Theropoda: Troodontidae). *American Museum Novitates*, 1-32.

Manning, P. L., Edwards, N. P., Wogelius, R. A., Bergmann, U., Barden, H. E., Larson, P. L., Schwarz-Wings, D., Egerton, V. M., Sokaras, D., & Mori, R. A. (2013). Synchrotron-based chemical imaging reveals plumage patterns in a 150 million year old early bird. *Journal of Analytical Atomic Spectrometry, 28*(7), 1024-1030.

Manning, P. L., Margetts, L., Johnson, M. R., Withers, P. J., Sellers, W. I., Falkingham, P. L., Mummery, P. M., Barrett, P. M., & Raymont, D. R. (2009a). Biomechanics of Dromaeosaurid Dinosaur Claws: Application of X-Ray Microtomography, Nanoindentation, and Finite Element Analysis. *The Anatomical Record, 292*(9), 1397-1405.

Manning, P. L., Morris, P. M., McMahon, A., Jones, E., Gize, A., Macquaker, J. H., Wolff, G., Thompson, A., Marshall, J., & Taylor, K. G. (2009b). Mineralized soft-tissue structure and chemistry in a mummified hadrosaur from the Hell Creek Formation, North Dakota (USA). *Proceedings of the Royal Society of London B: Biological Sciences*, rspb20090812.

Mao, J., Fang, X., Lan, Y., Schimmelmann, A., Mastalerz, M., Xu, L., & Schmidt-Rohr, K. (2010). Chemical and nanometer-scale structure of kerogen and its change during thermal maturation investigated by advanced solid-state ^{13}C NMR spectroscopy. *Geochimica et Cosmochimica Acta, 74*(7), 2110-2127.

Markevich, V. S. (1995). Cretaceous palynoflora of northeastern Asia. *Vladivostok: Dalnauka*, 200.

Markevich, V. S., & Bugdaeva, E. V. (2009). Palynological evidence for dating Jurassic-Cretaceous boundary sediments in the Bureya basin, Russian Far East. *Russian Journal of Pacific Geology, 3*(3), 284-293.

Marmi, J., Luján, A., Riera, V., Gaete, R., Oms, O., & Galobart, A. (2012). The youngest species of *Polysternon*: a new bothremydid turtle from the uppermost Maastrichtian of the southern Pyrenees. *Cretaceous Research, 35*, 133-142.

Marmi, J., Vila, B., & Galobart, À. (2009). *Solemys* (Chelonii, Solemydidae) remains from the Maastrichtian of Pyrenees: evidence for a semi-aquatic lifestyle. *Cretaceous Research, 30*(5), 1307-1312.

Marsh, O. C. (1877). Notice of new dinosaurian reptiles from the Jurassic Formation. *American Journal of Science*(84), 514-516.

Martill, D. M., & Heimhofer, U. (2007). Stratigraphy of the Crato Formation. . In B. G. a. L. R. F. Martill D.M. (Ed.), *The Crato Fossil Beds of Brazil: window into an Ancient World.* Cambridge: Cambridge University Press.

Martin, D., Briggs, D. E., & Parkes, R. J. (2004). Experimental attachment of sediment particles to invertebrate eggs and the preservation of soft-bodied fossils. *Journal of the Geological Society, 161*(5), 735-738.

Martinez-Hernandez, A. L., Velasco-Santos, C., De Icaza, M., & Castano, V. M. (2005). Microstructural characterisation of keratin fibres from chicken feathers. *International journal of environment and pollution, 23*(2), 162-178.

Mayr, G., Peters, D. S., Plodowski, G., & Vogel, O. (2002). Bristle-like integumentary structures at the tail of the horned dinosaur *Psittacosaurus*. *Naturwissenschaften, 89*, 361-365. doi:10.1007/s00114-002-0339-6

McGraw, K. J., & Hill, G. (2006). Mechanics of carotenoid-based coloration *Bird coloration* (Vol. 1, pp. 177-242).

McKittrick, J., Chen, P.-Y., Bodde, S. G., Yang, W., Novitskaya, E. E., & Meyers, M. A. (2012). The structure, functions, and mechanical properties of keratin. *JOM, 64*(4), 449-468. doi:10.1007/s11837-012-0302-8

McLennan, S. M. (2001). Relationships between the trace element composition of sedimentary rocks and upper continental crust. *Geochemistry, Geophysics, Geosystems, 2*.

McNamara, M., Kaye, J., Benton, M., & Orr, P. (2014). *Non-integumentary melanosomes can bias reconstructions of the colours of fossil vertebrate skin.* Paper presented at the EGU General Assembly Conference Abstracts.

McNamara, M. E. (2013). The taphonomy of colour in fossil insects and feathers. *Palaeontology, 56*(3), 557-575.

McNamara, M. E., Briggs, D. E., Orr, P. J., Field, D. J., & Wang, Z. (2013). Experimental maturation of feathers: implications for reconstructions of fossil feather colour. *Biology Letters, 9*(3), 20130184.

McNamara, M. E., van Dongen, B. E., Lockyer, N. P., Bull, I. D., & Orr, P. J. (2016). Fossilization of melanosomes via sulfurization. *Palaeontology*, 1-14.

Mengchang, H., Yehong, S., & Chunye, L. (2008). Characterization of humic acids extracted from the sediments of the various rivers and lakes in China. *Journal of Environmental Sciences, 20*(11), 1294-1299.

Meunier, A. (2005). *Clays*: Springer Science & Business Media.

Meyers, P. A., & Ishiwatari, R. (1993). The early diagenesis of organic matter in lacustrine sediments *Organic Geochemistry* (pp. 185-209): Springer.

Miknis, F. P., Lindner, A. W., Gannon, A. J., Davis, M. F., & Maciel, G. E. (1984). Solid state 13C NMR studies of selected oil shales from Queensland, Australia. *Organic Geochemistry, 7*(3-4), 239-248.

Mitsuda, T. (1960). Pseudomorphs of Kaolinite after Biotite (Studies on Mechanism of Weathering, 1st report). *Journal of the Faculty of Science, Hokkaido University. Series 4, Geology and mineralogy, 10*(3), 481-494.

Mitta, V. V., Vuks, V. Y., Glinskikh, L. A., Dzyuba, O. S., Zakharov, V. A., Kirikov, V. P., Kostyleva, V. V., Malenkina, S. Y., Nikitenko, B. L., Pestchevitskaya, E. B., Rogov, M. A., Rostovtseva, Y. I., Seltser, V. B., & Tesakova, E. M. (2012). *The Unified Regional Stratigraphic Scale of the Jurassic of the East European Platform. Explanatory Note.* Retrieved from Moscow:

Mogutcheva, N. K. (2009). Problems of phytostratigraphy and the correlation of the Lower Jurassic continental sediments in West Siberia and Kuznetsk and Kansk-Achinsk basins. *Stratigraphy and Geological Correlation, 17*(3), 283-290.

Moldoveanu, S. C. (2009). *Pyrolysis of organic molecules: applications to health and environmental issues* (Vol. 28): Elsevier.

Morey, G. B., & Setterholm, D. R. (1997). Rare earth elements in weathering profiles and sediments of Minnesota: implications for provenance studies. *Journal of Sedimentary Research, 67*(1).

Moyer, A. E., Zheng, W., Johnson, E. A., Lamanna, M. C., Li, D.-q., Lacovara, K. J., & Schweitzer, M. H. (2014). Melanosomes or microbes: testing an alternative hypothesis for the origin of microbodies in fossil feathers. *Scientific Reports, 4*.

Muroya, S., Tanabe, R.-I., Nakajima, I., & Chikuni, K. (2000). Molecular characteristics and site specific distribution of the pigment of the silky fowl. *Journal of Veterinary Medical Science, 62*(4), 391-395.

Murphy, M. E., King, J. R., Taruscio, T. G., & Geupel, G. R. (1990). Amino acid composition of feather barbs and rachises in three species of pygoscelid penguins: nutritional implications. *The Condor, 92*(4), 913-921.

Murru, M., Ferrara, C., Da Pelo, S., & Ibba, A. (2003). The Palaeocene–Middle Eocene deposits of Sardinia (Italy) and their palaeoclimatic significance. *Comptes Rendus Geoscience, 335*(2), 227-238.

Mushnikov, A. F., Anashkina, K. K., & Oleksiv, B. I. (1966). Stratigraphy of Jurassic sediments in the eastern Trans-Baikal region. *Bulletin of Geology and Mineral Resources of the Chita Region, 2*, 57-99.

Nan, P., Yongqing, L., Hongwei, K., Xiaojun, J., & Huan, X. (2012). Stratigraphy and geochronology of vertebrate fossil-bearing Jurassic strata from Linglongta, Jianchang County, Western Liaoning, Northeastern China. *Acta Geologica Sinica (English Edition), 86*(6), 1326-1339.

Nesbitt, H. W., & Young, G. M. (1982). Early Proterozoic climates and plate motions inferred from major element chemistry of lutites. *Nature, 299*(5885), 715-717.

Nichols, G., & Fisher, J. (2007). Processes, facies and architecture of fluvial distributary system deposits. *Sedimentary Geology, 195*(1), 75-90.

Nordstrom, D. K. (1982). *Aqueous pyrite oxidation and the consequent formation of secondary iron minerals*: Soil Science Society of America.

Norell, M., Makovicky, P. J., Akademi, M. S. U., & Project, M.-A. M. P. (1999). Important features of the dromaeosaurid skeleton. 2, Information from newly collected specimens of Velociraptor mongoliensis. American Museum novitates; no. 3282.

Norris, G. (1965). Triassic and Jurassic miospores and acritarchs from the Beacon and Ferrar groups, Victoria Land, Antarctica. *New Zealand journal of geology and geophysics, 8*(2), 236-277.

O'Connor, J., & Chang, H. (2015). Hindlimb feathers in paravians: Primarily'wings' or ornaments? *Biology Bulletin, 42*(7).

O'Connor, P. M. (2004). Pulmonary pneumaticity in the postcranial skeleton of extant Aves: a case study examining Anseriformes. *Journal of morphology, 261*(2), 141-161.

O'Connor, P. M. (2006). Postcranial pneumaticity: An evaluation of soft-tissue influences on the postcranial skeleton and the reconstruction of pulmonary anatomy in archosaurs. *Journal of morphology, 267*(10), 1199-1226.

O'connor, P. M., & Claessens, L. P. (2005). Basic avian pulmonary design and flow-through ventilation in non-avian theropod dinosaurs. *Nature, 436*(7048), 253.

O'Donnell, I., & Inglis, A. (1974). Amino acid sequence of a feather keratin from Silver Gull (*Larus novae-hollandiae*) and comparison with one from Emu (*Dromaius novae-hollandiae*). *Australian journal of biological sciences, 27*(4), 369-382.

O'Connor, J., Wang, X., Sullivan, C., Zheng, X., Tubaro, P., Zhang, X., & Zhou, Z. (2013). Unique caudal plumage of *Jeholornis* and complex tail evolution in early birds. *Proceedings of the National Academy of Sciences, 110*(43), 17404-17408.

Orange, F., Lalonde, S. V., & Konhauser, K. O. (2013). The formation and preservation of Synechococcus elongatus cell molds in simulated silica sinter: implications for the identification of microfossils. *Geomicrobiology Journal, 30*(4), 327-336.

Orr, P. J., Briggs, D. E., & Kearns, S. L. (1998). Cambrian Burgess Shale animals replicated in clay minerals. *Science, 281*(5380), 1173-1175.

Osmólska, H., Currie, P. J., & Barsbold, R. (2004). Oviraptorosauria *The Dinosauria* (pp. 165-183). California.

Ostrom, J. H. (1969). *Osteology of Deinonychus antirrhopus, an unusual theropod from the Lower Cretaceous of Montana* (Vol. 30): Peabody Museum of Natural History, Yale University.

Owocki, K., Niedźwiedzki, G., Sennikov, A. G., Golubev, V. K., Janiszewska, K., & Sulej, T. (2012). Upper Permian vertebrate coprolites from Vyazniki and Gorokhovets, Vyatkian regional stage, Russian Platform. *Palaios, 27*(12), 867-877.

Pacton, M., Fiet, N., & Gorin, G. (2006). Revisiting amorphous organic matter in Kimmeridgian laminites: what is the role of the vulcanization process in the amorphization of organic matter? *Terra Nova, 18*(6), 380-387.

Pan, Y., Sha, J., & Fuersich, F. T. (2014). A model for organic fossilization of the Early Cretaceous Jehol Lagerstätte based on the taphonomy of "*Ephemeropsis trisetalis*". *Palaios, 29*(7), 363-377.

Pan, Y., Sha, J., Zhou, Z., & Fürsich, F. T. (2013). The Jehol Biota: definition and distribution of exceptionally preserved relicts of a continental Early Cretaceous ecosystem. *Cretaceous Research, 44*, 30-38.

Parker, A. (1970). An index of weathering for silicate rocks. *Geological Magazine, 107*(06), 501-504.

Pauling, L., & Corey, R. B. (1951). The pleated sheet, a new layer configuration of polypeptide chains. *Proceedings of the National Academy of Sciences, 37*(5), 251-256.

Pestchevitskaya, E. B. (2007). Lower Cretaceous biostratigraphy of Northern Siberia: palynological units and their correlation significance. *Russian Geology and Geophysics, 48*(11), 941-959.

Pike, A., & Maitland, D. (2004). Scaling of bird claws. *Journal of Zoology, 262*(1), 73-81.

Pimentel, N., Wright, V., & Azevedo, T. (1996). Distinguishing early groundwater alteration effects from pedogenesis in ancient alluvial basins: examples from the Palaeogene of southern Portugal. *Sedimentary Geology, 105*(1-2), 1-10.

Pinheiro, F. L., Horn, B. L. D., Schultz, C. L., De Andrade, J. A. F. G., & Sucerquia, P. A. (2012). Fossilized bacteria in a Cretaceous pterosaur headcrest. *Lethaia*. doi:10.1111/j.1502-3931.2012.00309.x.

Plaziat, J.-C. (1981). Late Cretaceous to Late Eocene palaeogeographic evolution of southwest Europe. *Palaeogeography, Palaeoclimatology, Palaeoecology, 36*(3-4), 263-320.

Plonka, P. M., & Grabacka, M. (2006). Melanin synthesis in microorganisms-biotechnological and medical aspects. *Acta Biochimica Polonica, 53*(3), 429-443.

Poirier, N., Derenne, S., Rouzaud, J.-N., Largeau, C., Mariotti, A., Balesdent, J., & Maquet, J. (2000). Chemical structure and sources of the macromolecular, resistant, organic fraction isolated from a forest soil (Lacadée, south-west France). *Organic Geochemistry, 31*(9), 813-827.

Polet, C., & Orban, R. (2001). La diagenèse *Les dents et les ossements humains: que mangeait-on au Moyen Āge?*. Turnhout, Belgium: Brepols.

Prokof ev, V. Y., Bortnikov, N., Zorina, L., Kulikova, Z., Matel, N., Kolpakova, N., & Il ina, G. (2000a). Genetic features of the Darasun gold-sulfide deposit (Eastern Transbaikal Region). *GEOLOGY OF ORE DEPOSITS C/C OF GEOLOGIIA RUDNYKH MESTOROZHDENII, 42*(6), 474-495.

Prokof ev, V. Y., Bortnikov, N. S., Zorina, L. D., Kulikova, Z. I., Matel, N. L., Kolpakova, N. N., & Il ina, G. F. (2000b). Genetic features of the Darasun gold-sulfide deposit (Eastern Transbaikal Region). *GEOLOGY OF ORE DEPOSITS C/C OF GEOLOGIIA RUDNYKH MESTOROZHDENII, 42*(6), 474-495.

Prum, R. O., & Brush, A. H. (2002). The evolutionary origin and diversification of feathers. *The Quarterly review of biology, 77*(3), 261-295.

Rauhut, O. W., Foth, C., Tischlinger, H., & Norell, M. A. (2012). Exceptionally preserved juvenile megalosauroid theropod dinosaur with filamentous integument from the Late Jurassic of Germany. *Proceedings of the National Academy of Sciences, 109*(29), 11746-11751.

Ravel, B., & Newville, M. (2005). ATHENA, ARTEMIS, HEPHAESTUS: data analysis for X-ray absorption spectroscopy using IFEFFIT. *Journal of synchrotron radiation, 12*(4), 537-541.

Ribecai, C. (2007). Early Jurassic miospores from Ferrar Group of Carapace Nunatak, South Victoria Land, Antarctica. *Review of Palaeobotany and Palynology, 144*(1), 3-12.

Riley, P. A. (1997). Melanin. *The international journal of biochemistry & cell biology, 29*(11), 1235-1239.

Rodziewicz, A., & Laba, W. (2008). Biodegradation of feather keratin by *Bacillus cereus* in pure culture and compost. *EJPAU, 11*(2), 03.

Rudenko, V. E., & Starchenko, V. V. (2010). *Explanatory note to the geological map of the Russian Federation. Aldan-Transbaikalian Series. Sheet N-50 - Sretensk*. Retrieved from Saint-Petersburg:

Ruiz-Omeñaca, J. I., Pereda Suberbiola, X., & Galton, P. M. (2006). *Callovosaurus leedsi*, the earliest dryosaurid dinosaur (Ornithischia: Euornithopoda) from the Middle Jurassic of England *Horns and Beaks: Ceratopsian and ornithopod dinosaurs* (pp. 3).

Rutschke, E. (1966). Untersuchungen über die Feinstruktur des Schaftes der Vogelfeder. *Zool. Jahrb, 93*, 223-288.

Rutshtein, I., & Chaban, N. (1997). Geologic Structure of the Chita Region. *Explanatory Note to a Geological Map of Scale, 1*(500,000).

Rutshtein, I. G., & Chaban, N. N. (1992). Geological Map of the Chita region (1: 500,000). *MPGIT, Moscow, 23*.

Ruxton, B. P. (1968). Measures of the degree of chemical weathering of rocks. *The Journal of Geology, 76*(5), 518-527.

Ruzhentsev, S., & Nekrasov, G. (2009). Tectonics of the Aga zone, Mongolia-Okhotsk belt. *Geotectonics, 43*(1), 34-50.

Sacchi, R., Addeo, F., & Paolillo, L. (1997). ^{1}H and ^{13}C NMR of virgin olive oil. An overview. *Magnetic resonance in chemistry, 35*(13).

Sajjadi, F., & Playford, G. (2002). Systematic and stratigraphic palynology of Late Jurassic-earliest Cretaceous strata of the Eromanga Basin, Queensland, Australia: Part one.

Sambrook, J., Fritsch, E. F., & Maniatis, T. (1989). *Molecular cloning: a laboratory manual*: Cold spring harbor laboratory press.

Samylina, V. A., & Kiritchkova, A. I. (1993). The genus Czekanowskia Heer: principles of systematics, range in space and time. *Review of Palaeobotany and Palynology, 79*(3-4), 271-284.

Saravanan, K., & Dhurai, B. (2012). Exploration on the amino acid content and morphological structure in chicken feather fiber. *Journal of Textile and Apparel, Technology and Management, 7*(3).

Sardessai, S., & Wahidullah, S. (1998). Structural characteristics of marine sedimentary humic acids by CP/MAS ^{13}C NMR spectroscopy. *Oceanologica Acta, 21*(4), 543-550. doi:http://dx.doi.org/10.1016/S0399-1784(98)80037-6

Schaefer, J., Kramer, K. J., Garbow, J. R., Jacob, G. S., Stejskal, E. O., Hopkins, T. L., & Speirs, R. D. (1987). Aromatic cross-links in insect cuticle: detection by solid-state ^{13}C and ^{15}N NMR. *Science, 235*(4793), 1200-1204.

Schnyder, J., Dejax, J., Keppens, E., Tu, T. T. N., Spagna, P., Boulila, S., Galbrun, B., Riboulleau, A., Tshibangu, J.-P., & Yans, J. (2009). An Early Cretaceous lacustrine record: organic matter and organic carbon isotopes at Bernissart (Mons Basin, Belgium). *Palaeogeography, Palaeoclimatology, Palaeoecology, 281*(1), 79-91.

Schwark, L., Ferretti, A., Papazzoni, C. A., & Trevisani, E. (2009). Organic geochemistry and paleoenvironment of the early Eocene "Pesciara di Bolca" *Konservat-Lagerstätte*, Italy. *Palaeogeography, Palaeoclimatology, Palaeoecology, 273*(3), 272-285.

Schweigert, G. (2007). Ammonite biostratigraphy as a tool for dating Upper Jurassic lithographic limestones from South Germany–first results and open questions. *Neues Jahrbuch für Geologie und Paläontologie-Abhandlungen, 245*(1), 117-125.

Schweitzer, M. H. (2011a). Soft tissue preservation in terrestrial Mesozoic vertebrates. *Annual Review of Earth and Planetary Sciences, 39*, 187-216.

Schweitzer, M. H. (2011b). Soft Tissue Preservation in Terrestrial Mesozoic Vertebrates. *Annual Review of Earth and Planetary Sciences, 39*(1), 187-216. doi:10.1146/annurev-earth-040610-133502

Schweitzer, M. H., Watt, J. A., Avci, R., Forster, C. A., Krause, D. W., Knapp, L., Rogers, R. R., Beech, I., & Marshall, M. (1999). Keratin immunoreactivity in the Late Cretaceous bird Rahonavis ostromi. *Journal of Vertebrate Paleontology, 19*(4), 712-722.

Schwimmer, D. R., & Montante, W. M. (2007). Exceptional fossil preservation in the Conasauga Formation, Cambrian, northwestern Georgia, USA. *Palaios, 22*(4), 360-372.

Scott, A. C., Cripps, J. A., Collinson, M. E., & Nichols, G. J. (2000). The taphonomy of charcoal following a recent heathland fire and some implications for the interpretation of fossil charcoal deposits. *Palaeogeography, Palaeoclimatology, Palaeoecology, 164*(1), 1-31.

Seeley, H. G. (1870). X.—Remarks on Prof. Owen's monograph on *Dimorphodon*. *Journal of Natural History, 6*(32), 129-152.

Seilacher, A., Reif, W.-E., Westphal, F., Riding, R., Clarkson, E., & Whittington, H. (1985). Sedimentological, ecological and temporal patterns of fossil Lagerstatten. *Philosophical Transactions of the Royal Society of London. Series B, Biological Sciences*, 5-24.

Seitz, L. M., & Ram, M. (2000). Volatile methoxybenzene compounds in grains with off-odors. *Journal of agricultural and food chemistry, 48*(9), 4279-4289.

Seltmann, R., Soloviev, S., Shatov, V., Pirajno, F., Naumov, E., & Cherkasov, S. (2010). Metallogeny of Siberia: tectonic, geologic and metallogenic settings of selected significant deposits. *Australian Journal of Earth Sciences, 57*(6), 655-706.

Sereno, P. C. (2012). Taxonomy, morphology, masticatory function and phylogeny of heterodontosaurid dinosaurs. *ZooKeys*(226), 1.

Sereno, P. C., Martinez, R. N., Wilson, J. A., Varricchio, D. J., Alcober, O. A., & Larsson, H. C. (2008). Evidence for avian intrathoracic air sacs in a new predatory dinosaur from Argentina. *PLoS ONE, 3*(9), e3303.

Shawkey, M. D., D'Alba, L., Xiao, M., Schutte, M., & Buchholz, R. (2015). Ontogeny of an iridescent nanostructure composed of hollow melanosomes. *Journal of morphology, 276*(4), 378-384.

Shurygin, B. N., Nikitenko, B. L., Devyatov, V. P., Ilyina, V. I., Meledina, S. V., Gaideburova, E. A., Dzyuba, O. S., Kazakov, A. M., & Mogucheva, N. K. (2010). *Stratigraphy of Petroleum-bearing Basins of Siberia. Jurassic*. . Novosibirsk: Izd. SO RAN, Filial Geo.

Simmonds, P., Medley, E., Ratcliff, M., & Shulman, G. (1972). Thermal decomposition of aliphatic monoaminomonocarboxylic acids. *Analytical chemistry, 44*(12), 2060-2066.

Sinitsa, S. M. (2011a). *Environmental Cooperative Studies in the Cross-Border Ecological Region: Russia, China, and Mongolia*. Chita, Russia: Institute of Natural Resources, Ecology and Cryology, Siberian Branch of the Russian Academy of Sciences.

Sinitsa, S. M. (2011b). Transitional horizons in the stratigraphy of the Upper Mesozoic of Transbaikalia. *Bulletin of Chita University, 70*(3), 98-103.

Sinitsa, S. M., & Starukhina, S. (1986). *Novye dannye po geologii Zabaikal'ya*. Moscow: Ministry of Geology, Russian Soviet Federative Socialist Republic.

Sinitsa, S. M., & Vil'mova, E. S. (2016). Paleoecological and taphonomic biota features of the Jurassic Dinosaur's locality (Kulinda, Olov Depression, Transbaikalia). *Scientific Notes of the Transbaikal State University, 1*(11).

Sinninghe-Damsté, J. S., & De Leeuw, J. W. (1990). Analysis, structure and geochemical significance of organically-bound sulphur in the geosphere:

state of the art and future research. *Organic Geochemistry, 16*(4-6), 1077-1101.

Sinninghe-Damsté, J. S., Eglinton, T. I., De Leeuw, J. W., & Schenck, P. (1989). Organic sulphur in macromolecular sedimentary organic matter: I. Structure and origin of sulphur-containing moieties in kerogen, asphaltenes and coal as revealed by flash pyrolysis. *Geochimica et Cosmochimica Acta, 53*(4), 873-889.

Sinninghe-Damsté, J. S., Irene, W., Rijpstra, C., de Leeuw, J. W., & Schenck, P. (1988). Origin of organic sulphur compounds and sulphur-containing high molecular weight substances in sediments and immature crude oils. *Organic Geochemistry, 13*(4-6), 593-606.

Smokotina, I. V. (2006). *Palynostratigraphy of Jurassic deposits of Kansk-Achinsk Basin.* Krasnoyarsk, Russia: Krasnoyarskgeolsjomka.

Smoot, J. P. (1991). Sedimentary facies and depositional environments of early Mesozoic Newark Supergroup basins, eastern North America. *Palaeogeography, Palaeoclimatology, Palaeoecology, 84*(1-4), 369-423.

Sodhi, R. N., Mims, C. A., Goacher, R. E., McKague, B., & Wolfe, A. P. (2013). Preliminary characterization of Palaeogene European ambers using ToF-SIMS. *Surface and Interface Analysis, 45*(1), 557-560.

Solano, F. (2014). Melanins: skin pigments and much more—types, structural models, biological functions, and formation routes. *New Journal of Science, 2014*.

Solé, V., Papillon, E., Cotte, M., Walter, P., & Susini, J. (2007). A multiplatform code for the analysis of energy-dispersive X-ray fluorescence spectra. *Spectrochimica Acta Part B: Atomic Spectroscopy, 62*(1), 63-68.

Spiridonov, A., Zorina, L., & Kitaev, N. (2006). Gold-bearing ore-magmatic systems of Transbaikalia. *Novosibirsk Acad Publ House "Geo"(in Russian)*.

Spiridonov, A. M., Kozlov, V. D., Zorina, L. D., Men'shikov, V. I., & Bychinskii, V. A. (2010). Distribution of gold in igneous granitoid complexes in the central and southwestern areas of eastern Transbaikalia. *Russian Geology and Geophysics, 51*(8), 846-856.

Squire, J., & Vibert, P. J. (1987). *Fibrous protein structure*: Academic Press.

Srebrodolskaya, I. N. (1980). New Late Mesozoic mosses from Transbaikalia [Новые позднемезозойские листостебельные мхи из Забайкалья]. *Proceedings of VSEGEI (Vsesoyuznogo Nauchno-Issledovatelskogo Geol. Inst), 204*, 27-28.

Srebrodolskaya, I. N. (1983). Two new species of the genus Eguisetum (Eguisetaceae) from transbaikalia [Dva novykh vida roda Equisetum (Equisetaceae) iz Zabaikalia] *Botanical Journal, 68*(9), 1249-1254.

Srivastava, P. (2006). Meso–Neoproterozoic coated grains and palaeoecology of associated microfossils: The Deoban Limestone, Lesser Himalaya, India. *Palaeogeography, Palaeoclimatology, Palaeoecology, 239*(3), 241-252.

Stacey, J. t., & Kramers, J. (1975). Approximation of terrestrial lead isotope evolution by a two-stage model. *Earth and Planetary Science Letters, 26*(2), 207-221.

Stankiewicz, B., Briggs, D., Michels, R., Collinson, M., Flannery, M., & Evershed, R. (2000). Alternative origin of aliphatic polymer in kerogen. *Geology, 28*(6), 559-562.

Stankiewicz, B., Scott, A., Collinson, M. E., Finch, P., Mösle, B., Briggs, D., & Evershed, R. (1998). Molecular taphonomy of arthropod and plant cuticles

from the Carboniferous of North America: implications for the origin of kerogen. *Journal of the Geological Society, 155*(3), 453-462.

Starchenko, V. V. (2010). *Geological map of Russian federation. Aldan-Transbaikalia series. List M-50, Borzya. Explanatory note [Gosudarstvennaya geologicheskaya karta Rossiyskoy Federatcii. Seriya Aldano-Zabaikalskaya. List M50 – Borzya. Ob'yasnitelnaya zapiska]*. Retrieved from Saint-Petersburg:

Staroń, P., Banach, M., & Kowalski, Z. (2011). Keratyna: źródła, właściwości, zastosowanie. *Chemik, 65*(10), 1019-1026.

Steiger, R. H., & Jäger, E. (1977). Subcommission on geochronology: convention on the use of decay constants in geo-and cosmochronology. *Earth and Planetary Science Letters, 36*(3), 359-362.

Stewart, D. (1981). A meander-belt sandstone of the Lower Cretaceous of Southern England. *Sedimentology, 28*(1), 1-20.

Stiksel, T. A. (1966). *Permian phytostratigraphy of Middle Asia [K fitostratigrafii permi v Sredney Azii]*: Tashkent: Fan.

Stupak, F. M., Kudryashova, E. A., & Lebedev, V. A. (2016). On the Jurassic volcanism and on volcanoes in the Shadoron Basin, eastern Transbaikalia. *Journal of Volcanology and Seismology, 10*(2), 18-31.

Sulaimon, S. S., & Kitchell, B. E. (2003). The biology of melanocytes. *Veterinary dermatology, 14*(2), 57-65.

Sullivan, C., Wang, Y., Hone, D. W., Wang, Y., Xu, X., & Zhang, F. (2014). The vertebrates of the Jurassic Daohugou Biota of northeastern China. *Journal of Vertebrate Paleontology, 34*(2), 243-280.

Sun, G., Dilcher, D. L., Zheng, S., & Zhou, Z. (1998). In search of the first flower: a Jurassic angiosperm, Archaefructus, from northeast China. *Science, 282*(5394), 1692-1695.

Sun, S.-s., & McDonough, W. F. (1989). Chemical and isotopic systematics of oceanic basalts: implications for mantle composition and processes. *Geological Society, London, Special Publications, 42*(1), 313-345.

Szpoganicz, B., Gidanian, S., Kong, P., & Farmer, P. (2002). Metal binding by melanins: studies of colloidal dihydroxyindole-melanin, and its complexation by Cu (II) and Zn (II) ions. *Journal of Inorganic Biochemistry, 89*(1), 45-53.

Tabuce, R., Tortosa, T., Vianey-Liaud, M., Garcia, G., Lebrun, R., Godefroit, P., Dutour, Y., Berton, S., Valentin, X., & Cheylan, G. (2013). New eutherian mammals from the Late Cretaceous of Aix-en-Provence Basin, south-eastern France. *Zoological Journal of the Linnean Society, 169*(3), 653-672.

Tanaka, G., Parker, A. R., Hasegawa, Y., Siveter, D. J., Yamamoto, R., Miyashita, K., Takahashi, Y., Ito, S., Wakamatsu, K., & Mukuda, T. (2014). Mineralized rods and cones suggest colour vision in a 300 Myr-old fossil fish. *Nature Communications, 5*, 5920.

Taylor, K. G., & Macquaker, J. H. S. (2000). Early diagenetic pyrite morphology in a mudstone-dominated succession: the Lower Jurassic Cleveland Ironstone Formation, eastern England. *Sedimentary Geology, 131*(1), 77-86.

Tegelaar, E. W., de Leeuw, J. W., Derenne, S., & Largeau, C. (1989). A reappraisal of kerogen formation. *Geochimica et Cosmochimica Acta, 53*(11), 3103-3106. doi:http://dx.doi.org/10.1016/0016-7037(89)90191-9

Templier, J., Gallois, N., & Derenne, S. (2013). Analytical TMAH pyrolysis of dipeptides: Formation of new complex cyclic compounds related to the presence of the peptide bond. *Journal of Analytical and Applied Pyrolysis, 104*, 684-694.

Terwagne, G. (2015). Cours de Physique des faisceaux d'ions de haute énergie. Namur: University of Namur.

Thouand, E. (2004). *Biodiversité reptilienne et paléoenvironnement d'un gisement campanien du Bassin d'Aix-en-Provence: La Bastide Neuve (Velaux).*

Tófalo, O. R., & Pazos, P. J. (2010). Paleoclimatic implications (Late Cretaceous–Paleogene) from micromorphology of calcretes, palustrine limestones and silcretes, southern Paraná Basin, Uruguay. *Journal of South American Earth Sciences, 29*(3), 665-675.

Tognarelli, J. M., Dawood, M., Shariff, M. I., Grover, V. P., Crossey, M. M., Cox, I. J., Taylor-Robinson, S. D., & McPhail, M. J. (2015). Magnetic resonance spectroscopy: principles and techniques: lessons for clinicians. *Journal of clinical and experimental hepatology, 5*(4), 320-328.

Tomurtogoo, O., Windley, B. F., Kröner, A., Badarch, G., & Liu, D. Y. (2005). Zircon age and occurrence of the Adaatsag ophiolite and Muron shear zone, central Mongolia, constraints on the evolution of the Mongol-Okhotsk Ocean, suture and orogeny. *Journal of the Geological Society, London, 162*, 125-134.

Toni, M., Dalla Valle, L., & Alibardi, L. (2007). Hard (Beta-) keratins in the epidermis of reptiles: composition, sequence, and molecular organization. *Journal of Proteome Research, 6*, 3377-3392. doi:10.1021/pr0702619

Traverse, A. (1988). *Paleopalynology*. Boston: Unvin Hyman.

Trueman, C., Rogers, R. R., Eberth, D. A., & Fiorillo, A. R. (2007). Trace element geochemistry of bonebeds *Bonebeds: genesis, analysis, and paleobiological significance* (pp. 397-435): University of Chicago Press Chicago.

Trueman, C. N. (1999). Rare earth element geochemistry and taphonomy of terrestrial vertebrate assemblages. *Palaios, 14*(6), 555-568.

Trueman, C. N., & Tuross, N. (2002). Trace elements in recent and fossil bone apatite. *Reviews in mineralogy and geochemistry, 48*(1), 489-521.

Turick, C. E., Tisa, L. S., & Caccavo Jr, F. (2002). Melanin production and use as a soluble electron shuttle for Fe (III) oxide reduction and as a terminal electron acceptor by Shewanella algae BrY. *Applied and Environmental Microbiology, 68*(5), 2436-2444.

Türkmen, İ., Aksoy, E., & Taşgin, C. K. (2007). Alluvial and lacustrine facies in an extensional basin: The Miocene of Malatya basin, eastern Turkey. *Journal of Asian Earth Sciences, 30*(1), 181-198.

Turner, A. H., Makovicky, P. J., & Norell, M. A. (2012). A review of dromaeosaurid systematics and paravian phylogeny.

Turutonova-Ketova. (1950). Some Jurassic seeds and flowers of gymnosperms from Middle Asia and Kazakhstan [Nekotorye yurskie semena n tcvety golosemennykh iz Sredney Azii i Kazakhstana] *Palaeontological questions [Voprosy paleontologii]* (pp. 237-347). Leningrad: Leningrad University.

Upchurch, P., Barrett, P., & Dodson, P. (2004). Sauropoda *The Dinosauria. Second edition.* (pp. 259–322). Berkeley, CA, University of California Press.

Vakhrameev, V. A. (1970). Range and palaeoecology of Mesozoic conifers, the Cheirolepidiaceae. *Paleontological Journal, 4*(1), 12-24.

Vakhrameev, V. A. (1991). Jurassic floras *Jurassic and Cretaceous floras and climates of the Earth*. Cambridge: Cambridge University Press.

Valentin, X., Godefroit, P., Tabuce, R., Vianey-Liaud, M., Wu, W., & Garcia, G. (2012). First late Maastrichtian (latest Cretaceous) vertebrate assemblage from Provence (Vitrolles-la-Plaine, southern France) *Bernissart Dinosaurs and Early Cretaceous Terrestrial Ecosystems. Indiana University Press, Bloomington* (pp. 582-597).

van Bergen, P. F., Collinson, M. E., Hatcher, P. G., & de Leeuw, J. W. (1994). Lithological control on the state of preservation of fossil seed coats of water plants.*Organic Geochemistry, 22*(3),683-702. doi:http://dx.doi.org/10.1016/0146-6380(94)90133-3

Varnes, D. J. (1978). Slope movement types and processes. *Special report, 176*, 11-33.

Védrine, S., Strasser, A., & Hug, W. (2007). Oncoid growth and distribution controlled by sea-level fluctuations and climate (Late Oxfordian, Swiss Jura Mountains). *Facies, 53*(4), 535-552.

Vila, B., Galobart, A., Canudo, J., Le Loeuff, J., Dinarès-Turell, J., Riera, V., Oms, O., Tortosa, T., & Gaete, R. (2012). The diversity of sauropod dinosaurs and their first taxonomic succession from the latest Cretaceous of southwestern Europe: clues to demise and extinction. *Palaeogeography, Palaeoclimatology, Palaeoecology, 350*, 19-38.

Vinther, J. (2015). A guide to the field of palaeo colour. *BioEssays, 37*(6), 643-656.

Vinther, J., Briggs, D. E., Clarke, J., Mayr, G., & Prum, R. O. (2009). Structural coloration in a fossil feather. *Biology Letters*, rsbl20090524.

Vinther, J., Briggs, D. E., Prum, R. O., & Saranathan, V. (2008). The colour of fossil feathers. *Biology Letters, 4*(5), 522-525.

Vinther, J., Nicholls, R., Lautenschlager, S., Pittman, M., Kaye, T. G., Rayfield, E., Mayr, G., & Cuthill, I. C. (2016). 3D camouflage in an ornithischian dinosaur. *Current Biology, 26*(18), 2456-2462.

Viseras, C., Soria, J. M., Durán, J. J., Pla, S., Garrido, G., García-García, F., & Arribas, A. (2006). A large-mammal site in a meandering fluvial context (Fonelas P-1, Late Pliocene, Guadix Basin, Spain): sedimentological keys for its paleoenvironmental reconstruction. *Palaeogeography, Palaeoclimatology, Palaeoecology, 242*(3), 139-168.

Vogt, T. (1927). *Sulitelmafeltets geologi og petrografi*: Aschehoug i. Komm.

Voorhies, M. R. (1969). *Sampling difficulties in reconstructing late Tertiary mammalian communities.* Paper presented at the Proceedings North American Palaeontological Convention, Part E.

Vorontsov, A. A., Yarmolyuk, V. V., & Komaritsyna, T. Y. (2016). Late Mesozoic – Early Cenozoic rifting magmatism in the Uda sector of Western Transbaikalia. *Russian Geology and Geophysics, 57*, 723-744.

Wang, B., Yang, W., McKittrick, J., & Meyers, M. A. (2016). Keratin: Structure, mechanical properties, occurrence in biological organisms, and efforts at bioinspiration. *Progress in Materials Science, 76*, 229-318.

Wang, B., Zhao, F., Zhang, H., Fang, Y., & Zheng, D. (2012). Widespread pyritization of insects in the Early Cretaceous Jehol Biota. *Palaios, 27*(10), 708-712.

Wang, T., Guo, L., Zhang, L., Yang, Q., Zhang, J., Tong, Y., & Ye, K. (2015a). Timing and evolution of Jurassic-Cretaceous granitoid magmatisms in the

Mongol-Okhotsk Belt and adjacent areas, NE Asia: implications for transition from contractional crustal thickening to extensional thinning and geodynamic settings. *Journal of Asian Earth Sciences, 97*, 365-392.

Wang, T., Guo, L., Zhang, L., Yang, Q., Zhang, J., Tong, Y., & Ye, K. (2015b). Timing and evolution of Jurassic–Cretaceous granitoid magmatisms in the Mongol–Okhotsk belt and adjacent areas, NE Asia: Implications for transition from contractional crustal thickening to extensional thinning and geodynamic settings. *Journal of Asian Earth Sciences, 97*, 365-392.

Wang, X., O'Connor, J. K., Zheng, X., Wang, M., Hu, H., & Zhou, Z. (2014). Insights into the evolution of rachis dominated tail feathers from a new basal enantiornithine (Aves: Ornithothoraces). *Biological Journal of the Linnean Society, 113*(3), 805-819.

Wang, X., Pittman, M., Zheng, X., Kaye, T. G., Falk, A. R., Hartman, S. A., & Xu, X. (2017). Basal paravian functional anatomy illuminated by high-detail body outline. *Nature Communications, 8*, 14576.

Wang, Y.-X., & Cao, X.-J. (2012). Extracting keratin from chicken feathers by using a hydrophobic ionic liquid. *Process Biochemistry, 47*(5), 896-899.

Watt, B., Raposo, G., & Marks, M. (2010). Functional Amyloid Aggregation.

Webby, B. (1959). Sedimentation of the alternating greywacke and argillite strata in the Porirua district. *New Zealand journal of geology and geophysics, 2*(3), 461-478.

Wedel, M. (2007). What pneumaticity tells us about 'prosauropods', and vice versa. *Special Papers in Palaeontology, 77*, 207-222.

Wellnhofer, P. (1991). *The illustrated encyclopedia of pterosaurs*: Crescent Books.

Wellnhofer, P. (2009). *Archaeopteryx: The icon of evolution*: F. Pfeil.

Westall, F. (1999). The nature of fossil bacteria: a guide to the search for extraterrestrial life. *Journal of Geophysical Research: Planets, 104*(E7), 16437-16451.

Westall, F., Boni, L., & Guerzoni, E. (1995). The experimental silicification of microorganisms. *Palaeontology, 38*(3), 495-528.

Westphal, M., & Durand, J. P. (1989). An Upper Cretaceous paleomagnetic pole for stable Europe from Aix-en-Provence (France). *Earth and Planetary Science Letters, 94*(1-2), 143-150.

Wilby, P. R., Briggs, D. E., & Riou, B. (1996). Mineralization of soft-bodied invertebrates in a Jurassic metalliferous deposit. *Geology, 24*(9), 847-850.

Williams, C. T., Henderson, P., Marlow, C. A., & Molleson, T. I. (1997). The environment of deposition indicated by the distribution of rare earth elements in fossil bones from Olduvai Gorge, Tanzania. *Applied Geochemistry, 12*(4), 537-547.

Williams, M., Siveter, D. J., Ashworth, A. C., Wilby, P. R., Horne, D. J., Lewis, A. R., & Marchant, D. R. (2008). Exceptionally preserved lacustrine ostracods from the Middle Miocene of Antarctica: implications for high-latitude palaeoenvironment at 77 south. *Proceedings of the Royal Society of London B: Biological Sciences, 275*(1650), 2449-2454.

Wilson, M. (2004). Weathering of the primary rock-forming minerals: processes, products and rates. *Clay Minerals, 39*(3), 233-266.

Witte, E., Schenk, H., Müller, P., & Schwochau, K. (1988). Structural modifications of kerogen during natural evolution as derived from ^{13}C CP/MAS NMR, IR

spectroscopy and Rock-Eval pyrolysis of Toarcian shales. *Organic Geochemistry, 13*(4-6), 1039-1044.

Wogelius, R., Manning, P., Barden, H., Edwards, N., Webb, S., Sellers, W., Taylor, K., Larson, P., Dodson, P., & You, H. (2011). Trace metals as biomarkers for eumelanin pigment in the fossil record. *Science, 333*(6049), 1622-1626.

Wondrak, G. T., Jacobson, M. K., & Jacobson, E. L. (2006). Endogenous UVA-photosensitizers: mediators of skin photodamage and novel targets for skin photoprotection. *Photochemical & Photobiological Sciences, 5*(2), 215-237.

Woodin, A. (1954). Molecular size, shape and aggregation of soluble feather keratin. *Biochemical journal, 57*(1), 99.

Wright, V. (1992). Paleosol recognition: a guide to early diagenesis in terrestrial settings. *Developments in Sedimentology, 47*, 591-619.

Wright, V. P., Zarza, A. A., Sanz, M., & Calvo, J. (1997). Diagenesis of late Miocene micritic lacustrine carbonates, Madrid Basin, Spain. *Sedimentary Geology, 114*(1), 81-95.

Xing, L., McKellar, R. C., Xu, X., Li, G., Bai, M., Persons, W. S., Miyashita, T., Benton, M. J., Zhang, J., & Wolfe, A. P. (2016). A feathered dinosaur tail with primitive plumage trapped in Mid-Cretaceous amber. *Current Biology, 26*(24), 3352-3360.

Xu, X., Currie, P., Pittman, M., Xing, L., Meng, Q., Lü, J., Hu, D., & Yu, C. (2017). Mosaic evolution in an asymmetrically feathered troodontid dinosaur with transitional features. *Nature Communications, 8*, 14972.

Xu, X., Forster, C. A., Clark, J. M., & Mo, J. (2006). A basal ceratopsian with transitional features from the Late Jurassic of northwestern China. *Proceedings of the Royal Society of London B: Biological Sciences, 273*(1598), 2135-2140.

Xu, X., & Guo, Y. (2009). The origin and early evolution of feathers: insights from recent paleontological and neontological data. *Vertebrata PalAsiatica, 47*(4), 311-329.

Xu, X., Harbert, W., Dril, S., & Kravchinsky, V. (1997). New paleomagnetic data from the Mongol-Okhotsk collision zone, Chita region, south-central Russia: implications for Paleozoic paleogeography of the Mongol-Okhotsk Ocean. *Tectonophysics, 269*, 113-129.

Xu, X., & Norell, M. A. (2004). A new troodontid dinosaur from China with avian-like sleeping posture. *Nature, 431*(7010), 838-841.

Xu, X., Norell, M. A., Wang, X.-l., Makovicky, P. J., & Wu, X.-c. (2002). A basal troodontid from the Early Cretaceous of China. *Nature, 415*(6873), 780-784.

Xu, X., Wang, K., Zhang, K., Ma, Q., Xing, L., Sullivan, C., Hu, D., Cheng, S., & Wang, S. (2012). A gigantic feathered dinosaur from the Lower Cretaceous of China. *Nature, 484*(7392), 92-95.

Xu, X., Wang, X.-L., & Wu, X.-C. (1999). A dromaeosaurid dinosaur with a filamentous integument from the Yixian Formation of China. *Nature, 401*(6750), 262-266.

Xu, X., You, H., Du, K., & Han, F. (2011). An *Archaeopteryx*-like theropod from China and the origin of Avialae. *Nature, 475*(7357), 465-470.

Xu, X., & Zhang, F. (2005). A new maniraptoran dinosaur from China with long feathers on the metatarsus. *Naturwissenschaften, 92*(4), 173-177.

Xu, X., Zhao, Q., Norell, M., Sullivan, C., Hone, D., Erickson, G., Wang, X. L., Han, F. L., & Guo, Y. (2009a). A new feathered maniraptoran dinosaur fossil that fills a morphological gap in avian origin. *Chinese Science Bulletin, 54*(3), 430-435.

Xu, X., Zheng, X., Sullivan, C., Wang, X., Xing, L., Wang, Y. X., Zhang, X., O'Connor, J. K., Zhang, F., & Pan, Y. (2015). A bizarre Jurassic maniraptoran theropod with preserved evidence of membranous wings. *Nature, 521*(7550), 70-73. doi:10.1038/nature14423

Xu, X., Zheng, X., & You, H. (2009b). A new feather type in a nonavian theropod and the early evolution of feathers. *Proceedings of the National Academy of Sciences, 106*(3), 832-834.

Xu, X., Zheng, X., & You, H. (2010). Exceptional dinosaur fossils show ontogenetic development of early feathers. *Nature, 464*(7293), 1338.

Xu, X., Zhong-he, Z., & Prum, R. O. (2001). Branched integumental structures in *Sinornithosaurus* and the origin of feathers. *Nature, 410*(6825), 200.

Xu, X., Zhou, Z., Wang, X., & Kuang, X. (2003). Four-winged dinosaurs from China. *Nature, 421*(6921), 335.

Yang, J.-H., Wu, F.-Y., Shao, J. A., Wilde, S. A., Xie, L.-W., & Liu, X.-M. (2006). Constraints on the timing of uplift of the Yanshan Fold and Thrust Belt, North China. *Earth and Planetary Science Letters, 246*, 336-352. doi:10.1016/j.epsl.2006.04.029

Yang, W., & Li, S. (2008). Geochronology and geochemistry of the Mesozoic volcanic rocks in Western Liaoning: implications for lithospheric thinning of the North China Craton. *Lithos, 102*(1), 88-117.

Yoshimizu, H., & Ando, I. (1990). Conformational characterization of wool keratin and 5'-(Carboxymethy1) kerateine in the solid state by ^{13}C CP/MAS NMR spectroscopy. *Macromolecules, 23*, 2908-2912.

Yoshimizu, H., Mimura, H., & Ando, I. (1991). ^{13}C CP/MAS NMR study of the conformation of stretched or heated low-sulfur keratin protein films. *Macromolecules, 24*(4), 862-866.

Yu, B., Dong, H., Jiang, H., Lv, G., Eberl, D., Li, S., & Kim, J. (2009). The role of clay minerals in the preservation of organic matter in sediments of Qinghai Lake, NW China. *Clays and Clay Minerals, 57*(2), 213-226.

Yuan, H., Liu, X., Liu, Y., Gao, S., & Ling, W. (2005). Geochemistry and U-Pb zircon geochronology of Late-Mesozoic lavas from Xishan, Beijing. *Science in China: Series D Earth Sciences, 49*(1), 50-67. doi:10.1007/s11430-004-0009-y

Zelenitsky, D. K., Therrien, F., Erickson, G. M., DeBuhr, C. L., Kobayashi, Y., Eberth, D. A., & Hadfield, F. (2012). Feathered non-avian dinosaurs from North America provide insight into wing origins. *Science, 338*(6106), 510-514.

Zhang, F., Kearns, S. L., Orr, P. J., Benton, M. J., Zhou, Z., Johnson, D., Xu, X., & Wang, X. (2010). Fossilized melanosomes and the colour of Cretaceous dinosaurs and birds. *Nature, 463*(7284), 1075.

Zhang, F., Zhou, Z., & Dyke, G. (2006). Feathers and 'feather-like'integumentary structures in Liaoning birds and dinosaurs. *Geological Journal, 41*(3-4), 395-404.

Zhang, H., Wang, M. X., & Liu, X. M. (2008). Constraints on the upper boundary age of the Tiaojishan Formation volcanic rocks in West-Liaoning –North Hebei by LA-ICP-MS dating. *Chinese Science Bulletin, 53*(22), 3574-3584.

Zhang, M., Dai, S., Heimhofer, U., Wu, M., Wang, Z., & Pan, B. (2014). Palynological records from two cores in the Gongpoquan Basin, central East Asia: Evidence for floristic and climatic change during the Late Jurassic to Early Cretaceous. *Review of Palaeobotany and Palynology, 204*, 1-17.

Zhang, Q., Liebeck, B. M., Yan, K., Demco, D. E., Körner, A., & Popescu, C. (2012). Alpha-helix self-assembly of oligopeptides originated from beta-sheet keratin. *Macromolecular chemistry and physics, 213*, 2628-2638.

Zheng, X.-T., You, H.-L., Xu, X., & Dong, Z.-M. (2009a). An Early Cretaceous heterodontosaurid dinosaur with filamentous integumentary structures. *Nature, 458*(7236), 333-336.

Zheng, X., O'connor, J., Huchzermeyer, F., Wang, X., Wang, Y., Wang, M., & Zhou, Z. (2013a). Preservation of ovarian follicles reveals early evolution of avian reproductive behaviour. *Nature, 495*(7442), 507.

Zheng, X., Zhou, Z., Wang, X., Zhang, F., Zhang, X., Wang, Y., Wei, G., Wang, S., & Xu, X. (2013b). Hind wings in basal birds and the evolution of leg feathers. *Science, 339*(6125), 1309-1312.

Zheng, X. T., You, H. L., Xu, X., & Dong, Z. M. (2009b). An Early Cretaceous heterodontosaurid dinosaur with filamentous integumentary structures. *Nature, 458*, 333-336.

Zhou, Z., Jin, F., & Wang, Y. (2010). Vertebrate assemblages from the middle-late Jurassic Yanliao Biota in Northeast China. *Earth Science Frontiers, 17*(Special Issue), 252-254.

Zhou, Z., & Li, F. Z. Z. (2009). A new Lower Cretaceous bird from China and tooth reduction in early avian evolution. *Proceedings of the Royal Society of London B: Biological Sciences*, rspb20090885.

Zhou, Z., & Wang, Y. (2010). Vertebrate diversity of the Jehol Biota as compared with other lagerstätten. *Science China Earth Sciences, 53*(12), 1894-1907.

Zhou, Z., & Zhang, F. (2002a). Largest bird from the Early Cretaceous and its implications for the earliest avian ecological diversification. *Naturwissenschaften, 89*(1), 34-38.

Zhou, Z., & Zhang, F. (2002b). A long-tailed, seed-eating bird from the Early Cretaceous of China. *Nature, 418*(6896), 405.

Zhou, Z., & Zhang, F. (2003). Anatomy of the primitive bird *Sapeornis chaoyangensis* from the Early Cretaceous of Liaoning, China. *Canadian Journal of Earth Sciences, 40*(5), 731-747.

Zhu, M., Babcock, L. E., & Steiner, M. (2005a). Fossilization modes in the Chengjiang Lagerstätte (Cambrian of China): testing the roles of organic preservation and diagenetic alteration in exceptional preservation. *Palaeogeography, Palaeoclimatology, Palaeoecology, 220*, 31-46. doi:10.1016/j.palaeo.2003.03.001

Zhu, M., Babcock, L. E., & Steiner, M. (2005b). Fossilization modes in the Chengjiang Lagerstätte (Cambrian of China): testing the roles of organic preservation and diagenetic alteration in exceptional preservation. *Palaeogeography, Palaeoclimatology, Palaeoecology, 220*(1), 31-46.

Zorin, Y. A. (1999). Geodynamics of the western part of the Mongolia-Okhotsk collisional belt, Trans-Baikal region (Russia) and Mongolia. *Tectonophysics, 306*, 33-56.

Zorin, Y. A., Belichenko, V. G., Turutanov, E. K., Mazukabzov, A. M., Sklyarov, E. V., & Mordvinova, V. V. (1995). The East Siberia transect. *International Geology Review, 37*(2), 154-175.

Zorin, Y. A., Zorina, L. D., Spiridonov, A. M., & Rutshtein, I. G. (2001). Geodynamic setting of gold deposits in eastern and central Trans-Baikal (Chita Region, Russia). *Ore Geology Reviews, 17*, 215-232.


J. Dos Remedios